Multiscale mathematical biology

Lisanne Rens

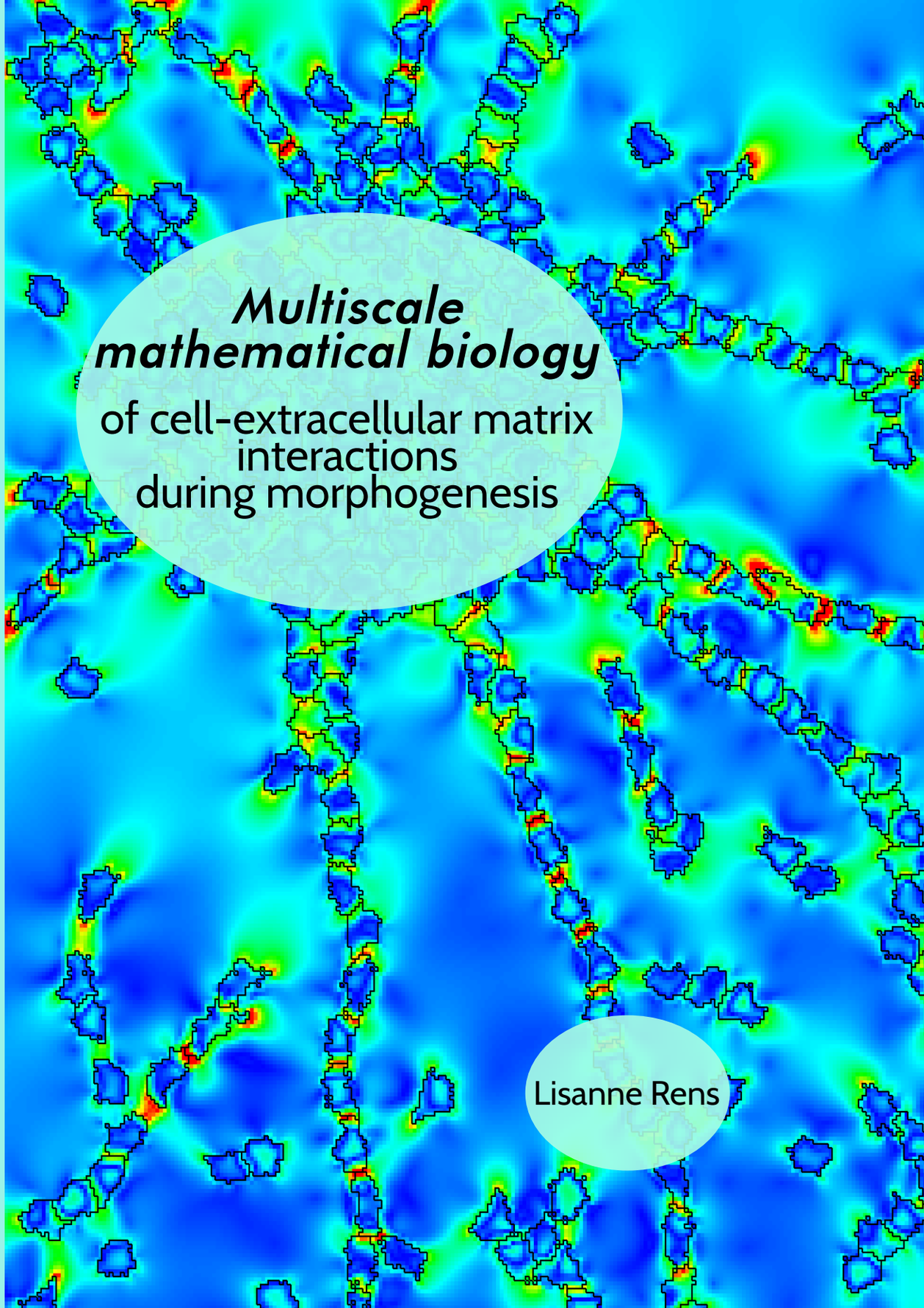

Stellingen

behorende bij het proefschrift

Multiscale mathematical biology of cell-extracellular matrix interactions during morphogenesis

van

Elisabeth Rens

1. Cel-celcommunicatie door middel van krachten uitgeoefend op de extracellulaire matrix leidt in computersimulaties tot de formatie van netwerkachtige structuren (Hoofdstuk 2).

2. Door willekeurige bewegingen te maken, kunnen cellen “ontsnappen” uit een aggregaat en door middel van communicatie tussen cellen via krachten in de matrix ontstaan spruiten in computersimulaties (Hoofdstuk 2).

3. Door een gerekte matrix lokaal nog meer op te rekken kunnen gesimuleerde cellen zich beter langs de rek oriënteren (Hoofdstuk 3).

4. Doordat gesimuleerde cellen sneller krachten kunnen uitoefenen op stijvere substraten dan op flexibele substraten en daardoor de cel-substraatbindingen verstevigen, kunnen ze zich uitspreiden over een stijf substraat. (Hoofdstuk 4).

5. Doordat gesimuleerde cellen op een substraat met een stijfheidsgradiënt zich sterker binden aan de stijvere kant van het substraat, kunnen cellen naar stijvere delen van het substraat migreren. (Hoofdstuk 4).

6. Het versnellen van het klieven van een eiwit naar zijn gematureerde vorm in de cel kan de reikwijdte van de eiwitgradiënt in de extracellulaire ruimte vergroten (Hoofdstuk 5).

7. Een gesimuleerd weefsel kan zich vertakken door een chemische stof uit te scheiden die lokaal celbewegingen onderdrukt (Hoofdstuk 6).

8. Een wiskundig model is uitermate geschikt voor mechanobiologisch onderzoek omdat mechanische en chemische processen losgekoppeld kunnen worden om ze afzonderlijk te bestuderen.

9. Door stap voor stap fysische krachten en biologische schalen aan een wiskundig model toe te voegen kunnen we gedetailleerder inzicht verkrijgen in het effect van schaalinteracties in mechanobiologie.

10. Een wiskundig model kan pas opgeschaald worden naar een meercellig systeem als het gedrag van de individuele cellen voldoende goed beschreven wordt.

11. Niet-significante variaties in fysische krachten op celniveau kunnen significante veranderingen teweegbrengen op het weefselniveau.

12. Een kwantitatieve fit van een wiskundig model aan een experimenteel model beperkt zich tot dat modelsysteem, terwijl een kwalitatief model inzicht kan geven in de biologie onafhankelijk van deze speciale context.

13. Het verenigen van equivalente computationele modellen tot een standaard set generieke modellen zou samenwerkingsverbanden binnen de biologische wetenschap kunnen bevorderen.

14. Het versnellen van multischaal modelsimulaties biedt de mogelijkheid om het model op een relevante schaal toe te passen in klinische praktijken.

15. Een goed geschreven artikel draagt bij aan de wetenschappelijke impact van interessante resultaten.

16. In tegenstelling tot een computationeel bioloog, kan een computationeel biologe tijdens haar promotieonderzoek ook een embryologisch *in vivo* experiment uitvoeren.

17. De aanwezigheid van kolfruimtes op wetenschappelijke conferenties zou de participatie van wetenschapsters met jonge kinderen kunnen bevorderen.

Multiscale mathematical biology of cell-extracellular matrix interactions during morphogenesis

Elisabeth Rens

ISBN: XXX-XX-XXXX-XXX-X

Printed by X

Multiscale mathematical biology of cell-extracellular matrix interactions during morphogenesis

Proefschrift

ter verkrijging van
de graad van Doctor aan de Universiteit Leiden,
op gezag van Rector Magnificus prof.mr. C.J.J.M. Stolker,
volgens besluit van het College voor Promoties
te verdedigen op dag datum maand 2018
klokke XX.XX uur

door

Elisabeth Géraldine Rens
geboren te Hoorn
in 1990

Promotiecommissie:

Promotor:	prof.dr. Roeland M.H. Merks
Voorzitter:	prof.dr. Adrianus W. van der Vaart
Overige leden:	prof.dr. Peter D. Grünwald
	prof.dr. Ulrich S. Schwarz
	prof.dr. Thomas Schmidt
	dr.ir. Sandra Loerakker

This research has been carried out at Centrum Wiskunde & Informatica (CWI) in the Scientific Computing group. The investigations were supported by the Division for Earth and Life Sciences (ALW; Vidi 864.10.009) with financial aid from the Netherlands Organization for Scientific Research (NWO).

Voor Daniel,
mijn onderzoekend mannetje

Contents

1

Introduction

This chapter is in part based on

Antonivici CC, Boas SEM, Rens EG, Tahir H and Merks RMH, Multiscale Analysis of Morphogenesis (2016) In P.D Stahl, R.A Bradshaw, D A. Lauffenburger, J M. Haugh, H.M Byrne, & R Linding (Eds.), Encyclopedia of Cell Biology, Academic Press/Elsevier,

Boas SEM, Jiang Y, Merks RMH, Prokopiou SA and Rens EG, Cellular Potts model: applications to vasculogenesis and angiogenesis (2016) In: Louis, P.-Y. and Nardi, F.R. (Eds.) Probabilistic Cellular Automata: Theory, Applications and Future Perspectives Springer. (in press)

and

Hirashima T, Rens EG and Merks RMH, Cellular Potts modeling of complex multicellular behaviors in tissue morphogenesis (2017) Development Growth and Differentiation 59(5):329-339

1.1 Morphogenesis

Every multi-cellular organism originates from a single fertilized egg cell. This cell multiplies and the resulting clump of cells undergoes complex shape changes to form different tissues and organs, resulting in a full functioning organism. This process is called morphogenesis and involves a seemingly fixed choreography of cells, which move collectively while differentiating and interacting with each other. Much like in a ballet choreography, slight missteps of a member of the *corps de ballet*, will not result in a complete failure of the formation. Indeed, the mechanisms behind morphogenesis are quite robust. However, if many members fail to do their part, and errors are not compensated, the resulting formation will not be right. Indeed, failure of migration and differentiation of cells during embryonic growth leads to numerous birth defects, such as cardiac diseases.

Morphogenesis is not only important during embryonic growth, it also plays a crucial role throughout development. During the lifetime of an organism, cells reorganize and reshape tissues to maintain optimal functioning of organs. For example, capillaries continuously reorganize in order to keep properly distributing the oxygen in the body and comply to the changing demands of the surrounding tissues [1]. The ability of tissues to adapt can be very helpful. Continuing on the example of blood vessels, the growth of new blood vessels during wound healing supplies the new tissue with oxygen. Blood vessel formation, however, may also be harmful. Excessive growth of blood vessels induced by a tumor can further progress growth of the tumor and metastases [2, 3]. Thus, morphogenesis is involved in tissue homeostasis, healing and disease. In order to better treat diseases and heal organs, we need a good understanding of the mechanisms behind morphogenesis.

Due to great progress in genetic sciences since the 1970s, developmental biology has largely focused on gene regulation of developmental growth and disease. It was, and is, often investigated how the knock-out or over-expression of genes affects the shape and state of the organism [4, 5]. Such studies provided us with insights into which genes control which developmental process and which diseases are associated with them [4, 5]. Furthermore, it is even possible to visualize the activity of multiple genes concurrently [6]. This enables the association of spatial and temporal patterns of gene expressions with the development of organs and disease [7]. However, such data does not fully explain how and what cell behavior, that is regulated by gene expressions, drives the growth and form of multicellular organisms. Signaling molecules that affect the transcription rate of genes, either directly or indirectly through a gene regulatory network, are often considered to regulate morphogenesis. Signaling molecules are produced by cells and diffuse through the tissue. If cell behavior depends on the local level of the signaling molecule, a cell can “read out” its position based on the distribution/gradient of the signaling molecule [8]. In 1952, Alan Turing showed that two diffusive chemicals that react with one another, can produce patterns such as stripes and spots, depending on their diffusibility [9]. Such chemicals were termed “morphogens” and their concentration gradients have since often been postulated to drive

various morphogenetic processes. For instance, reducing the binding rate of the signaling molecule FGF10, involved in epithelial branching, to the substrate lowered its diffusion rate and as a result the tissue branched instead of elongated [10]. Gradients of morphogens are thought to provide tissues with global positional information [8] by regulating cell proliferation, differentiation and motility through gene transcription. Non-diffusive membrane-bound signaling molecules can also regulate morphogenesis by inducing cell-cell communication. For instance, in the Delta-Notch signaling pathway [11], Delta production of one cell activates Notch in a neighbouring cell, inhibiting the production of Delta. This mechanism results in a salt-pepper pattern of two cell types in a tissue [12]. Thus, both global and local chemical signaling can drive morphogenesis.

1.1.1 Physical forces in development

It has become increasingly clear that not only chemical signals but also mechanical forces, originating from, for instance, tissue movements, greatly impact morphogenesis. In 1917, D'Arcy Thompson published his famous book "On Growth and Form" [13], where he argued how physical forces and environmental constraints can shape biological forms, such as cells and whole organisms. If a tissue is subject to forces, it undergoes shape changes, similar to non-biological materials. A recent example of this phenomenon is a physical model resembling the gut, made of silicone rubber, attached to a latex sheet resembling the dorsal mesenteric sheet, which showed that differential growth of the two tissues may drive looping of the gut [14]. Experimental data seems to confirm this mechanism, as the gut tube experiences strain due to tension of the mesentery and only loops when attached to it [14]. Theoretical modeling of elastic tissues has given further insight into how physical forces and environmental constraints can mediate shape changes, such as bending, buckling and extensions of tissues [15]. Besides such "passive" responses of tissues to forces, the cells in tissues also change their activity in response to force. Physical forces can change gene expression and other intracellular activities. For instance, mechanical loading of bone stimulates osteocytic cells to produce bone and also inhibits osteoclasts to break down bone [16]. Intricate interplays between osteocytes and osteoclasts is thought to regulate the formation of bone in response to mechanical loading [17, 18]. Because of the increasing evidence of the ability of forces to drive development, physical forces are thought to play an equally important role as chemical signaling in morphogenesis.

1.1.2 The cell as a contractile apparatus

Similar to chemical signaling, mechanical forces can originate from surrounding tissues or at a local level. In 1980, Harris and coworkers showed that mechanical forces can originate locally from cells itself [19]. By placing a cell on a silicone rubber substrata, the substrate started to wrinkle, indicating that cells apply forces to their environment [19]. Indeed, it has become clear that the cytoskeleton is able to resist

and generate forces, making the cell a mechanically active material. As a result, the cell has been modeled by a tensegrity model, which is originally a structural principle coined by the architect Buckminster Fuller and first applied to describe cell structure by Donald Ingber [20]. In this model, cells are thought to stabilize in shape by a balance of forces between tensed actin filaments, intermediate filaments, compressed microtubules within the cytoskeleton and adherence to its environment (Figure 1.1).

Actin filaments can assemble in large load bearing structures called stress fibers, which are actin filaments bundled by non-muscle myosin II molecules. Through hydrolysis of ATP, myosin motors convert chemical energy into mechanical energy and walk along the connected actin filaments, which makes the stress fiber become tensed [22]. This allows a cell to generate significant forces (locally up to tens of nano Newtons [23]), and since stress fibers attach to cell adhesion molecules at the membrane, these forces are transmitted to what the cell adheres to.

Cells in tissues adhere to each other through the Cadherin adhesion molecules, that link to the cytoskeleton [24], which allows for force transmission between cells in tissues. Long range force transmission has been shown to regulate tissue shaping. For instance, dorsal closure of *Drosophila melanogaster* (fruitfly) is mediated by the propagation of stresses, originating from collective cell contractions at various places of origin in the embryo (reviewed in [25]). Cell contraction via actin-myosin has been implicated in many other developmental processes, such as tissue elongation and collective cell migration (reviewed in [26]).

1.1.3 Mechanical interactions with the extracellular matrix

Cells in tissues are surrounded by the *extracellular matrix* (ECM), an interconnected network of fibers and proteins that supports tissues. By adhering to and applying forces on the ECM, cells are able to sense and respond to the mechanical cues in the ECM. The architecture of the ECM mediates cell migration [27]; cells move up ECM density gradients (haptotaxis), matrix stiffness gradients (durotaxis) and along fibers (contact guidance). Not only do cells respond to the structure of the ECM, but they can also actively change its local architecture. Cells deposit matrix fibers, reorient, degrade and link the fibers in the ECM. Also, cells locally stiffen the matrix either by contracting it, or by depositing matrix fibers. Because cells sense matrix deformations generated by adjacent cells, matrix remodeling allows cells to communicate via the ECM.

Advances in *in vitro* modeling of cells and the extracellular matrix has given more insight into mechanical cell-cell communication [28]. In such studies, synthetic gels or naturally-derived gels are used to mimic the extracellular matrix. Matrigel is a natural gel that contains a mixture of extracellular matrix proteins, such as growth factors and collagen fibers. Although Matrigel mimics the complex environment well, it is difficult to tune separate effects, such as fiber density or matrix stiffness or exclude the effects of unknown components of the gel. Instead, synthetic gels may be used, of which the components are controlled and its mechanical properties are tunable [29,

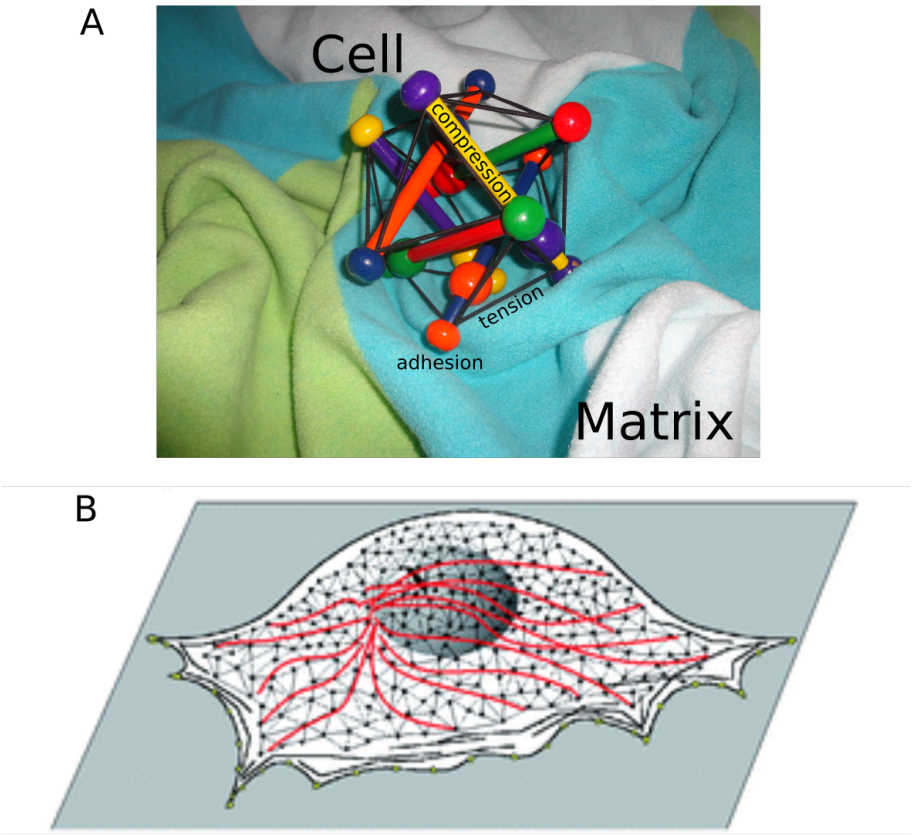

Figure 1.1: Tensegrity model of the cell its cytoskeleton. (A) A tensegrity toy illustrates the principle of a self-stabilizing network of compressed struts and tensed cables, courtesy of Daniel Lont; (B) A schematic representation of a cell adherent to the extracellular matrix. Red shows radially oriented microtubles that oppose the oppose the inward-directed forces of the actomyosin network depicted in black. Panel B was reproduced in part from [21] with permission of The Royal Society of Chemistry.

30]. An example of synthetic gels are polyacrylamide (PA) gels, which are flexible substrates with tunable stiffness. These gels are derivatized with RGD peptides or coated with matrix fibers, to allow cell-substrate binding.

PA gels have been used to reconstruct cell traction forces based on matrix deformations [31]. Similar experimental set-ups were used to show that these traction forces can mediate cell-cell communication (*e.g.* [32], Figure 1.2A). In this study [32], it was shown that cell-cell contact depends on the stiffness of the substrate. On the softest substrates, cells adhere to one another while on substrates of intermediate stiffness cells repeatedly touch and break contact. On the stiffest substrates, the cells first make contact but then migrate away. The cells were able to apply sufficient force to create substrate deformations under nearby cells and the range of substrate deformation was correlated with the separation distance between cells. This study showed that cells communicate short range ($\approx$ 25 μm) through matrix stresses on PA gels. The range of communication is much longer on collagen gels, and can even be up to 450 μm, depending on cell type and gel stiffness [33]. Long range communication has been attributed to strain-stiffening of fibrous gels [33, 34]. Indeed, cells can apply sufficient force to strain-stiffen the matrix (Figure 1.2B). This allows cells to elongate and align with one another, forming network-like structures [33]. Network formation has often been observed and depends on the magnitude of cell force, substrate stiffness and substrate density [35, 36]. Besides network formation, local substrate deformations also regulate other processes such as collective cell migration [37, 38].

Cells can also steer the migration of other cells by means of traction force induced realignment of matrix fibers [39, 40], to which cells migrate along by contact guidance. Since fibers are quite long and can span multiple cells, they allow for long range communication. Based on experimental images of cells and matrix fibers, a computational study was performed to that suggests that fiber alignment is crucial long range stress propagation (Figure 1.2C).

Theoretical models

Many theoretical models were developed to understand how cells respond to mechanical cues in the matrix [41, 42]. Theoretical models were often based on homeostatic principles, motivated by experimental observations of cells that maintain local stresses or strains in the substrate [43, 44]. For instance, a theoretical model of cells represented as contractile dipole forces suggested that cells can reorient to matrix stress if it attempts to maintain either local stresses or strains. Furthermore, either stress or strain optimization allowed cells to move towards neighboring cells. Using a similar theoretical model, it was proposed that cells minimize the amount of work needed to contract the matrix [45]. This allows cells to align to each other and form networks-like structures [46]. However, it is still poorly understood how and why a cell would maintain local stresses or strains or minimize the amount of work. Cytoskeleton remodeling is governed by the dynamics of stress fibers and cell-matrix adhesions, which are in turn influenced by matrix stresses and thus are considered to regulate the response of cells

to matrix mechanics. Theoretical models have suggested that cells can respond to matrix stresses by aligning stress fibers, upregulating traction forces [47] and stabilizing cell-matrix adhesions [48, 49]. Although such models have provided further insight into how cells can respond to the ECM, it is still poorly understood how this affects tissue organization.

Cell-cell communication through matrix stresses are very relevant to many morphogenetic processes. For instance, sprouting cells from an aggregate has been shown to be mediated by traction force induced reorientation of matrix fibers, which guides the directional outgrowth of cells [40, 51]. Furthermore, during Drosophila egg development, collagen deposition of cells generate a stiffness gradient, which instructs elongation of the follicle [52]. However, excessive matrix remodeling, which may occur during wound healing and is associated with fibrotic diseases, can lead to organ dysfunction [53]. Also, cancerous cells can significantly reorient and stiffen the matrix, which allows a tumor to grow and metastasize [53]. In conclusion, cell-matrix interactions have been implicated in morphogenesis, homeostasis and disease.

A better understanding of how cell-matrix interactions shape tissues, can greatly benefit medicine. For instance, cancer therapy would benefit from a better understanding on how the mechanical properties of cells and the matrix may drive cancer progression [53]. Cancer metastasis is associated with increased remodeling of the matrix [53]. By targeting, for instance, enzymes involved in matrix remodeling, we could obtain new therapeutic agents for cancer therapy [53]. Furthermore, mechanical loading of artificial tissues regulates the orientation and structural integrity of the tissue [54]. Artificial tissues may be implemented to promote healing of a damaged organ or even replace it and the efficiency of tissue engineered constructs depends on how well the artificial tissue resembles the present *in vivo* tissue structure [55]. So, a better understanding of how forces regulate tissue formation can benefit the design of such constructs [56].

1.2 Mathematical modeling of morphogenesis

Because of the complexity of biology, it is very challenging to study morphogenesis by solely doing experimental studies. Mathematical modeling has become a useful tool to study morphogenesis and has many benefits. In contrast to experimental approaches, in a mathematical model, every variable can be tracked, and it is relatively easy to knock out specific mechanisms or variables and interactions, while maintaining others. Hypotheses from experimental observations can be formulated in mathematical equations. Solving or simulating mathematical models can thus help us understand how certain mechanisms influence the behavior of the system [57]. Furthermore, models can be used to investigate how different mechanisms interact in a system. A mathematical model can also be used to make a prediction about the experimental system [57].

Mathematical models can be used to describe and study different scales of the bi-

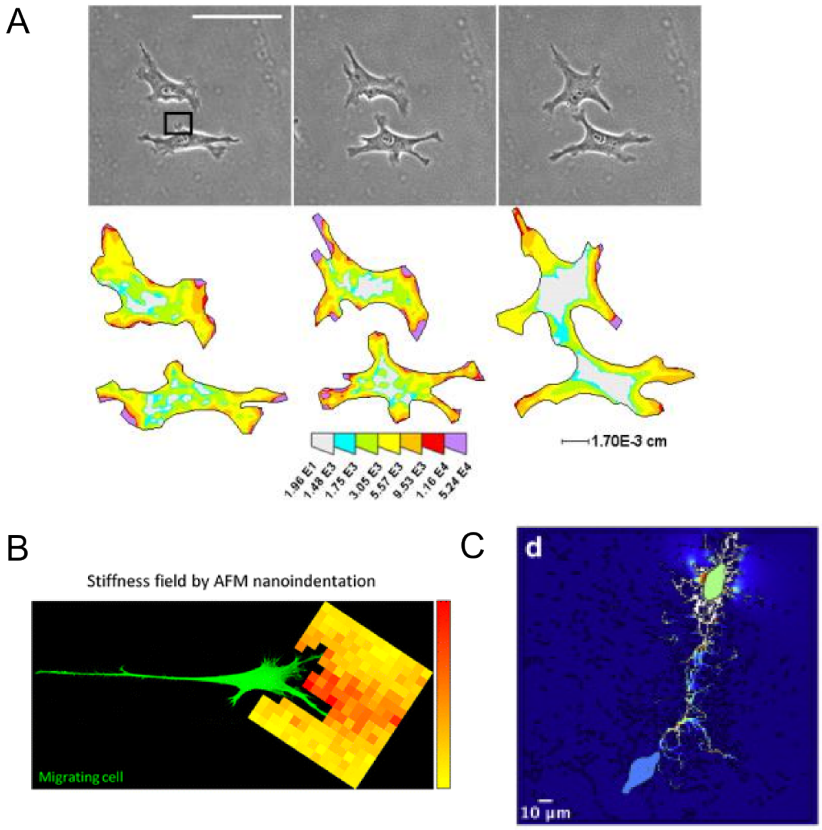

Figure 1.2: Experimental observations of matrix remodeling and mechanical cell-cell communication. (A) Two adjacent cells on polyacrylamide gels with traction stress distributions. The cell at the bottom extends a small pseudopod towards the top cell while it was moving away, revealing that the cell senses traction stresses of the adjacent cell. Reprinted from [32] with permission from Elsevier; (B) Heatmap of the matrix stiffness around a migration fibroblast, indicating that the cell locally stiffens the matrix. Adapted from [37] with permission from American Chemical Society; (C) Heatmap of stresses between two adjacent cells on a fibrous matrix. Stresses were calculated using a finite element model of a nonlinear strain-hardening material based on the experimental images of the cells and fibers. This shows that stresses propagate between cells via matrix fibers. Adapted from [50] with permission from Elsevier.

ological system. The microscale of cell biology, like for instance protein and gene interactive networks within cells, has been described by mathematical models [58]. Although we can measure how proteins and genes interact, we can not grasp what the consequence is of all interactions between different genes and proteins. Mathematical modeling can provide insights into how changes in such large interactions networks affect the expression of the cell [58]. However, such models do not translate to the impact on the tissue level. Other mathematical models focused on dynamics at the tissue level by modeling the tissue as a continuum by averaging out individual cells. These models give insight how laws of motions for the cells results in tissue patterning. Such models have been used to study pattern formation in a wide variety of developmental processes [59]. However, continuum models do not provide sufficient detail of cellular mechanisms, such as cell shape changes, that are relevant to morphogenesis. It has been proposed that mathematical biology should take a cell-centered approach [60]. More specifically, it was argued that cells should be considered as black boxes that behave a certain way, while neglecting the intercellular mechanisms that drive this behavior. The individual cell behavior can be inferred from experimental observations and be put into a cell-based model. Then, we can use this cell-based model to understand how a specific input (*i.e. cell behavior*) leads to a certain output (tissue formation). By comparing the model output to experimental observations, we can determine if this cell behavior suffices to explain the experimental data. If not, the model can be further adapted and subsequently tested with experiments to find the cell behavior that suffices to reproduce certain experimental observations.

As morphogenesis is an inherently multi-scale problem we believe that we should take a multi-scale mathematical modeling approach. Organisms consist of tissues, which consist of cells, the extracellular matrix and their molecules. During development, all different scales in biology interact and feed back on one another. For instance, gene expressions change cell behavior, which change tissue forces, which in turn change gene expressions. So, a better understanding of how forces can drive morphogenesis should take into account the forces acting and interacting at all different scales. A multi-scale model consists of separate models that describe the scales of interest, from the molecular scale, to the cellular scale to the tissue scale [61]. We believe that we should start with modeling only the scales and interactions of interest, like for instance cells and the extracellular matrix and their interactions. Then, if the model is not able to explain the experimental observations, we can further build up the model, by adding more mechanisms, scales and interactions between scales. Doing complementary biological experiments allows us to validate model predictions but also to investigate what aspects are missing in our model. Such a feedback loop between experimental biologists and mathematical modelers allows for a systematic exploration of the necessary mechanisms in a biological system and thus increases our understanding of the system.

1.2.1 Cell based modeling

Because cells are the building blocks of tissues, we aim to develop multi-scale models that explicitly describe cells. Discrete cell-based models describe cells as individual elements, and thus, in contrast to continuum models, provide sufficient detail on the cellular level. We can divide cell based models in single and multi-particle methods. Single-particle models represent cells as point particles or ellipsoids. Multiple-particle-based models use a collection of particles to represent each cell, allowing for a more detailed description of cell shape [62]. A further distinction is made between representations on regular lattices, which can be computationally more efficient, and off-lattice representations, which allows more flexibility in cell shape. An overview of cell-based methodology is given in Figure 1.3. In single particle-based models cell migration is described by differential equations of motion for each particle. These differential equations usually include active, random or directed cell migrations and external forces applied to the cell, which can be either cell-cell interactive forces or forces from the environment [see, *e.g.* 63]. Alternatively, particles comply to a set of behavioral or migratory rules [see, *e.g.* 64], as in an agent-based model.

Using particle-based methods, various cell migration behaviors have been modeled. For instance, Szabo *et al.* [66] included diffusion, directional persistence and an attraction to anisotropic structures to model cell organization into network-like patterns. Cell-cell interactions, such as pressure and velocity adaption to neighbors, were added by Sepulveda *et al.* [67] and Byrne *et al.* [64] respectively. Dallon *et al.* [68, 69] simulated contact guidance, haptokinesis and chemotaxis in a particle-based model.

While particle-based methods make it possible to simulate how individual cell behaviour is responsible for collective cell motility during morphogenesis, more detail may be needed. The shape of the cell is key to many developmental processes. The shape of the cell determines the extent of cell-cell interactions, *i.e.* cell-cell signalling or cell-cell adhesion. To account for differerential cell shape, multiple particle methods describe cells as a collection of connected particles, so that the boundary or interior of a cell is defined (Figure 1.3). Thus, cell shape is explicit and can change in response to external forces and interactions with adjacent cells. The subcellular elements method [70] is an example of an off-lattice multiple particle method, where cells are divided into subcellular elements (for instance, points in space), which can locally interact with elements of the same cell and elements of other cells via equations of motion. These equations describe both the internal rheology of individual cells, as well as the adhesive and repulsive forces with adjacent cells. Mechanotactic and chemotactic cell migration can be included in such models [see *e.g.,* 71]. Alternative off-lattice and lattice-based multi-particle methods are the vertex-based models and the cellular Potts model (CPM). The CPM describes cell shape and cell movement on the level of protrusions. It can be easily extended to describe various cell behaviors and other scales such as intercellular dynamics and the extracellular matrix. For this reason, the research presented in this thesis has employed the CPM, so we will describe the CPM in more detail here.

The CPM [72, 73] represents cells as a set of connected lattice sites (Figure 1.4) on a 2D square lattice $\Lambda \subset \mathbb{Z}^2$. Each lattice site, $\vec{x} \in \Lambda$, has a state $\sigma(\vec{x}) \in \{0, 1, ..., n\}$ that identifies the individual cell the lattice site belongs to, where $\sigma = 0$ represents the surrounding medium, and n is the total number of cells in the lattice. Forces acting on the cells are described in the Hamiltonian,

$$H = \sum_{(\vec{x},\vec{x}\prime)} J(\tau(\sigma(\vec{x})), \tau(\sigma(\vec{x}\prime)))\,(1 - \delta(\sigma(\vec{x}), \sigma(\vec{x}\prime))) + \lambda \sum_{\sigma\in[1,n]} (a_\sigma - A_\sigma)^2\,, \quad (1.1)$$

where J is an adhesive energy between two adjacent sites $\vec{x}$ and $\vec{x}\prime$ and δ is the Kronecker delta function: $\delta(x, y) = 1$ if $x = y$ and $\delta(x, y) = 0$ otherwise, such that the first term counts the total adhesive energy across cell-cell and cell-medium interfaces (Figure 1.4). The second term is a cellular volume conservation term, with a_σ the cell area, A_σ, the resting area of cell σ, and λ a compressibility parameter. To mimic cell motility and membrane fluctuations, the cellular Potts model iteratively attempts to copy the state $\sigma(\vec{x})$ of a randomly selected lattice site $\vec{x}$, into a randomly selected, adjacent lattice site $\vec{x}\prime$; If such a copy reduces the value of the Hamiltonian ($\Delta H \leq 0$), it is accepted. If the attempt would increase the value of the Hamiltonian ($\Delta H > 0$) it is accepted with a Boltzmann probability, $P(\Delta H) = \exp(-\Delta H/T)$. These copy steps account for the intrinsic random motility of cells, with large values of T corresponding with more random motility. During one time step, N copy attempts are made, with N the total number of lattice sites in the lattice.

The CPM has often been extended to account for additional cell behaviours, which are typically described by additional terms in the Hamiltonian (Eq. 1.1). Hybrid Cellular Potts models, in which the CPM is combined with discretized continuum models (PDEs) to account for secreted chemical signals [75] were developed to study how chemical signaling affects tissue patterning. Other extensions include anisotropic cell adhesion [76], cell elongation [77] and persistent cell motility [78].

1.2.2 Modeling of mechanical cell-matrix interactions

Various modeling techniques can be used to model the extracellular matrix. Similar to cells, depending on the context and objective, the ECM can be modeled using continuum or discrete approaches. Within continuum models we can make a further distinction between models excluding and including matrix fibers. In this section, we will give a overview of matrix models that were coupled to cell models in order to investigate how cell-matrix interactions can influence morphogenesis.

Murray and Oster [79] developed a continuum model for the extracellular matrix. Here, the ECM was modeled as an viscoelastic material that deforms in response to external forces and the laws of motions are described using partial differential equations (PDEs). To study cell-matrix interactions, PDEs that describe cell movement can be coupled to the PDEs that describe the matrix. In the model by Murray and Oster, cells are assumed to contract the matrix so that the matrix deforms. Cells then are pulled passively along substrate deformations. This causes an initially random dis-

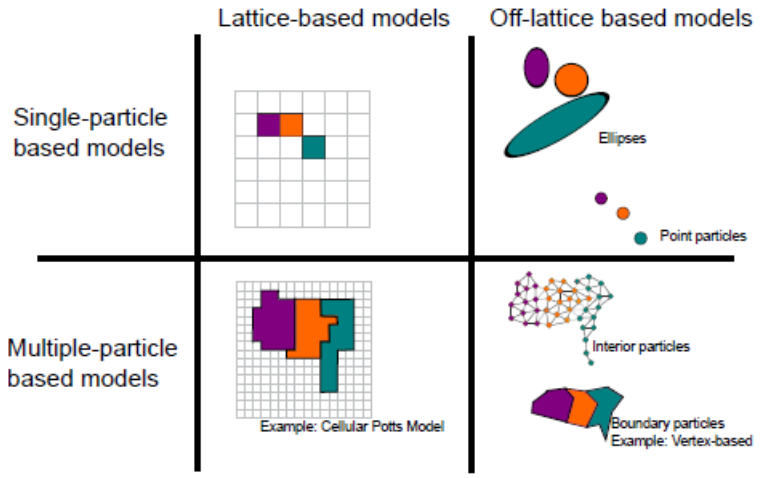

Figure 1.3: An overview of cell-based modeling methods. Reprinted [65] with permission from Elsevier.

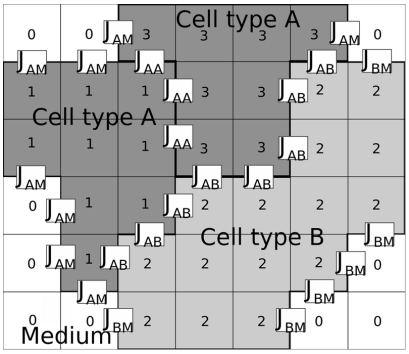

Figure 1.4: An overview of the cellular Potts model. Three cells with two cell types interact via adhesive energies and the surrounding medium. Reprinted from [74].

persed cells to accumulate the matrix underneath them so that cells form aggregates. Then, tension lines between aggregates enable the aggregates to connect and form patterns. This model has been extended many times to include active cell-matrix interactions. For instance, models that included active cell movement along matrix strains, chemotaxis and haptotaxis were used to study cellular network formation [80–82].

Continuum modeling approaches have also been used to describe matrix fibers. For instance, the ECM has been modeled by a vector field that describes the orientation of fibers [68]. The reorientation of the vector field is modeled by a ordinary differential equation, where it assumed that the vector field reorients to an external force field with a rate proportional to the magnitude of the external force. As the ECM is anisotropic and not unidirectional it was proposed that the ECM should be modeled as a tensor field instead [83]. These vector or tensor fields of matrix fibers were coupled to discrete models of cells and applied to study wound healing [68, 83].

Continuum models that describe both matrix elasticity and fiber orientation have also been developed. Barocas and Tranquillo developed a biphasic theory for tissues, where the tissue is described a mixture of the matrix and cells [84]. This model defines the fraction of volume that contains either cells or the matrix and describes how the two phases deform and interact through forces. An additional tensor field is introduced that describes the fiber orientation which rotates in response to cell forces and affects cell migration [85]. Recently, a similar multiphase modeling framework was adopted that in addition describes how the fiber orientation affect the stress in the matrix. Using this model, it was studied how matrix anisotropy affects cellular pattern formation [86]. Matrix fibers can also be included in elastic material models by considering fiber-reinforced elastic materials. Checa *et al.* [87] modeled an elastic material where the orientation of fibers determines the stress in the material [87]. It was assumed that the fibers rotate towards the principal stress orientation of the tension field generated by discrete cells. This model was used to study the effect of boundary conditions on cellular self-organization and fiber alignment [87]. Yang *et al.* [88] modeled how the orientation of the fibers but also that the density of the fibers affect matrix stresses. This model was coupled to a discrete model of cells to study the effect of matrix fiber realignment during wound healing (Figure 1.5A).

Because fibers can be of the same length or even longer than cells, it may not be appropriate to model a fibrous matrix as a continuum. Instead, models were developed that describe both the cell and matrix fibers as discrete objects. Schluter *et al.* modeled fibers as thin cylinders that rotates as a lever as a cell pulls on it [89]. Discrete cells then move along the orientation of the fibers. Fibers and cells have also been represented as a set of connected nodes and springs [90, 91]. In such models, fibers are multiple springs connected to each other by particles that can be anchored to the cell. The sum of all forces between cells and the matrix deform the elements, effectively resulting in cell migration. Typically, discrete models are computationally more expensive and thus have focused on single cell migration or the migration of two interacting cells (Figure 1.5B) [89–91]. In the CPM, the architecture of the ECM has

been modeled by including ECM fibers as immovable lattice sites in the medium surrounding the cells in the CPM (Figure 1.5C) [92, 93]. By allowing more lattice sites to be of type fiber, higher densities of matrix fibers can be modeled. Note however that the fibers in this model are static.

In the models described in this section, cell-matrix interactions were often based on the alignment of fibers in the matrix. However, experimental observations indicate that cells can also communicate through matrix stresses in the absence of fibers [32]. Some continuum models [80–82] have focused on how matrix stresses influence pattern formation. In this thesis, we take a cell-based modeling approach to study how matrix stresses affects morphogenesis.

1.3 Thesis outline

In this thesis, we address the overarching question "How do cell-matrix interactions drive morphogenesis?". We mainly focus on mechanical cell-interactions through matrix stresses but also study chemical signaling via the matrix. We take a multiscale computational modeling approach to attempt to answer our research question. We have developed a multiscale model, by extending the Cellular Potts Model with a finite element model of the substrate. In our model, the cell and the ECM interact through a feedback-loop. By pulling on the matrix, the cell adapts the matrix, and in turn, the cells sense the matrix and respond to it, a process called *dynamic reciprocity*. By testing different hypotheses on cell-matrix interactions, we can use our model to understand how this affects morphogenesis. Since our model is generic it does not specify a certain cell type or other tissue-specific constraints, so we can use our model to study different systems.

In chapter 2, we use our model to explain how matrix stiffness regulates vasculogenesis. Experimental observations have shown that endothelial cells on compliant polyacrylamide gels only form vascular network-like patterns on substrates of intermediate stiffness [36]. In our model, we assume that by straining the matrix, the matrix strain-stiffens. Furthermore, the cells respond to the matrix by preferentially extending protrusions on stiffer matrix sites, based on the observation that cell-matrix adhesions are larger on stiff matrices, and in the direction of strain. This minimal assumption already reproduces observed single cell behavior; cells elongate on substrates of intermediate stiffness. When simulating a group of cells, the cells elongate and locally align with each other because they respond to the matrix strains induced by neighbouring cells. This local cell-cell alignment then results in global cellular network formation. We furthermore show that this cell behavior enables cells to sprout from a circular blob of cells, suggesting that the proposed mechanical cell-matrix interactions might also drive sprouting angiogenesis.

In chapter 3, we dive a little deeper into cell alignment. Here, we aim to understand how cells and tissues can align along matrix strains. *In vitro* experiments where a tissue is uniaxially loaded show that many cell types elongate along the orientation of

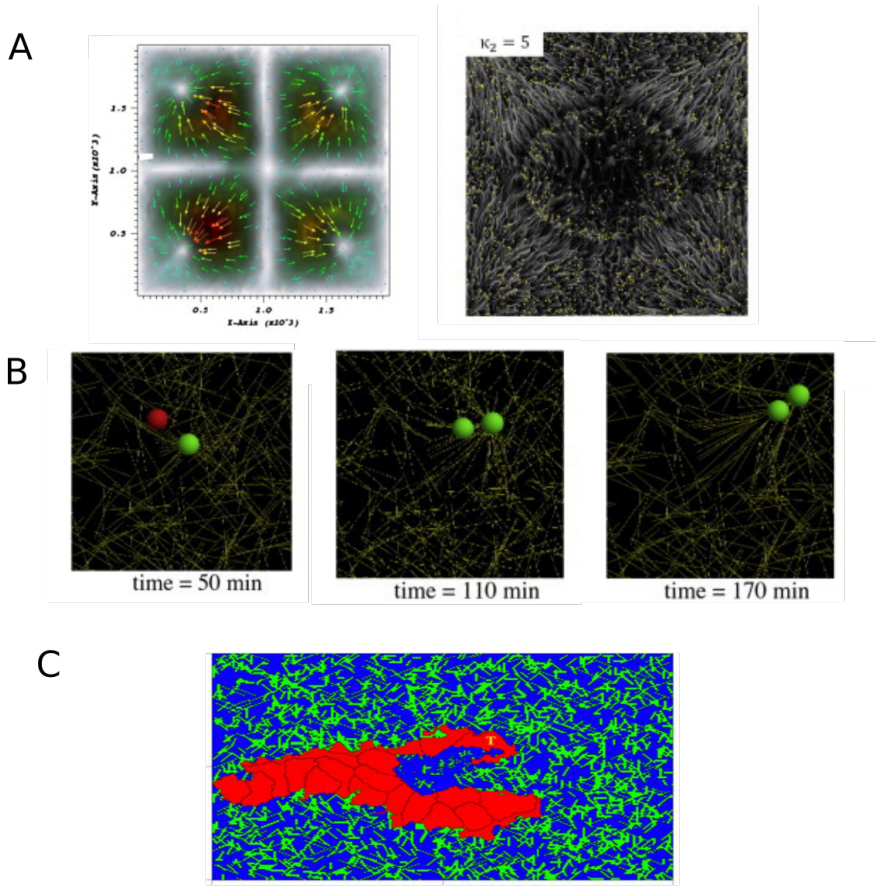

Figure 1.5: Examples of multiscale models of cell-extracellular matrix interactions. (A) Substrate deformation given by natural tension lines around the wound (Left), collagen fibers (grey) align with tension field, discrete cells are indicated by yellow spots and invade the wound (Right). Adapted from [88] with permission from Elsevier; (B) Two discrete circular cells pulling on and migrating in a fibrous matrix, one cell follows the other by contact guidance along the track of fibers that were aligned by the leader cell. Adapted from [89] with permission from Elsevier; (C) cellular Potts model (red cells) coupled to discrete matrix fibers (green), cells form sprout that branches. Adapt from [93].

static matrix strain. Furthermore, whole tissues can align to strain [94] or cells organize into stripes oriented along the strain [95]. Our model suggests that cell alignment to static strain is promoted by cellular forces. Cells respond to the static strain by slightly elongating. If a cell then applies a force to the matrix, it locally increases the strain of the matrix at the tip of its body. This increased strain then allows cells to elongate even further, compared to a cell that would not have strained the matrix. So, a positive feedback loop between cell extensions and cell contractility enables a cell to align along the strain. Simulations of multiple cells suggest that this mechanism enables cell-cell alignment so that cells form stripes of cells along strain. Increasing cell-cell adhesions and cell density makes the stripes disappear, while cells still elongate, suggesting that tissue level alignment depends on cell specific parameters.

In chapter 4, we present a hybrid model that includes focal adhesion dynamics, in order to gain a molecular level understanding of how cells respond to matrix rigidity. Focal adhesions are mechanosensitive molecular structures that bind the cell to the ECM. In our model, the cells apply a force to the focal adhesions and the rate of force build-up depends on matrix stiffness and the velocity of motor proteins [96]. We assume that the likelihood of cell-matrix deadhesion decreases with focal adhesion size. Our model suggests that on stiff matrices, the cells build up enough force so that focal adhesions grow and the cell is able to spread. If we included that matrix stresses induces adhesion strengthening, the simulated cells elongated on matrices of intermediate stiffness. We show that the range on which cells elongate depends on the velocity of the motor protein. Finally, we show that cells in our model durotact: move up a stiffness gradient. So, with a more detailed model of focal adhesions we can now explain cell spreading, elongation and durotaxis on a molecular level.

In chapter 5 and 6, we will focus on chemical signaling through the extracellular matrix. In chapter 5, we introduce a model that describes the formation of a Nodal signaling gradient. Nodal is one of the signaling molecules that is involved in left-right patterning of embryos. Experimental observations in zebrafish show that the protein FurinA is able to cleave the Nodal protein Southpaw to a mature form, so that it can be secreted by cells [97]. The experiments suggest that FurinA regulates the signaling range of Nodal [97]. To better understand the dynamics, we introduce a PDE model that assumes that the rate of maturation of Southpaw depends on the level of FurinA. The model shows that the speed of extracellular Southpaw gradient formation and the range of this gradient increases with FurinA levels, which was confirmed by our experimental data.

In chapter 6, we introduce a multiscale cell based model for epithelial branching. Here, we show that gradients of an autocrine signaling factor can drive branching morphogenesis. Experimental observations of mammary epithelial cells [98] indicated that branching sites are regulated by TGF-β, an inhibitory autocrine signal. Based on these observations, we assume that cell extensions at the tissue boundary negatively depend on the local level of the autocrine signal. In this cellular Potts model, the tissue secretes the autocrine that accumulates at concave tissue boundaries. This curvature

effect allows the simulated tissue to branch.

2

Mechanical Cell-Matrix Feedback Explains Pairwise and Collective Endothelial Cell Behavior In Vitro

This chapter is published as:

van Oers RFM, Rens EG, LaValley DJ, Reinhart-King CA, Merks RMH (2014) Mechanical Cell-Matrix Feedback Explains Pairwise and Collective Endothelial Cell Behavior In Vitro. PLOS Computational Biology 10(8): e1003774.

Abstract

In vitro cultures of endothelial cells are a widely used model system of the collective behavior of endothelial cells during vasculogenesis and angiogenesis. When seeded in an extracellular matrix, endothelial cells can form blood vessel-like structures, including vascular networks and sprouts. Endothelial morphogenesis depends on a large number of chemical and mechanical factors, including the compliancy of the extracellular matrix, the available growth factors, the adhesion of cells to the extracellular matrix, cell-cell signaling, etc. Although various computational models have been proposed to explain the role of each of these biochemical and biomechanical effects, the understanding of the mechanisms underlying *in vitro* angiogenesis is still incomplete. Most explanations focus on predicting the whole vascular network or sprout from the underlying cell behavior, and do not check if the same model also correctly captures the intermediate scale: the pairwise cell-cell interactions or single cell responses to ECM mechanics. Here we show, using a hybrid cellular Potts and finite element computational model, that a single set of biologically plausible rules describing (a) the contractile forces that endothelial cells exert on the ECM, (b) the resulting strains in the extracellular matrix, and (c) the cellular response to the strains, suffices for reproducing the behavior of individual endothelial cells and the interactions of endothelial cell pairs in compliant matrices. With the same set of rules, the model also reproduces network formation from scattered cells, and sprouting from endothelial spheroids. Combining the present mechanical model with aspects of previously proposed mechanical and chemical models may lead to a more complete understanding of *in vitro* angiogenesis.

2.1 Introduction

How the behavior of cells in a multicellular organism is coordinated to form structured tissues, organs and whole organisms, is a central question in developmental biology. Keys to answering this question are chemical and mechanical cell-cell communication and the biophysics of self-organization. Cells exchange information by means of diffusing molecular signals, and by membrane-bound molecular signals for which direct cell-cell contact is required. In general, these developmental signals are short-lived and move over short distances. The extracellular matrix (ECM), the jelly or hard materials that cells secrete, provides the micro-environment the cells live in. Apart from its supportive function, the ECM mediates molecular [99] and biomechanical [32] signals between cells. Mechanical signals, in the form of tissue strains and stresses to which cells respond [100], can act over long distances and integrate mechanical information over the whole tissue [101], and also mediate short-range, mechanical cell-cell communication [32]. How such mechanical cell-cell communication via the ECM can coordinate the self-organization of cells into tissues is still poorly understood. Here we propose a cell-based model of endothelial cell motility on compliant matrices to address this problem.

A widely used approach to study the role of cell-ECM interactions in coordinating collective cell behavior is to isolate cells (*e.g.*, endothelial cells isolate from bovine aortae or from human umbilical cords or foreskins) and culture them on top of or inside an artificial or natural ECM (*e.g.*, Matrigel). This makes it possible to study the intrinsic ability of cells to form tissues in absence of potential organizing signals or pre-patterns from adjacent tissues. A problem particularly well-studied in cell cultures is the ability of endothelial cells to form blood vessel-like structures, including the formation of vascular-like networks from dispersed cells and the sprouting of spheroids. To this end, cell cultures can be initialized with a dispersion of endothelial cells on top of an ECM material (*e.g.*, Matrigel, collagen, or fibrin) [36, 102], with endothelial spheroids embedded within the ECM [51, 103], or with confluent endothelial monolayers [104–106]. Although the conditions required for vascular-like development in these *in vitro* culture systems are well established, the mechanisms driving pattern formation of endothelial cells are heavily debated, and a wide range of plausible mechanisms has been proposed in the form of mathematical and computational models reproducing aspects of angiogenesis (reviewed in [107–109]).

Typical ingredients of network formation models are (a) an attractive force between endothelial cells, which is (b) proportional to the cell density, and (c) inhibited or attenuated at higher cellular densities. The attractive force can be due to mechanical traction or due to chemotaxis. Manoussaki, Murray, and coworkers [80, 81] proposed a mechanical model of angiogenic network formation, based on the Oster and Murray [79, 110] continuum mechanics theory of morphogenesis. In their model, endothelial cells exert a uniform traction force on the ECM, dragging the ECM and the associated endothelial cells towards them. The traction forces saturated at a maximum cell density. Namy and coworkers [82] replaced the endothelial cells' passive motion along with the ECM for active cell motility via haptotaxis, in which cells move actively towards higher concentrations of the ECM. Both models also included a strain-biased random walk term for the endothelial cells, but they found that it had little effect on network formation; the mechanism was dominated by cell aggregation. In their model based on chemotaxis, Preziosi and coworkers [111, 112] assumed that cells attract one another via the secreted chemoattractant VEGF. Due to diffusion and first-order degradation, the chemoattractant forms exponential gradients around cells leading to cell aggregation in much the same way as that assumed in the Manoussaki and Namy models. These chemotaxis-based hypotheses formed the basis for a series of cell-based models based on the cellular Potts model (CPM). Assuming chemotactic cell-cell attraction, and a biologically-plausible overdamped cell motility, the cells in these CPM models form round aggregates, in accordance with the Keller-Segel model of cell aggregation [113]. Additional assumptions, including an elongated cell shape [77] or contact inhibition of chemotaxis [114] are needed to transform these circular aggregates into vascular-like network patterns. Related network formation models studied the role of ECM-bound growth factors [115–117] and a range of additional secreted and exogenous growth factors [117], and studied the ability of the contact-inhibition

mechanism to produce three-dimensional blood-vessel-like structures [118]. Szabó and coworkers found that in culture, astroglia-related rat C6 cells and muscle-related mouse C2C12 cells organize into network-like structures on rigid culture substrates [66], such that ECM-density or chemoattractant gradients are excluded. They proposed a model where cells were preferentially attracted to or preferentially adhered to locally elongated structures. As an alternative mechanism for "gel-free" network formation it was found that elongated cells can also produce networks in absence of chemoattractant gradients [119].

Paradoxically, despite the diverse assumptions underlying the mathematical models proposed for vascular network formation, many are at least partly supported by experimental evidence. This suggests that a combination of chemotaxis, and chemical and mechanical cell-ECM interactions drives network formation, or that each alternative mechanism operates in a different tissue, developmental stage, or culture condition. A problem is that one mathematical representation may represent a range of equivalent alternative underlying mechanisms. For example, a model representing cell-cell attraction cannot distinguish between chemotaxis-based cellular attraction [77, 111, 112, 114], attraction via haptotaxis [82], direct mechanical attraction [80, 120] or cell shape dependent adhesion [66, 121], because the basic principles underlying these models are equivalent [107, 114]. As a solution to this problem, a sufficiently correct complete description of endothelial cell behavior should suffice for the emergence of the subsequent levels of organization of the system, an approach that requires that the system has been experimentally characterized at all levels of organization.

The role of cell traction and ECM mechanics during *in vitro* angiogenesis have been characterized experimentally particularly well, making it a good starting point for such a multiscale approach. Endothelial cells apply traction forces on the extracellular matrix, as demonstrated by a variety of techniques, *e.g.*, wrinkle formation on elastic substrates [104], force-generation on micropillar substrates [122], and traction force microscopy [36, 123]. Using scanning electron microscopy, Vernon and Sage [104] found that ECM ribbons radiate from endothelial cells cultured in Matrigel, suggesting that the traction forces locally reorient the extracellular matrix. The cellular traction forces produce local strains in the matrix, which can affect the motility of nearby cells [32]. Thus endothelial cells can both generate, and respond to local strains in the extracellular matrix, suggesting a feedback loop that may act as a means for mechanical cell-cell communication [32] and hence coordinate collective cell behavior. Here, we use a hybrid cellular Potts and finite element model to show that a set of assumptions mimicking mechanical cell-cell communication via the ECM suffices to reproduce observed single cell behavior [124, 125], pairwise cell interactions [32], and collective cell behavior: network formation and sprouting.

2.2 Results

2.2.1 Response of endothelial cells to static strains in ECM

First we set out to capture, at a phenomenological level, the response of endothelial cells to static strains in the ECM in absence of cellular traction forces. When grown on statically, uniaxially stretched collagen-enriched scaffolds, murine embryonic heart endothelial (H5V) cells orient in the direction of strain, whereas cells grown on unstrained scaffolds orient in random directions [94]. Because the collagen fibers make the scaffold stiffen in the direction of strain, we hypothesized that the observed alignment of cells is due to durotaxis, the propensity of cells to migrate up gradients of substrate rigidity [126] and to spread on stiff substrates [127, 128]. In our model we assumed (a) *strain stiffening*: a strained ECM is stiffer along the strain orientation than perpendicular to it, such that (b) due to durotaxis the endothelial cells preferentially extend pseudopods along the strain orientation, along which the ECM is stiffest, giving cells the most grip. To keep the ECM mechanics simulations computationally tractable, we assumed an isotropic and linearly elastic ECM. With these assumptions it is not possible to model strain stiffening explicitly. We therefore mimicked strain stiffening by assuming that stiffness is an increasing, linear function of the local strain.

Durotaxis was modelled as follows, to reflect the observation that focal adhesion maturation occurs under the influence of local tension [129]: At low local stiffness, we applied standard cellular Potts dynamics to mimic the iterative formation and breakdown of ECM adhesions, producing "fluctuating" pseudopods. However, if the stiffness was enhanced locally, we assumed that the resulting tension in the pseudopod led to maturation of the focal adhesion [129, 130], stabilizing the pseudopod as long as the tension persists. To mimic such focal adhesion maturation in the cellular Potts model, we increased the probability of extension along the local strain orientation, and reduced the probability of retraction (see Methods for detail).

Figure 2.1A shows the response of the simulated cells to uniaxial stretch along the vertical axis. With increasing values of the durotaxis parameter $\lambda_{\text{durotaxis}}$ (see Eq. 2.8), the endothelial cells elongate more. To test the sensitivity of the durotaxis model for lattice effects, we varied the orientation of the applied strain over a range $[0 - 180]^\circ$ and measured the resulting orientation of the cells. Figure 2.1 shows that the average orientation of the cells follows the orientation of the stretch isotropically. Thus the durotaxis component of our model phenomenologically reproduces published responses of endothelial cells to uniaxial stretch [94].

2.2.2 Generation of strains in ECM due to cellular traction

We next attempted to mimic the forces applied by cells onto the extracellular matrix, in absence of durotaxis. Traction-force microscopy experiments [123, 127] show that endothelial cells contract and exert tensional forces on the ECM. The forces are typically directed inward, towards the center of the cell, and forces concentrate at the tips

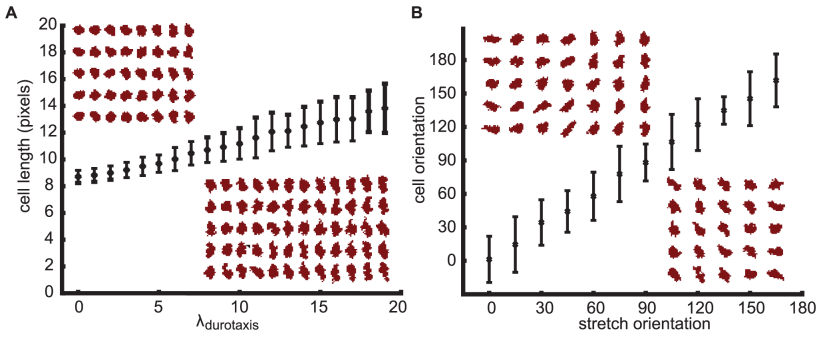

Figure 2.1: Simulated cellular responses to static strains. Cells do not generate traction forces in this figure. (A) Cell length as a function of the durotaxis parameter, $\lambda_{\text{durotaxis}}$, on a substrate stretched along the vertical axis; (B) Cell orientation as a function of the stretch orientation (simulated with $\lambda_{\text{durotaxis}} = 10$). Error bars show standard deviation for $n = 100$. Insets show five simulations per value tested.

of pseudopods. A recent modeling study by Lemmon and Romer [131] found that an accurate prediction of the direction and relative magnitudes of these traction forces within the cell can be obtained by assuming that each lattice node i covered by the cell pulls on every other node the cell covers, j, with a force proportional to their distance, $d_{i,j}$. Because this model gives experimentally plausible predictions for fibroblasts, endothelial cells, and keratocytes [131], we adopted it to mimic the cell-shape dependent contractile forces that endothelial cells exert onto the ECM. Figure 2.2 shows the contractile forces (*black*) and resulting ECM strains (*blue*) generated in our model by two adjacent cells. The traction forces and ECM strains become largest at the cellular "pseudopods", qualitatively agreeing with traction force fields reported for endothelial cells [123].

2.2.3 Mechanical cell-ECM feedback qualitatively reproduces effect of substrate stiffness on cell shape and motility

The two previous sections discussed how the simulated cells can respond to and induce strain in the ECM in an experimentally plausible way. To test how the simulated cells respond to the strains they generate themselves, we studied the behavior of simulated, single cells in presence of both the cell traction mechanisms and the durotaxis mechanisms. During each time step, we used the Lemmon and Romer [131] model to calculate traction forces corresponding to current cell positions. Next, we started the finite element analysis from an undeformed matrix, calculating steady-state strains for the current traction forces. To simulate cell movement, which was biased by the local matrix strains using the durotaxis mechanism, we then applied one cell motility simulation time step, or Monte Carlo step (MCS; the MCS is the unit of time of our

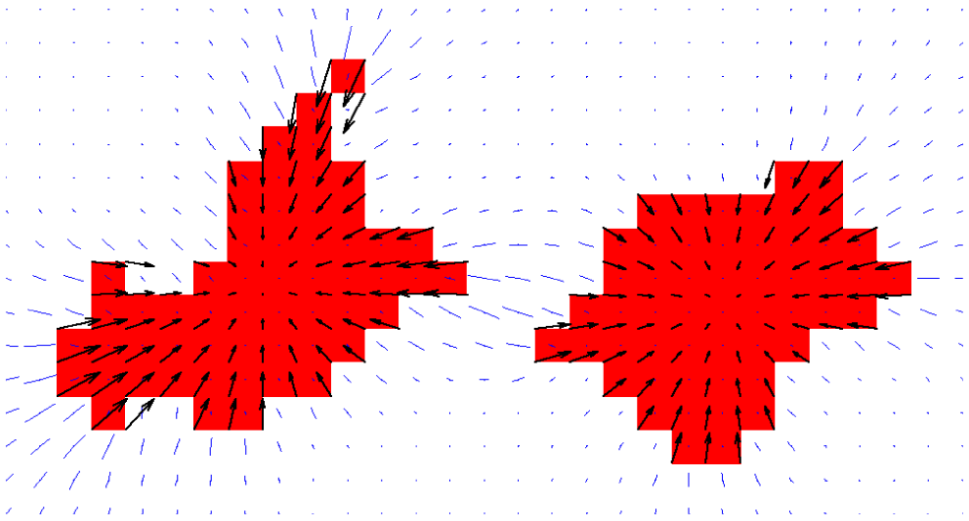

Figure 2.2: Visualization of simulated traction forces (black arrows) and resulting matrix strains (blue line segments) generated in the proposed hybrid cellular Potts and finite element simulation model.

simulation; see Methods for detail and Discussion for an estimate of the real time corresponding to an MCS). After running the CPM for one MCS we again relaxed the matrix such that the next step started with an undeformed matrix. Thus we currently did not consider cell memory of substrate strains.

As Figure 2.3 and Video S1 demonstrate, in this model matrix stiffness affects both the morphology and motility of the simulated cells. On the most compliant substrate tested (0.5 kPa) the simulated cells contract and round up, whereas cells spread isotropically on the stiffest substrate tested (32 kPa). Overall, the cellular area increases with substrate stiffness (Figure 2.3B). On matrices of intermediate stiffnesses (around 12 kPa) the cells elongate, as reflected by measurements of the cell length (Figure 2.3C) and eccentricity (Figure 2.3D) that both have maximum values at around 12 kPa. Such a biphasic dependence of cellular morphology on the stiffness of the ECM mimics the behavior of endothelial cells [127] and cardiac myocytes [125] in matrices of varying stiffness. The dependence of cell shapes on substrate stiffnesses is due to the transition from fluctuating to adherent pseudopods with increasing stiffness. Focal adhesions of cells on soft substrates all remain in the "fluctuating" state, irrespective of the local strains. On intermediate substrates, some pseudopods, due to increased traction, move to an extended state (mimicking a mature focal adhesion), generating more traction in this direction. Hence an initial stochastic elongation self-enhances in a feedback loop of increasing traction and strain stiffening. Such a self-enhancing cell-elongation starting from an initial anisotropy in cell spreading

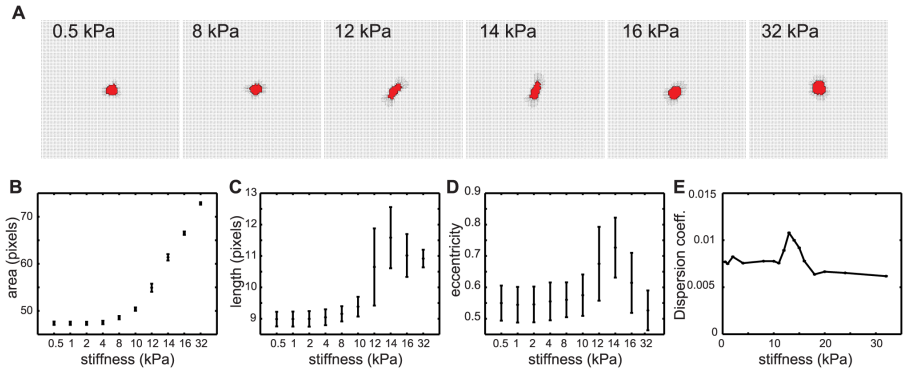

Figure 2.3: Simulated individual cell responses to mechanical cell-ECM feedback. (A) Single cells on substrates of varying stiffness after 100 MCS. Line pieces indicate strain magnitude and orientation; (B) cell area ($a(\sigma)$) of cells; (C) cell length (length of major axis if the cell is seen as an ellipse) as a function of substrate stiffness; (D) cell eccentricity ($\xi = \sqrt{1 - b^2/a^2}$, with a and b the lengths of the cell's major and minor semi-axes) as a function of stiffness. Mean and standard deviation shown for $n = 100$ in panels B-D; (E) Dispersion coefficients of individual, simulated cells, derived from a linear fit on the mean square displacements (Supplementary Figure 2.8); $n = 1000$. Error bars indicate 95% confidence intervals of linear fits.

has previously been suggested by Winer et al [33]. Extensions perpendicular to the long axis of an elongated cell do not occur since there is insufficient traction and the volume constraint is limiting. At matrices of high stiffness all pseudopods attempt to extend, mimicking the formation of static focal adhesion, until the volume constraint becomes limiting. This makes the cells spread more on stiff substrates than on soft substrates, with weaker volume constraints (lower values of λ) producing a stronger effect of substrate stiffness on cell shape and cell area (Supplementary Figure 2.7) .

We also measured the random motility of the cells by characterizing their dispersion coefficients, which we derived from the mean square displacements of the cells (Supplementary Figure 2.7; see section Morphometry for detail). The dispersion coefficients show biphasic behavior, with the highest motilities occurring at around 12 kPa (Figure 2.3E). The biphasic dependence of the dispersion to substrate stiffness is in accordance with *in vitro* behavior of neutrophils [132], and smooth muscle cells [133]. Here it is typically thought to be due to a balance of adhesion and actin polymerization, or due to the interplay between focal adhesion dynamics and myosin-based contractility [132]. In our model, the effect is more likely due to the appearance of eccentric cell shapes at intermediate stiffnesses; as a result, only the tips of the cell generate sufficient strain in the matrix to extend pseudopods, producing more persistent motion than the round cells at stiff or soft substrates. It will be interesting to see if a similar relationship between cell shape and cell motility holds *in vitro*. Thus the model rules

for cell traction and stretch guidance based on durotaxis and strain stiffening suffice to reproduce an experimentally plausible cellular response to matrix stiffness.

2.2.4 Mechanical cell-ECM feedback coordinates behavior of adjacent cells

Strains induced by endothelial cells on a compliant substrate with low concentrations of arginine-glycine-aspartic acid(RGD)-containing nonapeptides can affect the behavior of adjacent cells [32]. On soft substrates (5.5 kPa or below) the cells reduced the motility of adjacent cells, whereas on stiff substrates (33 kPa) such an effect was not found. On substrates of intermediate stiffness (5.5 kPa), adjacent endothelial cells repeatedly attached and detached from one another, and cells moved more slowly in close vicinity of other cells, than when they were on their own. Because the extent to which cells could affect the motility of nearby cells depended on matrix compliancy, mechanical traction forces could act as a means for cell-cell communication [32]. To test if the simple strain-based mechanism represented in our model suffices for reproducing such mechanical cell-cell communication, we initiated the simulations with pairs of cells placed adjacent to one another at a distance of fourteen lattice sites corresponding to a distance of 35 μm, and ran a series of simulations on substrates of varying stiffness (Figure 2.4A and Video S2).

The cells behaved similar to the single cell simulations (Figure 2.3), with little cell-cell interactions at the lower and higher stiffness ranges. Consistent with previous observations [32], cell pairs on substrates of intermediate stiffness (12 kPa) dispersed more slowly than individual cells (paired two-sample t-test at 5000 MCS, $p < 0.05$ for 12 kPa), whereas individual cells and cell pairs dispersed at indistinguishable ($p > 0.05$) rates on stiff (14 kPa or more) or soft (10 kPa or below) substrates (Figure 2.4, *B-D*) and Supplementary Figure 2.9).

Also in agreement with the previous, experimental observations [32], on a simulated substrate of intermediate stiffness (12 kPa) the cells responded to the matrix strains induced by the adjacent cell by repeatedly touching each other, and separating again (Figure 2.4E). The contact duration of cells on soft and stiff substrates, when they get close enough to each other, are typically longer than for intermediate substrates. This behavior is also similar to observations *in vitro* [32]. As one might expect that strongly adherent cells will not repeatedly touch and retract, but rather stay connected upon first contact, we investigated the effect of cell adhesion on these parameters (Supplementary Figure 2.10). Consistent with this intuition, for stronger adhesion, the contact count tends to be reduced and the contact durations tend to increase, but the overall trend holds: at intermediate matrix stiffnesses we continue to observe more frequent cell contacts than for more soft or more stiff matrices. Thus the observed pairwise cell behavior is primarily driven by durotaxis.

Mechanical strain can also coordinate the relative orientation of cells. Fibroblasts seeded on a compliant gel tend to align in a head-to-tail fashion along the orientation of mechanical strain [134]. Bischofs and Schwarz [135] proposed a computational

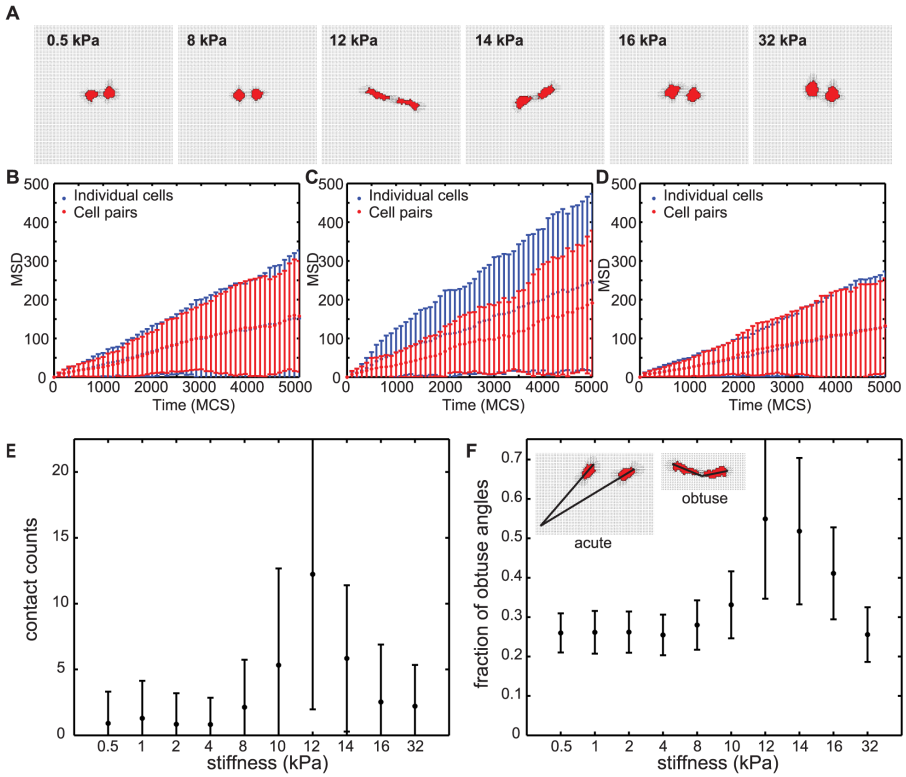

Figure 2.4: Simulated cell-cell interactions on substrates of varying stiffnesses. (A) Visualization of cell shapes and substrate strains in absence of external strain. Line pieces indicate strain magnitude and orientation, (B-D) Mean square displacement of individual cells (blue errorbars) and cell pairs (red errorbars) on simulated substrates; (B) 4 kPa; (C) 12 kPa; (D) 32 kPa. Error bars in panels B to D indicate standard deviation for $n = 100$; (E) Number of cell-cell contacts made over 500 MCS between two simulated cells initiated at a distance of fourteen lattice sites from each other. Error bars show standard deviation over $n = 100$ simulations; (F) Quantification of head-to-tail alignment of cells. An obtuse angle between the two cells' long axes indicates that cells are oriented head-to-tail. Plotted is the fraction of Monte Carlo steps over MCS 20-500 that the two cells are aligned head-to-tail. Shown are means and standard deviations over 100 independent simulations on a field of 0.25×0.25 mm^2 (100×100 pixels). Insets: examples of acute (left) and obtuse (right) cell configurations.

model to explain this observation. Their model assumes that cells prefer the direction of maximal effective stiffness, where the cell has to do the least work to build up a force. This work is minimal between two aligned cells, because maximum strain stiffening occurs along the axis of contraction. Interestingly, visualization of our model results (Figure 2.1C) suggested similar head-to-tail alignment of our model cells at around 12 kPa. To quantify cell alignment in our simulations, we measured the angle α between the lines l_1 and l_2, defining the long axes of the cells and crossing the centers of mass of the cells (Figure 2.4F). We classified the angles as acute ($\alpha < \pi/2$; *i.e.* no alignment) or obtuse ($\alpha \geq \pi/2$; alignment). At matrix stiffnesses up to around 10 kPa, about one fourth of the angles α were obtuse, corresponding to the expected value for uncorrelated cell orientations. However, at 12 kPa and 14 kPa significantly more than a fourth of the angles α between the cell axes were obtuse (55/100 for 12 kPa, $p < 1\times10^{-8}$ and 52/100 for 14 kPa, $p < 1\times10^{-8}$, binomial test), and for substrate compliancies of 8 to 16 kPa significantly more of the angles α were obtuse than for 4 kPa ($p < 0.01$ for 8 kPa, and $p < 1 \times 10^{-12}$ for 10 kPa to 16 kPa; two-tailed Welch's t-test), suggesting that the mechanical coupling represented in our model causes cells to align in a head-to-tail fashion.

2.2.5 Mechanical cell-cell communication drives biologically-realistic collective cell behavior

After observing that the local, mechanical cell-ECM interactions assumed in our model sufficed for correctly reproducing many aspects of the behavior of individual endothelial cells on compliant matrices and of the mechanical communication of pairs of endothelial cells on compliant matrices, we asked what collective cell behavior the mechanical cell-cell coordination produced. When seeded subconfluently onto a compliant matrix (*e.g.*, Matrigel), endothelial cells tend to organize into polygonal, vascular-like networks [36, 102, 136, 137]. To mimic such endothelial cell cultures, we initialized our simulations with (approximately) 450 cells uniformly distributed over a lattice of 300×300 pixels (0.75×0.75 mm^2), corresponding to a cell density of 800 endothelial cells per mm^2. In accordance with experimental observations on gels with low concentrations of collagen [36] or RGD-peptides [32], after 3000 MCS networks had not formed on soft matrices (0.5-4 kPa) or on stiff matrices (16-32 kPa) (Figure 2.5A): The cells tended to form small clusters (Figure 2.5A). Interestingly, on matrices of intermediate stiffness after around 300 MCS the cells organized into chains (8 kPa) or network-like structures (10 kPa and 12 kPa) similar to vascular network-like structures observed in endothelial cell cultures [36, 102, 136, 137]. The optimal stiffness ($\approx$ 10 kPa) for network formation is slightly lower than the stiffness of the substrate ($\approx$ 12 kPa) on which single cells elongate the most (Figure 2.3A). In comparison with a single cell, the collective pulling of a cell colony creates larger strains in the substrate. Consequently, the strain threshold inducing cell elongation is crossed at smaller substrate stiffness.

Figure 2.5B and Video S3 show a time-lapse of the development of a network con-

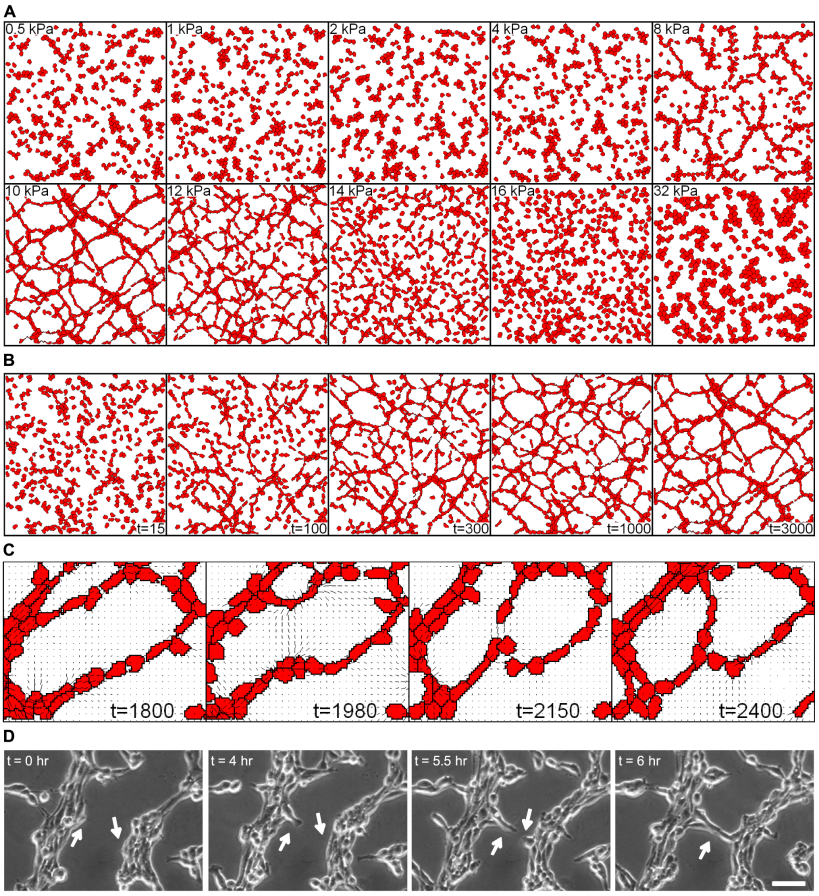

Figure 2.5: Simulated network formation assay. (A) Simulated collective cell behavior on substrates of varying stiffness, with a uniformly distributed initiated configuration of cells; (B) Time lapse showing the development of a polygonal network on a 10kPa substrate (time in MCS). Panels A and B represent a 0.75×0.75 mm^2 area (300×300 pixels) initiated with 450 cells. *(C)* Close-up of simulated network formation on a 10 kPa substrate, showing the reconnection of two sprouts. Time in MCS; (D) Time lapse imaging of bovine aortic endothelial cells seeded onto a 2.5 kPa polyacrylamide gel functionalized with RGD-peptide. Arrows indicate cells that join together and elongate into a network. Time scale is in hours. Scale bar is 50 ; μm.

figuration on a substrate of 10kPa. The cells organized into a network structure within a few hundred MCS. The network was dynamically stable, with minor remodeling events taking place, including closure and bridging of lacunae. Figure 2.5C shows such a bridging event in detail. In an existing lacuna (1800 MCS) stretch lines bridged the lacuna, and connected two groups of cells penetrating the lacuna (1980 MCS). The cells preferentially followed the path formed by these stretch lines (2150 MCS) and reached the other side of the lacuna by 2400 MCS. Such bridging events visually resemble sprouting in bovine endothelial cell cultures on compliant matrices (Figure 2.5D, Video S4, and [36]). To stay close to the experimental conditions used for the observations of pairwise endothelial cell-cell interaction on compliant substrates [32] that we compared the simulations of pairwise interactions with, in this experiment we used a 2.5 kPa gel functionalized with 5 μg/ml RGD peptide - a stiffness at which no network-formation is found in our simulations. Although we thus do not yet reach full quantitative agreement between model and experiment, note that network formation occurs at substrate stiffness of 10kPa on polyacrylamide matrices enriched with a low (1 μg/ml) concentration of collagen [36].

We next asked if the mechanical model could also reproduce sprouting from endothelial spheroids [51, 103]. Video S5 and Figure 2.6 shows the results of simulations initiated with a two-dimensional spheroid of cells after 3000 MCS. On soft (0.5-8 kPa) and on stiff (32 kPa) matrices the spheroids stayed intact over the time course of the simulation. On matrices of intermediary stiffness (10-12 kPa) the spheroids formed distinct sprouts, visually resembling the formation of sprouts in *in vitro* endothelial spheroids [51, 103]. On the 14 kPa and 16 kPa matrices the cells migrated away from the spheroid, with some cell alignment still visible for the 14 kPa matrices. Observation of a sprout protruding from a spheroid at 10 kPa suggests that a new sprout starts when one of the cells at the edge of the cluster protrudes and increases the strain in front of it. In a positive feedback loop via an increase in perceived stiffness the strain guides the protruding cell forward. The strain in its wake then guides the other cells along (Figure 2.6C).

2.3 Discussion

In this paper we introduced a computational model of the *in vitro* collective behavior of endothelial cells seeded on compliant substrates. The model is based on the experimentally supported assumptions that (a) endothelial cells generate mechanical strains in the substrate [123, 131], (b) they perceive a stiffening of the substate along the strain orientation, and (c) they extend preferentially on stiffer substrate [94]. Thus, in short, the assumptions are: cell traction, strain stiffening, and durotaxis. The model simulations showed that these assumptions suffice to reproduce, in silico, experimentally observed behavior of endothelial cells at three higher level spatial scales: the single cell level, cell pairs, and the collective behavior of endothelial cells. In accordance with experimental observation [125, 127], the simulated cells spread out on stiff

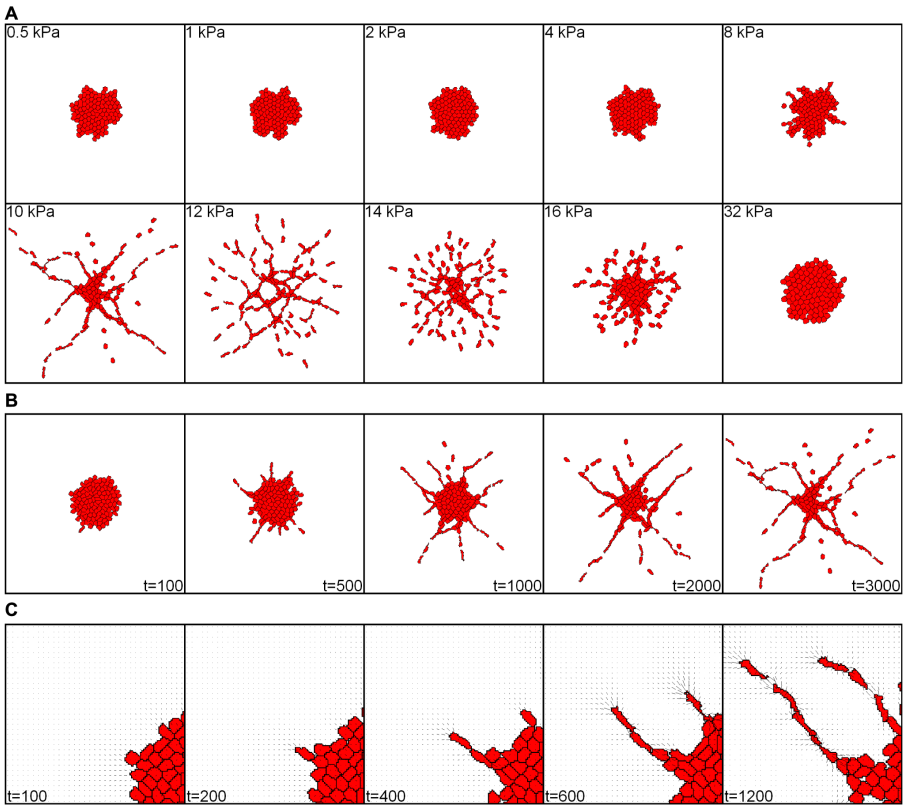

Figure 2.6: Simulated spheroid assay. (A) Collective behavior in a simulation initiated with a two-dimensional "spheroid" of cells, on substrates of varying stiffness; (B) Time lapse showing a sprouting spheroid on a 10kPa substrate. Time in MCS. Panels A and B represent a 0.75×0.75 mm^2 area (300×300 pixels) initiated with a spheroid consisting of 113 cells; (C) Close-up of sprouting on a 10 kPa substrate. Time in MCS. Black line pieces indicate strain magnitude and orientation.

matrices, they contracted on soft matrices, and elongated on matrices of intermediate stiffness (Figure 2.3). The same assumptions also sufficed to reproduce experimentally observed pairwise cell-cell coordination. On matrices of intermediate stiffness, endothelial cells slowed down each other (Figure 2.4B) and repeatedly touched and retracted from each other (Figure 2.4E and Video S2), in agreement with *in vitro* observations of bovine aortic endothelial cells on acrylamide gels [32]. Also, in agreement with experimental observations of fibroblasts on compliant substrates [134] and previous model studies [135] the cells repositioned into an aligned, head-to-tail orientation (Figure 2.4F). The model simulations further suggest that these pairwise cell-cell interactions suffice for vascular-like network formation *in vitro* (Figure 2.5) and sprouting of endothelial spheroids (Figure 2.6).

The correlation between pairwise cell-cell interactions and collective cell behavior observed in our computational model parallels observations *in vitro*. Cells elongate due to positive feedback between stretch-guided extension and cell traction, as previously suggested by Winer *et al.* [33]. Elongated and spindle-shaped cells are considered indicative of future cell network assembly [36]. Our model suggests that the elongated cell shapes produce oriented strains in the matrix, via which cells sense one another at a distance. In this way new connections are continuously formed over "strain bridges" (see, *e.g.*, Figure 2.5*C,D* and Video S4), while other cellular connections break, producing dynamically stable networks as illustrated in Video S3. Such dynamic network restructuring was also observed during early embryonic development of the quail embryo [138] and in bovine aortic endothelial cell cultures (Figure 2.5D and [36]), but not in human umbilical vein endothelial cell cultures [77, 137]. Also in agreement with experimental results, the collective behavior predicted by our model strongly depends on substrate stiffness. The strongest interaction between cell pairs is found on substrates of intermediate stiffness, enabling network formation [32], whereas network assembly does not occur on stiffer or on softer substrates[36].

These agreements with experimental results are encouraging, but our model also lacks a number of properties of *in vitro* angiogenesis that pinpoint key components still missing from our description. We compared the simulation of pairwise cell-cell interactions with previous experiments conducted on polyacrylamide gels, functionalized with RGD ligands [32], which have linear elastic behavior for small deformations [139–141]. Strain-stiffening of polyacrylamide gels has been reported for deformations over 2 μm [142]. Thus with pixels in our model measuring 2.5 μm × 2.5 μm, strain-stiffening seems a reasonable assumption. Nevertheless, a possible alternative interpretation of the cell pair simulations is that the increased tension generated in pseudopods pulling on the matrix leads to a higher probability of focal adhesion maturation[129, 130]. A further issue is that in our simulations, single cells dispersed somewhat more quickly on soft gels than on stiff gels (Figure 2.3E and Supplementary Figure 2.8). This model behavior contradicts experimental observations that endothelial cells move fastest on stiff substrates [32]. Another open issue concerns the time scales of our simulations. In the present paper time we use the Monte Carlo step as a

(computational) unit of time. To estimate the actual time corresponding to 1 MCS, we scale the single cell dispersion coefficients shown in Figure 2.3E to experimental dispersion coefficients of bovine endothelial cells on compliant substrates *in vitro* [32]. Reported dispersion coefficients of endothelial cells range from around 1 $\mu m^2/min$ (on substrates of 500 Pa) to around 10 $\mu m^2/min$ (on substrates of 5500 Pa) (as derived from the MSDs in Figure 3a,c in [32] and based on $MSD(t) = 4Dt$; *cf.* Eq. 2.13). The dispersion coefficients of single cells in our simulations are in the range of $0.03 - 0.08$ $\mu m^2/MCS$ (Figure 2.3), assuming pixels of 2.5×2.5 μm^2. Thus, based on fitting of single cell dispersion rates, the estimated length of 1 MCS is 0.5 to 3 seconds. The typical time scale of a vascular network formation simulation is around 3000 MCS (Figure 2.5), *i.e.*, 12.5 min to 2.5 hr for these time scale estimates. In experiments, network formation takes longer, around 24 hr. Thus in our current model the time scales of cell dispersion and network formation do not match exactly. A possible reason of this discrepancy is the short persistent length of cell motility in standard cellular Potts models. To better match the time scales of single cells and collective cell behavior in our model, in our future work we will increase the persistence length of the endothelial cells by using the available cellular Potts methodology [143–145], or model the subcellular mechanisms of cell motility in more detail, *e.g.* by including mean-field models of actin polymerization [146, 147]. A further open issue is the interaction between substrate mechanics and cell-substrate adhesivity. Although the model correctly predicts the absence of network formation on stiff substrates, it cannot yet explain the observation that reducing the substrate adhesivity of the endothelial cells rescues network formation on stiff substrates [36]. On compliant gels endothelial cells must secrete fibronectin to form stable networks, whereas fibronectin polymerization inhibitors elicit spindle-like cellular phenotypes associated with network formation on stiff matrices, under conditions where networks do not normally form [36]. To explain these observations, straightforward future extensions of the model will include a more detailed description of cell-substrate adhesion, combined with models of ECM secretion and proteolysis [108, 115, 117, 148].

The current model also assumes a uniform density (*i.e.*, the infinitesimal strain assumption) and thickness of the extracellular matrix, whereas under some culture conditions the endothelial cells have been reported to pull the extracellular matrix underneath them [149], producing gradient in matrix density and/or thickness. To describe the role of viscous deformations of the extracellular matrix in morphogenesis, Oster and Murray [79, 110] developed a continuum mechanical model of pattern formation in mesenchymal tissues. Their model assumed (a) that cells exert contractile forces onto the surrounding extracellular matrix, that will (b) locally deform the ECM, resulting in passive displacements of cells along with the ECM, and (c) produce density gradients in the ECM along which cells move actively due to haptotaxis. These mechanisms together produce periodic cell density patterns. Manoussaki *et al.* [80] and Namy *et al.* [82] applied this work to investigate mechanical cell-ECM interactions during angiogenesis, and demonstrated that the mechanism can produce vascular-like

network patterns. In their model they also included an anisotropic diffusion term to simulate preferential movement along the local strain-direction, but the term was neither necessary nor sufficient for network formation. This finding contradicts our model in which strain-induced sprouting is the driving force of network formation and sprouting. The two models represent the two extremes of network formation on visco-elastic matrices. Here, the Manoussaki *et al.* [80] and Namy *et al.* [82] models represent patterning on viscous matrices, in which cellular traction forces pull the matrix together while inducing little strain or stress. Our model would represent elastic materials, in which pulling forces induce local strains. Future extensions of the model will include matrix remodelling (*e.g.*, by assuming a matrix thickness field) allowing us to study the full range of viscoelastic matrices.

Apart from these biological issues, we made several mathematical simplifications that we will improve upon in future models of cell-ECM interactions. In the current model, for mathematical simplicity, we assumed that after each Monte Carlo step the matrix was undeformed again. Thus we currently did not consider cell memory of substrate strains. Further developments of the model presented here will improve on this issue, because actin filament dynamics are typically influenced by the past evolution of substrate deformations, *e.g.*, due to reorientation of matrix fibers [149]. For computational efficiency, we assumed linearly elastic materials and infinitesimal strain in the finite element simulations, and mimicked durotaxis via a perceived strain-stiffening (Eq. 2.9) where cells perceive increased ECM stiffness due to local strain. In our ongoing work we are interfacing the open source package FEBio (`http://febio.org`) with the cellular Potts package CompuCell3D (`http://compucell3D.org`). This will allow us to run our model with any ECM material available to users of FEBio, including strain-stiffening materials. Using an actual strain stiffening material may lead to longer-range interactions between cells, because locally stiffer regions may channel the stress between the cells [150]. A further technical limitation of our model is that we currently only run two-dimensional simulations, representing cells moving on top of a two-dimensional culture system. The ongoing interfacing of FEBio and CompuCell3D will pave the way for modeling cell-ECM interactions in three-dimensional tissue cultures. We also plan to model fibrous extracellular matrix materials in more detail.

A quite puzzling aspect of vascular network formation and spheroid sprouting is that so many alternative, often equally plausible computational models can explain it (reviewed in [107]). Including the present model, there are at least three alternative computational models based on mechanical cell-ECM interactions [80–82, 120, 151], a series of models assuming chemoattraction between endothelial cells [77, 111, 112, 114, 152, 153] and extensions thereof [115, 117, 154], and models explaining network formation in absence of chemical or mechanical fields [66, 119, 121]. Each of the models explains one aspect of vascular network formation or a response to an experimental treatment that the other models cannot explain, *e.g.* the relation between spindle-shaped cell phenotypes and network formation [77, 119], the requirement of

VE-cadherin signaling for network formation and sprouting [66, 114], the binding and release of growth factors from the ECM [115, 116], the role of mechanical ECM restructuring and haptotaxis [80, 82, 120], the response of vascular networks to toxins [117], or the role of intracellular Ca^{2+} signaling [144]. Among these alternative models, we must now experimentally falsify incorrect mechanisms, and fine-tune and possibly combine the remaining models to arrive at a more complete understanding of the mechanisms of angiogenesis. To this end, we are currently quantitatively comparing the kinetics of patterns produced by chemotaxis-based, traction-based, and cell-elongation based models with the kinetics of *in vitro* networks [77, 137]. The resulting, more complete model would likely contain aspects of each of the available computational models and assist in explaining the conflicting results obtained from the available experimental systems, culture conditions, and in silico models of angiogenesis.

2.4 Methods

To model the biomechanical interactions between endothelial cells and compliant matrices, we developed a hybrid of the cellular Potts model (CPM) [72, 73] to represent the stochastic motility of the endothelial cells, and a mechanical model based on the finite element method (FEM) [155] of the compliant extracellular matrix. Related CPM-FEM models were proposed for the simulation of load-induced bone remodeling [18, 156], and recently a related approach was proposed in a model study of cell alignment [87]. A detailed list of parameter values is given in Supplementary Table 2.1.

2.4.1 Cellular Potts model

The CPM represents cells on a regular square lattice, with one biological cell covering a cluster of connected lattice sites. To mimic random cell motility, the CPM iteratively expands and retracts the boundaries of the cells, depending on the passive forces acting on them and on the active forces exerted by the cells themselves. These are summarized in a balance of forces, represented by the Hamiltonian,

$$H = \sum_{\sigma \in \text{cells}} \lambda \left(\frac{a(\sigma) - A(\sigma)}{A(\sigma)} \right)^2 + \sum_{(\vec{x},\vec{x}\prime)} J(\sigma(\vec{x}), \sigma(\vec{x}\prime))(1 - \delta(\sigma(\vec{x}), \sigma(\vec{x}\prime))). \qquad (2.1)$$

The first term is an (approximate) volume constraint, with $a(\sigma)$ the actual volume of the cells, $A(\sigma)$, a resting volume, and λ an elasticity parameter that regulates the permitted fluctuation around the resting volume. In contrast with the original formulation of the CPM [72], the deviation of the cell from its target volume is taken relative to the target volume, by analogy with the (non-dimensional) engineering strain. Alternative, similar volume constraints can be chosen [154]. We use a value $A(\sigma) = 50$ for all

cells; the medium does not have a volume constraint. The second term represents cell-cell and cell-medium adhesion, where $J(\sigma(\vec{x}), \sigma(\vec{x}\prime)) \geq 0$ is the contact cost between two neighboring pixels, and δ, the Kronecker delta. Throughout the manuscript we use neutral cell-cell adhesion settings; $J(\sigma(\vec{x}), \sigma(\vec{x}\prime)) = 2.5$ at cell-cell interfaces, and $J(\sigma(\vec{x}), 0) = 1.25$ at cell-medium interfaces, with $\sigma(\vec{x}) > 0$ and $\sigma(\vec{x}\prime) > 0$. In other words, cells have no preference for adhering to other cells or the medium. For these neutral cell adhesion parameter settings, cells will still adhere weakly to one another (a remedy for this effect was proposed in [157]). Additional terms in the Hamiltonian represent the cells' responses to ECM mechanics, and will be described in more detail below.

The CPM iteratively selects a random lattice site $\vec{x}\prime$ and attempts to copy its state, $\sigma(\vec{x}\prime)$, into a randomly selected adjacent lattice site $\vec{x}$. To reflect the physical, "passive" behavioral response of the cells to their environment, the copy step is always accepted if it decreases the Hamiltonian. To account for the active random motility of biological cells, we allow for energetically unfavorable cell moves, by accepting copies that increase the Hamiltonian with Boltzmann probability,

$$P(\Delta H) = \begin{cases} 1 & \text{if } \Delta H < 0 \\ e^{-\Delta H/T} & \text{if } \Delta H \geq 0, \end{cases} \tag{2.2}$$

where ΔH is the change in H if the copying were to occur, and $T > 0$ parameterizes the intrinsic cell motility. It represents the extent to which the active cell motility can overcome the reactive forces (*e.g.* volume constraint or adhesions) in the environment. We assume that all cells keep the same motility and thus set T to be constant throughout the simulations. During one Monte Carlo step (MCS), we perform n copy attempts, with n equal to the number of sites in the lattice. To prevent cells from splitting up into two or more disconnected patches, we use a connectivity constraint that rejects a spin flip $\sigma(\vec{x}\prime) \rightarrow \vec{x}$ if it would break apart the retracting cell $\sigma(\vec{x})$.

2.4.2 Model of Compliant Substrate based on Finite Element Method

A two-dimensional model describes the compliant substrate on which the cells move. Deformations are calculated using the finite element method (FEM; reviewed in [155]). The FEM represents the substrate as a lattice of finite elements, e, with each element corresponding to a pixel of the CPM. To obtain the finite element equations, the weak formulation (associated with the total potential energy) of the governing equations of the displacement u of the substrate is set up, in order to obtain the finite element equations,

$$\underline{\underline{K}}\,\underline{u} = \underline{f}, \tag{2.3}$$

with stiffness matrix $\underline{\underline{K}}$, displacement $\underline{u}$, and forces $\underline{f}$. The vector $\underline{u} = [u_{x_1}, u_{y_1}, u_{x_2}, ..., u_{x_n}, u_{y_n}]^T$ contains the displacements of all nodes, which are the unknowns that the

FEM calculates based on the active forces exerted onto the material, presented in $\underline{f}$. In this paper $\underline{f}$ only consists of traction forces that the cells apply onto the ECM, unless stated otherwise. In a two-dimensional analysis the forces $\underline{f}$ are divided by the thickness they are working on. For this we assume an effective substrate thickness $t = 10$ µm. We impose boundary conditions of $\underline{u} = \underline{0}$ at the boundary of the CPM grid, this means that the substrate is fixed along the boundaries.

To a first approximation, in this work we consider an isotropic, uniform, linearly elastic substrate [135, 158] and we apply infinitesimal strain theory: We assume that material properties, including local density and stiffness are unchanged by deformations. The global stiffness matrix $\underline{\underline{K}}$ is assembled from the element stiffness matrices $\underline{\underline{K}}_e$ [155], which describe the relation between nodes of each element, e,

$$\underline{\underline{K}}_e = \int_{\Omega_e} \underline{\underline{B}}^T \underline{\underline{D}} \underline{\underline{B}} d\Omega_e. \tag{2.4}$$

where $\underline{\underline{B}}$—the conventional strain-displacement matrix for a four-noded quadrilateral element [155]—relates the node displacements $\underline{u}_e$ to the local strains, as,

$$\underline{\epsilon} = \underline{\underline{B}} \underline{u}_e. \tag{2.5}$$

The strain vector $\underline{\epsilon}$ is a column notation of the strain tensor $\underline{\underline{\epsilon}}$ and $\underline{\underline{D}}$ is the material property matrix. Assuming plane stress conditions,

$$\underline{\underline{D}} = \frac{E}{1-\nu^2} \begin{pmatrix} 1 & \nu & 0 \\ \nu & 1 & 0 \\ 0 & 0 & \frac{1}{2}(1-\nu), \end{pmatrix} \tag{2.6}$$

where E is the material's Young's modulus, and ν is Poisson's ratio. Throughout this study, we use a Poisson's ratio $\nu = 0.45$ and Young's moduli ranging from $E = 0.5$ kPa to $E = 32$ kPa, which are plausible values for most cell culture substrates [135, 140, 159]. For more details of the derivation of Eq. 2.3, and the entries in $\underline{\underline{B}}$ [155].

As a reference configuration for the displacements we used an unstretched substrate, $\underline{u} = \underline{0}$. Thus, after each Monte Carlo step (during which the cells positions and shapes have changed) the substrate is assumed to be undeformed, such that the stiffness matrix, $\underline{\underline{K}}$, is constant in time. This prevents expensive calculations that would be necessary for recalculating $\underline{\underline{K}}$ in each iteration. Although the previous displacements do not influence the new deformation of the substrate, they are used as an initial guess for solving $\underline{\underline{K}}\underline{u} = \underline{f}$, in order to reduce the number of iterations necessary to converge to the FEM solution.

2.4.3 Mechanical cell-substrate coupling

To simulate cell-substrate feedback we alternate the cellular Potts model (CPM) steps with a simulation of the substrate deformations using the finite element method. We

assume that cells apply a cell-shape dependent traction on the ECM and the cells respond to the resulting ECM strains by adjusting their cell shape. Using the CPM grid as the finite element mesh, the pixels of the CPM become four-node square elements in the FE-mesh. Adopting the model by Lemmon & Romer [131], we assume that each node i covered by a CPM cell pulls on all other nodes j in the same cell, at a force proportional to distance $\vec{d}_{i,j}$. The resultant force $\vec{F}_i$ on node i then becomes,

$$\vec{F}_i = \mu \sum_j \vec{d}_{i,j}, \tag{2.7}$$

where Δx is the lattice spacing and μ gives the tension per unit length. This parameter has been scaled to $\mu = 0.01$ nN/µm, such that the total cell traction corresponds to experimentally reported values [160]. The resultant forces point towards the cell centroid, and are proportional to the distance from it (Figure 2.2). In this way a CPM configuration yields a traction force $\underline{F}$, which are collected in the forces $\underline{f}$ for the finite element calculation. To calculate the resulting ECM strains, we solve $\underline{\underline{K}}\underline{u} = \underline{f}$ for the node displacements $\underline{u}$ with a preconditioned conjugate gradient (PCG) solver [161], and derive the local strains using Eq. 2.5. The reference configuration for the displacements is an unstretched substrate, $\underline{u} = \underline{0}$. After a sufficiently accurate solution for the FEM equations has been obtained by the PCG solver, we run a Monte Carlo step of the CPM. After each MCS, which changes cell positions, the substrate is assumed to be undeformed again, for the sake of simplicity. Thus, the stiffness matrix, $\underline{\underline{K}}$, is constant in time.

We assume durotaxis, *i.e.*, the CPM cells preferentially extend pseudopods on matrices of higher stiffness (*e.g.*, because of strain stiffening). By analogy with chemotaxis algorithms [75] at the time of copying we add the following durotaxis term to ΔH in response to the strain- and orientation-dependent ECM stiffness E,

$$\Delta H_{\text{durotaxis}} = -g(\vec{x}, \vec{x}\prime)\lambda_{\text{durotaxis}} \left(h(E(\epsilon_1))(\vec{v}_1 \cdot \vec{v}_m)^2 + h(E(\epsilon_2))(\vec{v}_2 \cdot \vec{v}_m)^2 \right), \tag{2.8}$$

with $g(\vec{x}, \vec{x}\prime) = 1$ for extensions and $g(\vec{x}, \vec{x}\prime) = -1$ for retractions, $\lambda_{\text{durotaxis}}$ is a parameter, $\vec{v}_m = \widehat{\vec{x} - \vec{x}\prime}$, a unit vector giving the copy direction, and ϵ_1 and ϵ_2, and v_1 and v_2 eigenvalues and eigenvectors of $\underline{\epsilon}$ representing the principal strains and strain orientation. We use the strain $\underline{\epsilon}(\vec{x})$ in the target pixel when considering an extension, and for retractions we use the strain in the source pixel, $\underline{\epsilon}(\vec{x}\prime)$. Thus we consider the strain in the ECM adjacent to the pseudopod. The sigmoid $h(E) = 1/(1 + \exp(-\beta(E - E_\theta)))$, with threshold stiffness E_θ, and β, the steepness of the sigmoid, mimics maturation of focal adhesions under the influence of tension [129]. The tension in focal adhesions will increase with higher local matrix stiffness, E, because the matrix will deform less easily. The sigmoid function starts at zero, goes up when there is sufficient stiffness, and eventually reaches a maximum. This means that a certain level of stiffness is needed to cause a cell to spread. Alternative forms of $h(E)$ can be used: For an

overview see Supplementary Figure 2.11. Due to limitations of our current finite element code and for reasons of computational efficiency, we assumed a linearly elastic, isotropic material in the FEM, thus precluding explicit strain stiffening effects in the FEM calculations. Instead, we implemented the effect of strain-stiffening in the cell response, where cells perceive increased ECM stiffness as a function of the principal strains ϵ_1 and ϵ_2,

$$E(\epsilon) = E_0(1 + (\epsilon/\epsilon_{st})1_{\epsilon\geq 0}) \tag{2.9}$$

where E_0 sets a base stiffness for the substrate, and ϵ_{st} is a stiffening parameter. The indicator function $1_{\epsilon>0} = \{1, \epsilon > 0; 0, \epsilon \leq 0\}$ indicates that strain stiffening of the substrate only occurs for substrate extensions ($\epsilon \geq 0$); compression ($\epsilon < 0$) does not stiffen or soften the substrate.

2.4.4 Morphometry

To characterize the random motility of single cells and cell pairs, we measured the cells' mean square displacement,

$$\mathrm{MSD}(t) = \langle(\overline{C}(S,t) - \overline{C}(S,0))^2\rangle, \tag{2.10}$$

with $\overline{C}(S,t)$, the centroid of cell S at Monte Carlo step ("time") t, given by

$$\overline{C}(S,t) = \frac{1}{|C(S,t)|}\sum_{\vec{x}\in C(S,t)} \vec{x}, \tag{2.11}$$

with $C(S,t)$, the set of coordinates of the lattice sites comprising cell S at MCS t,

$$C(S,t) = \left\{\vec{x} : \vec{x} \in \mathbb{Z}^2 \wedge \sigma(\vec{x},t) = S\right\}, \tag{2.12}$$

and $\vec{x} = \{x_1, x_2\}$. The MSD is a reliable measure of random motility [162] and it can be directly compared with experimental data (*e.g.*, [32]).

The dispersion coefficient, defined as

$$D = \lim_{t\to\infty}\frac{1}{4t}\langle(\overline{C}(S,t) - \overline{C}(S,0))^2\rangle, \tag{2.13}$$

is derived from the slope of the MSD, and is used as a measure of the motility of random walkers. The length, orientation and eccentricity of cells were estimated from the inertia tensors $I(S)$ of the cells, defined as [76],

$$I(S) = \begin{pmatrix} \sum_{\vec{x}\in C(S)}(x_2 - \overline{C}_2(S))^2 & -\sum_{\vec{x}\in C(S)}(x_1 - \overline{C}_1(S))(x_2 - \overline{C}_2(S)) \\ -\sum_{\vec{x}\in C(S)}(x_1 - \overline{C}_1(S))(x_2 - \overline{C}_2(S)) & \sum_{\vec{x}\in C(S)}(x_1 - \overline{C}_1(S))^2 \end{pmatrix}.$$

(2.14)

Assuming cells are approximately ellipse-shaped, the length of cell σ is approximated as $l(\sigma) = 4\sqrt{e_2(I(S))/|C(S)|}$, with $e_2(I(\sigma))$ the largest eigenvalue of $I(S)$. The eccentricity of a cell is defined using the eigenvalues of the inertia tensor $I(\sigma)$ as $\xi(\sigma) = \sqrt{1 - \left(\frac{e_1(I(S))}{e_2(I(S))}\right)^2}$, where $e_1(I(S)) \leq e_2(I(S))$ are the eigenvalues of $I(S)$. An eccentricity close to zero corresponds to roughly circular cells and cells with an eccentricity close to unity are more elongated. The orientation of the cell is given by the eigenvectors of the inertia tensor $I(S)$.

2.4.5 Endothelial Cell Culture

Bovine aortic endothelial cells (BAECs) (VEC Technologies, Rensselaer, NY) were cultured through passage 12. Cells were kept at 37°C and 5% CO_2 and fed every other day with Medium 199 (Invitrogen, Carlsbad, CA) supplemented with 10% Fetal Clone III (HyClone, Logan, UT), 1% MEM amino acids (Invitrogen), 1% MEM vitamins (Medtech, Manassas, VA), and 1% penicillin-streptomyocin (Invitrogen). Polyacrylamide hydrogels were synthesized as previously described [36]. Briefly, a gel mixture was prepared from MilliQ water, HEPES, TEMED (Bio-Rad, Hercules, CA) and a 5%:0.1% ratio of acrylamide to bis-acrylamide (Bio-Rad) to generate substrates with a Young's modulus of 2,500 Pascals. Polymerization was initiated by the addition of N-6-((acryloyl)amido)hexanoic acid (synthesized according to Pless *et al.* [163]) and ammonium persulfate (Bio-Rad) into the gel mixture. Following polymerization, gels were incubated with 5 μg/ml RGD peptide (GCGYGRGDSPG) (Genscript), followed by ethanolamine (Sigma). Gels were stored in PBS overnight. Hydrogels were sterilized with ultraviolet light before cell culture. A T-75 flask with a confluent BAEC monolayer was seeded onto the hydrogels at 350,000 cells per gel (approximately 1,375 cells per mm^2). The gels were maintained at 37°C and 5% CO_2 for three days prior to imaging. ÊAfter replenishing with fresh complete media, the cells on hydrogels were visualized with a Zeiss Axio Observer.Z1 inverted spinning disc microscope with a Hamamatsu ORCA-R^2 digital camera. Images were captured every 30 minutes for 24 hours.

2.5 Supplementary tables

Parameter	symbol	value	unit
discretization parameters			
element size	Δx	2.5	μm
basic CPM parameters			
intrinsic cell motility	T	1	-
target volume	A	50	pixels
strength of volume constraint	λ	500	-
cell-medium contact cost	J_{cm}	1.25	pixelside^{-1}
cell-cell contact cost	J_{cc}	2.5	pixelside^{-1}
FEM parameters			
Young's modulus	E	0.5-32	kPa
Poisson's ratio	ν	0.45	-
substrate thickness	τ	10	μm
accuracy level of solver	ψ	0.00001	-
cell traction model			
traction per unit length	μ	0.01	nN μm^{-1}
stretch guidance model			
maximum guidance term	$\lambda_{\text{durotaxis}}$	10	-
threshold for stiffness preference	E_θ	15	kPa
steepness of stiffness preference	β	0.5	kPa^{-1}
strain stiffening parameters	ϵ_{st}	0.1	-

Table 2.1: Parameter settings.

2.6 Supplementary figures

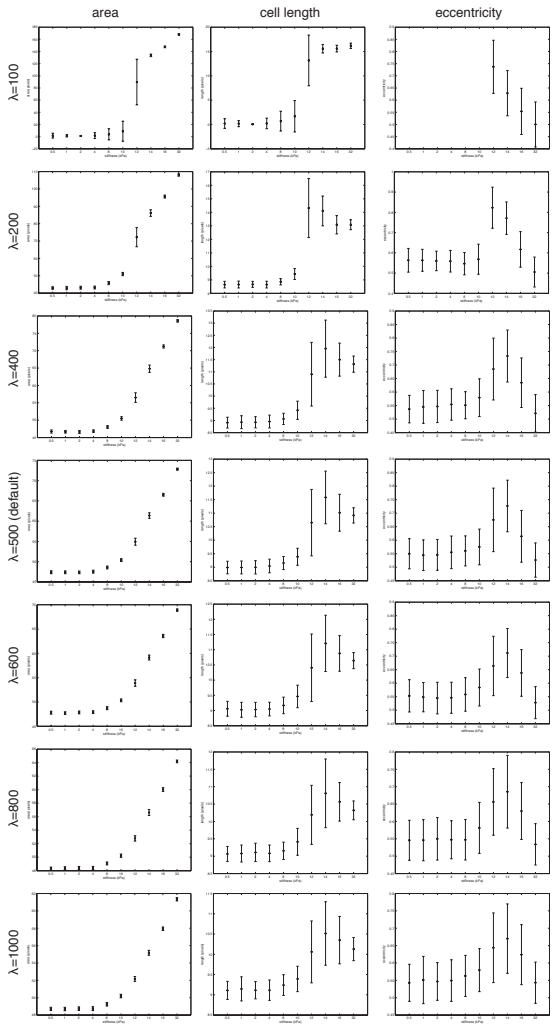

Figure 2.7: Simulated responses of individual cells to mechanical cell-ECM feedback as a function of the values of the volume restriction, λ. Columns: area (left), cell length (middle) and eccentricity (right). Mean and standard deviation shown for $n = 100$ after 500 MCS on simulated substrates of stiffness varying from 0.5 kPa to 32 kPa.

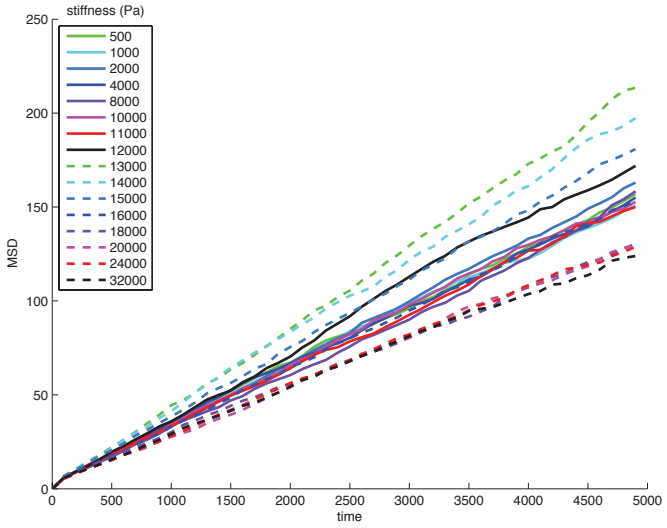

Figure 2.8: Mean square displacements of individual cells on simulated substrates of stiffness varying from 0.5 kPa to 32 kPa. Mean square displacement shown over $n = 1000$ cells.

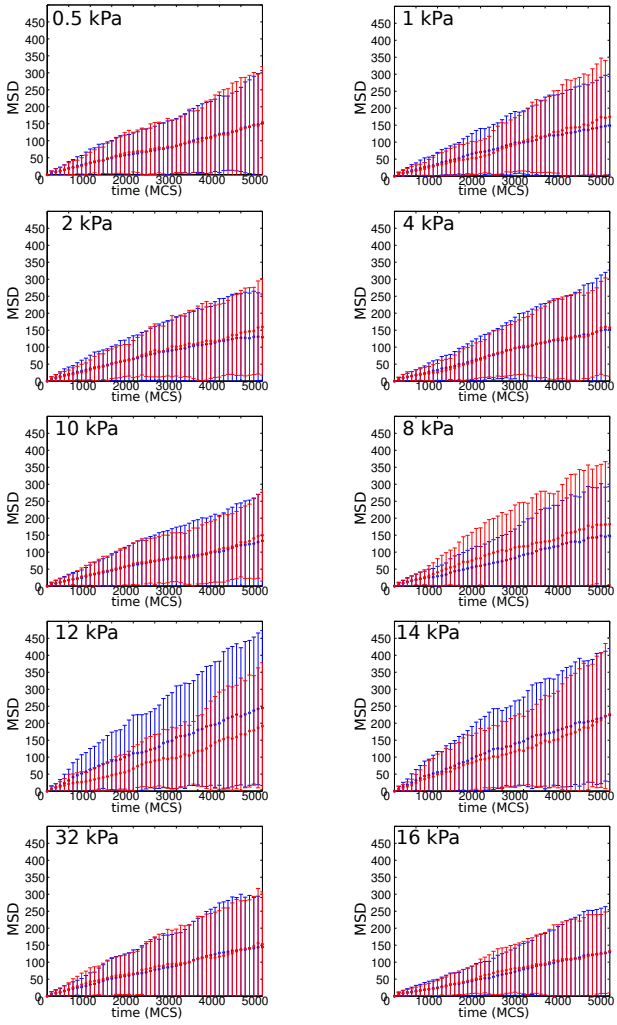

Figure 2.9: Mean square displacement of individual cells (blue errorbars) and cell pairs (red errorbars) on simulated substrates of stiffness varying from 0.5 kPa to 32 kPa. Error bars indicate standard deviation for $n = 100$.

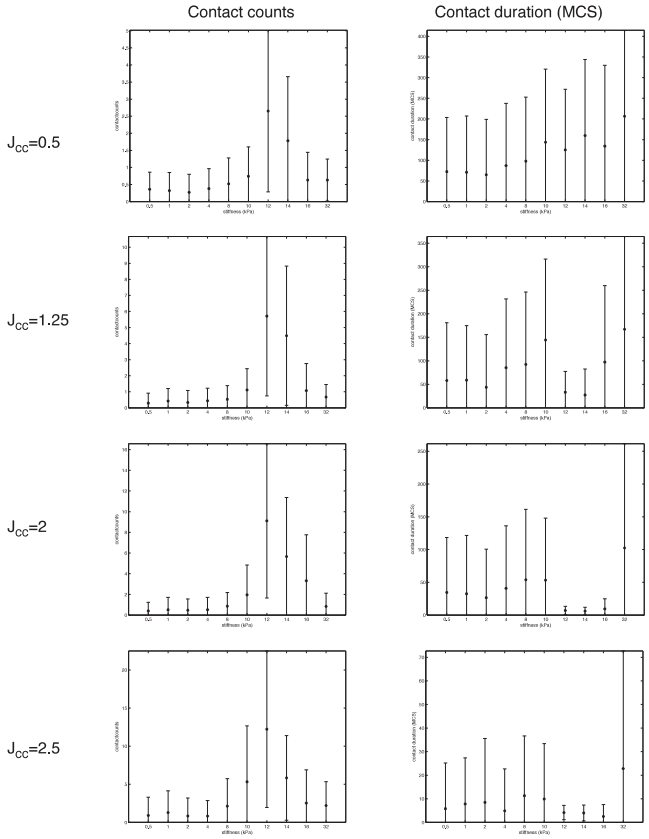

Figure 2.10: Number of cell-cell contacts made over 500 MCS (left column) and contact duration (right column) over 500 MCS between two simulated cells initiated at a distance of fourteen lattice sites from each other on simulated substrates of stiffness varying from 0.5 kPa to 32 kPa, for intercellular contact energies varying from $J(\sigma(\vec{x}), \sigma(\vec{x}\prime)) = 0.5$ (adhesive cells) to $J(\sigma(\vec{x}), \sigma(\vec{x}\prime)) = 4$ (repulsive cells), with $\sigma(\vec{x}) \geq 1$ and $\sigma(\vec{x}\prime) \geq 1$; $J(\sigma(\vec{x}), 0) = 1.25$ for all simulations.

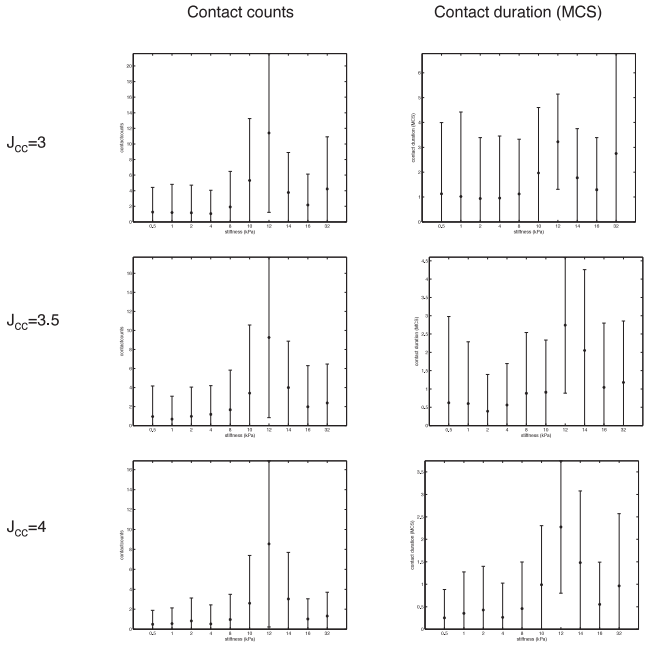

Part 2 of Figure 2.10

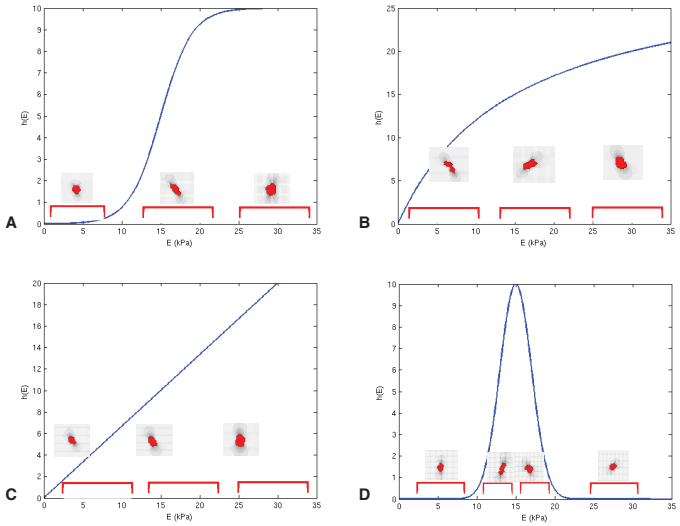

Figure 2.11: Effect of form of model function $h(E)$ on cell shapes on substrates of different stiffnesses. (A) Standard, sigmoid function, as used in main text, $h(E) = 1/(1 + \exp(-\beta(E - E_0)))$ with $E_0 = 15000$, $\beta = 0.0005$, and $\lambda_{\text{durotaxis}} = 10$; (B) Saturated function, $h(E) = (E/E_0)/(1 + E/E_0)$, with $E_0 = 15000$ and $\lambda_{\text{durotaxis}} = 25$; (C) Piecewise linear function, $h(E) = \{E/\alpha, E \leq E_{\max}, E \geq E_{\max}\}$, with $E_{\max} = 30000$, $\alpha = 30000$, and $\lambda_{\text{durotaxis}} = 20$; (D) Gaussian function, $h(E) = \exp\left(-(E - E_0)^2/(2\gamma^2)\right)$, with $E_0 = 15000$ and $\gamma = 2000$, $\lambda_{\text{durotaxis}} = 10$. Insets show typical cell shape for regions indicated by red bars.

2.7 Supplementary videos

All supplementary movies can be found at `https://doi.org/10.1371/journal.pcbi.1003774`

Video S1 Behavior in silico of a single cell on substrates of 4 kPa, 12 kPa, and 32 kPa, for a duration of 500 MCS per simulation. Parameter settings as in Figure 2.3.

Video S2 Pairwise cell-cell interactions in silico on substrates of 4 kPa, 12 kPa, and 32 kPa, for a duration of 500 MCS per simulation. Parameter settings as in Figure 2.4.

Video S3 Network formation in silico on a substrate of 10kPa, for a duration of 3000 MCS. Video represents a 0.75×0.75 mm^2 area (300×300 pixels) initiated with 450 cells. Parameter settings are as in Figure 2.5.

Video S4 Network formation of bovine aortic endothelial cells on a 2.5 kPa polyacrylamide gel functionalized with RGD-peptide. Time lapse images were captured in 30 minute intervals over an 8 hour time period. Image size as in Figure 2.5*D*.

Video S5 Sprouting in silico from a spheroid on a substrate of 10kPa, for a duration of 3000 MCS. Video represents a 0.75×0.75 mm^2 area (300×300 pixels) initiated with 450 cells. Parameter settings are as in Figure 2.6.

3

Cell Contractility Facilitates Alignment of Cells and Tissues to Static Uniaxial Stretch

This chapter is published as:

Rens, Elisabeth G. and Merks, Roeland M.H. (2017) Cell Contractility Facilitates Alignment of Cells and Tissues to Static Uniaxial Stretch Biophysical Journal , Volume 112 , Issue 4 , 755 - 766.

Abstract

During animal development and homeostasis, the structure of tissues, including muscles, blood vessels and connective tissues adapts to mechanical strains in the extracellular matrix (ECM). These strains originate from the differential growth of tissues or forces due to muscle contraction or gravity. Here we show using a computational model that by amplifying local strain cues, active cell contractility can facilitate and accelerate the reorientation of single cells to static strains. At the collective cell level, the model simulations show that active cell contractility can facilitate the formation of strings along the orientation of stretch. The computational model is based on a hybrid cellular Potts and finite-element simulation framework describing a mechanical cell-substrate feedback, where: 1) cells apply forces on the ECM, such that 2) local strains are generated in the ECM, and 3) cells preferentially extend protrusions along the strain orientation. In accordance with experimental observations, simulated cells align and form string-like structures parallel to static uniaxial stretch. Our model simulations predict that the magnitude of the uniaxial stretch and the strength of the contractile forces regulate a gradual transition between string-like patterns and vascular network-like patterns. Our simulations also suggest that at high population densities, less cell cohesion promotes string formation.

3.1 Introduction

During embryonic development, a single fertilized egg cell grows into a complex functional organism [164]. Even after years of studying morphogenesis, the organization of cells into tissues, organs and organisms, it still remains a puzzle how cells migrate and form the right pattern in the right part of the body at the right moment [165]. Apart from chemical signals [166], mechanical signals play an equally important role in morphogenesis [26, 167]. Static strains originating from differential growth of tissues are instrumental for the organization of cells in tissues *in vivo*. For example, in quail heart, the endocardium generates strains to which cardiomyocyte microtubules orient [168]. Wing hinge contractions in *Drosophila* cause anisotropic tension in the wing-blade epithelium, to which the cells align [169]. Using a multiscale computational modeling approach, here we unravel how static strains, *e.g.*, resulting from the differential growth of tissues, may drive the organization of cells and tissues.

In vitro and *in silico* experiments have helped to unravel the cellular mechanisms underlying the adaptation of tissues to strain. Myocytes [170], mesenchymal stem cells [171], muscle cells, and endothelial cells [94] orient in parallel to uniaxial static stretch. Furthermore, fibroblasts organize into string-like structures in parallel to the stretch orientation [95], whereas endothelial cells form monolayers of cells oriented in parallel to the stretch [94].

Active cell traction forces play a crucial role in the alignment of cells to static uniaxial stretch. Using contact guidance, cells can adjust their orientation to the fibers which align with strain [172, 173]. Then, by pulling on the matrix, cells can fur-

ther align the fibers [174]. Such mechanical cell-fiber feedback can coordinate cell alignment [90, 134, 175] and string formation [86] along strain. However, *in vitro* observations suggest that cell alignment to uniaxial stretch may not necessarily be driven by fiber alignment. Mesenchymal stem cells align along the orientation of strain on a *nonfibrous* matrix [171]. In stretched collagen matrices, fibroblasts were found to align along strain in the absence of fiber alignment [95, 176]. Other authors observed that collagen fibers aligned only after the cells had aligned [177, 178]. Moreover, fibroblasts can orient along the uniaxial stretch even if fibronectin fibers were aligned perpendicular to the stretch [179]. Altogether, these results suggest that cells can orient to stretch independently of the fiber orientation.

Mathematical modeling is a helpful tool to explore what biophysical mechanisms can explain the alignment of cells to strain. Previous mathematical models [45, 180] were based on optimization principles. Bischofs and Schwarz [45] proposed that cells minimize the amount of work needed for contracting the matrix. For dipolar cells, the work was minimized if they oriented in parallel with the uniaxial stretch. If the cells were assumed to generate strains in their local environment, cells formed strings, which aligned with an external strain field [45, 46, 181]. Based on the observation that cells reorganize focal adhesions and stress fibers to maintain constant local stresses, De *et al.* [180] proposed that cells adapt their contractility and orientation in order to find the minimal local stress in the matrix. They showed that the local stress becomes minimal if a dipolar cell orients in parallel to uniaxial stretch, as in this configuration the cell traction forces counteract the uniaxial stretch.

In this work, we explain cellular alignment to strain based on a mesoscopic, experimentally testable cellular mechanism. To simulate this mechanism, we propose a hybrid computational model in which the Cellular Potts Model (CPM) [72] is coupled to a finite-element model (FEM) of the matrix. The computational model [182] captures the mechanical cross-talk between the extracellular matric (ECM) and the cells as follows: 1) cells apply forces on the ECM [131]; 2) the resulting strains in the ECM are calculated using a Finite Element Method (FEM); and 3) cells extend protrusions oriented along strain [178].

Based on experimental observations of fibroblasts on elastic substrates [126] and on modeling studies [180], it has been suggested that cellular traction forces may dominate over, or even counteract global strain cues. Paradoxically, our model suggests that contractile cells locally increase the global uniaxial strain which *facilitates* cell alignment to static uniaxial stretch. Our model also suggests that by contracting the matrix, cells can form strings in parallel to the orientation of uniaxial stretch. Finally, our simulations show that differences in cell cohesion and population density may determine under what conditions cells form strings, and when they only align on a individual level.

3.2 Results

This work proposes a computational model for the collective response of cells to uniaxial stretch in compliant tissues. In the model, cells apply contractile forces onto a compliant substrate. The resulting strains in the matrix affect the motility of the cell itself and the motility of its neighbors. In all of the simulations described in this paper, we stretched a substrate of Young's modulus 12kPa with a stress of $\sigma_{\text{stretch}} = 1000$ N/m^2 applied to the boundary of the matrix in the FEM. This results in a static strain of around 8% on the matrix. The cellular tension μ (see Eq. 3.6) was set to 0.0025 nN/µm, resulting in local strains around the tips of elongated cells of up to 2%, amplifying the static strain to values of around 10%.

3.2.1 Individual cell response to uniaxial stretch is amplified by cell contractility

In order to elucidate how cell traction forces affect individual cell response to uniaxial stretch in our model, we simulated the response of a single cell to uniaxial stretch applied in the vertical orientation. This was carried out both in the presence ($\mu > 0$) and in the absence ($\mu = 0$) of active cell contraction. Figure 3.1A shows a non-contractile cell on a uniaxially stretched ECM after 500 MCS; the cell elongates slightly along the stretch orientation, in accordance with our previous results [182]. Figure 3.1B shows the same simulation set-up in the presence of active cell contraction. The contractile cell elongates more strongly than the non-contractile cell (Figure 3.1A). Interestingly, the cell orients itself along the strain orientation, despite the fact that the contractile forces (Eq. 3.6) counteract the uniaxial stretch. The current choice for Δx is based on balance between precision and computation time. To confirm that the model is scalable, we repeated the simulation on grids that were refined by a factor of two ($\Delta x = 1.25$µm, Supplementary Figure 3.9A) and four ($\Delta x = 0.625$µm, Supplementary Figure 3.9B), and observed qualitatively similar behavior. Out of the batch of 100 simulations, in 38 of the simulations, the middle part of contractile cells became rather slender (Supplementary Figure 3.8C), resulting in a cell shape that seems unrealistic, as elongated cells are typically reported to have a spindle-like shape. The area conservation (Eq. 3.1) imposes that extensions are, on average, balanced by retractions. Because contractile cells reduce the uniaxial stretch around the center of the cell, retractions are most likely to occur here, resulting in a slender middle part.

To study single cell orientation in more detail and check the isotropy of the model, we performed 100 simulations of single contractile and non-contractile cells for 500 MCS, using stretch angles in the range 0° to 180° with increments of 15° on a 100 × 100 lattice, representing a piece of tissue of 250 × 250 µm. Cells with a diameter of seven lattice sites were initiated in the middle of the matrix. The cell orientation was estimated from the inertia tensor of the cells (see Supplementary Methods). Figure 3.1C plots the cell orientation as a function of the orientation of stretch for cells without active contraction (red boxes) and with active contraction (green boxes). In

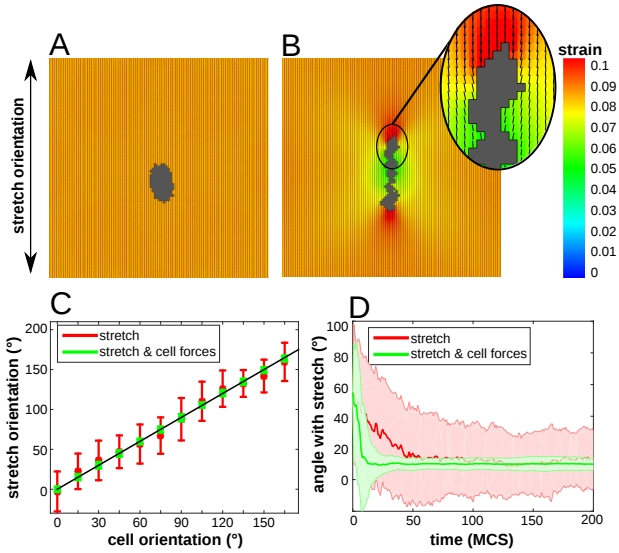

Figure 3.1: Single cell response to static stress. (A) Non-contractile cell on substrate stretched along 0° at 500 MCS; (B) contractile cell on substrate stretched along 0° at 500 MCS; (A-B) colors: principal strain magnitude; orientation and length of black line pieces: orientation and magnitude of principal strain; (C) cell orientation as a function of stretch orientation at 500 MCS; averaged over $n = 100$ simulations; error bars: standard deviations; black line shows linear fit; (D) time series of the orientation of a single cell on a substrate stretched over 0°, averaged over $n = 100$ simulations; shaded regions: standard deviations. Color coding (C-D): red (with large standard deviations): non-contractile cells; green (with larger standard deviations): contractile cells.

both conditions, the cells follow the strain orientation on average. However, the cells that apply active contractile forces on the matrix followed the orientation with much higher accuracy, as evidenced by the much smaller standard deviations. Also, the eccentricities of the contractile cells were much more narrowly distributed than those of non-contractile cells (Supplementary Figure 3.8A). Figure 3.1D shows that the contractile cells oriented more quickly to the stretch orientation than the non-contractile cells. This behavior was only observed on matrices of intermediate stiffness (Supplementary Figure 3.8B). On soft substrates, cells remain small [182] and as a result do not apply sufficient force on the matrix. On a very stiff matrix, cells protrude in all directions [182] and thus they cannot orient along a specific angle.

Altogether, the simulated contractile cells aligned with the strain more accurately than the non-contractile cells. This can be explained by a positive feedback loop between cell shape, cell traction forces and strain stiffening. Cells elongate slightly in response to uniaxial stretch. Due to the anisotropic cell shape, cells pull harder on the matrix around the tip of the cells, since the distance between the tip of the cell and the cell interior increases (see Eq. 3.6). So, the matrix stiffens around the tip of the cell

which further promotes cell elongation along uniaxial stretch.

3.2.2 Cell contractility enables cells to align with each other in parallel to uniaxial stretch

We next looked at the alignment of neighboring cells in uniaxially stretched matrices. We simulated the response of two circular cells placed horizontally next to each other on a substrate with a static strain along the vertical axis, both in the presence ($\mu > 0$) and in the absence ($\mu = 0$) of active cell contraction. Figure 3.2A shows a pair of cells on a statically stretched matrix at 500 MCS; the cells elongate slightly and do not align in a head-to-tail fashion. Figure 3.2B shows the same simulation set-up in the presence of active cell contraction. In contrast to non-contractile cells, a pair of contractile cells assume a head-to-tail configuration. Also, similar to the response of a single cell found in the previous section, both cells elongate more strongly than the non-contractile cell in Figure 3.2A. Notably, the pair of contractile cells assume a head-to-tail configuration along the orientation of uniaxial stretch.

To study this head-to-tail alignment in more detail, we performed 100 simulations of paired cells for 500 MCS for both scenarios on a 200×200 lattice, corresponding to 500×500 μm, for stretch angles in the range 0° to 180° with increments of 15°. Two cells with a diameter of seven lattice sites were initiated in the middle of the matrix, eight lattice sites apart. Cell-cell alignment was quantified by evaluating the triangle (A,B,C), where A and B are the center of masses of the two cells and C is the point where the lines describing the orientations of the two cells intersect. Supplementary Table 3.2 describes how this triangle is used to decide whether a pair of cells is aligned or not. Figure 3.2C plots the fraction of time that cells are aligned on a stretched substrate as a function of stretch orientation for cells without active contraction (red boxes) and with active contraction (green boxes). Contractile cells align more often with each other than non-contractile cells. To confirm that cells align along the stretch orientation, we measured the orientation of the line connecting the center of masses of the two cells. Figure 3.2D plots this cell-cell angle as a function of stretch orientation; a pair of contractile cells align along stretch, compared to non-contractile cells that stick around their initial position (placed horizontally next to each other) and thus keep their initial alignment angle of 90°.

Figure 3.2E plots the number of cell pairs that aligned as a function of time in $n = 100$ simulations. This shows that with stretch around 0°, cells cannot always align. This is because, after initial elongation, the tips of the cells are not in each other's vicinity, such that the cells cannot sense each other's strain. Interestingly, this phenomenon may provide an explanation for an experimental observation reported by Winer *et al.*[33]. Studying the behavior of endothelial cells on compliant matrices, they observed that cell pairs aligned more on 2 mg/ml polyacrylamide gels than on a softer, 1 mg/ml gel on which cell assumed an extremely elongated shape. They hypothesized that this "extremely elongated shape of the cells and thus the shape of the resulting strain field reduced the probability that a second cell would come in contact with the

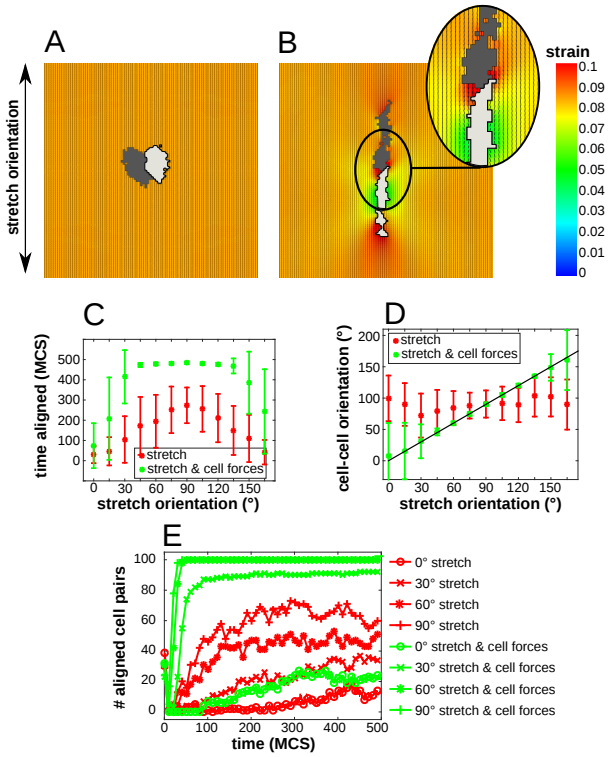

Figure 3.2: Response of two adjacent cells to static stress. (A) Non-contractile cell pair on substrate stretched along 0° at 500 MCS; (B) contractile cell pair on substrate stretched along 0° at 500 MCS; (A-B) colors: principal strain magnitude; orientation and length of black line pieces: orientation and magnitude of principal strain; (C) fraction of time a cell pair is aligned, averaged over $n = 100$ simulations, upper bars for contractile cells and lower bars for non-contractile cells; (D) angle of the line connecting the center of masses as a function of stretch orientation at 500 MCS, averaged over $n = 100$ simulations, contractile cells follow the extra plotted linear line piece. (C-D): error bars: standard deviations; (E) time series of the number of cell pairs that are aligned on stretched substrates with different stretch orientations; symbols are circle: 0°, cross: 30°, star: 60°, plus: 90°, upper lines for contractile cells and lower lines for non-contractile cells. Color coding (C-E): red: non-contractile cells; green: contractile cells.

affected gel". To test this hypothesis in our model, we increased the probability of a cell to come into contact with the strain field of the other cell, by increasing the cellular temperature T. Increasing T increases the probability that a cell makes a protrusion. Supplementary Figure 3.10A shows the fraction of time a pair of contractile cells are aligned as a function of T and Supplementary Figure 3.10B shows how the number of cell pairs that are aligned depend on T. This illustrates that pairs of cells more readily align at higher values of T. These simulation results thus match the hypothesis of Winer *et al.* [33]. At motilities larger than approximately $T = 20$ cell motility became randomized to the extent that the cells could no longer align.

In summary, in our model pairs of contractile cells aligned in head-to-tail configurations along the orientation of stretch, whereas non-contractile cells oriented with the stretch, but not in a head-to-tail fashion. The bipolar strain fields around the contractile cells were instrumental for this cell-cell alignment.

3.2.3 Cell contractility facilitates the self-organization of cells into strings oriented parallel to uniaxial stretch

After identifying the orientation response of a pair of cells, we asked how cell contractility affects the alignment of a large group of cells. We simulated a group of cells on a stretched matrix, both in the presence ($\mu > 0$) and in the absence ($\mu = 0$) of active cell contraction. The behavior of the model does not depend on the stretch orientation, so we only show the results for stretching in the vertical orientation in the next sections. Figure 3.3A shows a group of cells on a statically stretched matrix in the vertical orientation at 3000 MCS; the cells have elongated slightly and have not migrated away from their initial position. Figure 3.3B shows the same simulation set-up in the presence of active cell contraction. The contractile cell aligned locally with one another in a head-to-tail configuration, as observed in our simulation of paired cells. This cell-cell alignment enables cells to form strings along the orientation of uniaxial stretch, as observed experimentally by Eastwood *et al.* [95].

To study this behavior in more detail, we performed 25 simulations of a group of cells on a 400×400 lattice, representing a piece of tissue of 1×1 mm, for 3000 MCS for both scenarios, for a stretch angle of 0°. Cells are initially placed uniformly inside a region of 200×200 lattice sites in the middle of the matrix, as to minimize boundary effects. Cells are initially one lattice site in size. The density of cells was d =0.15, yielding around 120 cells. To characterize the collective orientation of cells, we measured a two-dimensional orientational order parameter $S(r)$, with range r (μm), defined for the Cellular Potts Model as in Ref.[119]. Briefly, $S(r) = \left\langle \cos 2\theta(\vec{X}(s), r) \right\rangle_s$, where $\vec{X}(s)$ is the center of mass of cell s and $\theta(\vec{X}(s), r)$ is the angle between the orientation of the cell of spin s and a local director, *i.e.*, the average orientation of the cells within a radius r around the centroid of cell s (see Supplementary Methods for detail). $S(r)$ ranges from $S(r) = 0$ for configurations of randomly oriented cells, to $S(r) = 1$ for fully aligned cells. Figure 3.3C plots the orientational order parameter as a func-

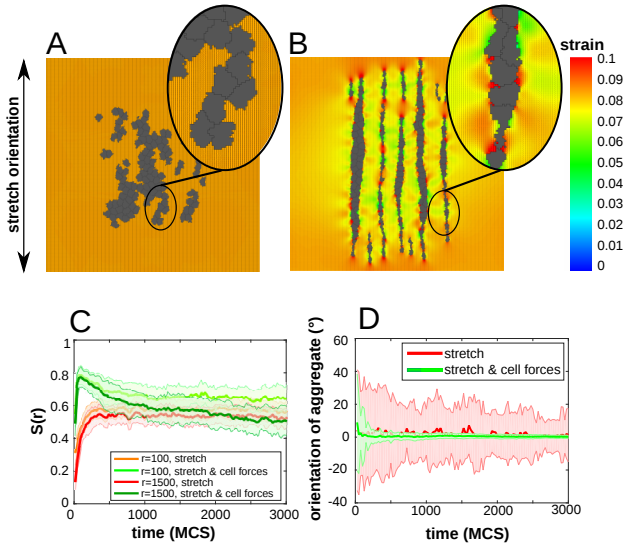

Figure 3.3: Collective cell response to static stress. (A) Non-contractile cells on substrate stretched along 0° at 3000 MCS; (B) contractile cells on substrate stretched along 0° at 3000 MCS; (A-B) colors: principal strain magnitude; orientation and length of black line pieces: orientation and magnitude of principal strain; (C) time series of orientational order parameter $S(r)$, averaged over $n = 25$ simulations; color coding: red (lowest line): r=100 μ m for non-contractile cells, orange (second lowest line): r=1500 μm for non-contractile cells, green (highest line): r=100 μm for contractile cells, dark-green (second highest line): r=1500 μm for contractile cells; (D) time series of the orientation of cell aggregates on a substrate stretched over 0° at 3000 MCS, averaged over $n = 25$ simulations; shaded regions: standard deviations. red (with large standard deviations): non-contractile cells; green (with larger standard deviations): contractile cells.

tion of time, showing a local orientational order ($r = 100\mu$m) for non-contractile cells (orange curve) and for contractile cells (green curve) and the global orientational order ($r = 1500\mu$m) for non-contractile cells (red curve) and for contractile cells (dark-green curve). Contractile cells achieve a higher local and similar global ordering than non-contractile cells. Note that contractile cells initially obtain a high orientational order, close to 0.8. Since cells initially have enough space, they elongate well. When cells start to adhere to another and form strings, cells in the interior of a string cannot orient well, such that the global orientational order parameter decreases. This is a model artifact which we investigated further in the Supplementary Methods and address in the discussion section.

To confirm that by contracting the matrix, cells co-align into strings oriented along uniaxial stretch, we measured the orientation of cell aggregates, with a cell aggregate defined as a connected patch of cells (see Supplementary Methods for details on the calculation). Figure 3.3D plots the orientation of cell aggregates as a function of

time, of non-contractile cells (green curve) and of contractile cells (red curve). In both conditions, cells form aggregates with an orientation around 0°, which is the orientation of stretch. The aggregates formed by contractile cells follow the stretch orientation more accurately, as shown by the smaller standard deviations, indicating that strings have formed.

In our model, contractility facilitates the formation of strings of cells along the stretch orientation, in agreement with experimental observations [95]. We have shown previously that in unstrained matrices, contractile cells organize into network-like structures [182]. We next studied what level of uniaxial stretching is needed for cells to prefer a string-like organization instead of a network-like organization.

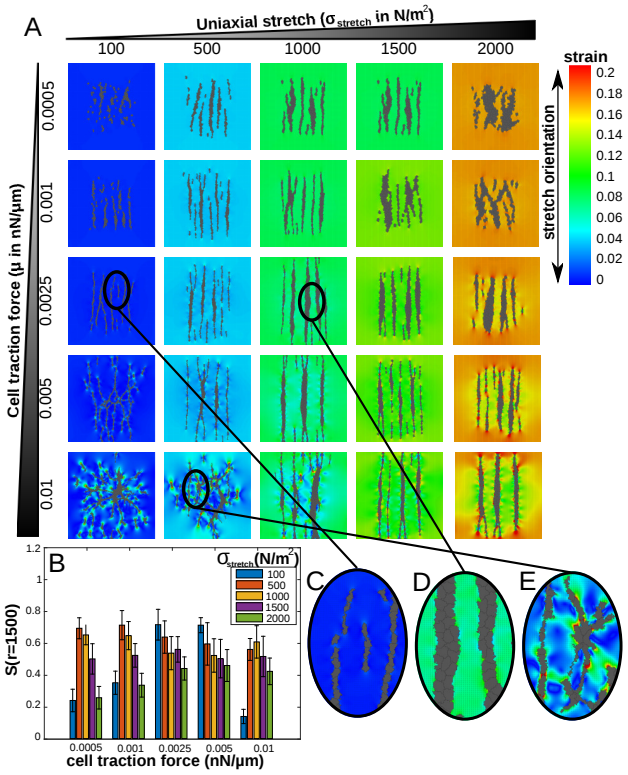

Figure 3.4: Model sensitivity to cell traction force and matrix stretching force. (A) Contractile cells on substrate stretched along 0° at 3000 MCS simulated with various values of cell traction force and matrix stretching force; (B) Global orientational order parameter $S(r = 1500\ \mu\text{m})$ at 3000 MCS, averaged over $n = 25$ simulations; error bars: standard deviations; bars in bar chart are sorted according to value of σ_{stretch} as indicated in figure inset; (C) zoom in of cell configuration of $\mu = 0.0025$, $F_{\text{stretch}} = 100$; (D) zoom in of cell configuration of $\mu = 0.0025$, $F_{\text{stretch}} = 1000$; (E) zoom in of cell configuration of $\mu = 0.01$, $F_{\text{stretch}} = 500$. Colors A,(C-E): principal strain magnitude; orientation and length of black line pieces: orientation and magnitude of principal strain.

The results of varying uniaxial stretch are shown in Figure 3.4. How the amount of uniaxial stretch affects string formation, depends on the magnitude of the cell traction forces. When we varied the uniaxial stretch and fixed the cell traction force to the default parameter value (middle row in Figure 3.4A), we observed that cells can more easily align in a head-to-tail configuration and form strings (Figure 3.4C) if stretching is lower than the default value (Figure 3.4D). Indeed, the global ordering decreases as a function of uniaxial stretch (middle set of barplots in Figure 3.4B). In our model, this is explained as follows. Due to the assumed strain stiffening behavior, the cells spread more [182] on highly stretched matrices. Then, within strings, cells have less space and orient less well. If cells apply little traction (first row in Figure 3.4A), they do not form strings with small uniaxial stretch, but do when stretching is increased. Then, with even more uniaxial stretch, cells orient along stretch, but do not forms strings, similar to non-contractile cells (Figure 3.3B). Indeed, the global orientational order parameter shows a biphasic dependence on uniaxial stretching (first set of bar plots in Figure 3.4B). This is explained in our model as follows. Cell forces cannot sufficiently amplify a small uniaxial stretch and thus more uniaxial stretch is needed to instigate string formation. However, at higher uniaxial stretch, the cell traction forces are insufficiently strong to amplify the uniaxial strain and as a result cells do not form strings. Note that these cells do not form networks with little uniaxial stretch, as they do not sufficiently contract the matrix to align with other cells. If cells are highly contractile (last row in Figure 3.4A) they form networks, similar to cells on non-stretched matrices (Figure 3.6F). Higher uniaxial stretching transforms a network into an oriented network (Figure 3.4E) and subsequently into strings. Indeed, the global order has a biphasic dependence on stretching (last set of barplots in Figure 3.4B). This is because with too little uniaxial stretch, cell generated strains dominate the global strain cue and thus cells do not collectively orient. Of course, if we would increase uniaxial stretch even more, cells would align but not form strings anymore.

To better understand the results in Figure 3.4, recall that cells extend towards areas that are stiffened by strain, as described by the sigmoid function $h(E(\epsilon)) = 1/(1 + \exp(-\beta(E(\epsilon) - E_\theta)))$ (Supplementary Figure 3.11B), where $E(\epsilon) = E_0(1 + (\epsilon/\epsilon_{st})$. Supplementary Figure 3.11A shows that cells can only form strings when the matrix is stiffened to values above E_θ (Supplementary Figure 3.11D). If the matrix is not stiffened, or becomes too rigid, the cells will not align (Supplementary Figure 3.11C and E). To relate this to Figure 3.4, instead of strain, we plotted normalized stiffness values $\frac{E(\epsilon)}{E_\theta}$ in Supplementary Figure 3.12. This shows that when the uniaxial stretch stiffens the matrix to values around E_θ and cell traction forces then stiffen the matrix more, strings can be formed. However, strings can not be formed when the matrix is stiffened too much by either the cells or the uniaxial stretch.

Altogether, the results suggest that an optimal balance between uniaxial stretch and cell contractility is needed for cells to form strings.

3.2.4 Decreasing cell-cell adhesion promotes string formation in populations with high cell density

Experimental work has reported two alternative cellular responses to uniaxial strain. Fibroblasts seeded at a density of 10^6 cells/ml form strings along the orientation of uniaxial stretch [95]. 3D cultures of endothelial cells at much higher density of 10^7 cells/ml to 10^9 cells/ml align along the stretch orientation, but do not form strings [94]. Thus, the differences between these two experiments could be due to cellular densities, or due to specific differences between fibroblasts and endothelial cells. In particular, endothelial cells have stronger cell-cell adhesion than fibroblasts, as the endothelial-specific VE-cadherins have stronger bond strengths than the N-cadherins found in fibroblast cell-cell junctions [183].

Figure 3.5A shows an overview of the final configurations of simulations in which we systematically varied cell density and cell-cell contact energies; Figure 3.5B shows the corresponding global orientational order parameters. To better mimic variable densities of cells, we initialized cells on the whole grid of 400×400 lattice sites. The configurations shown in Figure 3.5A suggest that fewer, thicker strings are formed if the cells adhere more strongly to one another (*i.e.*, low J_{cc}). Also, the global order parameter increases as the cell-cell contact energies increase (Figure 3.5B), suggesting that non-adhering cells respond more easily to the strain cue. At a seeding density $d = 0.35$ and mildly repellent cell-cell adhesion settings of $J_{cc} = 5$ the final configurations (Figure 3.5C) and the distribution of cell orientations (Figure 3.5D) qualitatively resemble the experiments by Van der Schaft *et al.* [94] (Figure 3.5 F and G). Decreasing cell-cell adhesion and cell densities to $d = 0.05$ and $J_{cc} = 6.25$ produces configurations similar to Eastwood *et al.* [95] (Figure 3.5E and H). Currently, in completely confluent cell layers with high cell-cell adhesion ($d = 0.35, d = 0.5$, $J_{cc} = 3.75, 2.5$ in Figure 3.5) the cells do not align at all, because in our model the cells cannot respond to strain at cell-cell interfaces. We investigated this issue further in the Supplementary Methods and address this in the discussion section.

3.3 Discussion

In this paper we have presented a computational model to show that active cell contraction can facilitate cellular alignment to the orientation of static uniaxial stretch. The computational model describes motile cells living on top of an elastic substrate, and is based on only a few, experimentally validated assumptions: (a) cells exert contractile forces on the substrate, which locally generate strains in the substrate [127, 131]; (b) cells move by repeatedly attempting to extend or retract pseudopods at random, and (c) along the substrate strain orientation, pseudopod extensions are promoted and pseudopod retractions are inhibited [178], a procedure mimicking the maturation of focal adhesions under strain [184]. We have shown previously [182] that these assumptions suffice to reproduce (1) the elongation of single cells on compliant substrates, (2) the alignment of two adjacent cells, and at the collective level (3) the for-

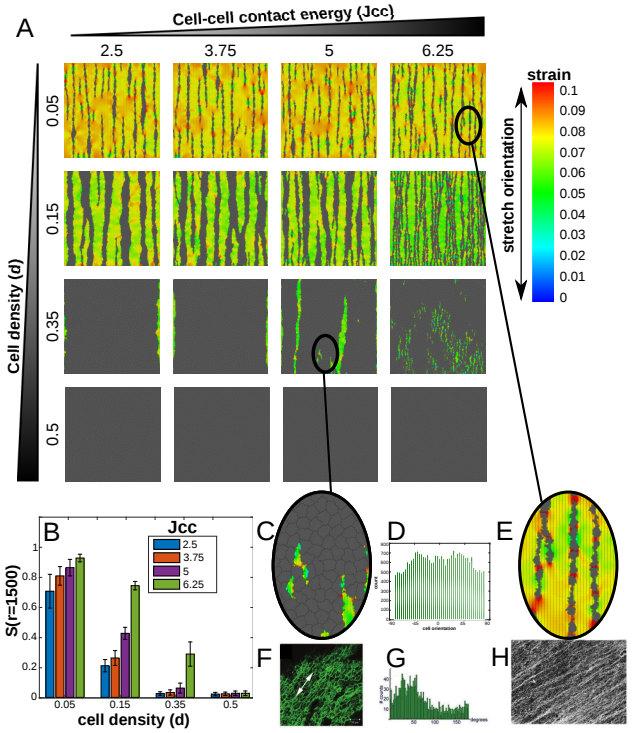

Figure 3.5: Model sensitivity to cell density and cell-cell adhesion. (A) Contractile cells on substrate stretched along 0° at 3000 MCS simulated with various values of cell density and cell-cell contact energy; (B) Global orientational order parameter $S(r = 1500\ \mu\text{m})$ at 3000 MCS, averaged over $n = 25$ simulations; error bars: standard deviations, first bar is for the lowest value of J_{cc}; (B) Global orientational order parameter $S(r = 1500\ \mu\text{m})$ at 3000 MCS, averaged over $n = 25$ simulations; error bars: standard deviations; bars in bar chart are sorted according to value of J_{cc} as indicated in figure inset; (C) zoom in of cell configuration of $J_{cc} = 5$, $d = 0.35$; (D) Cell orientations of $J_{cc} = 6.25$, $d = 0.35$; (E) zoom in of cell configuration of $J_{cc} = 6.25$, $d = 0.05$; (F) 3D culture of endothelial cells on uniaxially stretched matrix, taken from Van der Schaft *et al.* [94]; (G) Orientation of 3D culture of endothelial cells on uniaxially stretched matrix, taken from Van der Schaft *et al.* [94]; (H) Fibroblasts on uniaxially stretched matrix, taken from Eastwood *et al.* [95]. Colors A,C,E: principal strain magnitude; orientation and length of black line pieces: orientation and magnitude of principal strain.

mation of vascular-like network structures and angiogenesis-like sprouting structures. Here we show that a refined version of this model also reproduces experimentally observed behavior of fibroblasts, endothelial cells and myocytes on statically, uniaxially stretched substrates: (1) cells tend to align in parallel to the uniaxial stretch orientation [94, 170, 171] (*cf.* Figure 3.1); (2) cells align with one another in parallel to the uniaxial stretch orientation (Figure 3.2); and (3) collectively, the cells form strings oriented along the stretch (Ref. [95] and Figure 3.3) and they elongate along the stretch in close to confluent layers of cells (Ref. [94] and Figure 3.5). Although the assumed response to strains (assumption (c)) makes the simulated cells orient to the stretch without contractility (see Ref. [182] and Figure 3.1A), active contractility makes cells elongate more strongly (Figure 3.1B), and allows them to respond to strain cues more accurately (Figure 3.1C) and more rapidly (Figure 3.1D) than non-contractile cells. Thus, a crucial factor for these phenomena is the balance between active cell contractility and the magnitude of the uniaxial stretch cue. Provided the cellular traction forces are sufficiently strong, the cells will collectively organize into oriented strings even in response to very subtle strain cues (Figure 3.4). For stronger cell contractility, however, the local strains will override the global strain cue and the cells will organize into network-like patterns as reported previously (see Figure 3.4A, lower left panels; also *cf.* Ref [182]). The reported model behavior holds for substrates with stiffness of approximately 10 kPa to approximately 16 kPa, a wider range than the autonomous cell elongation reported previously [182]. Note that the exact magnitude of this range depends on the parameter settings and in particular threshold E_0 in sigmoid function $h(E(\epsilon))$, whose values were kept unchanged relative to Ref. [182].

Experimental validation of our model predictions would need to focus both on the response to uniaxial static stretch of single cells and on the collective behavior of multiple cells. Single cells in our models elongate more easily and reorient more easily to uniaxial static stretch if they contract the matrix. At the multicellular level, contractility induces string formation on uniaxially statically stretched matrices. A number of published *in vitro* experiments already support the single cell behavior that our model predicts. For example, oxidatively modified low density lipoprotein (oxLDL) stimulates the contractility of human aortic endothelial cells, which correlates with increased cell elongation [185]. Fibroblasts moving on stretched collagen gels align their trajectories more strongly to the strain orientation than less contractile neutrophils [186]. To validate single cell response to uniaxial static stretch, we propose experiments in which cells with different contractilities are seeded on a uniaxially stretched matrix as, *e.g.*, in Ref. [186]. Treatment with lysophosphatidic acid (LPA) can stimulate Rho-mediated contractility [181, 187], while treating cells with blebbistatin or cytochalasin D inhibits contractility [33]. At the multicellular level, with increasing uniaxial stretch, our model system switches gradually between networks and strings (Figure 3.4). Previous cell culture studies [94, 95] have not varied the strain magnitude, but in uniaxially, statically stretched *ex ovo* chick chorioallantoic membranes blood vessels realign along stretch [188]. Further *in vitro* experiments

could vary the magnitude of the uniaxial stretch and the degree of contractility using chemical treatments (see *e.g.*, Ref. [189] for a suitable experimental system). The cell density and the cell-cell adhesion strength also influenced the ability of cells to form strings. At high cell densities, simulated cells are less able to form strings, while decreasing cell-cell adhesion restores string formation. Uniaxial stretching experiments where cell-seeding densities are varied and cell-cell adhesion is controlled, by inhibiting or knocking out Cadherins, could validate these predictions.

Although our model is currently not resolved to molecular detail, its simulation results do suggest a mechanistic explanation for the response of cells to static uniaxial stretch. Previous theoretical models [45, 180] proposed that cells actively regulate their orientation in order to optimize a local mechanical property. Bischofs and Schwarz [45] represented cells as active dipoles, and showed that the dipole can minimize the amount of work required to contract the matrix by orienting along the external strain [45]. This optimization principle was motivated by force-induced focal adhesion maturation: maximum forces will develop at the focal adhesions that are displaced the least. Based on observations suggesting that cells maintain a constant local stress in their microenvironment, De *et al.* [180] proposed that dipolar cells actively regulate their orientation and contractility in order to maintain a constant optimal amount of local stresses in the matrix. In this model, the dipolar cells reorient to the uniaxial stretch and gradually reduce the magnitude of their contractility in order to reduce the stress in the matrix. Mechanistic rationales certainly motivated these optimization principles, but the mechanisms were not modelled explicitly and a dipole shape was presumed. Our approach instead aims to derive single-cell phenomena and collective cellular responses to strain from a small set of experimentally plausible assumptions at the subcellular level. The present work is only a first step towards this aim. Currently, the local substrate strains regulate the protrusion and retraction probabilities based on a phenomenological function (Eq. 3.2), which simulates focal adhesion maturation. In our ongoing work we are refining this part of the model by introducing explicit kinetic models of the focal adhesions.

The current, coarse-grained description has suggested new mechanisms for the experimental observations listed above, but due to a number of technical limitations it still fails to reproduce others. We cannot yet reproduce cell alignment to uniaxial stretch in a completely confluent layer, because the strain-bias of the cell protrusions and retractions is cancelled out at cell-cell interfaces (see Eq. 3.2 and Figures 3.13A and 3.13B). As a first exploration of the behavior of our model in absence of this effect, we ran a series of simulations in which we differentiated the probability of the retractions relative to extensions. With an decreased retraction probability ($\Delta H_{\mathrm{dir}}^{\mathrm{retraction}} = -2\Delta H_{\mathrm{dir}}^{\mathrm{extension}}$), fully confluent cell layers collectively oriented in parallel to stretch (Figures 3.13C and 3.13D). In contrast, in simulations with an increased retraction probability ($\Delta H_{\mathrm{dir}}^{\mathrm{retraction}} = -0.5\Delta H_{\mathrm{dir}}^{\mathrm{extension}}$), the cells oriented themselves perpendicular to the stretch orientations in a confluent layer (Figures 3.13E and 3.13F). Another result of the absence of strain-effects at cell-cell boundaries,

is that contractile cells do not achieve a high global ordering within strings (Figure 3.3A); this is because cells in the interior of the strings do not elongate. When the retraction probability is decreased ($\Delta H_{\mathrm{dir}}^{\mathrm{retraction}} = -2\Delta H_{\mathrm{dir}}^{\mathrm{extension}}$), the contractile cells reach a higher global ordering ($S(r = 1500\ \mu\mathrm{m}) = 0.71$) compared to the non-contractile cells ($S(r = 1500\ \mu\mathrm{m}) = 0.51$) (Supplementary Figure 3.14A). In simulations in which the retraction probability is increased ($\Delta H_{\mathrm{dir}}^{\mathrm{retraction}} = -0.5\Delta H_{\mathrm{dir}}^{\mathrm{extension}}$), the contractile cells reached a lower global ordering ($S(r = 1500\ \mu\mathrm{m}) = 0.37$) compared to the non-contractile cells ($S(r = 1500\ \mu\mathrm{m}) = 0.64$), as some cells in the interior of strings started to align perpendicular to strain (Supplementary Figure 3.14B). Despite these quantitative differences, note that cells form strings irrespective of the specific modeling choices (Supplementary Figure 3.14 C and D). Also related to this modeling choice is the apparent unrealistic cell shape as presented in Supplementary Figure 3.8C. Such cells appear less frequently in simulations where retraction probabilities are decreased ($\Delta H_{\mathrm{dir}}^{\mathrm{retraction}} = -2\Delta H_{\mathrm{dir}}^{\mathrm{extension}}$) (Supplementary Figure 3.14 C and D)). This work primarily focused on the collective behavior of cells; in our ongoing work we are developing more detailed, single-cell models.

Apart from this course-graining of the focal adhesion dynamics and cell motility, our model also relies on other methodological simplifications. The finite-element description of the substrate assumes that the ECM is isotropic, non-fibrous, and linearly elastic. Because of these assumptions, our model best applies to non-fibrous matrices (*e.g.*, synthetic polyacrylamide matrices), or to matrices with fibers much smaller than the size of the cells. Of course, more complex matrix mechanics can be modelled using FEM approaches. Interestingly, Aghvami *et al.* [190], who modelled an anisotropic fiber reinforced material showed similar increased local strains around (non-migratory) cells pulling on uniaxially stretched matrices as in our model. Alternative, agent-based approaches have been proposed for fibrous matrices [89, 90, 175]; in comparison to these models, an advantage of our hybrid approach is in particular its scalability to multicellular systems. As a disadvantage relative to these agent-based approaches, our hybrid set-up relies on an operator splitting approach, which alternates updates of the cell traction forces with the MCS's of the Cellular Potts Model. Although this process speeds up our computations and operator splitting approaches are routinely applied in hybrid modeling (see *e.g.*, Refs. [87, 191, 192]), it of course also introduces numerical errors: ideally we would recalculate the cellular traction forces and substrate strains after every copy attempt of the CPM. From a biophysical point of view the operator splitting assumption is valid if we can separate the time-scales of the growth and degradation of focal adhesions, such that cell traction forces remain approximately constant during the time represented by one MCS. Indeed, focal adhesion dynamics occur at a timescale of minutes, which is longer than one MCS, which in our model is equivalent to 0.5 to 3 seconds [182]. An ongoing improvement of our approach concerns the coupling between the cellular traction forces, as represented by the FMA model (Eq. 3.6), and the representation of these forces in the Hamiltonian (Eqs. 3.1). In the basic CPM, the area conservation and adhesive

energy terms in the Hamiltonian describe a pressure and approximate a membrane tension which together represent cell contractility. This allowed us to study the effects of cell-cell contact energies. These terms are not equal to the forces described by the FMA model. The strength of this model is that it produces experimentally validated strain fields. The decoupling of the CPM and the FMA model will become an issue at locations where the two sets of forces are unequal, *e.g.*, at cell-cell interfaces and can affect te mesoscopic cell behavior. Since we are interested in how mesoscopic cell behavior affects the macroscopic level, *i.e.*, collective behavior, these approximations and decoupling suffice here. In our ongoing work, we are adopting an approach proposed by Albert and Schwarz [191] to alleviate this issue.

In summary, we proposed a local cell-matrix feedback mechanism explaining the reorientation of cells to external stretch. In agreement with experimental observations, in this model cell contractility facilitates the reorientation of cells. The proposed mechanism also suffices for the formation of strings along the orientation of stretch. In our future work, we are refining the model by introducing explicit focal adhesion dynamics. This approach will pave the way for issues that our model can currently not explain, including the response of cells to cyclic stretch [193, 194], and the role of cell-substrate adhesivity in the formation of network-like patterns [36] and collective cell behavior [192].

3.4 Methods

We extended our previous hybrid, cell-based and continuum model [182] of mechanical cell-ECM feedback to include the effects of static strain. Figures 3.6(A-C) give an overview of the model structure. Active cell motility is simulated using the Cellular Potts Model [72]. The CPM is coupled to a finite-element method that is used to calculate substrate deformations. A time step of the simulation proceeds as follows. Based on the local strains in the matrix and the interactions with adjacent cells, the CPM calculates the cell shapes (Figure 3.6A). Based on the cell shapes, the traction forces that cells apply on the ECM are determined using the empirically validated first-moment-of-area (FMA) model, as proposed by Lemmon & Romer [131] (Figure 3.6B). The FEM calculates the deformation of the substrate resulting from these forces (Figure 3.6C). Subsequently, the strains in the ECM influence cell movement in the CPM. More precisely, we assume that cells preferentially extend along the orientation of high strain.

3.4.1 Cellular Potts Model

The CPM [72] describes cells on a regular lattice $\Lambda \subseteq \mathbb{Z}^2$ as a domain of connected lattice sites, $\vec{x}$, of identical spin, or *cell identifier*, $\sigma(\vec{x}) \in \mathbb{Z}_{\geq 0}$. Sites of spin $\sigma(\vec{x}) > 0$ identify sections of the substrate that are covered by a biological cell, whereas sites of spin $\sigma(\vec{x}) = 0$ identify exposed substrate sites. The configuration of cells evolves

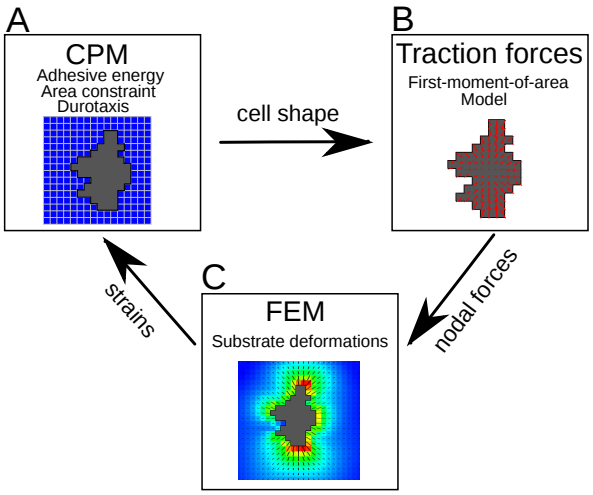

Figure 3.6: Structure of the coupled CPM-FEM model. (A) CPM calculates cell shapes in response to local ECM strains; (B) calculation of cellular traction forces based on cell shapes [131]; (C) substrate strains due to cellular traction forces.

according to the Hamiltonian,

$$H = \sum_{s \in \text{cells}} \lambda \left(\frac{a(s) - A(s)}{A(s)} \right)^2 + \sum_{(\vec{x},\vec{x}\prime)} J(\sigma(\vec{x}), \sigma(\vec{x}\prime))(1 - \delta(\sigma(\vec{x}), \sigma(\vec{x}\prime))). \tag{3.1}$$

The first term is a surface area constraint, with $a(s) = |\{\vec{x} | \vec{x} \in \Lambda \wedge \sigma(\vec{x}) = s\}|$, the number of lattice sites covered by cell s, $A(s)$ a target area and λ a Lagrange multiplier. The second term represents the interfacial energies in the system, *e.g.*, due to cell adhesion and cortical tensions. Here, $J(\sigma(\vec{x}), \sigma(\vec{x}\prime))$ is the interfacial energy between an adjacent lattice site pair $(\vec{x}, \vec{x}\prime)$ and $\delta(\sigma(\vec{x}), \sigma(\vec{x}\prime))$ is the Kronecker delta. The contact energy J_{cc} regulates the degree of cell-cell adhesion, with lower values of J_{cc} corresponding to strong cell-cell adhesion.

To mimic cellular protrusions and retractions of the cells, the cellular Potts model iteratively picks a random lattice site $\vec{x}$ and attempts to copy its spin $\sigma(\vec{x})$ into an adjacent site $\vec{x}\prime$. The algorithm then calculates the energy change ΔH associated with the copy attempt based on the Hamiltonian (Eq. 3.1) and any additional energy changes associated with the copy direction [195], in this case ΔH_{dir}. With ΔH_{dir} we express the cellular response to matrix strains, as outlined below. The copy is accepted if $\Delta H + \Delta H_{\text{dir}} \leq 0$, or with Boltzmann probability $P(\Delta H + \Delta H_{\text{dir}}) = \exp(-(\Delta H + \Delta H_{\text{dir}})/T)$ to allow for stochasticity of cell movements. $T \geq 0$ is a *cellular temperature* whose magnitude gives the amount of random cell motility. An additional connectivity constraint rejects copy attempts that would split cells into disconnected patches. During one Monte Carlo Step (MCS) N copy attempts are made, with $N = |\Lambda|$, *i.e.*, the number of sites in the lattice.

To simulate the response of cells to strains in the substrate, we assumed that local strains promote cellular protrusion and inhibit cellular retractions. Such a mechanism is motivated by focal adhesions, large integrin complexes that bind the cell to the matrix and maturate on stiffer matrices [184]. We assume a strain stiffening material, so that focal adhesions mature on highly strained areas. We thus set

$$\Delta H_{\text{dir}} = -g(\sigma(\vec{x}), \sigma(\vec{x}\prime))\lambda_{\text{dir}} \left(h(E(\epsilon_1))(\vec{v}_1 \cdot \vec{v}_m)^2 + h(E(\epsilon_2))(\vec{v}_2 \cdot \vec{v}_m)^2 \right), \tag{3.2}$$

where λ_{dir} is a parameter that describes the sensitivity of cells to strain. $\vec{v}_m = \widehat{\vec{x} - \vec{x}\prime}$, is the direction of copying, and ϵ_1 and ϵ_2, and v_1 and v_2 are the eigenvalues and eigenvectors of $\underline{\epsilon}$ that represent the principal strains and strain orientation in the target site $\vec{x}\prime$. We use $g(\sigma(\vec{x}), \sigma(\vec{x}\prime)) = 1$ if a cell is extending and $g(\sigma(\vec{x}), \sigma(\vec{x}\prime)) = -1$ if a cell is retracting, to impose that strain stiffening of the matrix promotes extensions and inhibits retractions. At cell-cell interfaces we assume that the forces due to strain (ΔH_{dir}) on the extending cell and the retracting cell are balanced, *i.e.*, $g(\sigma(\vec{x}, \vec{x}\prime)) = 0$ if $\sigma(\vec{x}) \neq \sigma(\vec{x}\prime)$ and $\sigma(\vec{x}) > 0 \wedge \sigma(\vec{x}\prime) > 0$. We thus assume that neither of the two cells involved in the copy attempt benefits more from occupying a strained lattice site than another cell. The sigmoid function $h(E(\epsilon)) = 1/(1 + \exp(-\beta(E(\epsilon) - E_\theta)))$ expresses that a minimum stiffness, E_θ, is required for focal adhesion maturation. We assume that cells perceive strain stiffening of the matrix, described by the function $E(\epsilon) = E_0(1 + (\epsilon/\epsilon_{st})$, where ϵ_{st} is a stiffening parameter. Compared to our previous implementation of this model [182], slight adaptations have been made in the Hamiltonian, which are discussed in the Supplementary Methods. They do not affect the qualitative behavior of the model. The parameter values used in this study are reported in Supplementary Table 3.1. We use a discretization of $\Delta x = 2.5\mu$m. Based on single cell dispersion rates in our model, we previously estimated the time interval Δt corresponding to one MCS to be between $\Delta t = 0.5$ seconds and $\Delta t = 3$ seconds [182].

3.4.2 Finite-element model of compliant substrate

A FEM [155] is used to calculate the strain on the substrate resulting from forces applied to the substrate. The substrate is assumed to be isotropic and linearly elastic. For simplicity, we applied infinitesimal strain theory, assuming that material properties, including local density and stiffness are unchanged by deformations. So, the strain tensor ϵ is given by

$$\epsilon = \begin{pmatrix} \epsilon_{xx} & \epsilon_{xy} \\ \epsilon_{yx} & \epsilon_{yy} \end{pmatrix} \approx \frac{1}{2}(\nabla\vec{u} + \nabla\vec{u}^T), \tag{3.3}$$

where $\vec{u} = (u_x, u_y)$ is the substrate deformation.

The elements of the FEM coincide with the lattice sites of the CPM, *i.e.,* the deformation in a lattice site $\vec{u}^e(x, y)$ is approximated by an interpolation of the shape functions $N_n^e(x, y)$, for $n = 1, 2, 3, 4$ corresponding to the four nodes (corners) of lat-

tice site/element e:

$$\vec{u}^e(x,y) = \sum_{n=1}^{4} N_n(x,y)\vec{u}_n, \tag{3.4}$$

where $\vec{u}_n$ is the substrate deformation at node n. We used conventional linear shape functions for four-noded quadrilateral elements [155]. The FEM is iterated until equilibrium ($K\vec{u} = \vec{f}$, where K denotes the stiffness matrix [155]), to calculate the deformation $\vec{u}_n$ at each node. All figures in this paper show the strain in equilibrium. The terms ϵ_{ij} in the strain tensor ϵ^e of element e are thus given by

$$\epsilon^e_{ij}(x,y) = \frac{1}{2}\sum_{n=1}^{4} \frac{\partial N_n(x,y)}{\partial i}\vec{u}_n + \frac{\partial N_n(x,y)}{\partial j}\vec{u}_n. \tag{3.5}$$

In our simulations, the unstretched substrate $\vec{u} = \vec{0}$ is used as a reference configuration for the displacements due to uniaxial stretch and cell contractility. This simplifies our calculations and speeds them up. For details, see Ref. [182].

3.4.3 Cellular traction forces

To model the traction forces that cells apply on the substrate we make use of an experimentally-validated, predictive model, called the first-moment-of-area (FMA) model [131]. The FMA model is based on the assumption that the network of actin fibers acts in the cells as a single, cohesive unit. In the context of our hybrid CPM-FEM model, we implement the FMA model as follows. Defining lattice nodes as the corners of the CPM lattice sites, each lattice node i covered by a CPM cell pulls on every other node j within the same cell, with a force $\vec{F}$ of magnitude proportional to the distance between the nodes, $\vec{d}_{i,j}$, and $\vec{d}_{i,j} = 0$ if line piece (i, j) intersects with the cell boundary (see Ref. [131], Figure 3.7A-D and Supplementary Methods for details). The total force $\vec{F}_i$ on node i then becomes,

$$\vec{F}_i = \mu \sum_j \vec{d}_{i,j}, \tag{3.6}$$

In accordance with the assumption that the cytoskeleton has uniform contractility, the line pieces have a constant tension per unit distance μ [131]. For convex cells, the resultant forces point towards the cell's center of mass. For non-convex cells, the resultant forces are directed towards the individual, convex compartments that the cell shape is composed of (see Supplementary Methods).

3.5 Supplementary methods

To quantify cell elongation and orientation, we used the inertia tensor I of a cell σ:

$$I(\sigma) = \begin{pmatrix} \sum_{\vec{x}\in C(\sigma)}(x_2 - \overline{C}_2(\sigma))^2 & -\sum_{\vec{x}\in C(\sigma)}(x_1 - \overline{C}_1(\sigma))(x_2 - \overline{C}_2(\sigma)) \\ -\sum_{\vec{x}\in C(\sigma)}(x_1 - \overline{C}_1(\sigma))(x_2 - \overline{C}_2(\sigma)) & \sum_{\vec{x}\in C(\sigma)}(x_1 - \overline{C}_1(\sigma))^2 \end{pmatrix}. \tag{3.7}$$

Here, $\overline{C}(\sigma, t)$, is the center of mass of cell σ at MCS (time) t, given by

$$\overline{C}(\sigma, t) = \frac{1}{|C(\sigma, t)|} \sum_{\vec{x}\in C(\sigma,t)} \vec{x}, \tag{3.8}$$

with $C(\sigma, t)$, the set of coordinates of the lattice sites occupied by cell σ at MCS t.

Cell elongation is quantified by the eccentricity ξ of a cell, given by

$$\xi(\sigma) = \sqrt{1 - \left(\frac{e_1(I(\sigma))}{e_2(I(\sigma))}\right)^2}, \tag{3.9}$$

where $e_1(I(\sigma)) \leq e_2(I(\sigma))$ are the eigenvalues of $I(\sigma)$. An eccentricity close to zero corresponds to roughly circular cells and cells with an eccentricity close to unity are more elongated. Further, the orientation of a cell is given by the orientation of the eigenvector associated with the largest eigenvalue of the inertia tensor $I(\sigma)$.

For the orientational order parameter $S(r)$ we calculated $\theta(\vec{x}, r)$: the angle between the direction of the long axis $\vec{v}(\sigma(\vec{x}))$ of the cell at $\vec{x}$, and a local direction $\vec{n}$, which is the weighted local average of cell orientations, taken within a radius r around $\vec{x}$, such that $\vec{n}(\vec{x}, r) = \langle \vec{v}(\sigma(\vec{y})) \rangle_{\{\vec{y}\in\mathbb{Z}:|\vec{x}-\vec{y}|<r\}}$. The orientational order parameter is then defined as $S(r) = \left\langle \cos 2\theta(\vec{X}(\sigma), r) \right\rangle_\sigma$ where $\vec{X}(\sigma)$ is the center of mass of cell σ.

To determine the orientation of strings (or cell aggregates), we first find the connected components of the cell pattern, by applying morphological closing on the pattern [196], using a line of five lattice sites with an angle equal to the stretch orientation. We then took the connected components larger than 300 lattice sites and determined the average orientation of those. Aggregate orientations were calculated in the same way as the orientation of a single cell, by using the inertia tensor.

In the FMA model [131], the force $\vec{F}_i$ acting on node $\vec{n}_i$ of a cell is determined by

$$\vec{F}_i = \mu \sum_{\vec{n}_j} |\vec{n}_i - \vec{n}_j|, \tag{3.10}$$

where the sum is over nodes $\vec{n}_j$ in the same cell of which the straight line connecting node j with node i is completely within the cell. μ is the cell tension in nN μm^{-1}. To determine whether a line between nodes stays within the cell, one needs to know which lattice sites this line crosses. The Bresenham algorithm [197] is used for this purpose. Now let $s(\vec{n}, \vec{n_1})$ be the lattice sites that the line $l(\vec{n}, \vec{n_1})$ between node $\vec{n} = (n_x, n_y)$ and node $\vec{n^1} = (n_x^1, n_y^1)$ crosses. In order to be consistent, we impose that

$s(-\vec{n_1}, \vec{n}) = s(\vec{n}, \vec{n_1})$ mirrored vertically and turned 180° clockwise, so that $\vec{n}$ pulls on $\vec{n_1}$ if and only if $\vec{n_1}$ pulls on $\vec{n}$. In order to prevent a bias in either 45° or −45°, we impose that $s(\vec{n}, \vec{n_1}) = s(\vec{n}, (n_x^1, -n_y^1))$ mirrored horizontally. The resulting lattice sites are shown in an example in Supplementary Figure 3.15.

In the calculation of the response of the CPM to the local strains in the substrate, we previously used the strain in the target site when a cell was extending and the strain in the source site was used when a cell was retracting. We changed this assumption to make cell behavior more compatible with focal adhesion dynamics on strained tissues. For an extending cell, *i.e.* when $\sigma(\vec{x}) > 0$, the strain in the target site promotes the maturation of a focal adhesion in the protrusion. When a cell is retracting, *i.e.* $\sigma(\vec{x}\prime) > 0$, it costs a lot of energy to unbind a matured focal adhesion from the target site.

A bias in the angle of cell orientations can occur as a result of the square lattice. In Van Oers *et al.* [182], forces were pointed towards the center of mass (Supplementary Figure 3.7A). With this model, a small bias in cell elongation oriented along ±45° was found (Supplementary Figure 3.16A). We found that the origin of this bias lies in the mechanotaxis term in the Hamiltonian ΔH_{dir}, that describes a cell perceiving stiffening of the matrix, as a result of positive, stretching strains. When we also let cells perceive strain stiffening as a result of negative strains, *i.e.* compression, the bias is reduced. This is shown in Supplementary Figure 3.16 A and B, in which we plot the orientation of cells on a unstretched matrix with stretch stiffening only and stretch and compression stiffening, respectively. With stretch and compression stiffening, cells are still able to elongate, as a Poisson ratio $\nu < 0.5$ makes sure that stretch strains are higher than compression strains, so cells protrude more preferably towards stretch strains and can thus promote elongation. It is not completely clear to us why the inclusion of compressions stiffening reduces the orientational bias: we found this bias effect by investigating the Hamiltonian for spin copies: with strain stiffening for stretch only, diagonal spin copies gave a higher $dH_{\text{mechanotaxis}}$. We discovered that the FMA model (in which nodes only pull on other nodes if they are connected by a straight line within a cell [131]) is another origin for a cell orientation bias, but now along 0° and 90°. We suspect a reason for this, which is illustrated in Supplementary Figure 3.17. Our reasoning is as follows. A cell that only experiences contact energy (surface tension) and an area constraint, will obtain a round shape. A cell that elongates wants to stay as round as possible and thus prefers to obtain an ellipse shape. Here we show that an ellipse shaped cell with an orientation of 0° has a wider tip than an ellipse orientated along 45°, because of the 2D grid. A wider tip makes the nodes able to pull on more other nodes, causing more highly strained lattice sites and thus more extensions along 0°. By increasing the cellular temperature T, this bias can sufficiently be reduced. This is shown in Supplementary Figure 3.16 C and D, in which we plot the orientation of cells on a unstretched matrix with the FMA model for cell temperature $T = 1$ and $T = 5$, respectively. Because cells elongate with slightly different parameters for the model with the FMA model compared to previous work

([182]), we changed some parameter values with respect to our original work [182]. So, in the analysis on cell orientation presented here, we used our previous parameter as in [182]: $J_{cc} = 1.25, J_{cm} = 0.625, \lambda = 500, \lambda_{dir} = 20, T = 1$. Finally, there is always a bias in the direction of ±45°, as a cell elongated in this direction has a lower adhesive energy due to the square lattice. This does not cause major problems as long as sufficient noise is introduced.

In our current model formulation [182] cells perceive an increase in matrix stiffness as a result of compressive ($\epsilon < 0$) and extension strains ($\epsilon > 0$), while in our original model this was only implemented for extensions strains. This was adapted to avoid a directional bias of cell elongation in ±45°, see next section.

3.6 Supplementary tables

Parameter symbol	Description	value	units
Δx	width of lattice site	2.5	μm
A	target area	50	lattice sites
J_{cc}	cell-cell contact energy	3.75	-
J_{cm}	cell-medium contact energy	1.875	-
λ	strength of volume constraint	250	-
λ_{dir}	strength of cell response to strain	24	-
T	cellular temperature	5	-
μ	cell traction per unit length	0.0025	nN μm^{-1}
E	Young's modulus	12	kPa
υ	Poisson's ratio	0.45	-
τ	substrate thickness	10	μm
E_0	threshold for stiffness sensitivity	15	kPa
β	steepness of stiffness sensitivity	0.5	kPa^{-1}
ϵ_{st}	strain stiffening parameter	0.1	-
$\sigma_{stretch}$	uniaxial stretch	1000	N/m^2
d	cell density	0.15	$\frac{\#\{\vec{x}:\sigma(\vec{x})>0\}}{\#\{\vec{x}:\sigma(\vec{x})=0\}}$

Table 3.1: Parameter settings

	condition	example	aligned?
case 1	$\theta_1, \theta_2, \theta_3 < 90$	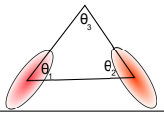	no
case 2	$\theta_3 \geq 90$	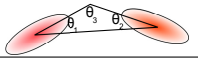	yes
case 3	$90 < \theta_2 < 135$	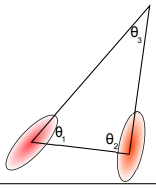	no
case 4	$\theta_2 \geq 135$	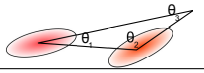	yes

Table 3.2: Determination of paired cell alignment.

3.7 Supplementary figures

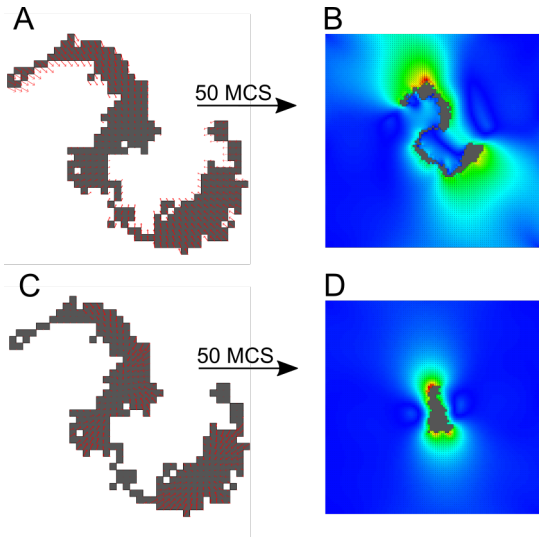

Figure 3.7: Traction forces for non-convex cell shapes (A) Cell traction forces towards center of mass (van Oers *et al.* [182]); (B) Cell shape 50 MCS after initial configuration in (A) with $\lambda_{dir} = 50$; (C) FMA model [131]; (D) Cell shape 50 MCS after initial configuration in (C) with $\lambda_{dir} = 50$; (A-C) length and direction of red arrows: traction force magnitude and direction. B and D colors: principal strain magnitude; orientation and length of black line pieces: orientation and magnitude of principal strain.

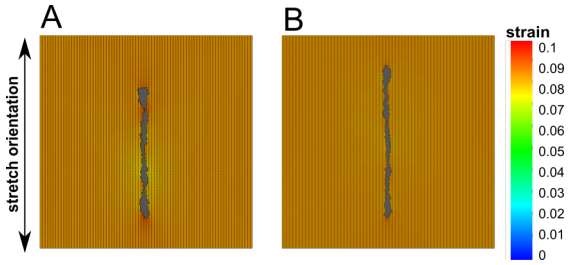

Figure 3.9: Effect of lattice refinement. Cells on substrate stretched along 0° at 500 MCS; (A) $\Delta x = 1.25\mu$m, *i.e.* refined by a factor of 2 in each lattice direction; (B) $\Delta x = 0.625\mu$m, *i.e.* refined by a factor of 4 in each lattice direction.

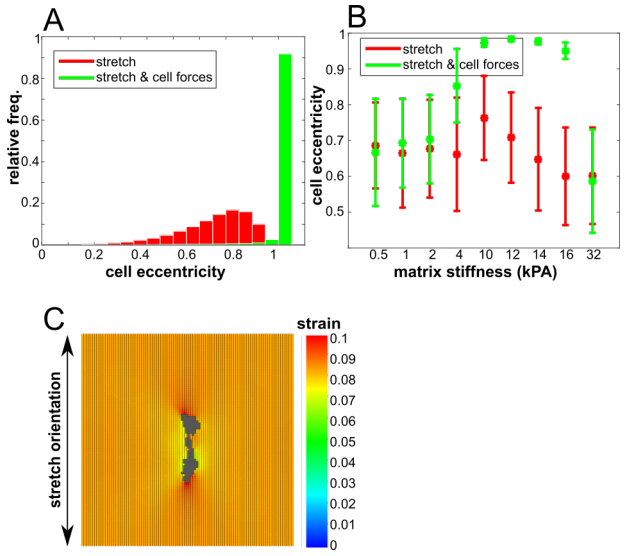

Figure 3.8: Cell eccentricity and orientation (A) Distribution of eccentricities of cells on substrate stretched along 0°, plotted are the eccentricities of cells during 500 MCS and 100 simulations; (B) Cell orientation as a function of matrix stiffness at 500 MCS; averaged over $n = 100$ simulations; error bars: standard deviations. Color coding (A-B): red: non-contractile cells; green: contractile cells; (C) Example of cell shape in which the middle part is much more slender.

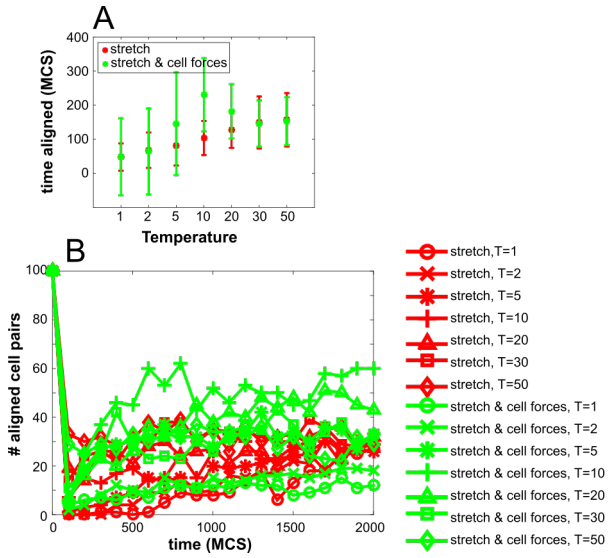

Figure 3.10: Effect of temperature on cell alignment. (A) Fraction of time a cell pair is aligned as a function of cellular temperature T, averaged over $n = 100$ simulations; error bars: standard deviations; (B) time series of the number of cell pairs that are aligned. symbols are circle: $T = 1$, cross: $T = 2$, star: $T = 5$, plus: $T = 10$, triangle: $T = 20$, square: $T = 30$, diamond: $T = 50$. Color coding: red: non-contractile cells; green: contractile cells

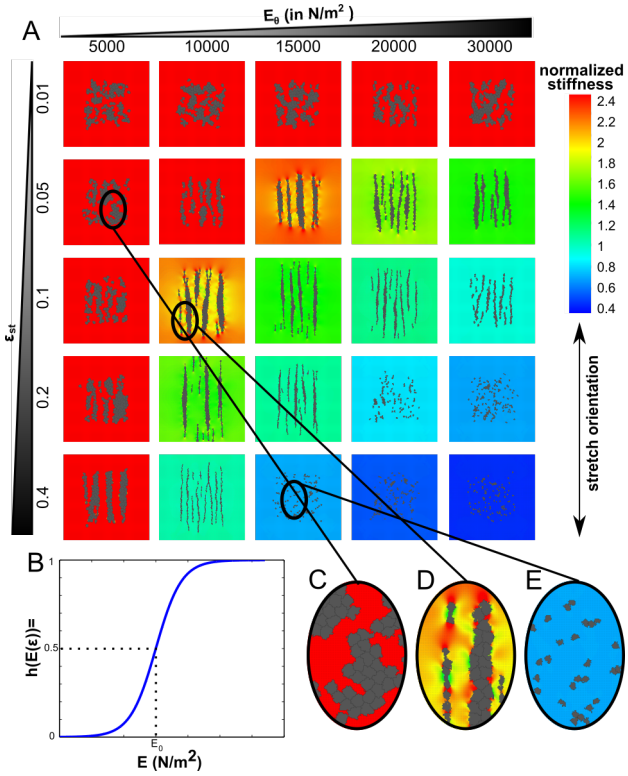

Figure 3.11: Model sensitivity to E_θ and ϵ_{st}. (A) Contractile cells on substrate stretched along 0° at 3000 MCS simulated with various values of E_θ and ϵ_{st}; (B) graph of $h(E(\epsilon)) = 1/(1 + \exp(-\beta(E(\epsilon) - E_\theta)))$; (C) zoom in of cell configuration of $E_\theta = 5000$,$\epsilon_{st} = 0.05$; (D) zoom in of cell configuration of $E_\theta = 10000$,$\epsilon_{st} = 0.1$ (E) zoom in of cell configuration of $E_\theta = 15000$,$\epsilon_{st} = 0.4$ Colors A,(C-E): normalized stiffness, defined as: $\frac{E(\epsilon)}{E_\theta} = \frac{E_0}{E_\theta}(1 + \frac{\epsilon}{\epsilon_{st}})$; orientation and length of black line pieces: orientation and magnitude of principal strain.

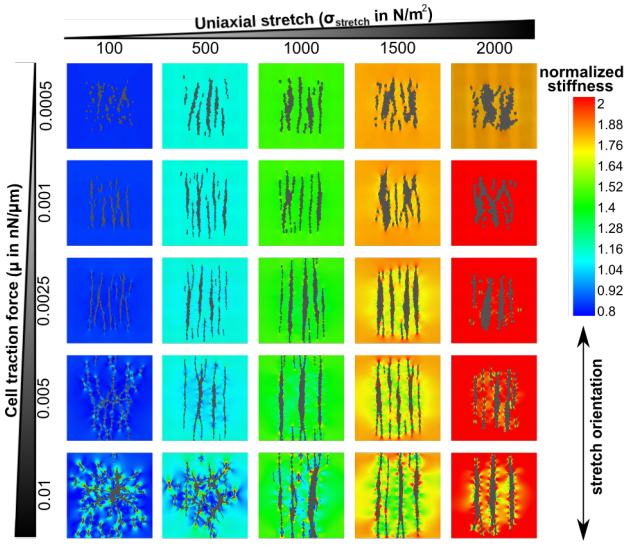

Figure 3.12: Model sensitivity to cell traction force and matrix stretching force. Contractile cells on substrate stretched along 0° at 3000 MCS simulated with various values of cell traction force and matrix stretching force; Colors: normalized stiffness, defined as: $\frac{E(\epsilon)}{E_\theta} = \frac{E_0}{E_\theta}(1 + \frac{\epsilon}{\epsilon_{st}})$; orientation and length of black line pieces: orientation and magnitude of principal strain.

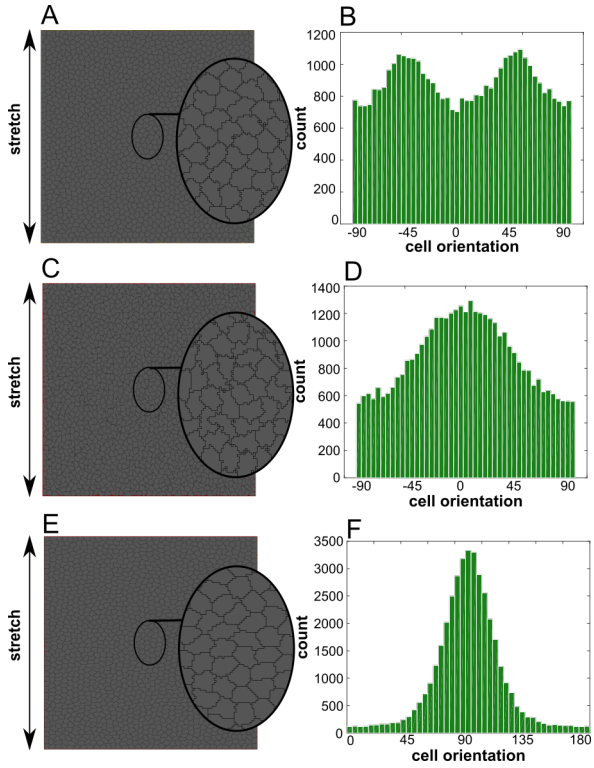

Figure 3.13: Model sensitivity to ΔH_{dir} in confluent conditions. Contractile cells on substrate stretched along 0° at 3000 MCS with cell density $d = 0.5$. (A) Original model; (B) corresponding cell orientations; (C) Model with $\Delta H_{\text{dir}}^{\text{retraction}} = -0.5\Delta H_{\text{dir}}^{\text{extension}}$; (D) corresponding cell orientations; (E) Model with $\Delta H_{\text{dir}}^{\text{retraction}} = -2\Delta H_{\text{dir}}^{\text{extension}}$; (F) corresponding cell orientations.

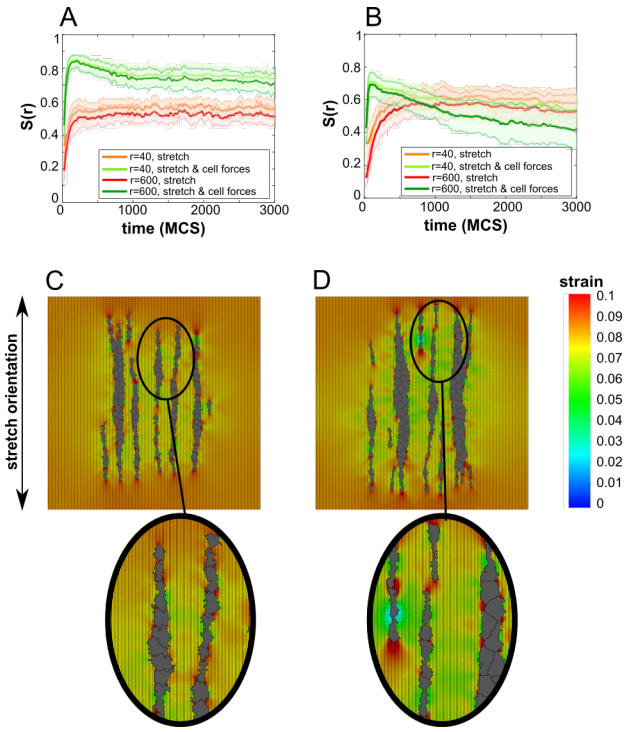

Figure 3.14: Model sensitivity to ΔH_{dir} in string formation. Time series of orientational order parameter, averaged over $n = 25$ simulations; color coding: red: r=40 for non-contractile cells, orange: r=600 for non-contractile cells, green: r=40 for contractile cells, dark-green: r=600 for contractile cells. (A) Model with $\Delta H_{\mathrm{dir}}^{\mathrm{retraction}} = -0.5\Delta H_{\mathrm{dir}}^{\mathrm{extension}}$; (B) Model with $\Delta H_{\mathrm{dir}}^{\mathrm{retraction}} = -0.5\Delta H_{\mathrm{dir}}^{\mathrm{extension}}$; Contractile cells on substrate stretched along 0° at 3000 MCS. (C) Model with $\Delta H_{\mathrm{dir}}^{\mathrm{retraction}} = -0.5\Delta H_{\mathrm{dir}}^{\mathrm{extension}}$; (D) Model with $\Delta H_{\mathrm{dir}}^{\mathrm{retraction}} = -0.5\Delta H_{\mathrm{dir}}^{\mathrm{extension}}$.

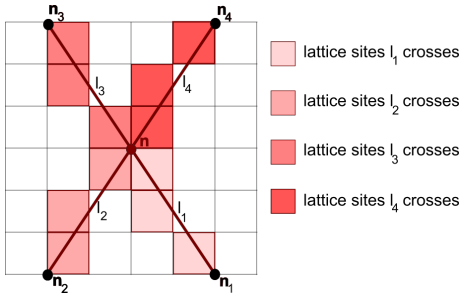

Figure 3.15: Lines between nodes. The lattice sites s_1 that the line l_1 from node n to n_1 crosses is determined using the Bresenham line algorithm. The lattice sites s_2, s_3, s_4 corresponding to lines l_2, l_3, l_4 from node n to node n_2, n_3, n_4 are such that $s_4 = s_1$ mirrored horizontally, $s_3 = s_1$ mirrored vertically and turned 180° clockwise and $s_2 = s_3$ mirrored horizontally.

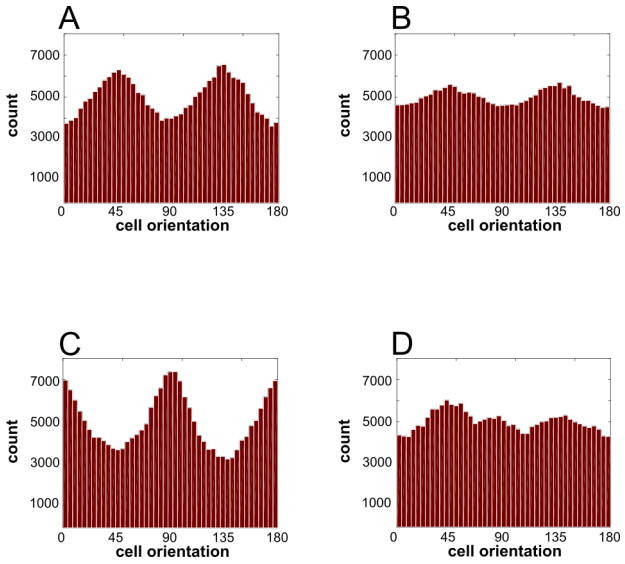

Figure 3.16: Exploring a bias in cell orientation. Cell orientations, one contractile cell on a unstretched substrate, 500 simulations and 500 MCS are plotted. (A) Forces pointed towards center of mass (Van Oers *et al.* [182]), no compression stiffening and $T = 1$; (B) Forces pointed towards center of mass (Van Oers *et al.* [182]), compression stiffening and $T = 1$; (C) FMA model [131], compression stiffening and $T = 1$; (D) FMA model [131], compression stiffening and $T = 5$.

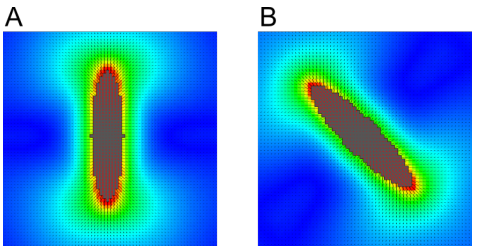

Figure 3.17: Exploring a grid effect. Strain field around ellipse shaped cell (A) oriented along 0°; (B) oriented along 45°.

4

From Focal Adhesion Dynamics to Cell Shape Changes and Durotaxis: a multiscale cell-based model

This chapter is based on:

Rens, Elisabeth G. and Merks, Roeland M.H. (2018) From Focal Adhesion Dynamics to Cell Shape Changes and Durotaxis: a multiscale cell-based model (in preparation).

Abstract

Cells adapt their behavior in response to physical properties of the matrix, such as matrix stiffness. Cells are able to sense the mechanical properties of the matrix through transmembrane integrin molecules, which assemble into large multimolecular complexes called focal adhesions. Focal adhesions grow and assemble in response to force application. Here we show with a multiscale cell based computational model that force based growth of focal adhesions suffices to explain the response of cells to substrate stiffness. We base our model on the fact that individual integrins within focal adhesions, such as $\alpha_5\beta_1$, have been shown to behave as catch-bonds; special bonds whose lifetime is maximal under positive force. In our model, cells apply a contractile force on integrin clusters. How fast this force builds up, depends on the stiffness of the substrate. The integrin clusters then grow according to catch-bond dynamics. These integrin clusters affect the probability of a cell detaching from the substrate. The model can accurately predict cell area as a function of substrate stiffness. The model can also reproduce cell elongation when we added another force based molecular mechanism of focal adhesions; where matrix stresses induces adhesion strengthening. The model suggests that the stiffness regime on which cells elongate is regulated by the velocity of its myosin motors. Furthermore, our model reproduces durotaxis, suggesting that is regulated by a bias in integrin clustering due to the catch-bond behavior of integrins.

4.1 Introduction

Embryonic development, structural homeostasis and developmental diseases are driven by biochemical signals and biomechanical forces. By interacting with the extracellular matrix (ECM), a network of fibers and proteins that surrounds tissues, cells can migrate and communicate with other cells, which contributes to tissue development. Mechanical interactions between cells and the ECM are crucial for the formation and function of tissues. By sensing and responding to physical forces in the ECM, tissues can adapt accordingly.

In particular, many mammalian cells change their shape and migrate in response to matrix stiffness. On soft matrices, cells are small and rounded, while on stiffer matrices cells are elongated. On matrices of glass like rigidity, cells can spread out like pancakes. This behavior has been observed for many cell types (endothelial cells: [198], fibroblasts: [128, 199], smooth muscle cells: [200], osteogenic cells: [201]), although the range of stiffness on which the cell becomes elongated varies between cell types [202, 203]. Another generic cell behavior is durotaxis, cell migration upwards a stiffness gradient [126, 204, 205]. However, it is still poorly understood what molecular mechanism regulates cell response to matrix stiffness [206].

Cells are able to sense matrix stiffness through focal adhesions, which are multimolecular complexes consisting of integrin molecules and structural proteins [207]. Integrins are receptors for ECM proteins and mediate cell-ECM binding and force

transmission. Structural proteins, such as vinculin and talin, bind integrin to actin stress fibers in the cytoskeleton. On compliant matrices, adhesions dynamically assemble and disassemble, while on more stiff matrices, focal adhesions stabilize [128]. Such mechanosensitivity of focal adhesion assembly is regulated by molecular components, like talin and p130Cas, that change conformation in response to mechanical force [206, 207], which allows focal adhesions to assemble or disassemble in response to forces. For instance, stretching the structural protein talin reveales vinculin binding sites, allowing additional vinculin to bind to focal adhesions [208] and stabilize the adhesion [209]. Also, integrins such as $\alpha_5\beta_1$, behave as "catch-bonds" [210], bonds of which the lifetime increases under force [211]. Because focal adhesions regulate cell spreading, orientation and migration [212–217], the mechanosensitive growth of focal adhesions is the key to our understanding of how cells respond to matrix stiffness.

Previous mathematical models proposed that cell spreading on compliant matrices is due to dynamic reciprocity: cells apply a force to the matrix and respond to the reaction of the substrate by changing cellular activities. On stiff matrices, cells experience more stress, as the matrix does not deform. If this stress positively feeds back on cellular traction forces, a cell can polarize because an initial asymmetric cell shape is reinforced by this feedback mechanism [47]. Similarly, it was proposed that cells elongate because of a positive feedback loop between contraction and strain stiffening of the matrix [182]. A feedback between stress induced recruitment of motor proteins and increased traction forces has been proposed to regulate cell spreading [218].

Other mathematical models predicted cell spreading by integrating a focal adhesion model into a cell-based model [219–221]. In these models, it was assumed that stress induces the recruitment of adhesive molecules [48, 49]. It was proposed that as substrate stiffness increases, stress fibers become more tensed and thus apply larger forces which stabilizes focal adhesions and allows a cell to spread [219, 220]. These models included many variables, including cytoskeleton/actin fiber dynamics, adhesion dynamics and their interactions. This made it difficult to dissect how exactly cell shape changes are regulated. A model including focal adhesions but no stress fiber dynamics could predict the localization of focal adhesions in a cell but could not explain increased cell area on stiffer matrices [221]. So, it is still not clear what the minimal condition is for cell spreading in response to matrix stiffness.

A range of mathematical models have also been used to explain durotaxis. For instance, it was proposed that the mechanosensitivity of stress fibers regulates durotaxis. It was suggested that a stress fiber becomes more tensed and thus stabilizes if it attaches to a stiff substrate, which results in movement up the stiffness gradient [222]. Another model proposed that a stress fiber durotacts because tensing of a stress fiber resulted in faster sliding of adhesions on the softer side of the matrix [223]. It has also been suggested that cell polarization drives durotaxis. It was proposed that cells durotact by polarizing more on stiffer substrates [224] or by polarizing towards stiffer substrates [225]. Furthermore, it was proposed that durotaxis is driven by a stiffness mediated traction force [226], bias in velocity [227], viscous force and cell stiffening

[228], motor protein recruitment [218], cell-matrix adhesion strength [229] or persistence time [230]. Many of the proposed mechanisms for durotaxis [224, 226, 227, 229] are based on the fact that focal adhesions stabilize on stiff matrices, but it is still poorly understood how the mechanosensitive growth of focal adhesions can drive durotaxis.

By integrating a focal adhesion model in a cell-substrate model, we show that dynamic reciprocity through focal adhesion dynamics are sufficient to explain three important cell generic phenonema 1) cell area increases with matrix stiffness; 2) cell elongation depends on matrix stiffness; 3) durotaxis. We model focal adhesions as clusters of integrin-ligand bonds and assume that the unbinding of integrin bonds decreases with force [231]. The cells pull on these clusters and the rate of force build-up depends on the matrix stiffness [96]. In our cell based model, we assume that cell-matrix adhesion strength increases with integrin cluster size. This model explains cell spreading as a function of substrate stiffness. We also include an adhesion strength reinforcement due to matrix stresses. This matrix stress feedback allows cells to elongate on matrices of intermediate stiffness. We show that the range of stiffness on which cells elongates depends on the velocity of myosin motor proteins. Finally, our model suggests that durotaxis speed increases with the slope of the stiffness gradient.

4.2 Results

Using a multiscale computational model, we propose that focal adhesion dynamics can explain cell spreading, cell elongation and durotaxis in response to substrate stiffness. Figure 4.1 gives an overview of the model, showing the flow and feedback between the cell, its focal adhesions and the elastic substrate it adheres to. In a first version of our model (M1), we only follow the loop with arrows 1 and 2 in the flowchart, thus excluding a feedback with matrix stress. We start out with model M1, to study how this minimal model, which describes focal adhesions as clusters of catch bonds, translates to cell spreading.

Model M1 proceeds as follows. A cell is described as a collection of discrete lattice sites in a cellular Potts model (CPM), see Figure 4.1A. The cell applies a contractile force upon focal adhesions that adhere to the matrix. We use the shape of the cell to calculate the contractile force based on a First Moment of Area (FMA) model [131], see Figure 4.1B. Because focal adhesions adhere to the substrate, how fast a cell can build up this force, depends on the substrate stiffness. We adopt a model of Schwarz *et al.* [96] to describe the build up of force in time due to myosin motor activity: $F(t) = F_s(1 - \exp(-t \cdot \frac{v_0 K}{F_s}))$, with v_0 the free velocity of the motor proteins and K the substrate stiffness. So, in model M1, matrix stiffness only affects the rate of force build-up. The more compliant the substrate is, the longer it takes for a cell to build up this force. In part B of the model, we let the forces build up for t_{FA} seconds. At the same time, part C of the model is executed. At each site of the CPM, a focal adhesions is defined (see Figure 4.1C) as a cluster of bound integrin bonds. We assume that the

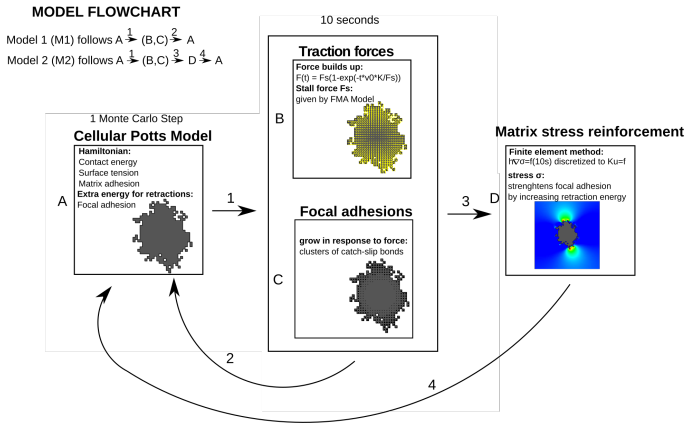

Figure 4.1: Flowchart of the multiscale CPM. (A) CPM calculates cell shapes in response to focal adhesions and substrate stresses; (B) calculation of cellular traction forces based on cell shape and force build-up dynamics; (C) focal adhesion grow according to dynamics of catch-slip bond clusters; and (D) calculation of substrate stresses due to cellular traction forces.

growth of each integrin cluster is a function of the force it experiences, according to the catch-slip bond behavior described as an ODE proposed by Novikova and Storm [231]. Simultaneously with the force build-up, we let the integrin clusters grow. After these t_{FA} seconds, we perform one timestep in the CPM. Cells in the CPM change shape by iteratively making extensions and retractions, modeling the formation and break down of adhesions with the substrate. We assume that retractions from the substrate are less likely at sites with larger integrin clusters. After one timestep of the CPM, we again let the forces build up and the integrin clusters grow for t_{FA}, and so forth.

4.2.1 Integrin catch-bond dynamics suffices to predict cell area as a function of substrate stiffness

In this section, we show with model M1, that catch-bond dynamics of integrin bonds suffices to explain cell spreading on elastic substrates. Figure 4.2A shows the response of cells on substrate of 500 μm by 500 μm with a Young's modulus of 1 kPa, 5 kPa, 10 kPa, 20 kPa, 50 kPa, 100 kPa and 10^8 kPa after 2000 MCS (≈ 5.5 h). On the most soft substrate, focal adhesions do not grow and the cell does not spread. On a slightly stiffer substrate of 5 kPa, focal adhesions have grown and the cell has significantly increased in size. Increasing the substrate further also increases the cell area, although from 50 kPa the cell does not seem to change in size. On stiffer substrates, there are more larger focal adhesions visible and they seem to accumulate more around the cell membrane, as shown in the two insets in Figure 4.2A.

Figure 4.2B plots the cell area as a function of substrate stiffness. Cell area increases from around 2500 μm^2 on the softest substrate and plateaus at around 6500 μm^2 at a stiffness of 50 kPa. Thus, the cell area has increased more than 2.5 fold on the stiffest substrate compared to the softest substrates. This factor is consistent with experimental observations [198, 232, 233]. We also investigated if the model could quantitatively predict spreading dynamics. Figure 4.2C plots the cell area as a function of time. The cells quickly increase in size and and reach their final size after 30 to 60 minutes. Experimental curves of cell area versus time follow a similar trend [123, 202].

We also investigated the distribution of the integrin cluster sizes. Figure 4.2D plots the distribution of the cluster sizes and the median cluster size (average cluster size is roughly the same). The median cluster size and variance are unaffected by substrate stiffness, in contrast with experimental observations [234]. We performed a more detailed analysis of the distribution of integrin clusters and describe two observations. 1) On stiffer substrates, there are more larger clusters. For instance, the percentage of adhesions with $N > 10000$ is 20% on 50000 kPa, 15% on 10 kPa and 10% on 5 kPa. 2) On stiffer substrates, large focal adhesions are found at the cell boundary (Figure 4.2A for 50 kPa and Supplementary Figure 4.6). On soft substrates, large focal adhesions are found further away from the cell center, where forces had time to build up because in the bulk of the cell no retractions take place (Figure 4.2A for 5 kPa and Supplementary Figure 4.6).

All in all, the results presented in this section suggest that the catch-slip bond dynamics of single integrins within focal adhesions suffice to predict cell area and spreading dynamics from substrates stiffness. Our model explains that cells spread due to intertwined dynamics of force build-up, focal adhesion growth and cell-matrix adhesion. On soft substrates, forces build up slowly, so there is not enough time for a focal adhesion to grow to strongly adhere the cell to the matrix. So, the cell will continuously make extensions and retractions. In contrast, on stiff substrates, forces build up fast and focal adhesions are able to grow and extensions have a long lifetime, allowing the cell to spread.

4.2.2 Adhesion strengthening due to matrix stress induces cell elongation

After having captured, at a quantitative level, the rate of spreading as a function of substrate stiffness, we now set out to explain the ability of mammalian cells to elongate on stiff enough substrates. Because the first version of the model (M1) could not yet explain cell elongation, we aimed to find an additional focal adhesion mechanism that can explain cell elongation.

Since cell traction forces are transferred to the matrix through the integrins, stresses develop in the matrix. Such stresses have been observed to affect focal adhesion assembly [216]. We therefore hypothesized that such a feedback may explain cell shape changes. We extended our model to Model M2, that includes a finite element model

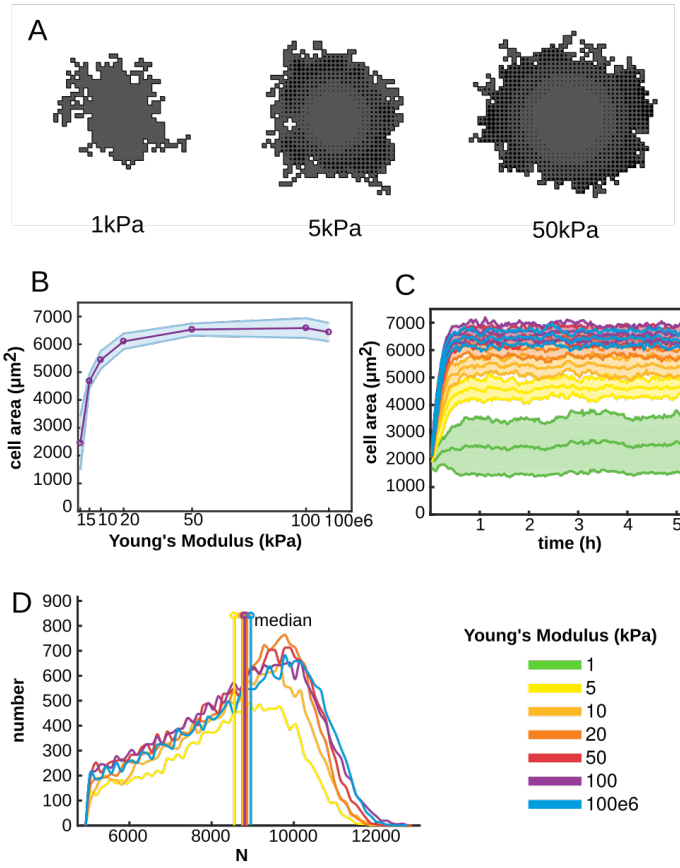

Figure 4.2: Cell area increases with increasing substrate stiffness. Model M1 was used. (A) Example configurations of cells at 2000 MCS on substrates of 1,50 and 50 kPa; (B) Cell area as a function of substrate stiffness, shaded regions: standard deviations of 25 simulations; (C) Timeseries of cell area, shaded regions: standard deviations of 25 simulations; and (D) distribution of N, the number of integrin bonds per cluster, all clusters at 2000 MCS from 25 simulations were pooled. We indicate the median. Color coding (C and D): See legend next to (D).

to calculate the matrix stress (Figure 4.1D) as a result of the cell traction forces. So, model M2 follows arrows 1, 3 and 4 in Figure 4.1D. We assume that matrix stresses reinforces cell-matrix adhesions. We model adhesion strengthening by reducing the probability of retractions from the matrix due to matrix stress, *i.e.* we multiply the energy it takes for a cell to make a retraction with $1 + p\frac{g(\underline{\underline{\sigma}}(\vec{x}))}{\sigma_h + g(\underline{\underline{\sigma}}(\vec{x}))}$. Here, parameter p regulates the strengthening and σ_h its saturation and $g(\underline{\underline{\sigma}}(\vec{x}))$ denotes the hydrostatic stress on the lattice site of retraction. Such a strengthening due to matrix stress can have various molecular origins. We hypothesize that this strengthening is due to stretching of the structural protein talin exposes binding sites for vinculin, which binds to the cytoskeleton and thus strengthens the actin-integrin linkage [208, 209].

Figure 4.3A shows representative configurations of cells after running model M2. Similar to model M1, on the most soft substrate (1 kPa), the cell stays small and round. From around 10 kPa/20 kPa, the cells start to slightly elongate. On stiffer matrices, 50 kPa and 100 kPa, cells are very much polarized in shape and large focal adhesions have grown at the tips of the cell. On the very rigid substrate, the cell is more circular again. To quantify cell elongation, we measured the eccentricity of cells as $\sqrt{(1 - \frac{b^2}{a^2})}$ with a and b the lengths of the cell's major and minor semi-axes, calculated as the eigenvalues of the inertia tensor. Figure 4.3B shows that the eccentricity of cells has a biphasic dependence on substrate stiffness. We also again quantified the distribution of the integrin cluster size again. Figure 4.3C shows the distribution of the cluster sizes for the different elastic substrates. The median cluster size does not vary much between substrate stiffness. The shape of the distributions, however, is much more flat and with higher variance on the substrates where cells have elongated. This is because an elongated shape results in large traction force at the tip of the cells, such that focal adhesions grow larger in size there, while at the sides of the cell, the forces are much smaller and focal adhesion stay small there.

The model explains the process of cell elongation as follows. On sufficiently stiff matrices, the cell initially starts to spread. The cell continuously makes random protrusions, allowing the cell shape to become slightly anisotropic. Around these cell protrusions, matrix stresses develop, which strengthens cell-matrix adhesion in this region. So, the cell can continue to build up forces, allowing the focal adhesion to grow larger. In contrast, at site of lower matrix stress, focal adhesions are more likely to disassemble. At protruding sites, cell traction forces increase due to an increased distance from the cell centroid. This results in a breaking of symmetry and the cell starts to elongate due to a positive feedback loop of force build-up, focal adhesion growth and matrix stress induced adhesion strengthening. On soft matrices, matrix stresses are not high enough to initiate a symmetry breaking. On the most rigid surface, matrix stresses are too high, allowing adhesions to strengthen equally well such that no symmetry breaking can occur. So, cell elongation is only possible on substrates with an optimal rigidity. Similar dynamics of cell spreading followed by a symmetry breaking has also been observed experimentally [214]. Note that the spindle-like shape that cells obtain in our model is similar to observed *in vitro* [127].

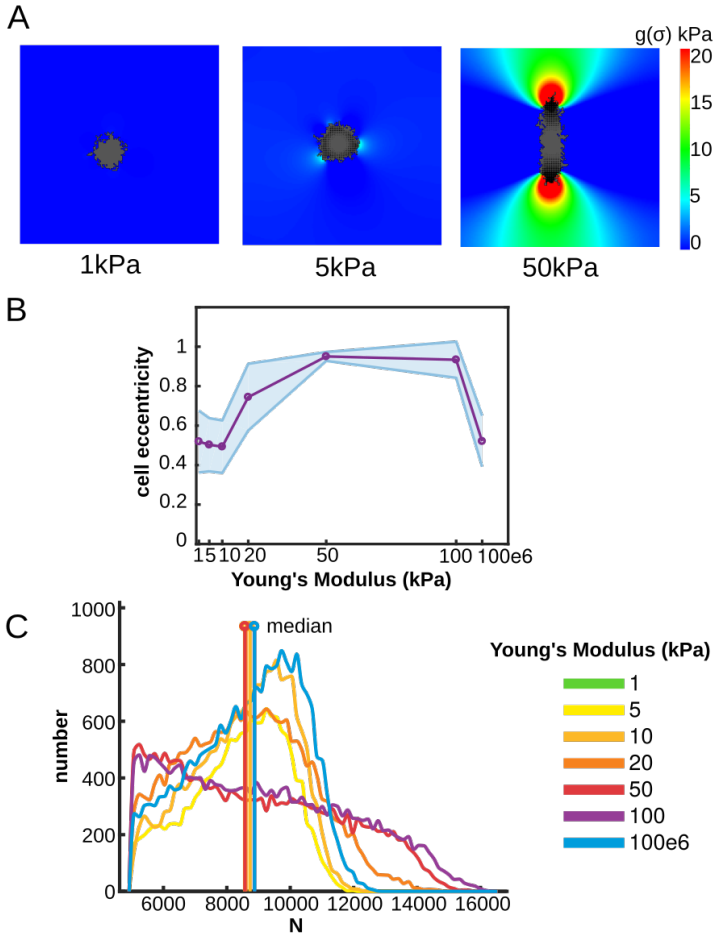

Figure 4.3: Cells elongate on substrates of intermediate stiffness. Model M2 was used. (A) Example configurations of cells at 2000 MCS on substrates of 1,50 and 50 kPa. Colors: hydrostatic stress; (B) Cell eccentricity as a function of substrate stiffness, shaded regions: standard deviations of 25 simulations; (C) distribution of N, the number of integrin bonds per cluster, all adhesion at 2000 MCS from 25 simulations were pooled. We indicate the median. Color coding (C): See legend next to (C).

Some parameters, such as p and σ_h were chosen arbitrarily. So, we tested the sensitivity of our model M2 to these parameters. Increasing p which regulates the extend of adhesion strengthening by matrix stress, enables cells to start elongating on softer matrices and also induces cell elongation on the most rigid surface (Supplementary Figure 4.7). Variations in σ_h, which regulates the saturation of stretch exposed binding sites for vinculin does not greatly affect model behavior (Supplementary Figure 4.8). Other parameters might be cell type specific, such as the lifetime of protrusions t_{FA} (Supplementary Figure 4.9), extent of random motility T (Supplementary Figure 4.10) and the magnitude of traction forces μ (Supplementary Figure 4.11). The qualitative behavior is conserved for variations of these parameters, but all parameters affect the range of substrate stiffness on which the cell can elongate.

Symmetry breaking due to matrix stress can also occur by a matrix stress mediated increase in traction force. If, instead of adhesion strengthening, we assume in our model that the stall force increases as a function of matrix stress, *i.e.* $\vec{F}_s = \vec{F}_s \cdot \left(1 + p\frac{g(\overline{\sigma}(\vec{x}))}{\sigma_h + g(\overline{\sigma}(\vec{x}))}\right)$, we obtain similar results as in Figure 4.3 (see Supplementary Figure 4.12). Such a mechanism can have various molecular origins. For instance, addition of vinculin through talin stretching can induce increased traction forces [235]. Stretching also induces α-smooth muscle actin recruitment to stress fibers [236], and myosin motor binding [237].

In conclusion, our model suggests that by applying a force on the matrix, cells develop an anistropic matrix stress field that can induce a symmetry breaking of the cell by reinforcing adhesion sites. This allows a cell to elongate on substrates of intermediate stiffness. Such a matrix stress reinforcement can be from various molecular origins, such as a matrix stress induced adhesion strengthening or increased traction forces.

4.2.3 Motor protein velocity changes stiffness regime on which cells elongate

The regime of substrate stiffness on which cells spread and elongate varies per cell type. For instance, neutrophils do not respond to changes of substrate stiffness in the range of substrate stiffness where both fibroblasts and endothelial change in area and shape [202]. To try and understand why this is the case, we can vary cell related parameters in our model. One cell specific parameter is the velocity of the myosin motors. Many cells express non-muscle myosin II, which exists in isoforms A,B and C [238]. Other cell types also expresses myosin isoforms such as skeletal, cardiac and smooth muscle myosin [238]. Different cell types may have different expression profiles of myosin isoforms [239] and since the velocity of myosin motors varies among isoforms [240, 241], this may impact the response of cells to matrix stiffness. Using our model, we study how myosin motor velocity, v_0, can impact cell shape. We study a range from 10 nm/s (order of non-muscle myosin II B [240]) to 1000 nm/s (can be achieved by muscle myosin [242]).

Figure 4.4A and B shows the cell configurations for a slow (10 nm/s) and fast mo-

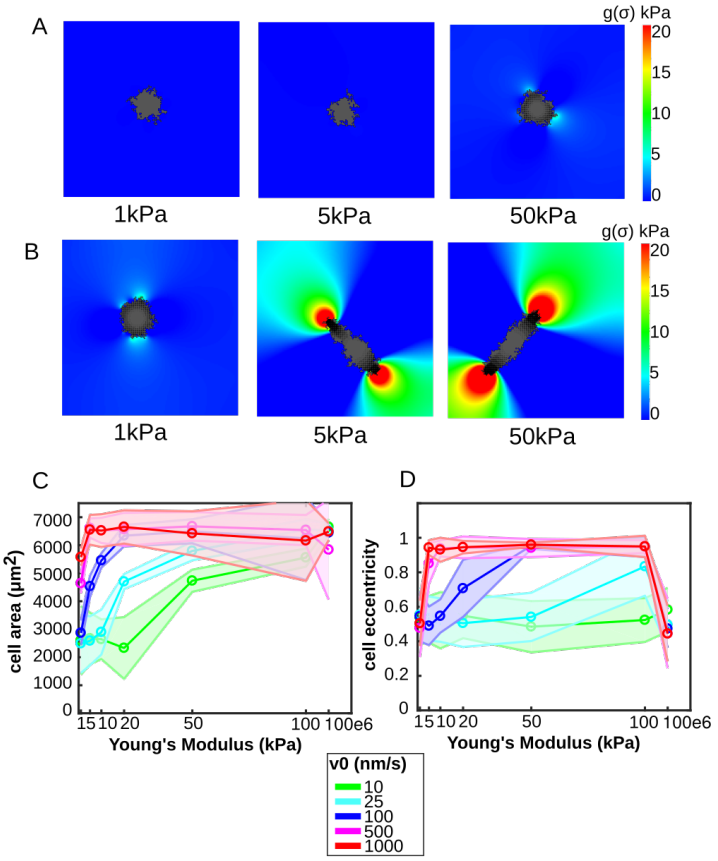

Figure 4.4: Range of stiffness on which cells elongate depends on myosin motor velocity. Model M2 was used. (A) Example configurations of cells at 2000 MCS on substrates of 1,50 and 50 kPa with motor velocity 10 nm/s; (B) Example configurations of cells at 2000 MCS on substrates of 1,50 and 50 kPa with motor velocity 1000 nm/s. Colors (A-B): hydrostatic stress; (C) Mean cell area as a function of motor velocity, error bars: standard deviations of 25 simulations; (D) Mean cell eccentricity as a function of motor velocity, error bars: standard deviations of 25 simulations.

tor velocity (1000 nm/s), compared to the default value of 100 nm/s as shown in Figure 4.3A, respectively. This shows that cells with slow motors do not spread significantly and do not elongate, even on stiffer substrates. In contrast, cells with fast motors already spread more and elongate on softer matrices. We quantified this further by running 25 simulations for each combination of substrate stiffness and motor velocity. Figure 4.4B and Figure 4.4C plot the cell area and eccentricity, respectively, as a function of motor protein velocity. With the fastest velocity tested here (1000 nm/s), cell area saturates already at 5 kPa and cells elongate on a larger stiffness regime (5 kPa - 100 kPa). With the slowest motor velocity (10 nm/s), cells do not elongate at all, while they still spread well on stiff matrices. This is explained as follows. Decreasing v_0 is very similar to decreasing the stiffness of the substrate, because they both contribute to the rate of force build-up in the same way, given by $\frac{|\vec{F}_s|}{v_0 K}$. So, in terms of cell area, cells with slower motor proteins would obtain a larger spreading area at stiffer matrices. However, they are not able to elongate because forces are not built up fast enough to generate high enough matrix stress that induces the adhesion strengthening.

So, in summary, we predict that cells with faster motor proteins start spreading/elongating at softer substrates, while cells with slower motor proteins need a stiffer substrate to instigate a response.

4.2.4 Durotaxis explained by a bias in integrin clustering

On substrates with a stiffness gradient, cells move up the stiffness gradient, a phenomena called durotaxis. Cells may durotact by sending out protrusions which better stick to stiff substrates because focal adhesions grow on stiff substrates [126, 243]. Here, we investigate if force induced focal adhesion growth is sufficient to reproduce durotaxis. We simulated durotaxis by placing an initial circular cell with its center at x=y=250 μm on a grid of 1250 μm by 500 μm for 10000 MCS ($\approx 28h$). In the x-direction, we let the stiffness increase from 1 kPa to 26 kPa, so with a slope of 20 Pa/μm. Figure 4.5A plots ten different trajectories of the cell, showing that most cells have moved significantly in the x-direction, up the stiffness gradient. Cells, on average, move in the x-direction with a constant speed of around 4.3 μm/h, measured as the slope of the x-coordinate of the cell from 25 simulations. Vincent *et al.* [205] found speeds of 6.2 μm/h with gradient slope 10 Pa/μm *in vitro* for mesenchymal stem cells. In our model, how far cells can move up the gradient, depends on the flexibility and motility of the cell. We varied λ, the Lagrangian multiplier of the area constraint, controlling cell flexibility, and the cellular temperature T, and found that both affect cell speed (Table 4.2).

In the CPM, cell movement is a result of subsequent protrusions and retractions. In stiffer areas the focal adhesions grow larger, so that retraction are more likely to be made at more flexible parts of the matrix. As a result, the cell moves up the stiffness gradient. So, naturally, one would expect that durotaxis depends on the slope of the stiffness gradient. Figure 4.5B shows the speed of the cell as a function of the slope of the stiffness gradient. Indeed, simulated cells move faster up the gradient if the

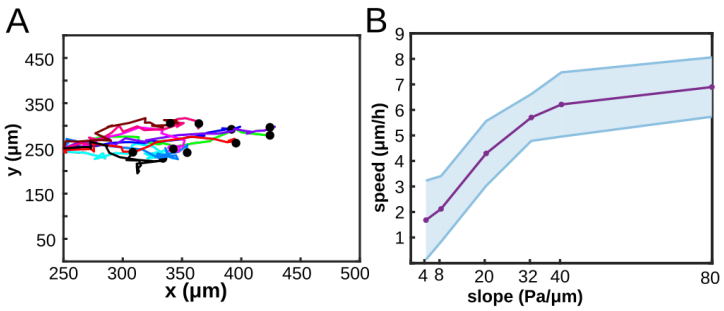

Figure 4.5: Durotaxis as a result of integrin catch-bond dynamics. (A) Ten trajectories of durotacting cells on a matrix with slope 20 kPa/ µ m; (B) Cell speed as a function of the slope of the stiffness gradient.

slope is steeper, as observed in experimental conditions [204, 205]. This is because the difference in focal adhesion growth between the front and the back of the cell is larger with a higher slope, causing a larger bias. We suspect that the durotaxis speed saturates at steep slopes, because the growth rate of focal adhesions is limited.

In conclusion, durotaxis is an emergent behavior in our model, cells exhibit durotaxis as a result of a biased growth of focal adhesions. A cell can build up forces faster on stiffer matrices, allowing focal adhesions to grow larger here. So, the cell better attaches at the stiffer part and will retract at the softer side. As a result, the cell moves up the stiffness gradient.

4.3 Discussion

We have presented a multiscale computational model to show that force induced focal adhesion dynamics can explain 1) cell area increasing with substrate stiffness (Figure 4.2A-B), 2) cell elongation on substrates of intermediate stiffness (Figure 4.3A-B) and 3) durotaxis (Figure 4.5A). The model described cells spreading on an elastic substrate via focal adhesions, which are modelled as integrin clusters. Cells applied traction forces on integrin clusters, which grow according to catch-slip bond dynamics as proposed by Novikova and Storm [231]. How fast a cell in our model can build up this force depended on the stiffness of the matrix, based on a model by Schwarz et al. [96]. On soft matrices, forces build up slowly such that integrin clusters do not have enough time to grow, while on stiff matrices forces build up fast such that integrin clusters can grow in size. Because we assumed that larger focal adhesions detach less likely from the substrate than smaller ones, cell spreading area increased on stiffer substrates (Figure 4.2B). If we included a feedback between matrix stresses and cell-matrix adhesion, simulated cells were able to elongate. Based on experimental observations [216], we assumed that matrix stress stabilizes focal adhesions. We

modeled this by reducing the likelihood of cell-matrix deadhesion. This allowed cells to elongate on matrices of intermediate stiffness (Figure 4.3A-B). The model suggests that the range of substrate stiffness on which cells elongate depends on the velocity of the myosin molecular motors, which determine the rate of force build-up. Cells with higher motor protein velocity started to elongate on softer matrices (Figure 4.4). Finally, our model explains durotaxis as a bias in focal adhesion growth on stiffer matrices. Because extensions are more likely to stick at these regions and retractions are more likely to be made on the softer side, cells obtain a bias in cell motility up the stiffness gradient (Figure 4.5A). Our model predicted that cell velocity increases with the slope of the stiffness gradient (Figure 4.5B), which compares well with experimental data [204, 205]. The spreading dynamics in our model also qualitatively compare well with *in vitro* dynamics: the spreading dynamics in Figure 4.2C are similar to spreading area curves found *in vitro* [123, 202] and the dynamics of cell elongation (Movie S1) resemble *in vitro* observations [214].

We hypothesized that the stabilization of focal adhesions by matrix stress is due to stretching of talin. Stretching of talin exposes vinculin binding sites [208] and vinculin in turn binds the focal adhesion to the cytoskeleton, which strengthens cell-matrix adhesion [209]. Our model suggests that this might regulate cell elongation. In agreement with this observation, vinculin regulates cell elongation on glass substrates [212]. We could attempt to further unravel how vinculin drives cell elongation by studying vinculin depleted cells on substrates of different stiffness, or by adapting talin in such a way that vinculin cannot bind as a result of talin stretching.

Interestingly, our model suggests that cells can also elongate if matrix stress induces an increase in cell traction forces (Supplementary Figure 4.12). This mechanism can be justified by two experimental observations; 1) vinculin increases cell traction forces [235] and 2) stressing focal adhesions induces α-smooth muscle actin recruitment to stress fibers that in turn increases traction forces [236]. Experimental testing can be done to elucidate which mechanism might be required for cell elongation, since our model does not differentiate between these two and vinculin adhesion strengthening.

Our model also predicts that cells elongate on different ranges of substrate stiffness, due to different velocities of their myosin motors (Figure 4.4). This could explain why different cell types elongate on different stiffness regimes [202, 203], as they might express different isoforms of myosin motors. Many studies of different types of cells on compliant substrates have been performed, but often either the range of substrate stiffness tested differs or the type of matrix (*i.e.* type of ligand, ligand density, or gel type) is different. Therefore, spreading of different cell types cannot be compared one to one. Model validation would benefit from more systematic *in vitro* experiments of different cell types on compliant matrices. To then confirm this model prediction, it could be measured which isoform of myosin the cells express. There are some experiments that seem to support our model prediction. For instance, cell elongation is promoted in Dlc1 deficient ovarian tumour [244]. Dlc1 leads to increases of phosphorylation level of nonmuscle IIA mysosin [244], which suggests that an in-

crease in motor protein velocity indeed enables cells to elongate more. Furthermore, cells treated with blebbistatin on stiff matrices obtain phenotype as if they are on a soft matrix [245], while upregulating myosin gives opposite results. In this paper by Jiang et al. [245] it was suggested that the actomyosin pulling speed produce has a similar effect on integrin stem cell lineage specification (which is highly associated with cell shape [246]) as the effective spring constant of the substrate.

The strength of our model is that we can associate response of cells to matrix stiffness with mechanisms at the level of adhesions. In our model, we differentiate between integrin size dependent adhesion strength and adhesion strength reinforcement by structural proteins, as observed experimentally [247] and studied what the effect was on cell shape. Previous models have explained cell responses based on how matrix stiffness influences cellular mechanisms. For instance, increased cell spreading on stiff matrices has been proposed to be regulated by a stiffness induced upregulation of cell traction forces [47], stress fiber stabilization [220] or motor protein recruitment [218]. In previous computational models, assumptions on cell dynamics were often motivated by adhesion dynamics and could explain stiffness sensing [45, 47, 248, 249] and durotaxis [224, 226, 227, 229].

Similarly, the mechanism for cell spreading proposed in our previous work [182], was based on focal adhesion dynamics. In this previous model, we suggested that protrusions are more likely to stick to highly strained matrices that have strain-stiffened. This was motivated by the observation that cells more efficiently build up forces on stiff matrices, which enables stabilization of focal adhesions [128]. In this work, we developed an explicit model for focal adhesion growth, to study how the mechanosensitive assembly of focal adhesions drives cell spreading and durotaxis. Previous computational models that included focal adhesions suggested that an intricate interplay between stress fiber remodeling and focal adhesion growth is required for cell spreading on compliant matrices [219, 220]. A model by Stolarska et al. [221] suggested that the mechanosensitive growth of focal adhesions alone could not explain increased cell spreading on stiff matrices [221]. In this model, rigid matrices induce increased cell contraction which resists cell spreading. We however suggest that the mechanosensitive growth of focal adhesions is sufficient to explain cell spreading as a function of substrate stiffness. In contrast to the model by Stolarska et al. [221], cells in our model are able to spread on rigid matrices, because the adhesion strength of large focal adhesions resist cell retractions on stiff matrices.

A previous coupled cell-based - focal adhesion model was used to study durotaxis [224]. In this model, the number of focal adhesions was assumed to be higher on stiff substrates and the distribution of focal adhesions was assumed to be more narrow on stiff substrates. Both the number and distribution of focal adhesion then controlled the deviation from the direction of motion: on stiff matrices cells move more persistent, causing it to durotact. Recently, it was also proposed that cells durotact by tugging on the matrix and changing their direction towards areas that the cell perceives as stiff [225]. Our model shows that the directed movement of cells emerges from the

mechanosensitive growth of focal adhesions and that no inherent persistent or directed cell migration is required.

A limitation of our model is that it cannot accurately predict increasing focal adhesion sizes as a function of substrate stiffness (see Figure 4.2D), while this has been observed experimentally [214]. This may be explained by modeling choices. In the CPM, cells only make retractions at the boundary of the cell, so in the middle of the cell, integrin clusters continue to grow even on soft matrices. Also, there is a constant pool of free integrin bonds, making the growth rate of new focal adhesions to go down due to existing focal adhesions. Furthermore, our lattice based model does not define spatial effects in integrin clustering. In reality, small clusters may merge into larger adhesions and the availability of integrins that can bind to ECM, active integrin, is spatially and temporally regulated. Cells produce integrins, that diffuse and are activated within the cell. This activation of integrin depends on interaction with other proteins, such as talin [250] and vinculin [251]. Furthermore, Stretching of p130cas induces its phosphorylation, which in turn activates the small GTPase Rap1 [252] which activates integrins [253]. So, to better reproduce focal adhesion growth in future models, we can include other relevant mechanisms such as diffusion and the activation of integrins [48, 220, 250, 254]. However, because we were interested in cell shape in this work, which can be predicted with our model, we find the level of detail of focal adhesion dynamics sufficient at the moment.

In summary, we propose that the mechanosensitive response of molecules in focal adhesions suffice to explain the response of cells to matrix stiffness. In agreement with experimental observations, cells spread more on stiff matrices and obtain an elongated shape if the matrix is stiff enough. Furthermore, cells durotact and move faster with steeper stiffness gradients. This model paves the way to study how specific molecular mechanisms within focal adhesions impact cell and tissue level responses to matrix mechanics. This can give rise to new targets of treatment and the design of tissue engineering experiments.

4.4 Methods

We developed a multiscale model where cell movement depends on force induced focal adhesion dynamics. The model couples a cell-based model, substrate model and focal adhesion model in the following way. The Cellular Potts Model (CPM) describes cell movement. The shape of the cell is used to describe the stall forces that the cell exerts on the focal adhesions attached to a flexible substrate. These forces affect the growth of the focal adhesions. We assume that focal adhesions are clusters of integrins that behave as catch-slip bonds. Its dynamics are described using ordinary differential equations (ODEs). Finally, we assume that the cell-matrix link is strengthened by matrix stresses, which we calculate using a finite element model (FEM). In all simulations described in this work, we employ the parameter values as described in Table 4.1.

4.4.1 Cellular Potts Model

To simulate cell movement, we used the Cellular Potts Model (CPM) [72]. The CPM describes cells on a lattice $\Lambda \subset \mathbb{Z}^2$ as a set of connected lattice sites. Since the simulations in this article are limited to one cell, we describe the CPM here for a single cell. To each lattice site $\vec{x} \in \Lambda$ a spin $s(\vec{x}) \in \{0, 1\}$ is assigned. This spin value indicates if the cell $s(\vec{x}) = 1$ or the extracellular matrix $s(\vec{x}) = 0$ occupies this site. So, the cell configuration is given by $C = \{\vec{x} : s(\vec{x}) = 1\}$. The cell configuration evolves by dynamic Monte Carlo simulation. During one Monte Carlo Step (MCS), copies of a spin $s(\vec{x})$ from a source site $\vec{x}$ into a neighboring target site $\vec{x}\prime$ are attempted. Such copies mimic active cellular protrusions and retractions. During a MCS, N copy attempts are made, with N the number of lattice sites in the grid. Whether a copy is accepted or not depends on a balance of forces, which are represented in a Hamiltonian H.

A copy is accepted if H decreases, or with a Boltzmann probability otherwise, to allow for stochasticity of cell movements:

$$P(\Delta H) = \begin{cases} 1 & \text{if } \Delta H + Y < 0 \\ e^{(-\Delta H + Y)/T} & \text{if } \Delta H + Y \geq 0. \end{cases} \tag{4.1}$$

Here $\Delta H = H_{\text{after}} - H_{\text{before}}$ is the change in H due to copying, and the cellular temperature $T \geq 0$ determines the extent of random cell motility. Furthermore, Y denotes a yield energy, an energy a cell needs to overcome to make a movement. Finally, to prevent cells from splitting up into disconnected patches, we use a connectivity constraint that rejects a copy if it would break apart a cell in two or more pieces.

We use the following Hamiltonian:

$$H = \underbrace{\lambda A^2}_{\text{compression}} + \underbrace{\sum_{\text{neighbours}(\vec{x},\vec{x}\prime)} J(s(\vec{x}), s(\vec{x}\prime))}_{\text{line tension}} - \underbrace{\lambda_C \frac{A}{A_h + A}}_{\text{cell-matrix adhesion}} \tag{4.2}$$

The first term of H denotes a area constraint or compression, where A is the area of cell and λ is the corresponding Lagrange multiplier. In the second term, $J(s(\vec{x}), s(\vec{x}\prime)$ are the adhesive energy between two sites $\vec{x}$ and $\vec{x}\prime$ with spins $s(\vec{x})$ and $s(\vec{x}\prime)$. When taking a sufficient large neighborhood, the second term describes a line tension, as it approximates the perimeter of a cell [255]. We take a neighborhood order of 10. The third term describes the formation of adhesive contacts of cells with the substrate, where the bond energies lower the total energy [191], causing the cells to spread. The parameter λ_C is the corresponding Lagrange multiplier. The energy gain of occupying more lattice sites saturates with the cell area, as the total number of binding sites is limited. The parameter A_h regulates this saturation.

To describe cell-matrix binding via focal adhesions, we implement the following yield energy in the CPM

$$Y = \lambda_N \frac{N(\vec{x}\prime) - N_0}{N_h + N(\vec{x}\prime)} \cdot \mathbf{1}_{s(\vec{x}\prime)=1} \cdot \mathbf{1}_{s(\vec{x})=0}, \tag{4.3}$$

where $N(\vec{x}')$ is the size of the focal adhesion at the target site. This models that a retraction is energetically costly for a cell to make, because it needs to break the actin-integrin connection. We assume that the size of the actin-integrin link is proportional to the size of the focal adhesion, *i.e.* the number of integrin bonds [256], and that the strength of adhesion saturates [209] with a parameter N_h. The substraction of N_0 represents that an adhesion only creates extra linkage if it is greater than a nascent adhesions. Note that the Y can not become negative, because we assume that adhesions smaller than N_0, a nascent adhesion, breaks down due to its short lifetime, see section C. So, only adhesions larger than N_0 create a yield energy. In section C, we further adapt this yield energy to describe a matrix stress induced focal adhesion reinforcement.

4.4.2 Cell traction forces

Following Schwarz et al [96], we assume that traction forces are generated by myosin II molecular motors on the actin fibers, of which the velocity is given by

$$v(\vec{F}) = v_0\left(1 - \vec{F}/\vec{F_s}\right), \tag{4.4}$$

where v_0 is a free velocity. The traction forces are applied to the ECM, which we assume is in plane stress. The constitutive equation is given by $h\vec{\nabla}\underline{\underline{\sigma}} = \vec{F}$ where $\underline{\underline{\sigma}}$ is the ECM stress tensor and h is the thickness of the ECM. We assume that the ECM is isotropic, uniform, linearly elastic and we assume infinitesimal strain theory. We solve this equation using a Finite Element Model (FEM). In the FEM, traction field $\vec{f}$ and ECM deformation $\vec{u}$ are related by:

$$\mathbf{K}\vec{u} = \vec{f}, \tag{4.5}$$

where $\mathbf{K}$ is the stiffness matrix given by

$$\mathbf{K} = h\int \mathbf{B}^T \frac{E}{1-\nu^2}\begin{pmatrix} 1 & \nu & 0 \\ \nu & 1 & 0 \\ 0 & 0 & \frac{1-\nu}{2} \end{pmatrix}\mathbf{B}, \tag{4.6}$$

where $\mathbf{B}$ is the conventional strain-displacement matrix for a four-noded quadrilateral element [155] and E is the Young's modulus and ν is the Poisson's ratio of the ECM. For more details on this part of the model, we refer to our previous work [182, 257].

Following Schwarz *et al.* [96], the force build-up is given by the ODE:

$$\mathbf{K}\vec{v}(\vec{f}) = \frac{d\vec{f}}{dt}. \tag{4.7}$$

However, since this equation is complex and also expensive to solve, we, for now, ignore the interactions between neighbouring sites, *i.e.* we reduce $\mathbf{K}$ to it's diagonal components. This gives us:

$$\vec{F}(\vec{x}, t) = \vec{F_s}(\vec{x}) + (\vec{F_0}(\vec{x}) - \vec{F_s}(\vec{x}))\exp(-t/t_k) \tag{4.8}$$

where $\vec{F}_0$ is the force already exerted by the actin, and t_k is given by $\frac{|\vec{F}_s|}{v_0 K}$ where K is given by the diagonal entry of **K** Since the cell configuration and therefore the traction forces change each MCS, the tension on the focal adhesions does not build up from zero, but from the tension that was built up during the previous MCS: $\vec{F}_0$ at the current MCS is given by $\vec{F}(t_{\mathrm{FA}})$ of the previous MCS.

To calculate $\vec{F}_s$, the stall force of the cells, we employ a first-moment-of-area (FMA) model, proposed and experimentally validated by Lemmon & Romer [131]. This model infers stall forces from the shape of the cell of the CPM, based on the assumption that a network of actin fibers in the cell acts as a single, cohesive unit.

$$\vec{F}_s(\vec{x}) = \frac{\mu}{A} \sum_{\text{line piece } \vec{x}\to\vec{y}\subset C} \vec{x} - \vec{y}, \tag{4.9}$$

We divided with the cell area A such that force increases roughly linear with cell area, as experimentally observed [127].

4.4.3 Focal adhesions

At each lattice site ($\vec{x}$) occupied by the cell ($s(\vec{x}) = 1$), a focal adhesion is modeled as a cluster of bound integrin bonds N. Each individual integrin bond behaves as a catch-slip bond, whose lifetime is maximal under a positive force [231]. Accordingly, the growth of a cluster of such bonds is described by an ODE derived by Novikova and Storm [231]:

$$\frac{dN(\vec{x},t)}{dt} = \gamma N_a(t)(1 - \frac{N(\vec{x},t)}{N_b}) - d(\phi(\vec{x},t))N(\vec{x},t) \tag{4.10}$$

with γ a binding rate, N_a the number of free bonds, and N_b the maximal number of bound bonds a lattice site can contain. This logistic growth term is a slight adaptation compared to Novikova and Storm [231]. The degradation of the focal adhesions $d(\phi)$ depends on the tension ϕ on the focal adhesion N. This degradation rate is given by

$$d(\phi(\vec{x},t)) = \exp(\frac{\phi(\vec{x},t)}{N(\vec{x},t)} - \phi_s) + \exp -(\frac{\phi(\vec{x},t)}{N(\vec{x},t)} - \phi_c) \tag{4.11}$$

where ϕ_s and ϕ_c describe the slip and catch bond regime in N/m^2, respectively. Here, $\phi(\vec{x},t) = \frac{|\vec{F}(\vec{x},t)|}{\Delta x^2}$ is the stress applied to the lattice site of the focal adhesion. We assume that the number of free bonds N_a is limited by the number of available integrin receptors in the entire cell, N_m. These N_m receptors can be recruited to each focal adhesion site and enable binding of a bond. Thus, $N_a(t) = N_m - \sum_{\{\vec{x}|s(\vec{x})=1\}} N(\vec{x},t)$. We let the focal adhesions grow after each MCS for t_{FA} seconds with time increments of Δt_{FA}. If $N(\vec{x}) = 0$ and $s(\vec{x}) = 1$, we set $N(\vec{x}) = N_0$, such that degraded focal adhesions have the potential to grow again. This models that the cell creates focal complexes, precursors of focal adhesions that contain a small amount of integrins and have a very short lifetime. During a MCS, a cell breaks adhesions if it retracts, so, we set $N(\vec{x}) = 0$ when a retraction occurs. We assume that if a cell extends, it binds a number of integrins

to the matrix. So, after an extension we set $N(\vec{x}) = N_0$. Furthermore, after the focal adhesions were allowed to grow, *i.e.* at $t = t_{\mathrm{FA}}$ we set all $N(\vec{x}) = 0$ if $N(\vec{x}) < N_0$. This models that the cell fails to build a focal adhesion from a focal complex/nascent adhesion, which subsequently breaks down quickly do to its short lifetime [258].

4.4.4 Substrate stresses

The forces that were build up during a MCS, $\vec{F}(t_{\mathrm{FA}})$, are plugged into a finite element model (FEM) to calculate the stress tensor $\underline{\underline{\sigma}}(\vec{x})$ on each lattice site. We assume that the integrin-cytoskeletal adhesion strengthens as a result of stress. We define

$$g(\underline{\underline{\sigma}}) = \begin{cases} \frac{1}{2}(\sigma_{xx} + \sigma_{yy}) & \text{if } \frac{1}{2}(\sigma_{xx} + \sigma_{yy}) \geq 0 \\ 0 & \text{if } \frac{1}{2}(\sigma_{xx} + \sigma_{yy}) < 0 \end{cases} \tag{4.12}$$

the positive hydrostatic stress of the stress tensor that describes how much stress the adhesion experiences. Now, we extend the yield energy as follows:

$$Y = \lambda_{\mathrm{N}} \frac{N(\vec{x}') - N_0}{N_h + N(\vec{x}')} \cdot \left(1 + p \frac{g(\underline{\underline{\sigma}}(\vec{x}'))}{\sigma_h + g(\underline{\underline{\sigma}}(\vec{x}'))}\right) \cdot \mathbf{1}_{s(\vec{x}')=1} \cdot \mathbf{1}_{s(\vec{x})=0} \tag{4.13}$$

We thus assume that stress strengthens the adhesion, with parameter p and that this strengthening saturates with parameter σ_h.

4.4.5 Stiffness gradient

To study durotaxis, we model a stiffness gradient in the x-direction on a lattice of 1250 μm by 500 μm. The Young's modulus of the substrate $E(Pa)$ is given by $E(x) = \max\{1, 6000 + (x - 250) \cdot \text{slope}\}$, with x in μm, such that the Young's modulus at the center of the cell at time $t = 0$ is 6000 Pa and is nonzero. The default value for the slope is 20 20 Pa/μm.

4.5 Supplementary methods

In the main text, we proposed that matrix stress induces adhesion strengthening but noted that matrix stress might also reinforce cell contractility. Supplementary Figure 4.12 shows the results of having $\vec{F}_s = \vec{F}_s \cdot \left(1 + p\frac{g(\underline{\underline{\sigma}}(\vec{x}'))}{\sigma_h + \overline{\overline{g}}(\underline{\underline{\sigma}}(\vec{x}'))}\right)$ instead of equation 4.13 in the main text. Since matrix stresses are defined on the lattice sites while forces are defined on the nodes of the lattice, we needed to assume some interpolation. We choose to take

$$\vec{F}_s = \vec{F}_s \cdot \frac{1}{4} \sum_{\text{surrounding4nodes}} \left(1 + p\frac{g(\underline{\underline{\sigma}}(\vec{x}'))}{\sigma_h + \overline{\overline{g}}(\underline{\underline{\sigma}}(\vec{x}'))}\right) \tag{4.14}$$

4.6 Supplementary tables

parameter	description	value	unit	value was
CPM				
Δx	lattice site width	2.5	μm	chosen
λ	area constraint	0.0002	N/m per lattice site^2	chosen
$J(0, \text{cell})$	adhesive energy	3000	Nm per lattice site	chosen
nbo	neighbourhood order	10	-	estimated based on accuracy of line tension [255]
λ_C	adhesion strength	600	Nm per lattice site	chosen
A_h	area saturation	1000	lattice sites	chosen
λ_N	focal adhesion strength	4	Nm	chosen
p	actin-integrin strength	1	-	chosen
σ_h	saturation actin-integrin binding	5000	N/m^2	chosen
T	cellular temperature	2	Nm	chosen
Forces				
μ	traction magnitude	0.001	Nm per lattice site	estimated based on endothelial traction stresses [198]
v_0	free velocity of myosin molecules	100	nm/s	estimated based on non-muscle myosin IIB [240, 242]
E	Young's modulus	10000	N/m^2	varies
ν	Poisson's ratio	0.45	-	chosen
τ	substrate thickness	10	μm	[158]
FAs				
γ	growth rate	0.05	/s	estimated [231]
N_0	size initial adhesion	5000	-	estimated based on nascent adhesions [258]
N_m	maximum free bonds	8000000	-	chosen

N_b	maximum size focal adhesion	39062	-	estimated based on number of integrins that fit in one lattice site [258]
ϕ_s	slip tension	4.02	pN/m^2	[231]
ϕ_c	catch tension	7.76	pN/m^2	[231]
t_{FA}	focal adhesion growth time	10	s	estimated based on protrusion lifetimes [259]
Δt_{FA}	time steps	0.01	s	chosen

Table 4.1: Parameter setting.

λ/T	1	2	3
0.0015	7.5106 ± 0.7971	5.3998 ± 1.1767	5.1622 ± 0.7922
0.002	6.7372 ± 1.1609	4.2945 ± 0.9978	3.8785 ± 1.1845
0.0025	5.5544 ± 1.3991	4.0823 ± 1.4943	3.0196 ± 1.3468

Table 4.2: Durotaxis speed in μm/h as a function of λ and T. Values: mean ± standard deviation of 25 simulations.

4.7 Supplementary figures

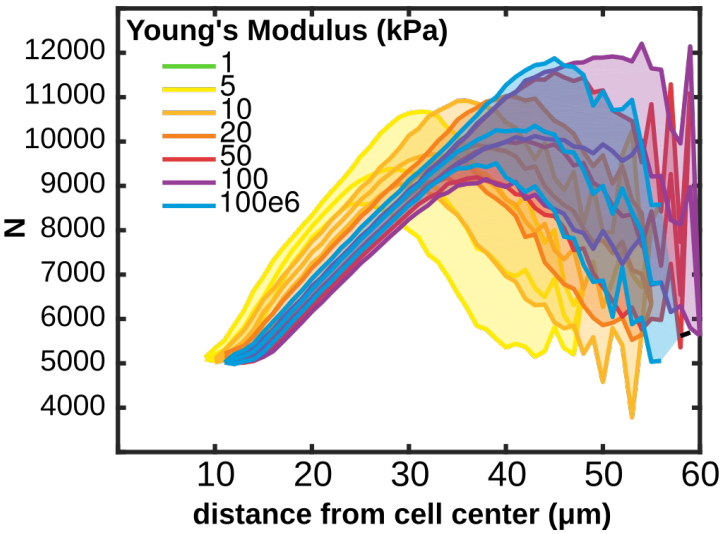

Figure 4.6: The number of integrin bonds per cluster (N) in model M1 as a function of distance from the cell center. All clusters at 2000 MCS from 25 simulations were pooled. Shaded regions show standard deviations.

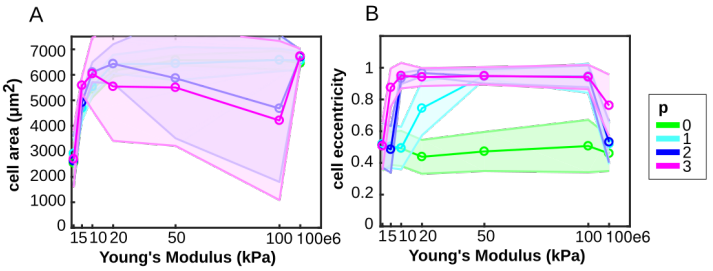

Figure 4.7: Model sensitivity to p. (A) Cell area as a function of substrate stiffness, shaded regions: standard deviations of 25 simulations; (B) Cell eccentricity as a function of substrate stiffness, shaded regions: standard deviations of 25 simulations.

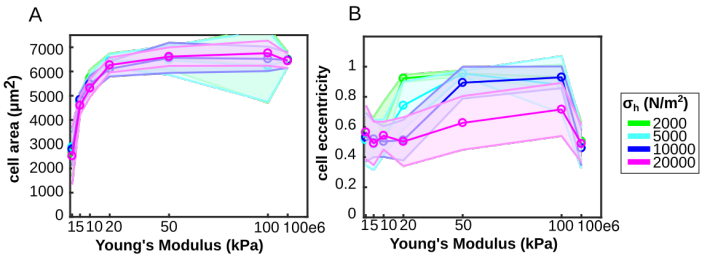

Figure 4.8: Model sensitivity to σ_h. (A) Cell area as a function of substrate stiffness, shaded regions: standard deviations of 25 simulations; (B) Cell eccentricity as a function of substrate stiffness, shaded regions: standard deviations of 25 simulations.

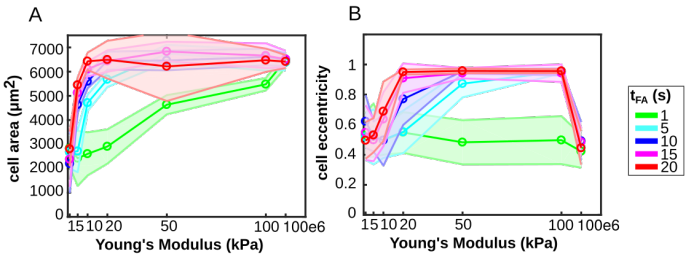

Figure 4.9: Model sensitivity to t_{FA}. (A) Cell area as a function of substrate stiffness, shaded regions: standard deviations of 25 simulations; (B) Cell eccentricity as a function of substrate stiffness, shaded regions: standard deviations of 25 simulations.

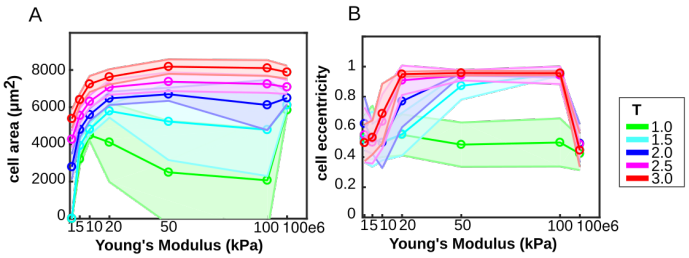

Figure 4.10: Model sensitivity to T. (A) Cell area as a function of substrate stiffness, shaded regions: standard deviations of 25 simulations; (B) Cell eccentricity as a function of substrate stiffness, shaded regions: standard deviations of 25 simulations.

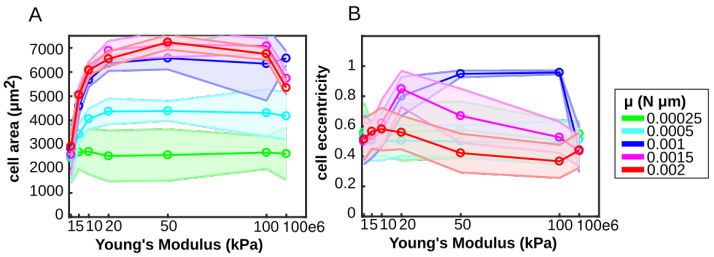

Figure 4.11: Model sensitivity to μ. (A) Cell area as a function of substrate stiffness, shaded regions: standard deviations of 25 simulations; (B) Cell eccentricity as a function of substrate stiffness, shaded regions: standard deviations of 25 simulations.

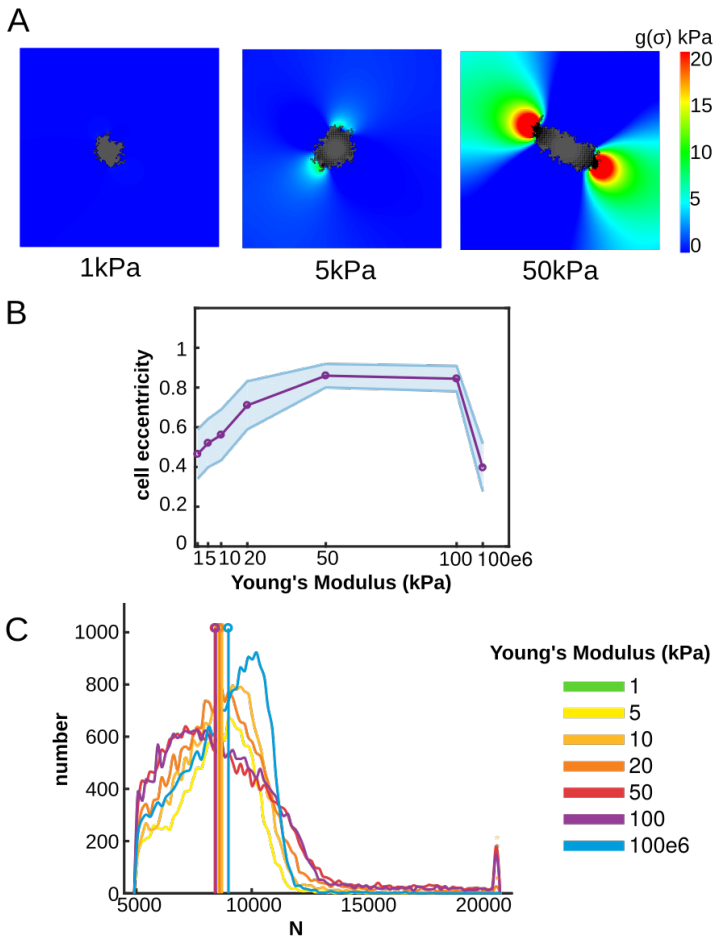

Figure 4.12: Cells elongate on substrates of intermediate stiffness if matrix stress reinforces traction force $\vec{F}_s$ with $p = 5$. (A) Example configurations of cells at 2000 MCS on substrates of 1,50 and 50 kPa. Colors: hydrostatic stress; (B) Cell eccentricity as a function of substrate stiffness, shaded regions: standard deviations of 25 simulations; (C) distribution of N, the number of integrin bonds per cluster, all adhesion at 2000 MCS from 25 simulations were pooled. We indicate the median. Color coding (C): See legend next to (C).

5

Mathematical Modeling of the Nodal Signaling Range Regulated by FurinA induced Nodal Maturation

This chapter presents the mathematical modeling aspects of

Federico Tessadori, Emily S. Noël, Elisabeth G. Rens, Roberto Magliozzi, Inkie J.A. Evers-van Gogh, Daniele Guardavaccaro, Roeland M.H. Merks, Jeroen Bakkers, Nodal Signaling Range Is Regulated by Proprotein Convertase-Mediated Maturation (2015) Developmental Cell 32(5): 631-639

Abstract

Morphogens that diffuse through tissues drive tissue patterning. In many animal species, left-right patterning is governed by a reaction- diffusion system relying on the different diffusivity of an activator, Nodal, and an inhibitor, Lefty. In a genetic screen, a zebrafish loss of function mutant for the proprotein convertase FurinA was identified. The Spaw protein in zebrafish is a Nodal-related proprotein and is able to induce its own expression trough extracellular signaling. Embryological and biochemical experiments demonstrate that FurinA cleaves the Nodal-related Spaw proprotein into a mature form. This mature form can then be secreted and diffuse, allowing for long range Nodal signaling. We developed a model that describes inter and extracellular Nodal dynamics and included cleavage by FurinA. This mathematical shows that FurinA is required for Spaw gradient formation. The model suggests that the speed of gradient formation and the range of Spaw signaling is regulated by FurinA, which is validated by *in vivo* experiments. Finally, the model suggests that the effect of FurinA saturates with increasing levels of FurinA. This study shows that tissue patterning, such as left-right patterning, can be regulated by proprotein convertases.

5.1 Introduction

In the previous chapters, we focused on how mechanical forces can drive tissue patterning. Cells sense and respond to mechanical forces that are present in the extracellular matrix. However, cells also respond to chemical signals from the extracellular matrix. For decades, tissue patterning has been thought to be mainly regulated by morphogens, chemical signals or growth factors diffusing through the extracellular space, that affect the gene transcription of cells. In this chapter, we focus on how chemical signaling is involved in the left-right patterning of tissues. During embryogenesis, an asymmetry between the left and right part of the body is established. This left-right (LR) assymetry is crucial for the formation, positioning and function of organs [260]. During somitogenesis, the vertebrate LR axis is patterned by the interplay of Nodal and its repressor Lefty [261, 262]. Nodal and Lefty form a activator/inhibitor pair and have different diffusivities, activation ranges. As such, the pair behaves as a reaction-diffusion model for tissue patterning. Lefty inhibits the expression of Nodal and Nodal induces its own expression. An initial assymetry between left and right, caused by the accumulation of Nodal in the left lateral plate mesoderm (LMP) (due to cilia-induced flow in the node), is amplified by the Nodal/Lefty interactions [260]. Since Lefty acts on a long range, the expression of Nodal is repressed in the right side of the body.

Nodal is an extracellular protein that induces its own gene expression, by signaling through cell membrane receptors. Nodal protein can only be secreted by cells once it matures, which is regulated by proprotein convertases such as Furin. In this chapter, we focus on the model system zebrafish to study the signaling range of Nodal. In

zebrafish, the Nodal gene southpaw (Spaw) is required for LR patterning. At early somatogenesis, Spaw expression is initiated around the posteriorly localized Kupffer's vesicle, which is the functional homolog to the mouse's node [263]. Experimental studies on the ace of hearts (aoh), a zebrafish mutant for the proprotein convertase FurinA, shows that Spaw acquires its biological activity and signaling range via FurinA-mediated maturation. A combination of *in vivo* and *in silico* experiments shows that the level of FurinA expression in the zebrafish embryo controls the signaling range of Spaw.

5.1.1 Zebrafish aoh mutant

Tessadori *et al.* [97] identified a zebrafish mutant that displayed a defect in left-right patterning; it had a midline-positioned cardiac tube, which is normally located at the left side. This mutant is called the aoh mutant. For more details, we refer to the original paper [97]. In this chapter, we only describe the most relevant observations for the mathematical modeling. The left-right defect was due to a reduced expression of the gene Spaw in the LPM (Figure 5.1). But what characteristic of this mutant affected the signaling range of Spaw?

It was determined that aoh mutants carry a point mutation resulting in a premature truncation of the FurinA subtilisin-like proprotein convertase (SPC). Furin is part of a larger family of SPCs, which are crucial for conferring biological functionality to a wide variety of substrates including growth factors belonging to the Tgf-β superfamily [264, 265]. To confirm that the lack of FurinA is responsible for reduced Nodal signaling, additional experiments were performed. This showed that FurinA can cleave Nodal and that the *in vitro* addition of Furin protein resulted in the efficient cleavage of Spaw. By *in vivo* mutation of cleavage sites of Spaw, it was shown that if Furin could not cleave Spaw, the function of Spaw was abrogated.

5.1.2 The role of FurinA

Studies showed that Spaw induces the activity of Spaw [266] and that Spaw acts on a long range [97]. Furthermore, it was shown that the cell-autonomous cleavage of Spaw by FurinA is required for this long range signaling [97]. Localization of Spaw maturation by FurinA correlates positively with extracellular Spaw localization and thus mediates the formation of an extracellular Spaw gradient [97]. To understand how FurinA processing of Spaw controls the establishment of the Nodal signaling domain in the LPM during LR patterning, we developed a mathematical model.

5.2 Model description

The mathematical model considers the intercellular and extracellular Spaw protein dynamics and their interactions in a 1D domain. The domain represents an embryonic

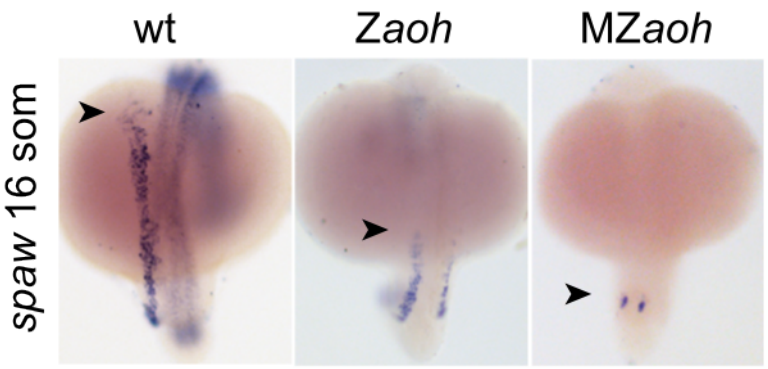

Figure 5.1: Expression of Spaw (arrowhead indicates anterior-ward expansion) in WT, Zaoh, and MZaoh embryos.

tissue, where $x = 0$ corresponds to the source of Nodal and $x = L$ represents the boundary of the relevant tissue.

The model is given by the following reaction-diffusion system

$$\frac{\partial S_i}{\partial t} = \underbrace{cm_e \frac{\frac{S_e}{h_e}}{1+\frac{S_e}{h_e}}}_{\text{production}} - \underbrace{\epsilon_i S_i}_{\text{degradation}} - \underbrace{kFS_i}_{\text{maturation}}, \tag{5.1}$$

$$\frac{\partial S_i^m}{\partial t} = \underbrace{kFS_i}_{\text{maturation}} - \underbrace{\epsilon_i^m S_i^m}_{\text{degradation}} - \underbrace{sS_i^m}_{\text{secretion}}, \tag{5.2}$$

$$\frac{\partial S_e}{\partial t} = \underbrace{D\nabla^2 S_e}_{\text{diffusion}} - \underbrace{\epsilon_e S_e}_{\text{degradation}} + \underbrace{sS_i^m}_{\text{secretion}}, \tag{5.3}$$

with boundary conditions,

$$\frac{\partial S_e}{\partial x}(x = L, t) = 0, \tag{5.4}$$

$$D\frac{\partial S_e}{\partial x}(x = 0, t) = -P, \tag{5.5}$$

and initial conditions,

$$S_i(x, t = 0) = 0, \tag{5.6}$$

$$S_i^m(x, t = 0) = 0, \tag{5.7}$$

$$S_e(x, t = 0) = 0. \tag{5.8}$$

Here, $S_i(x,t)$, $S_i^m(x,t)$ and $S_e(x,t)$ denote the concentration (in molecules/liter) of synthesized intercellular Spaw, mature intercellular Spaw and extracellular Spaw, re-

spectively. The model takes into account that the extracellular Spaw diffuses with diffusion coefficient D (m^2s^{-1}) and degrades with an extracellular clearance rate of ϵ_e (s^{-1}). Further, the intracellular Spaw degrades with an intercellular clearance rate of ϵ_i (s^{-1}) and ϵ_i^m (s^{-1}) for its mature form. The mature form of Spaw is secreted with a rate s (s^{-1}). Spaw only spreads between cells through the extracellular space, so there is no diffusion of $S_i(x,t)$ or $S_i^m(x,t)$. We assume that FurinA promotes the maturation of Spaw. This is represented by the term kFS_i, present in both of the intercellular Spaw equations. Here, F is the concentration of FurinA (molecules/liter) and k is a constant. We thus assume that the rate of maturation, which is kF (s^{-1}), is linearly dependent on the level of FurinA.

The model describes the production of intercellular Spaw, at a maximum of cm_e (s^{-1} molecules/liter), in response to the cells' binding of extracellular Spaw. We assume that this activation of intercellular protein production becomes saturated when the level of $S_e(x,t)$ increases, as then the number of receptors sensing the extracellular Spaw depletes. This is indicated by the Michaelis-Menten kinetics function, where m_e and h_e are constants. More specifically, m_e is the extracellular Spaw concentration at which all Spaw receptors of the cells are occupied and h_e is the extracellular Spaw concentration at which the synthesis activation rate is at half-maximum.

The boundary condition at $x = L$ reflects the fact that extracellular Spaw can not leave the tissue. At $x = 0$, we assume a constant influx of P (molecules s^{-1} m^{-2}) of extracellular Spaw. As initial conditions, we assumed $S_e(x,t) = S_i(x,t) = S_i^m(x,t) = 0$; that is, at no extracellular or intracellular Spaw is present anywhere in the domain.

5.3 Results

The results and comparison with *in vivo* data of the mathematical model are shown in Figure 5.2; the mathematical equations are shown in Figure 5.2). In brief, in this one-dimension reaction-diffusion model (Figures 5.2A and 5.2B), the maturation of Spaw is controlled by FurinA processing. Once processed, Spaw is secreted and forms an extracellular gradient. Extracellular mature Spaw diffuses to surrounding cells, where it binds to its receptor and stimulates the production of intracellular Spaw. Both intracellular and extracellular Spaw are assumed to be degraded according to first order kinetics, *i.e.*, due to proteolysis independent of Spaw or FurinA.

5.3.1 FurinA expression levels controls speed and range of Spaw gradient formation

The model produces a front of extracellular, mature Spaw protruding into the LPM, with a propagation speed that is enhanced by the level of FurinA. In Movie S1, snapshots of which are shown in Figure 5.2D, the faster propagation of extracellular Spaw resulting from an increase in FurinA levels can be appreciated. The mathematical model predicts that the distance reached by a specific amount of extracellular Spaw within a given time is a function of FurinA levels (Figure 5.2E). Due to its self-

inducing activity, we used the Spaw expression domain as a readout for extracellular Spaw activity *in vivo*. With increasing FurinA levels, the model predicts an increasing anterior extension of the Spaw expression domain at a given developmental stage. To test this prediction *in vivo*, we determined the signaling range of Spaw in the LPM by measuring the length of the Spaw expression domain in embryos with different levels of FurinA (Figure 5.2F). First, we compared the Spaw expression domain in embryos with no FurinA (MZaoh mutant), low levels of FurinA (Zaoh), and normal FurinA expression (wild-type [WT] embryos). In agreement with the prediction of the mathematical model, we observed that the Spaw expression domain in the LPM was absent in the MZaoh mutant embryos, while the extension of the Spaw expression domain was limited in Zaoh mutant embryos, which is consistent with its expression in the posterior, but not in the anterior LPM.

Next, we examined whether increasing FurinA levels in WT embryos would be sufficient to expand the signaling range of Spaw even further in the anterior direction, as the mathematical model predicts. Since endogenous FurinA is broadly expressed at early developmental stages and during somitogenesis [267], we overexpressed FurinA in all cells by mRNA injection into WT embryos and determined the anterior-posterior length of the Spaw expression domain. We observed that increasing FurinA was sufficient to induce an expansion of the signaling range of Spaw (Figure 5.2F). Interestingly, increased FurinA expression levels resulted not only in faster expansion of Spaw expression toward the anterior LPM, but also in an increased incidence of bilateral Spaw expression and the appearance of right-sided Spaw expression in the LPM. This could be the consequence of the saturation of the midline barrier and of the activity of a self-enhancement lateral-inhibition system, as described for mouse Nodal and Lefty [268] (Figure 5.2F; see Nakamura *et al.*, 2006). Altogether, we conclude that the level of FurinA determines the signaling range of Spaw in the LPM, which is critical for the establishment of correct LR patterning of the embryo.

5.3.2 Signaling range saturates by increasing level of FurinA

Increasing FurinaA levels, F in the model, leads to an increase of extracellular Spaw, as its promotes maturation of Spaw that can subsequently be secreted. The amount of Spaw maturation depends on the production rate of intercellular Spaw, so the effect of increasing F is likely limited. In order to better understand the effect of F, we linearized the original model to

$$\frac{\partial S_i}{\partial t} = cS_e - \epsilon_i S_i - kFS_i, \tag{5.9}$$

$$\frac{\partial S_i^m}{\partial t} = kFS_i - \epsilon_i^m S_i^m - sS_i^m, \tag{5.10}$$

$$\frac{\partial S_e}{\partial t} = D\nabla^2 S_e - \epsilon_e S_i + sS_i^m, \tag{5.11}$$

with the same boundary conditions and initial conditions as described in the model formulation given in the methods section.

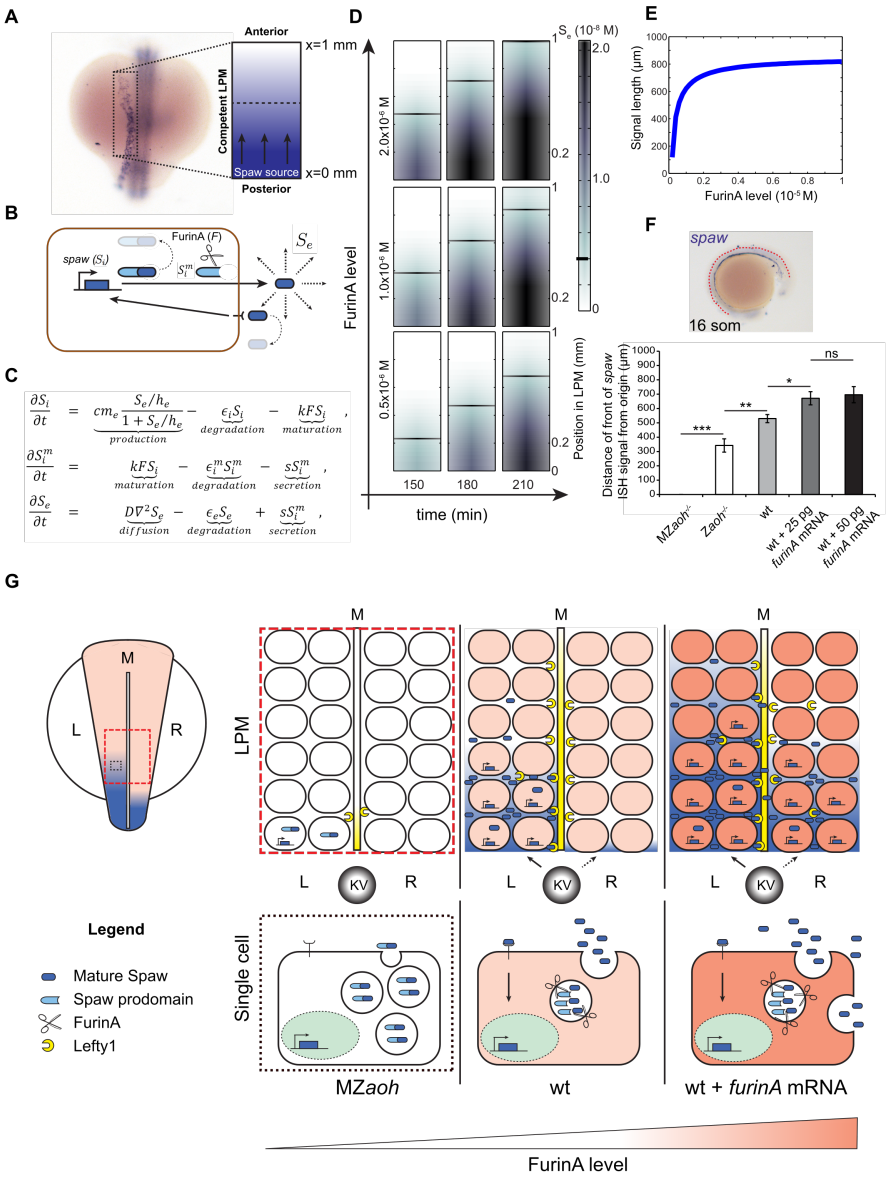

Figure 5.2: Caption is on next page

Caption of figure on previous page: FurinA Levels Control the Expansion of the Spaw Expression Domain in the LPM. (A and B) For the purpose of mathematical modeling, we have considered the left LPM of the developing zebrafish embryo as a linear domain (displayed as a rectangle here) with a source of Spaw at the posterior end (x = 0); (B) behavior of Spaw in the competent LPM described in (A). Synthetized intracellular Spaw (S_i), mature intracellular Spaw (S_i^m), and extracellular Spaw (S_e). (C) Partial-differential equation model of the system described in (B). (D) Snapshots of Movie S1 showing a simulation of the model defined in (C). The speed of progression of Se, and consequently of the domain of Spaw expression in the LPM, increases with the level of FurinA. (E) The model predicted that increasing FurinA levels, resulting in enhanced maturation of Spaw, results in increased length of the Spaw expression domain at a given time (180 min here). (F) Quantification of the length of the Spaw expression domain (anterior-posterior) in embryos with no (MZaoh; n = 12), low (Zaoh mutants; n = 7), normal (WT; n = 15), or high (WT injected respectively with 25 pg; n = 25 and 50 pg; n = 17 FurinA mRNA) FurinA levels. Histograms display average value Âś SEM; *p < 0.05, **p < 0.01, and ***p < 0.005 in Student's t test. (G) Cartoon illustrating the effect of FurinA on the signaling range of Spaw in the LPM. In a WT situation, Spaw is cleaved prior to secretion by cells at the posterior end of the LPM (10 somite stage, 13 hpf). Spaw induces its own expression in a paracrine fashion, and the Spaw expression domain expands toward the anterior end of the developing LPM, reaching the heart field at the 23-somite stage (20 hpf). Spaw also induces expression of *Lft1* at the midline, which prevents it from reaching the right LPM. Spaw expression is consequently limited to the left LPM and establishes LR patterning. In the MZaoh mutants, the absence of FurinA processing of Spaw results in failure to induce Spaw expression in the LPM and of *Lft1* in the midline. As a consequence, LR patterning is affected. Overexpression of FurinA results in increased presence of mature Spaw in the extracellular space. The activation of Spaw in the LPM progresses faster toward the anterior left LPM. LR patterning is affected, likely as a result of an excess of Spaw protein overcoming the Lft1 midline barrier, Kupffer's Vesicle (KV) and midline (M).

Let us first consider the steady state solution, which is obtained by solving

$$\frac{\partial S_i}{\partial t} = 0, \tag{5.12}$$

$$\frac{\partial S_i^m}{\partial t} = 0, \tag{5.13}$$

$$\frac{\partial S_e}{\partial t} = 0, \tag{5.14}$$

or,

$$cS_e - \epsilon_i S_i - kFS_i = 0, \tag{5.15}$$

$$kFS_i - \epsilon_i^m S_i^m - sS_i^m = 0, \tag{5.16}$$

$$D\nabla^2 S_e - \epsilon_e S_e + sS_i^m = 0. \tag{5.17}$$

This can be rewritten to

$$D\nabla^2 S_e + \alpha S_e = 0 \tag{5.18}$$

with simply

$$S_i(x) = \frac{c}{\epsilon_i + kF} S_e(x), \tag{5.19}$$

$$S_i^m(x) = \frac{kF}{\epsilon_i^m + s} S_i(x). \tag{5.20}$$

Here, α is given by $\alpha = \frac{sc}{\epsilon_i^m + s} \frac{kF}{\epsilon_i + kF} - \epsilon_e$.
The case $\alpha > 0$ represents a system where the production of Spaw exceeds Spaw's extracellular degradation rate. This implies that no steady state exists. Thus, for high values of c, the level of extracellular Spaw will increase indefinitely in the linear model. For this reason, we take this case out of consideration in this analysis. We also omit the case $\alpha = 0$, because it can generally only be obtained when $\epsilon_e = 0 \wedge (c = 0 \vee s = 0 \vee F = 0)$, which are all irrelevant cases, because then only diffusion of extracellular Spaw is present. For $\alpha < 0$, we obtain the steady state solution

$$S_e(x) = C_1 \exp(-\sqrt{|\alpha|/D}x) + C_2 \exp(\sqrt{|\alpha|/D}x), \tag{5.21}$$

where C_1 andC_2 are constants of integration. These constants are given by the prescribed boundary conditions. We find the following expressions for the constants C_1 and C_2:

$$C_2 = \frac{\frac{-P}{D}}{\sqrt{|\alpha|/D}} + C_1, \tag{5.22}$$

$$C_1 = -\left(\frac{\frac{-P}{D}}{\sqrt{|\alpha|/D}}\right) \cdot \frac{\exp(\sqrt{|\alpha|/D})}{\exp(\sqrt{-|\alpha|/D}) - \exp(\sqrt{|\alpha|/D})}. \tag{5.23}$$

Note that in order to have $\alpha < 0$ for all values of F, we need that $c < \epsilon_e$. Figure 5.3 shows the steady states for $c = 90 \cdot 10^{-6}, \epsilon_e = 100 \cdot 10^{-6}$ and a range of values for F. The extracellular Spaw concentration in the domain correlates positively with the level of FurinA. To get an idea of how exactly the total concentration reached in the domain, is influenced by F, we consider the total amount of extracellular Spaw in the system at time t [269], which is given by

$$N_e(t) = \int_0^{x=L} S_e(x,t)dx. \tag{5.24}$$

Analogously, let the total amount of intercellular Spaw be denoted by

$$N_i(t) = \int_0^{x=L} S_i(x,t)dx, \tag{5.25}$$

$$N_i^m(t) = \int_0^{x=L} S_i^m(x,t)dx. \tag{5.26}$$

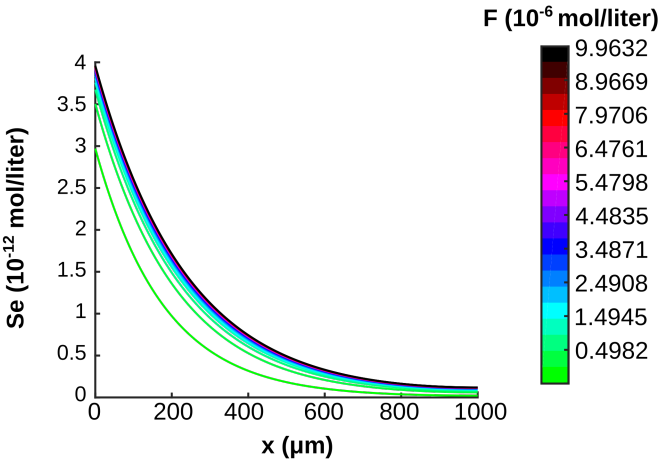

Figure 5.3: Steady state extracellular Spaw (S_e) concentration gradients over domain x = [0, 1000 μm] as a function of FurinA (F) concentration (color bar)

Now,

$$\frac{dN_e}{dt} = \int_0^{x=L} \frac{\partial S_e}{\partial t} dx, \tag{5.27}$$

$$= D \int_0^{x=L} \nabla^2 S_e dx - \epsilon_e \int_0^{x=L} S_e dx + s \int_0^{x=L} S_i^m dx, \tag{5.28}$$

$$= D[\nabla S_e]_0^{x=L} - \epsilon_e N_e(t) + s N_i^m(t), \tag{5.29}$$

$$= P - \epsilon_e N_e(t) + s N_i^m(t), \tag{5.30}$$

and similarly,

$$\frac{dN_i}{dt} = cN_e(t) - (\epsilon_i + kF)N_i(t) \tag{5.31}$$

$$\frac{dN_i^m}{dt} = kFN_i(t) - (\epsilon_i^m + s)N_i^m(t) \tag{5.32}$$

In steady state we have that

$$\frac{dN_e}{dt} = 0, \tag{5.33}$$

$$\frac{dN_i}{dt} = 0, \tag{5.34}$$

$$\frac{dN_i^m}{dt} = 0, \tag{5.35}$$

or,

$$P - \epsilon_e N_e(t) + sN_i^m(t) = 0, \tag{5.36}$$

$$cN_e(t) + (\epsilon_i + kF)N_i(t) = 0, \tag{5.37}$$

$$kFN_i(t) + (\epsilon_i^m + s)N_i^m(t) = 0, \tag{5.38}$$

which gives the following expression for $N_e(t)$

$$N_e(t) = \frac{-P}{\frac{sc}{\epsilon_i^m+s}\frac{kF}{\epsilon_i+kF} - \epsilon_e} = \frac{-P}{\alpha}. \tag{5.39}$$

This shows that a higher F implies a higher total amount of extracellular Spaw in steady state condition (as we assumed that $\alpha < 0$). However, this influence of F saturates with increasing levels of FurinA. This can be explained by the following observation: $lim_{F\to\infty}\alpha = lim_{F\to\infty}\frac{sc}{\epsilon_i^m+s}\frac{kF}{\epsilon_i+kF} - \epsilon_e = \frac{sc}{\epsilon_i^m+s} - \epsilon_e$, indicating that increasing F will ultimately not change the system behavior. Increasing FurinA only helps to increase the extracellular Spaw to a certain point, as it is limited by the intercellular production rate. Notably, the magnitude of the effect of Fon the system depends on the value of c. The higher the c, the larger the effect of F. In other words, with a lower value for c , the convergence due to F is faster. This is because how much Spaw is produced within the cell, limits the amount of mature Spaw. In conclusion, by regulating the maturation of intercellular Nodal, FurinA regulates the signaling range of Nodal. Increasing FurinA increases the signaling range, upto a maximum range determined by the maximum rate of intercellular production of Nodal.

5.4 Discussion

Based on experimental studies we developed a model that shows that cleavage of the Nodal-related Spaw proprotein into a mature form by FurinA is required for the formation of an extracellular Spaw gradient. In this model, extracellular Spaw induces intercellular Spaw production, which is cleaved by FurinA into a mature form that can be secreted and diffuse through the extracellular matrix. This diffusion allows for long range cell-cell signaling. In the absence of FurinA, this signaling can not take place. Increasing FurinA speeds up gradient formation and creates a longer signaling range, which has been validated with *in vivo* experiments. The model suggests that this positive effect of FurinA saturates, as the production of intercellular Spaw is bounded by the number of Spaw receptors that enable extracellular Spaw signaling. This study shows that proprotein convertase FurinA is essential for Spaw signaling, which in turn is essential for correct establishment of LR patterning and organ laterality.

We demonstrated how FurinA acts as a regulator of LR patterning by controlling the signaling range of Spaw. Signaling ranges are typically controlled by diffusion and reaction. This work suggests a new mechanism that also controls extracellular gradient formation: the maturation of intercellular proteins.

5.5 Supplementary methods

5.5.1 Numerical analysis

For the numerical simulations, we used a backward Euler scheme in time and a second-order central difference scheme in space, with spatial discretization sizes of $\Delta x = \frac{L}{1000}$ and time steps of $\Delta t = 15s$. The simulation ends when time t_{end} is reached. In order to evaluate the time it takes for the system to reach a given state, we need to define a position in the domain, denoted by x_{signal}, at which we test if the concentration of extracellular Spaw exceeds a threshold level of extracellular Spaw, $S_e^{threshold}$. So, more specifically, we determine $t_{\text{signal}}(x) = min\{t : S_e(x_{\text{signal}}, t) > S_e^{\text{threshold}}\}$. We also identify how far the signal has extended at each point in time, as $x_{\text{signal}}(t) = min\{x : S_e(x, t) < S_e^{\text{threshold}}\}$. These measures help illustrate how FurinA speeds up the extracellular Spaw propagation.

5.5.2 Parameter value estimation

Values for parameters were either adopted from literature, or estimated based on our data. The parameter values are given in Table 5.1. The length of the tissue and the simulation duration is based on our data. The parameters D and ϵ_e are chosen according to values for the protein Squint as described in [270], because Spaw protein dynamics are comparable to Squint. The constant k, a measure of how efficiently FurinA converts Spaw into its mature form, is assumed to be 10^{-4} s^{-1} liter/mol, which is comparable to typical values for various enzymes [271]. The concentration of FurinA in the system was estimated using our data as follows. We consider an injection of 25 pg of FurinA mRNA in 200 nl and assume a translational efficiency of 10^3 [272], which gives us a FurinA protein concentration of 10^{-6} mol/liter. The influx P of extracellular Spaw was estimated based on HER2 secretion rates in [273]. Here, 1500 pg of HER2 was secreted into 1 ml of medium by $3 \cdot 10^5$ mammalian cells in 24 hours. We assume that the secreted protein is transported over at membrane of one spherical cell with radius $5\mu m$. With these values, we obtain an influx of in the order of 10^{-8} mol m^{-2} s^{-1} The values for h_e and m_e were estimated based on the lower range of the concentrations of signaling molecules, of around 10 nM (BioNumbers.org). The $S_e^{\text{threshold}}$ was chosen such that this threshold could not be reached in the absence of FurinA, in correspondence to the experiments. The parameters s and ϵ_i^m were given the same value as ϵ_e. The parameters ϵ_i and c were chosen such that the time it takes for the modeled system to reach a certain state in the presence of FurinA is similar to our data. To be more specific, these parameters were chosen such that after 180 min, the signal is roughly between 0 and 700 μm and the time it takes for the signal to reach 1000 μm is roughly between 180 and 360 min. Within the limits identified using the theoretical analysis of the linearized model, however, the overall behavior of the non-linear system described here does not depend on the specific choice of parameter values. Further, we would like to point out that we assume a round number

of molecules for a number of parameters. We divide these by Avogadro's number, yielding the non-intuitive molarity values.

5.6 Supplementary tables

parameter	description	value	unit
Δx	Spatial discretization stepsize	1	µm
Δt	Time discretitazion stepsize	15	s
L	Length of tissue	1000 (data)	µm
t_{end}	Simulation end	360 (data)	min
D	Diffusion coefficient	3.2 [270]	$\mu m^2\ s^{-1}$
ϵ_e	Extracellular clearance rate	$1 \cdot 10^{-4}$ [270]	s^{-1}
ϵ_i	Intercellular clearance rate	$75 \cdot 10^{-4}$	s^{-1}
ϵ_i^m	Intercellular clearance rate for mature form	$1 \cdot 10^{-4}$	s^{-1}
c	Synthesis activation rate	$200 \cdot 10^{-4}$	s^{-1}
s	Secretion rate	$1 \cdot 10^{-4}$	s^{-1}
k	Constant that relates level of FurinA to rate of Spaw maturation	10^4 [271]	s^{-1}liter/mol
F	FurinA concentration	ranges from 0 to $5{\cdot}10^{-6}$ (data, [272])	mol/liter
h_e	Extracellular Spaw concentration at which the synthesis activation rate is at half-maximum	$4.15 \cdot 10^{-10}$	mol/liter
m_e	Concentration of extracellular Spaw at which all Spaw receptors of the cells are occupied	$8.3 \cdot 10^{-10}$	mol/liter
P	Extracellular Spaw flux	$1.66 \cdot 10^{-8}$	mol $m^{-2}s^{-1}$ [273]
$S_e^{\text{threshold}}$	Signalling threshold	$4.15 \cdot 10^{-10}$	mol/liter

Table 5.1: Parameter settings.

5.7 Supplementary videos

Video S1 shows numerical simulations of the progression of extracellular Spaw (S_e) and, subsequently, of the domain of spaw expression in the LPM, in the presence of increasing levels of FurinA. It can be found at `http://dx.doi.org/10.1016/j.devcel.2014.12.014`

6

Autocrine Inhibition of Membrane Ruffling Drives Branching Morphogenesis

This chapter is based on:

Rens, Elisabeth G., Zeegers, Mathé T. and Merks, Roeland M.H. (2018) Autocrine Inhibition of Membrane Ruffling Drives Branching Morphogenesis (in preparation).

Abstract

Branching morphogenesis, the emergence of tree-like structures in organs such as lungs, kidneys and the mammary gland, has been the subject of many *in vitro* and *in silico* experiments. Branching morphogenesis involves many mechanisms, such as cell proliferation, differentiation and migration and is regulated by a network of signaling factors. In this work, we aim to explain how an epithelial tissue can branch autonomously; without cell proliferation and in the absence of signaling from the surrounding mesenchymal tissue. *in vitro* evidence suggests that branching sites are regulated in a curvature dependent manner by an autocrine inhibitory signal that diffuses through the matrix and locally inhibits cell protrusions. Based on this hypothesis, we developed a multiscale cellular Potts model. Using this model, we show that autocrine inhibition of cell protrusions is sufficient to induce branching morphogenesis. The model suggests that the autocrine signal accumulates at concave tissue boundaries, so that cell extensions are more preferable at convex sites. This curvature effect initiates a positive feedback loop where convex sites become even more convex, allowing even more extensions which results in a fully branched structure.

6.1 Introduction

During the development of organs such as lungs, kidneys and the mammary gland, epithelial tissues undergo shape changes during embryonic development resulting in a tree-like structure of branches [274, 275]. The function of branched tissues is to optimize the exchange of chemicals with the surrounding tissue by maximizing its surface. The dynamics of branching from an initially tube shaped epithelial tissue, called the duct, into the surrounding mesenchymal tissue involves involves many cellular mechanisms such as directed cell migration, oriented cell division, cell shape changes, cell differentiation and cell competition (see reviews [276–278]). The specific process of branching morphogenesis varies per organ, but the key mechanisms are believed to be conserved [279, 280]. Although the dynamics of branching in various organs have been characterized well (see for instance, lung: [281], kidney: [282], mammary gland: [283], pancreas [284]), it is still poorly understood what drives branching morphogenesis and which mechanisms are necessary or merely instructive.

For a long time, it was thought that localized cell proliferation is the main driving factor of branching, but more recent experimental data indicate that this is not always true (for review see Ref. [277]). Branches have been observed to initiate and extend prior to the localization of cell proliferation [217, 285]. Signaling factors from the mesenchyme have also been proposed to drive branching [286]. However, the mesenchyme is not required either, as epithelial tissues can branch in the absence of a surrounding mesenchyme *in vitro* [287–289]. In conclusion, it is still poorly understood how epithelial tissues branch autonomously in the absence of cell proliferation and the mesenchyme. Here we propose a cellular mechanism for such autonomous branching of epithelial tissues.

Previous models were often based on tissue growth. They employed known, physical principles of branching growth. It has been thus proposed that epithelial branching can be described by Laplacian growth models. Laplacian growth underlies branching in many non-biological systems, like crystal growth [290] and viscous fingering [291]. In Laplacian growth, the interface of a domain advances with a velocity proportional to the gradient of a field that obeys the Laplacian equation (in quasi-steady state) ($\nabla^2 u = 0$), *i.e.* is dominated by diffusion [292], with $u = 0$ at the interface. Positive curvatures, that arise due to small deviations from a initially homogeneous boundary, experience a higher gradient of the Laplacian field and thus will advance. This curvature effect is then enhanced and the initial deviations advance further. This is known as the Mullins-Sekerka instability that causes branching. In viscous fingering [291], for instance, water is injected into oil between two parallel flat plates. As water is less viscous then oil, the pressure between the two substances makes the water branch out into the oil. It has been proposed that epithelial branching resembles viscous fingering. A mathematical model showed that an epithelial tissue branches into the surrounding mesenchyme if the mesenchyme is less viscous than the luminal fluid in the epithelium [293]. Biological branching has also been proposed to be driven by diffusion limited aggregation (DLA), a concept that is mathematically very similar to Laplacian growth [294]. It was proposed that branching patterns of bacterial colonies are governed by DLA of nutrients [295]. Similarly, it has been suggested that a tumor branches out as proliferating cells consume oxygen [296] and that an epithelial tissue can branch by consuming fibroblastic growth factor (FGF) that upregulates cell proliferation [297].

Other mathematical models proposed that patterns of stimulatory growth factors from the mesenchyme can drive branching by locally upregulated cell proliferation. These models are based on experimental observations that suggest that in the developing lung bud, the position and levels of FGF10 are associated with the mode of branching [298]; domain/lateral branching, planar bifurcation and orthogonal bifurcation [281, 286]. Hirashima *et al.* [299] developed a reaction-diffusion model including FGF10 signaling in the mesenchyme which is inhibited by TGF-β and SHH and activated by SHH. This model suggests that the pattern of FGF10 and thus the mode of branching depends on the curvature of the lung bud, like in Laplacian models. Menshykau *et al.* [300] extended the reaction-diffusion model by including FGF10 induced SHH production in epithelial cells. Furthermore, binding of SHH to its receptor both up-regulates the expression of this receptor and upregulates FGF10 expression in the mesenchyme. During simulated bud growth, the curvature of the domain increases, which causes a localized spot of FGF10 at the tip of the bed. The models suggests that the SHH ligand-receptor interactions allows the localized spots to stabilize. By letting the growth rate of the tissue domain depend on the level of ligand-receptor signaling, it was shown that the tissue branches out [301]. In many branched organs, there are homologies of FGF10 and SSH that drive branching [277] and the ones involved in branching of the kidney have been shown to produce a similar Turing mechanism as in lung [302]. So, it has been suggested that an intricate signaling network between

the epithelium and mesenchyme results in a pattern of growth factors, which drives branching by locally upregulating tissue growth.

Another class of models asked how stereotypic rules for branching splitting determines the architecture of the whole organ. A model that describes branching by chemotaxis towards a growth factor, showed that the number of branches depends on the ratio between the proliferation rate and the chemotaxis speed [303]. Another modeling paper proposed that branch splitting is controlled by an inhibitory signal produced by the epithelium [304]. In this model, it was assumed that a branch bifurcates if the inhibitory signal is below a certain threshold, resulting in a network of branches that avoid each other similar to experimental data [304].

Because there is increasing experimental evidence that inhibitory signals and not stimulatory growth factors are associated with sites of branching [98, 305, 306], mathematical models have explored the role of inhibitory signals. Two different models have suggested that an autocrine signal can drive branching by locally inhibiting tissue growth. One modeling paper argued that the displacement field of a modeled growing domain more accurately fitted to experimental data if an autocrine signal inhibited, instead of stimulated, tissue growth [307]. A cell-based model suggests that a tissue branches due to a curvature effect on an autocrine signal that inhibits cell proliferation [308]. Due to diffusion, the autocrine inhibitor accumulates at concave tissue boundaries, such that cell proliferation occurs at a higher rate at convex tissue boundaries.

Our model is based on *in vitro* observations that suggest a mechanism by which mammary epithelial gland cells can branch out autonomously [98]. In this experimental study by Nelson *et al.* [98] it was asked how branching sites are determined. They embedded mammary epithelial cells in cavities with a specific geometry in 3D collagen gels, to study the extent of sprouting into the surrounding collagen gel. By varying the geometry, it was found that cell protrusions into the surrounding gel were most frequent at sites where the geometry was convex. It was hypothesized that an autocrine signal determines these sites of branching, but it was not known what molecule this could be. A numerical model describing a constant flux of a signal from the tissue (s) and its diffusion (D) and degradation (ϵ) in the matrix ($\frac{\partial c}{\partial t} = D\nabla^2 c - \epsilon c + s$) showed that the autocrine signal accumulated at concave boundaries and that its concentrations negatively correlated with the rate of *in vitro* cell movement. *In vitro* disruption and overexpression of TGF-β caused cell movements to appear or disappear throughout the tissue boundary, respectively. This suggests that TGF-β is responsible for the observed curvature dependent cell movement. Because cell movement and not tissue growth depends on the curvature, this mechanism is conceptually different from Laplacian growth.

We introduce a cellular Potts model to study if such autocrine inhibition of cell movement is sufficient to drive branching morphogenesis. We assume that local concentration of the autocrine signal inhibits cell protrusions at the boundary of the tissue. This model thus suggests that a tissue branches as a result of a curvature effect on cell

movement caused by diffusion and degradation of an autocrine signal in the matrix. In the model the autocrine signal accumulates at concave areas, allowing extensions to occur around the convex areas. Then, the tissue can branch further because tissue extensions at the convex sites makes the tissue more convex (which increases accumulation of the inhibitor at concave areas), making extensions at convex sites even more preferential. The model also suggests that the initiation and speed of branching is regulated by the extent of random motility of cells. Furthermore, the model suggests there is an optimal level of autocrine signaling that promotes branching and that lower surface tensions in our model induces branching.

6.2 Results

Experimental observations suggest that cell protrusions are inhibited by the local concentration of TGF-β [98]. It was hypothesized that diffusion of autocrine TGF-β drives curvature dependent sites of branching [98]. To test if this mechanism suffices to drive epithelial branching, we developed a coupled cell based - continuum model. A framework of this model is given in Figure 6.1. For more details of the model, we refer to the methods section. We model a tissue with the cellular Potts model (CPM) (Figure 6.1A), which describes cells as a collection of lattice sites on a 2D square lattice. So, each lattice site $\vec{x}$ is assigned a spin $\sigma(\vec{x}) \in \mathbb{Z}^{\{0,+\}}$ that describes which cell occupies this lattice site. The spin is assigned value 0 if the medium that surrounds the tissue occupies this site. Cells in the CPM move by making protrusions and retractions. The tissue evolves in time by a Monte Carlo simulation. At each Monte Carlo Step (MCS), a number of N movements are attempted, where N is the number of lattice sites. A movement is defined as copying the spin of a lattice site $\sigma(\vec{x})$ to a neighbouring lattice site $\vec{x}'$. Such a movement is accepted or declined based on a Hamiltonian H that describes the forces acting on the cells:

$$H = \sum_{(\vec{x},\vec{x}')} J(\sigma(\vec{x}), \sigma(\vec{x}'))\mathbf{1}_{\sigma(\vec{x})\neq\sigma(\vec{x}')} + \lambda \sum_{1\leq\sigma\leq n} (a(\sigma) - A_{\text{target}}(\sigma))^2. \tag{6.1}$$

In the first term $(\vec{x}, \vec{x}')$ is a pair of adjacent lattice sites and J the adhesion energy between two lattice sites [1]. The first term approximates a surface tension of the tissue. The second term describes a conservation of cell area. Here, $a(\sigma)$ denotes the area of cell σ and $A_{\text{target}}(\sigma)$ is the target area of cell σ. The parameter λ indicates the strength of this area constraint.

By making a movement, the Hamiltonian of the system changes by ΔH. We assume that the concentration of a diffusive signal inhibits cell protrusions into the surrounding medium. We model this by adding an extra term to the change in the energy (Hamiltonian) of the system:

$$\Delta\hat{H} = \Delta H + \chi \cdot c(\vec{x}') \cdot \mathbf{1}_{\sigma(\vec{x})>0} \cdot \mathbf{1}_{\sigma(\vec{x}')=0} \tag{6.2}$$

[1] The indicator function is defined as $\mathbf{1}_A = \begin{cases} 1 & \text{if } A \text{is true} \\ 0 & \text{if } A \text{is false} \end{cases}$

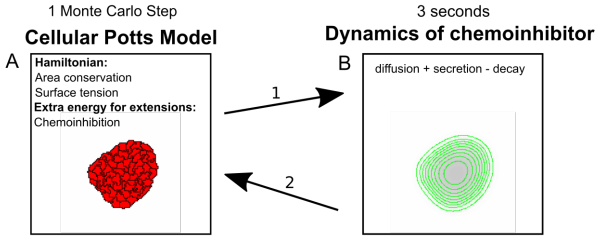

Figure 6.1: Flowchart of the model. (A) CPM calculates cell movement in tissue due to autocrine inhibition; (B) Autocrine signal is forwarded in space and time, according to PDE in Eq. 6.4.

where $c(\vec{x}')$ is the concentration of the inhibitory signal at the protruding site and χ regulates the strength of the inhibition. Now, the total change in energy $\Delta\hat{H}$ determines the probability that a movement is accepted:

$$P(\Delta\hat{H}) = \begin{cases} e^{\frac{-\Delta\hat{H}}{T}} & , \Delta\hat{H} \geq 0 \\ 1 & , \Delta\hat{H} < 0 \end{cases} \tag{6.3}$$

Here T is the cellular temperature, that regulates the extent of random cell motility. The higher the temperature T, the higher the probability a movement will be made against the forces acted on the cell. We assume that the inhibitory signal is secreted by the epithelial tissue and diffuses and decays in the medium (Figure 6.1B). So, we describe the dynamics of the signal by the following partial differential equation:

$$\frac{\partial c(\vec{x},t)}{\partial t} = \underbrace{D\nabla^2 c(\vec{x},t)}_{\text{diffusion}} + \underbrace{\alpha \mathbf{1}_{\sigma(\vec{x})>0}}_{\text{secretion}} - \underbrace{\varepsilon c(\vec{x},t)\mathbf{1}_{\sigma(\vec{x})=0}}_{\text{decay}} \tag{6.4}$$

A simulation consists of consecutive steps of the CPM and the PDE, where one timestep of the CPM is followed by 3 seconds of inhibitor dynamics. This time scale was chosen arbitrarily. Other parameter values are given in Supplementary Table 6.1.

6.2.1 Autocrine inhibition of cell movement drives branching

To study the dynamics of the model, we run the model for 20.000 MCS. The results should give insight in how the tissue morphology progresses over time, as well as why the observed behavior takes place. We initiate approximately 1000 cells, by randomly distributing one-site cells over a disk with radius 0.45 in a tissue of 0.9 mm by 0.9 mm. Then Eden growth [309] is applied for 10 iterations to let the cells grow, thus filling the circular domain. To let the tissue attain a roughly circular shape with cells of similar shape we run the CPM for 100 MCS without the autocrine signal dynamics. Figure 6.2A shows a timelapse of one model realization. A first look at the time

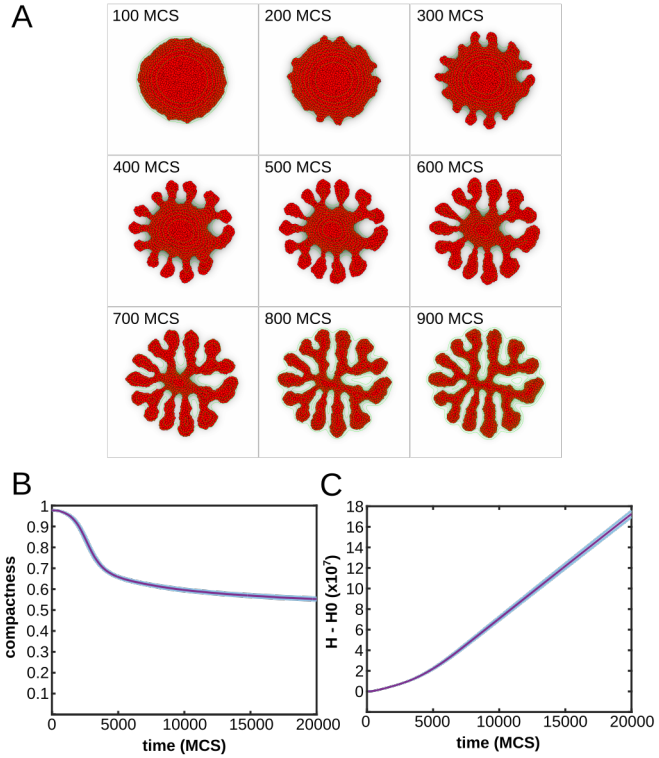

Figure 6.2: Simulation of branching by autocrine inhibition. (A) Timelapse of a model realization; (B) Compactness as a function of time, shaded regions: standard deviations of 100 simulations; (C) Energy spend by the system ($H - H_0 = \sum \Delta H$) as a function of time, shaded regions: standard deviations of 100 simulations.

series of the simulation shows that at approximately 1000 MCS the boundary of the tissue gets bumpy. Then around 3000 MCS, many droplet-like extensions appear. The length of these extensions increase and as a result, a fully branched structure, with evenly thick branches is formed, that stabilizes around 8000 MCS.

To quantify the extent of branching, we measured the compactness of the tissue [114] $C = (A_{\text{tissue}}/A_{\text{hull}})$, the ratio between the area of the largest connected component of the tissue and its convex hull, the smallest convex set that contains the tissue [310]. A compactness of 1 implies a perfectly circular tissue shape, whereas a low value of the compactness implies a high degree of branching. Figure 6.2B shows the compactness of the tissue over time. This shows that indeed branching rapidly takes place during the first 5000 MCS and afterwards, the compactness keeps on slowly decreasing, into a stabilized structure.

The behavior of the model can be explained as follows. Initially, due to the random motility of the cells, the boundary of the circular tissue will be become irregular. Consequently, by diffusion, high concentrations of the inhibitor are located at the concave

boundaries of the tissue, indicated by the darker grayscales at these locations (see Figure 6.2A), while low concentrations are located at convex boundaries. Because the contribution of the autocrine signal to the change in total energy in the system is always positive, extensions at concave sites are least energetically favourable. Instead, extensions are facilitated at the convex sites of the tissue. As a result, the the boundary at these sites becomes even more convex, allowing for more potential extensions. Thus, this mechanism reinforces itself.

In conclusion, our model suggests that inhibition of cell movement at negative curvatures of the tissue boundary due to autocrine signaling drives a branching instability.

Branching by dissipation

The mechanism in our model resembles a mechanism proposed for vascular network formation of endothelial cells by Merks *et al.* (2008) [114]. Here, it was proposed that cells chemotact towards an autocrine signal and that chemotaxis is contact-inhibited: cells only respond to the signal at cell-medium interfaces. Because cells at the boundary of the tissue experience a shallower gradient at positive curvatures, a branching instability occurs. Branching was enabled if cell retractions and protrusions responded to the signal, but also if only cell protrusions responded to the signal. In the latter case, the cumulative energy of the system $H_{\text{cum}}(t) = H(t) - H(t = 0) = \sum_{t_i=0}^{t_i=t} \sum \Delta\hat{H}(t_i)$ increased as a function of time, suggesting that the tissue branches by a dissipative mechanism. This is because $\Delta\hat{H}$ is on average positive, due to the relatively large positive energy contribution of protrusions against the chemoattractant. So, on average, cells make movements that cost energy. The intrinsic random motility of cells allows the tissue to deviate from the optimal configuration. Due to such random fluctuations, the tissue becomes unstable and converges to a state outside of thermal equilibrium. Since H_{cum} does not stabilize in time, it actually costs the system energy to stay in this new equilibrium. Figure 6.2C shows H_{cum} as a function of time in our model. Similar to Merks *et al.*, the energy of the system increases over time, indicating that our simulated tissue also branches by a dissipative mechanism. In our case, this is due to the large positive energy contribution of the autocrine inhibition of cell movement in $\Delta\hat{H}$ (see equation 6.4). Movements with a positive energy change, against the inhibitor, can only occur if there is sufficient random motility, which is regulated by the cellular temperature T (see equation 6.3).

6.2.2 Random motility regulates branch initiation and branching speed

Because the cellular temperature T regulates the extent of random fluctuations, *i.e.* how much the tissue may deviate from its optimal configuration, we will vary T to study how it affects branching morphogenesis in our model. Figure 6.3A shows the different morphologies of the tissue as a function of T. For low values of T, the tissue does not branch. Starting around $T = 20$, the tissue developed droplet-like extensions. For higher values of T the tissue has branched and the branches are longer and thinner.

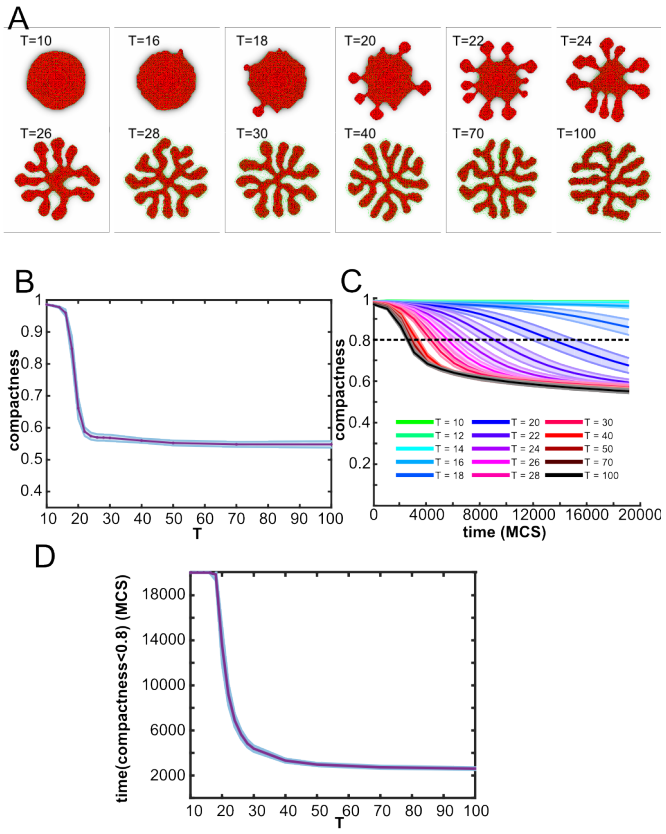

Figure 6.3: Cellular temperature regulates branching dynamics. (A) Example configurations of the tissue at 20000 MCS for different values of T; (B) Compactness as a function of T, shaded regions: standard deviations of 100 simulations; (C) Compactness as a function of time, shaded regions: standard deviations of 100 simulations; different colors: different values for T, see legend.

Figure 6.3B shows the compactness of the tissue as a function of T. This shows that the compactness rapidly decreases for increasing values of T and stabilized at around $T = 20$, reflecting that branching occurs from around $T = 20$.

Because a tissue always starts out with droplet-like extensions that later smooth out, see Figure 6.2A, we investigated how the temperature regulates the speed of branching. Figure 6.3B shows the compactness as a function of time for the various values of T. For low values of T such as $T = 18$ and $T = 20$, the compactness decreases, but it does not reach a low compactness before the end of the simulation. We quantified speed of branching by measuring the time $t(C < 0.8)$ it takes for the tissue to reach a compactness below 0.8 (dashed line in Figure 6.3C. Figure 6.3D plots $t(C < 0.8)$ as a function of the temperature T. This shows that the speed of branching quickly increases when T increases and then saturates.

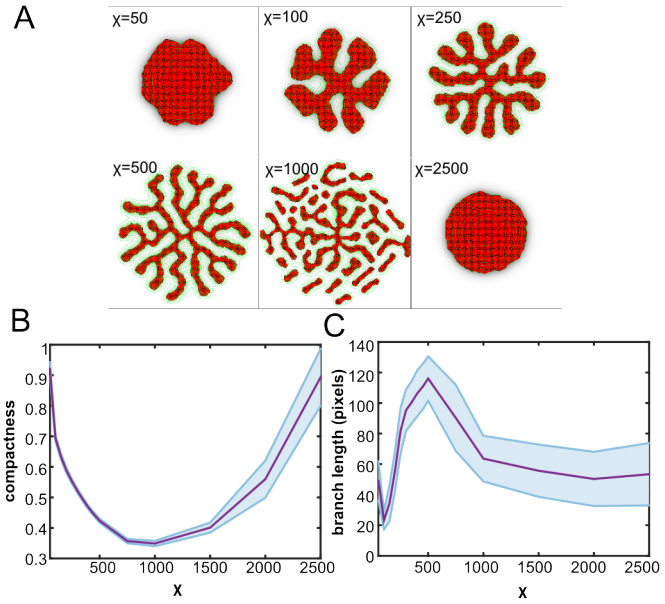

Figure 6.4: Strength of autocrine signal biphasically drives branching. (A) Example configurations of the tissue at 20000 MCS for different values of χ; (B) Compactness as a function of χ, shaded regions: standard deviations of 100 simulations; (C) Branch length as a function of χ, shaded regions: standard deviations of 100 simulations.

In conclusion, the temperature regulates both the initiation and the speed of branching. If $T < 18$, no branching takes place. If $T > 18$, branches start to extend but the tissue only develops in a fully branched structure before a certain time point if T is sufficiently high.

6.2.3 Strength of autocrine signal has biphasic effect on branching

The previous section showed that cellular temperature affects branch initiation and speed, but has little effect on the morphology of the tissue. We next studied how the chemoinhibition strength χ, that regulates the extent of inhibition of cell extensions due to the autocrine signal, affects branching morphology. Figure 6.4A shows the resulting morphologies as a function of the chemoinhibition strength χ. Interestingly, branching seems to be have a biphasic dependence on the chemoinhibition strength. For low values of χ, no branching takes places. This is because the impact of the autocrine signal is negligible in the total Hamiltonian of the CPM; there is no preference for low compared to high concentrations of the autocrine signal, hence the tissue retains its circular shape. Increasing the value of χ induces branch formation, as now the difference in levels of the autocrine signal concentration around concave and convex sites, do affect the Hamiltonian. However, by increasing χ even further, branching oc-

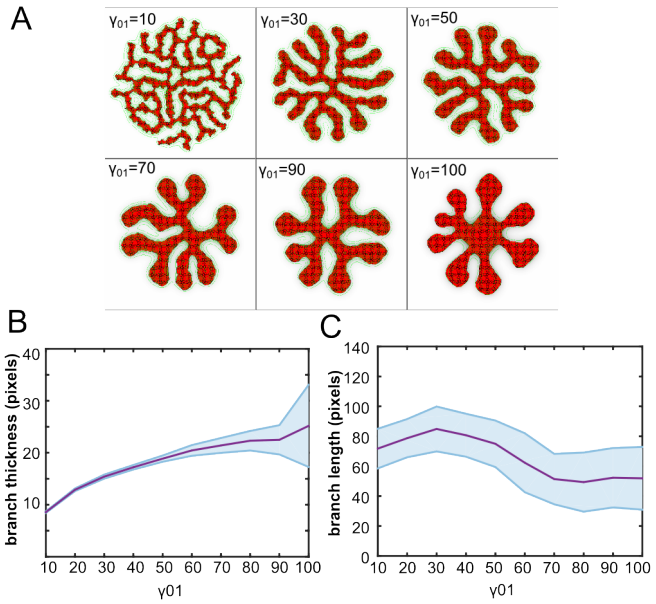

Figure 6.5: Surface tension affects branch morphology. (A) Example configurations of the tissue at 20000 MCS for different values of J_{01}; (B) Branch thickness as a function of γ_{01}, shaded regions: standard deviations of 100 simulations; (C) Branch length as a function of γ_{01}, shaded regions: standard deviations of 100 simulations.

curs at such a fast rate that branches start to break apart from the spheroid, since with high values of χ, the chemoinhibition term in the Hamiltonian starts to dominate over the cell-cell adhesive energy. Then, for more extreme values of χ, branching does not start, because every extension is very costly.

Figure 6.4B shows how the compactness of the tissue depends on the strength of the autocrine signal χ, confirming the biphasic effect of χ. Figure 6.4C shows that χ increases the length of the branches. In conclusion, our model suggests that the autocrine signal regulates the degree of branching in a biphasic manner. A tissue can branch within an optimal range of χ.

6.2.4 Decreasing surface tension promotes branching

Experimental studies have shown that cytoskeletal tension impacts branching morphogenesis [297, 311, 312]. In the CPM, cytoskeletal tension is associated with the surface tension γ_{01} defined as $\gamma_{01} = J_{01} - \frac{J_{11}}{2}$ [73], where J_{01} is the adhesive energy between cell and medium and J_{11} is the adhesive energy between two cells. Here we will study what effect the surface tension has on the branching morphology in our model, by varying J_{01} and thus γ_{01}.

Figure 6.5A shows the morphologies for different values of γ_{01}. For very low values

of γ_{01} there are many thin branches, which seem to have merged, almost resembling a network. Also, the surfaces of the branches are ragged. As γ_{01} increases, the branches become more smooth again and for high values of γ_{01} the branches become droplet-shaped. Figure 6.5B and Figure 6.5C show that decreasing γ_{01} decreases the length and increases the thickness of the branches. The effect of γ_{01} in our model can be explained as follows. At low values of γ_{01} the energy contribution of chemoinhibition dominates over that of adhesion, so that the tissue is able to branch. Because γ_{01} is low, cell-medium interfaces are allowed, so that branches may elongate and become thin. For high values of γ_{01} it becomes more energetically costly to have a larger cell-medium interface.

Taken together, a decrease in surface tension allows for more cell-medium interfaces so that the tissue is able to deform into a branched structure, with thinner and longer branches.

6.3 Discussion

Using a computational model, we show that inhibition of cell protrusion by an autocrine signal suffices to drive epithelial branching in the absence of cell proliferation and in absence of signaling with the surrounding mesenchyme. In a simulated epithelial spheroid, random cell motility causes the periphery to become bumpy. The tissue branches due to a curvature effect, leading to reduced concentrations of the autocrine signal at convex sites of the tissue boundary. So, cell protrusions are more preferentially at positive curvatures. This results in an instability where local extensions at positive tissue curvature make reinforces the curvature effect so that full branching proceeds (Figure 6.2) that is limited by the surface tension of the tissue.

6.3.1 An autonomous mechanism for branching

Previous mathematical models were often based on Laplacian growth principles, which assume that tissue growth is proportional the gradient of a Laplacian field. In such models, tissues branch due to a Mullins-Sekerka instability, where positive curvatures experience higher gradients of the field and become unstable. It has been proposed that a pressure field between epithelium and mesenchyme [293], or a growth factor field [297, 308] can drive branching. It has also been proposed that patterns of stimulatory growth factors, arising from Turing-type signaling interactions between the epithelium and mesenchyme [299, 300, 302], drive branching by locally up-regulating tissue growth [301, 302]. However, experimental data suggests that branches extend prior to localized cell proliferation [217, 277, 285]. Furthermore, epithelial tissues can branch in absence of the mesenchyme [287–289] and distributions of stimulatory growth factors are not always associated with branch localization [305, 306]. In contrast to previous models, we propose a cellular mechanism for branching and our model suggests that neither tissue growth nor signaling from the mesenchyme is required. Based on experimental data [98], our model suggests that an autocrine

inhibitory signal determines sites of branching and drives branching by a curvature effect where the autocrine signal accumulates at concave parts. This curvature effect is similar to curvature effect in Laplacian growth, but our model suggests that curvature dependent cell movement is sufficient to drive branching.

6.3.2 Experimental validation

Autocrine signaling strength

The experimental study on which we based our model suggests that TGF-β acts as the autocrine inhibitory signal [98]. Our model predicts that TGF-β can only drive branching if its signaling strength is around an optimal value (Figure 6.4). In agreement with our model predictions, several experimental studies suggest that TGF-β drives branching in a concentration dependent manner. High concentrations of TGF-β1 to obstructs mammary gland epithelial branching, while low concentrations promoted branching [313]. Furthermore, low concentration of TGF-β promote tubulogenesis in mammary glands *in vitro* [314]. Decreasing the response of TGF-β receptors leads to increased branching [315]. In our model, decreasing χ also increased branching, but decreasing χ even further stopped branching (Figure 6.4). To investigate if the biphasic effect of chemoinhibition strength on branching can be found *in vitro*, it would be interesting to extend the experimental set-up by Nelson *et al.* [98] to larger unconfined mammary epithelial tissues that exhibit full branching morphogenesis (not just sprouting movements) and modulating TGF-β response.

Since many organs have homologies of the TGF-β family and our model does not specify a certain cell type or specific signaling molecule, we may validate our model using experimental observations of various organ systems. In kidney, BMP7 stimulates branching at low concentrations while inhibiting branching at higher concentrations [316]. Similar to our model, the secreted inhibitor is thought to regulate branch avoidance [304]. The shape of the extensions also resembles experimental observations of kidney and lung branches. Initially, the extensions are broad and droplet-shaped, which then elongate over time [282, 297, 317]. In *in vitro* experiments, branch bifurcation occurs very often, which is not the case in our model. Simulations show that if we allow cell proliferation, branch splitting does occur. To better compare *in vitro* branching dynamics with our model in the future, we will generate time evolutions of the skeletal tree of the model configurations, similar to what has been done by Watanabe *et al.* [282]. Directly comparing *in vitro* with *in silico* data could provide us with realistic parameter values, such as the time scale of one MCS. This might alleviate the issue that the current time scale of our model (branching occurs within 2h) is much faster than *in vitro* (2-3 days) [282].

Surface tension

In our model, reducing surface tension promotes branching (Figure 6.5). This compares well with *in vitro* observations by Hartmann and Miura, who showed that dis-

ruption of the cytoskeleton in isolated lung epithelium increased branching [297]. Similarly, inhibiting cell contractility promotes branching morphogenesis in pancreas [289]. In contrast with these experiments, increasing cytoskeletal tension in embryonic lung explants increased branching [311, 312]. Because our model is incomplete, *i.e.* it does not involve intricate interplay between lung epithelium, the basement membrane and the surrounding mesenchyme, and remodeling of the matrix, it can not explain all these experimental observations.

Random motility

In our simulations, the cellular temperature T, that regulates cell motility, promotes branching (Figure 6.3). In agreement with our model, knockout of Btbd7 in kidney increases cell motility, which resulted in less end bends [318]. In these experiments, Btbd7 also decreased cell-cell adhesions. The experimental figures indicate that the buds and branches are thicker [318]. This is also consistent with our model, as an increase in the cell-cell adhesion energy J_{11} is equivalent to a decrease in surface tension γ_{01}, which leads less branches and increased thickness (Figure 6.5).

Our model has given insights into epithelial branching, but it disagrees with observations in kidney. Recent experimental observations suggest that the autocrine inhibitor BMP7 does not regulate curvature dependent protrusion [319]. Using a comparable system to Nelson *et al.* [98], but with renal epithelial cells, Martin *et al.* showed that renal cells did exhibit curvature dependent protrusions, but not because of BMP7 localization. They interfered with autocrine signals, by applying rapid flow to the medium and showed that cells still exhibited curvature dependent protrusions. The authors suggested that this might be regulated by a membrane tension mediated motility instead. The authors also suggest that the mechanism for curvature dependent protrusion could vary among organ systems; mammary cell do use an autocrine inhibitor for this purpose while renal cells do not. Pavlovich *et al.* [305] have argued that reliance of mammary epithelial branching on patterns of inhibitory signals might be unique. So, we might only be able to use our model to gain insights in epithelial branching of mammary gland and not other organs.

6.3.3 Limitations and future work

Like in any model, the model behavior depends on the assumptions that are made. Our model (Figure 6.1) relies on two major assumptions. Firstly, we view the tissue as a cross-section, so that decay of the autocrine signal only takes place outside of the cells. This affects the field of the autocrine signal, which also likely affects the tissue dynamics. Preliminary simulations show that the model also exhibits branching if we allow decay to occur everywhere in the tissue (*i.e.* consider the tissue as a 2D projection). The other major assumption concerns the definition of the Hamiltonian that describes chemoinhibiton of cell movements (Eq. 6.11). Here, cell-matrix extensions are inhibited by the autocrine signal, while cell-cell extensions are independent of the

autrocrine signal. As a result, cell copies within the tissue are more often accepted than at the boundary. If we view the tissue as a 2D projection, one could argue that cell-cell copies should also be affected by the autocrine signal, as the cells sense the matrix below them. Therefore, in subsequent research we will investigate the influence of inhibiting extensions at cell-cell copies, similar to Merks *et al.* [114].

The present model greatly simplifies *in vivo* branching, which involves many signaling molecules, from the epithelium and mesenchyme, and their interactions. We could study how interactions between stimulatory and inhibitory growth factors drive branching. Furthermore, signaling molecules such as TGF-β affect different pathways [320] and as such can regulate different types of cell behavior. We could for instance study how growth factor induced patterning of both cell movement and cell proliferation affects branching. The ability of cells to remodel the extracellular matrix has been shown to be involved in branching (for a review, see [277]). For instance, fiber assembly progresses branching in salivary glands [321]. Collagen fiber reorientation directs branch elongation in mammary epithelia [322]. The activity of matrix metalloproteinases (MMPs) has been highly implicated in mammary gland branching [323]. TGF-β is expressed by cells in a latent form that binds to the matrix, and matrix remodeling can release TGF-β from the matrix in an active form [324]. TGF-β can be released from the matrix in many ways (review [320]), for instance due to stretching of latent TGF-β [325]. On stiffer matrices, bound TGF-β experiences more stress, which induces its release [325]. Sites of branching are correlated with matrix stresses [326] and since many morphogenetic processes are highly influenced by matrix stiffness, it would be interesting to implement such interactions between matrix stresses and TGF-β into account.

In summary, we propose that an inhibitory autocrine signal can drive branching morphogenesis by locally inhibiting cell movement. In this model, the autocrine signal accumulates at concave areas, so that branching is reinforced at sites with higher curvature. This work paves the way for studying the effects of cell-cell signaling and other cellular level dynamics on branching morphogenesis.

6.4 Methods

We developed a combined continuum - cell based model to describe the secretion and diffusion of an autocrine growth factor that we assume to inhibit cell movement. The cellular Potts model (CPM) is used to describe cell movement within a tissue composed of discrete cells. The dynamics of the inhibitor are described by a PDE, of which the local concentration feeds back to the CPM by inhibiting pseudopods.

6.4.1 Cellular Potts Model

To simulate collective cell behaviour we use the Cellular Potts model (CPM)[72, 73]. The CPM defines a two-dimensional lattice $\Lambda \subset \mathbb{Z}^2$. The size of the lattice is determined by m and n, which denote the number of lattice sites in the vertical and horizontal axis respectively. The cells are represented as clusters of connected lattice sites. Every site is assigned a value $\sigma(\vec{x}) \in \mathbb{Z}^{\{0,+\}}$, which is called a spin, to identify the cell it belongs to. Spin $\sigma(\vec{x}) = 0$ is reserved for the ECM. Thus, a cell is defined as the set of lattice sites mapping to the same spin:

$$C(i) = \{\vec{x} \in \Lambda \mid \sigma(\vec{x}) = i\}. \tag{6.5}$$

The CPM uses a modified Metropolis Monte-Carlo algorithm to simulate cell movement. In this Monte Carlo algorithm, Monte Carlo Steps (MCSs) are taken. In one MCS, the CPM attempts N movements, where $N = mn$ is the number of lattice sites. Each movement is defined as follows. A random lattice site $\vec{x}$ is selected. Then, a random site $\vec{x}'$ in the Von Neumann neighbourhood of $\vec{x}$ is selected and the spin $\sigma(\vec{x})$ is attempted to be copied to $\vec{x}'$. The success of this copy depends the change of energy associated with this movement. A Hamiltonian function H represents the total energy of the system, reflecting the forces that are present in the system. The system aims to minimize H. In the simplest version of the CPM the Hamiltonian includes adhesion energies of cell-cell interfaces and area constraints [72]. The Hamiltonian is usually defined as follows:

$$H = H_{\text{adhesion}} + H_{\text{area}} \tag{6.6}$$

$$= \sum_{(\vec{x},\vec{x}')} J(\sigma(\vec{x}), \sigma(\vec{x}'))\mathbf{1}_{\sigma(\vec{x})\neq\sigma(\vec{x}')} + \lambda \sum_{1\leq\sigma\leq n} (a(\sigma) - A_{\text{target}}(\sigma))^2. \tag{6.7}$$

with $(\vec{x}, \vec{x}')$ a pair of adjacent lattice sites. Here J is a matrix with adhesion energies between cell types (ECM and epithelial cells) and δ is the Kronecker delta function ensuring that only cell boundaries are considered in the adhesion summation. In addition, $a(\sigma)$ denotes the current number of sites occupied by cell σ while $A_{\text{target}}(\sigma)$ is the target area of cell σ. The parameter λ indicates the strength of this area constraint. The difference in energy corresponding to a copy is given by:

$$\Delta H = H_{\text{after}} - H_{\text{before}}. \tag{6.8}$$

This difference determines the probability that the copy is accepted. If ΔH is negative, the movement will be accepted, since it will decrease the energy of the system. However, if ΔH is positive, the movement will be accepted according to a Boltzmann distribution, yielding:

$$P(\Delta H) = \begin{cases} e^{\frac{-\Delta H}{T}} & , \Delta H \geq 0, \\ 1 & , \Delta H < 0. \end{cases} \tag{6.9}$$

Here T is the cellular temperature, that regulates the magnitude of intrinsic random cell motility.

6.4.2 Dynamics of autocrine signal

We assume that cells secrete an inhibitor which diffuses and degrades in the ECM, giving rise to:

$$\frac{\partial c(\vec{x},t)}{\partial t} = D\nabla^2 c(\vec{x},t) + \alpha \mathbf{1}_{\sigma(\vec{x})>0} - \varepsilon c(\vec{x},t)\mathbf{1}_{\sigma(\vec{x})=0} \tag{6.10}$$

In this equation $c(\vec{x},t)$ is the concentration of the chemical at time t and site $\vec{x}$. The PDE contains three parameters, where D is the diffusion coefficient, α is the secretion rate and ε is the decay rate. We view the tissue as a cross-section, and assume decay of the autocrine signal in the medium as it binds to matrix components. Initially there is no signal in the system, thus $c(\vec{x},0) = 0$ for all $\vec{x}$. The boundary of the CPM grid acts as a sink, setting $c(\vec{x},t) = 0$. The PDE is solved by using a forward Euler PDE solver with $h = \Delta x = \Delta y$ being the distance between the lattice site centers, where Δx and Δy are the horizontal and vertical distances respectively. We set Δt to 0.2 seconds and during each Monte Carlo iteration 15 of the numerical integration steps are performed, so that the autocrine dynamics run for $t_c = 3$ seconds.

6.4.3 Local concentration of autocrine inhibits cell movement

To model the inhibitory effect of the autocrine c on the motility of cells, the concentration of the autocrine inhibitor feeds back to the CPM. We assume that, as experimentally observed by Nelson *et al.* [98], inhibition depends on the amount of local autrocrine. In accordance, we extend the expression for ΔH by an additional term:

$$\Delta H_{\text{inhibition}} = \chi \cdot c(\vec{x}') \cdot \mathbf{1}_{\sigma(\vec{x})>0} \cdot \mathbf{1}_{\sigma(\vec{x}')=0} \tag{6.11}$$

The idea of adding this term is that copies toward high concentrations lead to an increase in energy and thus are unfavored. Here, χ, is a parameter that regulates the strength of this inhibition term. The last two terms ensure that this chemoinhibition term comes into play only when a copy is made from a cell to the ECM, modeling a pseudopod extension at the boundary of the tissue.

6.4.4 Morphological measures

We introduce the following morphological measures.

Compactness

The compactness is defined as the ratio between A, the domain covered by the tissue, and the area of its convex hull $A_{\text{convex hull}}$ [310]:

$$C_{\text{comp}} = \frac{A_{\text{tisse}}}{A_{\text{convex hull}}} \tag{6.12}$$

The convex hull of A is the smallest convex set that contains A. The convex hull is determined by first finding the largest connected component [327] and then running

Graham's scan [310] to identify the set of points that make up the convex hull. In the context of our simulations, a compactness of $C_{\text{comp}} = 1$ implies a perfectly circular tissue shape, whereas a low value of the compactness implies a high the degree of branching.

Branch length

In order to find the branches of the structure, we generate the morphological skeleton of the tissue [328, 329]. Using this skeleton image, we calculate the length of the branches as follows. For every edge, the two nodes of the edge are removed from the skeleton image A_{skeleton} by removing all lattice sites around the nodes with increasing radius, until a radius w is found such that A_{skeleton} is divided in at least two separate components, of which one is the edge of interest. The length of branch is then determined by counting the pixels that make up the branch and adding twice the radius w to the final result.

Branch thickness

To calculate the branch thickness, we adopted an approach by Filatov *et al.* [330]. We take A to be the image of the tissue and let B be a disk $B^r = \{(x, y) \in \mathbb{R}^2 : x^2 + y^2 \leq r\}$ with variable radius r. The branch thickness can now be defined as the value of r for which branches disappear out of the morphological opening $A \circ B^r$. According to the graph in Figure 6.6 the area of the morphological closing decreases exponentially with the radius r, because more branches disappear from the image with increasing r. We approximate the branch thickness by finding a point where this graph decreases sufficiently fast and then becomes flat, indicating that most branches have disappeared. For more details, see the Supplementary Methods.

6.5 Supplementary methods

6.5.1 Calculating branch thickness

According to the graph in Supplementary Figure 6.6 the area of the morphological opening $A \circ B^r$ decreases exponentially with the radius r. At some point the graph is more or less horizontal. This region corresponds to the circular part of the tissue, in which many circles B^r fit. So, the value for r for which the graph becomes horizontal indicates is the thickness of the branches. We detect this horizontal region by first finding a region where the graph decreases sufficiently fast and then a region where it decreases slow. Let $M_A(r)$ be the area of $A \circ B^r$. We find an $0 < r_1 \leq r_{\max}$ for which $M_A(r_1) - M_A(r_1 - 1) < a_1$ and then the value $r_1 < r_2 \leq r_{\max}$ for which $M_A(r_2) - M_A(r_2 - 1) > a_2$ (r_2 is set to $r_{\max}$ if such a value does not exist). The branch thickness is then found by taking the value of r for which $M_A(r)$ is closest to $\frac{1}{2}(M_A(0) + M_A(r_2 - 1))$. The values of a_1 and a_2 are experimentally determined. The value of $r_{\max}$ is set to 30 to reduce computation time.

In case of no branches or very small branches ($M_A(r_1) - M_A(r_1 - 1) \geq a_1$ for all $0 < r_1 \leq r_{\max}$) we apply the following algorithm. When the decrease in $M_A(r)$ is not larger than $-a_1$ in the entire graph we simply take the distance from the center of mass of the tissue to an ECM point in four different directions and select the lowest distance as the radius. In this case, the radius represents the radius of the unbranched cell aggregate but we take this as the branch thickness. We take this approach since increasing the radius to the width of the initial circular tissue (typically more than twice as large as $r_{\max} = 30$) and repeatedly computing $M_A(r)$ requires a lot of computation time.

6.6 Supplementary tables

Parameter	Description	Value	Unit	value was
T	Cellular temperature	50	-	similar to [114]
A_σ	Target area	50	-	similar to [114]
χ	Chemoinhibition parameter	250	$\frac{Nm}{molL^{-1}}$	chosen
λ	Area constraint strength	50	$\frac{N}{\mu m^3}$	similar to [114]
D	Diffusion coefficient	$15 \cdot 10^{-13}$	$\mu m^2 s^{-1}$	similar to [114]
ε	Decay rate	0.005	s^{-1}	similar to [114]
α	Secretion rate	0.0005	s^{-1}	similar to [114]
$n_{\text{init cells}}$	Number of initial cells	1000	-	chosen
J_{01}	Cell-ECM adhesion energy	50	Nm	similar to [114]
J_{11}	Cell-Cell adhesion energy	20	Nm	similar to [114]
dt	Timestep in PDE integrator	0.2	s	similar to [114]
dx	Pixel size	$2 \cdot 10^{-6}$	m	chosen
P	PDE iterations per MCS	15	-	similar to [114]
m	Vertical size of field	450	-	chosen
n	Horizontal size of field	450	-	chosen

Table 6.1: Parameter settings.

6.7 Supplementary figures

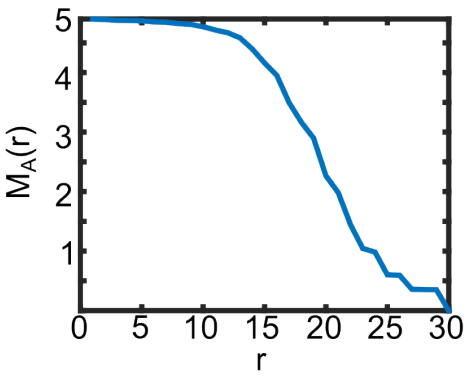

Figure 6.6: The radius r versus the area of the morphological closing.

7

Discussion

In this thesis we aimed to better understand how interactions between cells and the extracellular matrix can drive morphogenesis by making use of multiscale computational models. Mathematical modeling is a powerful tool that is often used alongside of experimental approaches. Mathematical models can test hypotheses on the driving mechanisms behind morphogenesis. Furthermore, it enables us to better understand a biological system, by studying the necessary mechanisms and the complex interplay between different mechanisms involved. In this thesis, we mainly focused on modeling of mechanical cell-matrix interactions at a cellular and molecular level and predicting how this influences the dynamics at the tissue scale. In the past, many models have neglected the interplay between cells and the extracellular matrix. Most models that did consider mechanical cell-matrix interactions mainly focused on matrix fiber remodeling as a result of stresses but not on the direct response of cells to stresses. Our model is based on experimental observations that show that cells communicate by sensing traction stresses in the substrate [32]. Our model couples the cellular Potts model (CPM) that describes cells as a collection of lattice sites, to a finite element model (FEM) that calculates substrate deformations. We assumed that cells apply a traction force to the substrate, inducing substrate strains, and that cells respond to this strain. With these models we studied how cells respond to matrix stiffness and how cell-cell communication through matrix stresses drives tissue patterning. Besides mechanical signaling, cells also use chemical signaling through the extracellular matrix to communicate. So, we also studied how chemical signaling can pattern tissues. The models described in this work pave the way to study the complex interplay between cells and mechanical and chemical forces in the extracellular matrix.

7.1 Summarizing discussion

In chapter 2, we showed that if cells preferentially extend pseudopods along substrate strains, cells are able to form network-like patterns, that resemble *in vitro* vascular networks. In accordance with experimental observations, cells only formed networks in simulations with substrates of intermediate stiffness. Furthermore, this model also reproduced cells sprouting from a cell aggregate. This model suggests a alternate mechanism for network formation and sprouting, among many existing ones which are often based on chemical signaling [77, 114].

In chapter 3, we showed that our model also explains cell alignment to static uniaxial stretch. The model suggests that by contracting the matrix, cells locally amplify substrate strains in the orientation of the global stretch cue, allowing the cell to elongate along the strain. By applying forces on the matrix, the simulated cells locally align with other cells, so that the cells forms string like patterns along the uniaxial strain. This string formation depended on cell-cell adhesivity and cell density, which could explain why tightly packed endothelial cells do orient [94] but do not form strings, while fibroblasts form strings [95].

To explain cell orientation to substrate strains, other mathematical models based on

homeostatic principles were employed: these assumed that cells reorient in order to optimize a certain physical quantity [45, 180], such as local stresses [180]or the applied work [45]. Our model suggests a cellular mechanism at a level of protrusions, that allows a cell to migrate and reorient by reshaping itself. Our multiscale models thus show how a relatively simple mechanism at the subcellular scale can induce complex tissue patterns. The complexity in our multiscale model presents itself not in the individual models or their assumptions, which are kept relatively simple, but in the coupling of different scales in our model. By introducing multiple scales in a model, we are able to translate lower scale dynamics to dynamics at a tissue level.

In chapter 4, we introduced dynamics at the scale of cell-matrix adhesions in our model, to understand how force based focal adhesion dynamics regulate cell response to matrix stiffness. We modeled focal adhesions as clusters of integrin bonds, which grow according to catch-slip bond dynamics [231]. Cells apply a force on these clusters, which builds up faster on stiffer matrices [96], so that the focal adhesions grow on stiffer matrices. We coupled focal adhesion model to the CPM by assuming that cell-matrix retractions are less probable for larger focal adhesions. This relatively simple model for focal adhesions and cell-matrix adhesion sufficed to explain cell spreading on compliant matrices. If we introduced that matrix stresses strengthen cell-matrix adhesion, we could also reproduce cell elongation on substrates of intermediate stiffness. Finally, in our model, cells movement up a stiffness gradient (durotaxis) is an emergent phenonemon. By introducing these focal adhesion dynamics in our multiscale model, we were able to better understand the response of cells to substrate stiffness.

Although physical forces can drive morphogenesis, chemical signaling is also important in tissue patterning. In chapter 5, we studied how chemical signaling through the extracellular matrix can regulate morphogen gradient formation. We developed a partial differential model of gradient formation of the Nodal protein that is involved in left-right patterning of embryos. Based on experimental data [97], we assumed that Nodal signaling induced intercellular Nodal production, and is cleaved into a mature form by the convertase FurinA. Once matured, it is able to be secreted into the extracellular space and diffuse. A combination of *in vitro* and *in silico* experiments indicate that FurinA is able to regulate speed of Nodal gradient formation and its signaling range.

Chapter 6 studies how chemical signaling can drive branching morphogenesis. Here, we introduce a CPM to explain branching morphogenesis. We base our model on *in vitro* observations of mammary epithelial cells that suggested that the autocrine growth factor TGF-β acts as a inhibitor of cell movement [98]. Due to a curvature effect of autocrine signal accumulation at concave tissue boundaries, extensions are more favorable at convex areas. This mechanism is reinforced, which allows the extensions to branch out. Thus, our model suggests that inhibition of cell movement by an autocrine signal suffices to reproduce branching morphogenesis.

Altogether, we have used multiscale models to study the role of cell-matrix interactions in morphogenesis. These models described components at different tissue scales

(such as growth factors, focal adhesions, cells and the substrate) and how these scales interact with each other. We studied how single cells respond to matrix stiffness and how matrix stiffness can regulate vascular network formation and sprouting. We also studied how matrix stresses regulate cell alignment. Furthermore, we investigated how chemical signaling through the matrix can drive branching morphogenesis. The multiscale models presented in this thesis pave the way to a more complete understanding of how cells can organize into tissues.

7.2 Model validation

A mathematical model is useful in itself because it gives a better understanding of a biological system, but to drive science even further, complementary experimental studies should be performed. Experimental data allows us to validate, or invalidate, a mechanism proposed by the model. Because a model is just a representation of reality, we can never proof concepts with our model, we can only provide clues. If an experimental system behaves the same way as the model system in response to varying a specific parameter, it becomes more likely that the mechanism proposed by the model is valid. For instance, in chapter 4, we propose that the range of substrate stiffness on which cells elongates depends on the velocity of the molecular motor proteins. This could be validated by either using different cell types that express different types of motor proteins with different velocities or by increasing motor protein velocity by affecting ATP levels. In chapter 6, we propose that an epithelial tissue can branch by secreting TGF-β which inhibits cell movement. Our model predicts that the extent of branching depends on the strength of the autocrine signal. Experiments in which TGF-β signaling is increased and decreased can help validate this mechanism.

If the experimental data does not coincide with the mathematical model, the effort has not been futile. Experimental data can provide insights into what is truly happening, provide a new hypothesis, which can then be further explored by the mathematical model. Maybe the model is wrong, but because models are typically a simple representation of reality, it is possible that the model just misses crucial elements. Experimental studies can provide clues into what aspects are missing. By iteratively extending our model and validating our model with *in vitro* experiments, we can obtain a better understanding of the mechanisms that drive the biological system. For instance, in chapter 2, we could explain why cells form networks of substrates of intermediate stiffness, but not why the range of substrate stiffness on which networks are formed changes when the matrix density changes [36]. Since cells respond to matrix mechanics through focal adhesions, it might be possible to explain this observation with our extended model that includes focal adhesion dynamics of chapter 4. *in vitro* experiments indicate that focal adhesion growth and thus cell spreading depends on matrix density. As a preliminary result, we show that our focal adhesion model (chapter 4) can already reproduce vascular network formation (Figure 7.1), which makes it promising to further study the relation between matrix properties and network forma-

tion.

Experimental approaches have made tremendous progress in tracking cell movement [331] and also the dynamics at a molecular level, such as cell traction forces [332, 333] and the imaging the molecules in focal adhesions [334]. This makes it possible to test mutiscale models at multiple tissue levels. Doing complementary experimental studies to mathematical modeling has other benefits as well. It can help us to formulate our model. For instance, for more focal adhesion molecules it is being unraveled how forces affect their structure and as a result their binding, so that qualitative models can be developed [335]. Experimental data can also provide us with realistic parameter values in our model. Unfortunately, this is not always possible, as some parameters can not directly be coupled to experimental quantities. In this case, we can tune parameters values qualitatively. For instance, cell-cell and cell-matrix adhesive energies in our model can be tuned so that they have the same relative relation as the adhesive forces of cell-cell adhesions and cell-matrix adhesions [336]. Or, we could tune the unknown parameter values so that the model best reproduces a particular system, enabling us to study deviations from that system. For instance, we could tune the unknown parameters in our focal adhesion model to a specific cell type that is spreading on a compliant substrate. Then, we can change the measurable parameters to fit to other cell types and use our model to understand why different cell types spread differently.

Mathematical models should also be validated by other modeling frameworks. Since the model behavior and thus its results may also depend on the model framework that is used [337], it is crucial to employ other modeling frameworks and implement similar dynamics and investigate the resulting model behavior. So, in order to be sure that our results are not an artifact of the particular framework that was used, ideally we should implement our assumptions into other cell-based modeling frameworks, to check if assumptions specific to the cellular Potts model, such as the lattice and definition of cell protrusions, do not greatly affect the model behavior. We do not suspect major effects, because we have applied sufficient noise and investigated various assumptions.

To gain a better idea of how all model parameters interact and affect our model output, we could perform a global sensitivity analysis [338]. This would be instead of the local sensitivity analysis as presented in this thesis, where we typically vary only one or two parameters while keeping others fixed. Sensitivity analysis requires many costly and time consuming simulations. Alternatively, it may be possible to formulate our model assumptions in a analytical framework. This can then be used to determine under which conditions the model obtains a certain configuration [339]. For instance, for which parameter values does a cell elongate? How does durotactic speed depend on the model parameters?

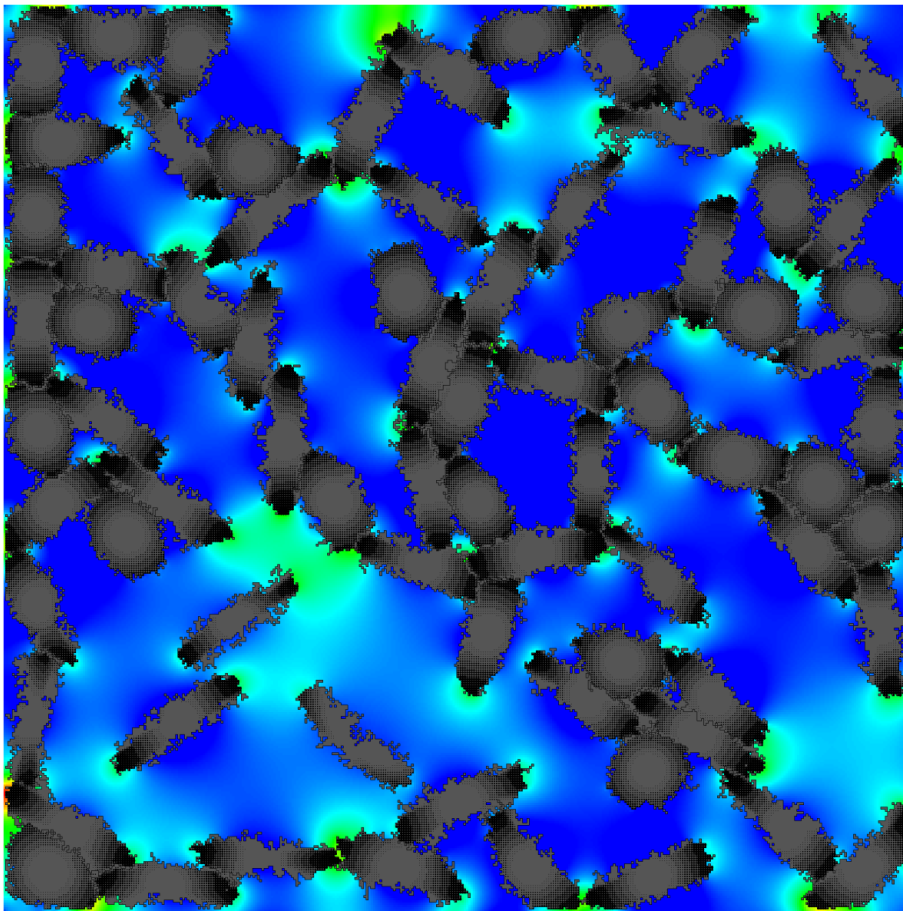

Figure 7.1: Network formation in the hybrid CPM-FEM model including focal adhesion dynamics, as presented in chapter 4. Cells apply a force on the matrix, which lets integrin clusters grow according to catch-slip bond dynamics. Matrix stresses generated by neighbouring cells stabilize these adhesions, so that the net movement of cells is towards each other and as cells elongate, they locally align and thus are able to form networks. Colors: hydrostatic stress.

7.3 Refinement of cell-matrix coupling

To better be able to understand the the biological system of interest and to be able to validate a model, the model should represent the system well. However, because we have made various simplifying assumptions in our model, we did not perfectly describe the system. For instance, in chapter 2 and 3, we assumed that cells perceive a strain stiffening of the substrate. However, we did not let the matrix actually stiffen over time. After every timestep in the CPM, we apply a FEM to calculate the substrate strains, but assumed a homogenous stiffness and initially undeformed matrix every time. So, there was no memory of previous displacements in the FEM. However, as a first step, making the model as simple as possible allows us to better understand its behavior.

Another computational simplification was the decoupling of the cellular forces in the Hamiltonian of the CPM from the cellular forces in the FEM. Ideally, these forces should be equivalent in both compartments of the model. In our model, this is not the case as the cellular forces are descriped by a CPM Hamiltonian while the forces in the FEM are described using the FMA model. Albert & Schwarz [192] who also coupled the CPM with a FEM for the substrate, did use the same force descriptions in their CPM and FEM. They assumed that cells have a surface and line tension, which they described in a CPM Hamiltonian. For a surface and line tension, the corresponding forces in the FEM was formulated as follows. The surface tension results in a force normal to the cell membrane and the line tension generates an additional normal force proportional to the curvature of the membrane. In the FEM, the normal force on the CPM cell boundary was approximated using a marching square algorithm. Furthermore, the resulting force was smoothed by a kernel around the cell membrane. We could do a similar thing, but we chose not to do so in this thesis, since we wanted to maintain the description of the line tension as in the usual CPM formulation. Here, the adhesive energy between cells and the matrix describes a line tension, if the neighbourhood is large enough [255]. The benefit of this formulation, is that it also describes cell-cell adhesion and is very useful to study cell-cell interactions.

In order to test if it would improve our model, we developed a method to calculate forces from a generic Hamiltonian formulation in the CPM. The method is described in Appendix A. This method is based on that the energy difference ΔH describes a force in the direction of the copy movement. Figure 7.2 shows a force field for $H = \lambda A + \sum J$ and the corresponding substrate stress field, which we compare to the FMA model for cell traction forces. The downside of this method is, that because CPM movements are always horizontal, vertical or diagonal, the forces align to the lattice as well. So, a grid effect occurs. We could alleviate this by considering a larger neighborhood order for copy attempts in the CPM. Furthermore, since CPM movements only occur at the cell boundary, the forces are only described on the cell membrane (Figure 7.2). We could alleviate this issue by smoothing the forces to a region around the cell membrane, using a kernel, similar to what Albert & Schwarz did. Another option, would be to formulate our forces in the FEM (the FMA model)

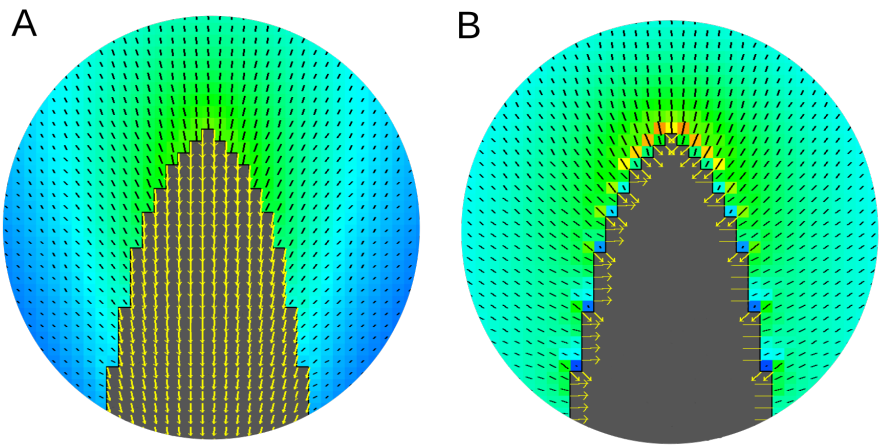

Figure 7.2: Cell forces around the tip of an elongated cell. (A) The FMA model as used in this thesis; (B) The traction forces derived from the Hamiltonian as presented in Appendix A. Colors: principal stress; orientation and length of black line pieces: orientation and magnitude of principal stress, yellow arrows: cell traction forces.

and than translate that to a Hamiltonian. However, this formulation does not separate a surface and line tension. In conclusion, there are currently too many unresolved issues with this method, so we decided to stick with the FMA model in this thesis. In order to have the same formulation for cell forces in the CPM and the FEM, more work should be done and we should outweigh the advantages and disadvantages of the different formulations that are possible.

7.4 Possible model extensions

In our modeling efforts we did not only make computational simplifications but also neglected various important known driving mechanisms of morphogenesis. An advantage of mathematical modeling is that we can focus on one specific mechanism, for instance matrix stiffness, while neglecting others. In this way, we can better understand how a specific factor influences the biological system. The disadvantage of such an incomplete model is that we can not explain all experimental observations, because we are missing important factors. Including more dynamics and interactions between cells, the substrate, cell-matrix adhesions and signaling factors can increase our understanding of a biological system. Here, we will give an overview of interesting aspects that can be included in our model and what it can be used for.

7.4.1 Matrix type and density

Because cell spreading does not only depend on matrix stiffness but also on other matrix properties, such as matrix type and density, it would be good to describe substrate mechanics in more detail. Cell spreading is typically increased on matrices with a higher density [123], or depends biphasically on matrix density [200]. To deal with matrix density, we could model this phenomenologically, by relating model parameters, such as the growth rate of focal adhesions, to matrix density. We could also model thus explicitly by including more detail in our substrate/FEM model. More detailed finite element models for the substrate have been coupled to circular discrete cells [88]. Coupling such models to a CPM will allow us to better understand how tissue respond to matrix mechanics on both a cellular level and tissue level. Cell spreading also depends on the type of matrix protein (*e.g.* fibronectin, collagen, laminin) that cells interact with [340]. Cells bind to different matrix proteins with different types of integrins. We could fit the catch and slip bond parameters of integrins in our model to those experimentally identified for the different integrins, to study how matrix type affects cell spreading.

7.4.2 Fibrous matrices

As the orientation of matrix fibers regulates cell migration [27], it is important to also take matrix fibers into consideration. Cells not only respond to matrix fibers, but also actively remodel matrix fibers. For instance, by applying forces on the matrix, cells can reorient matrix fibers [174]. Cells also deposit and degrade matrix fibers and even cross-link them [53]. Matrix fibers affect matrix stiffness and the extent of strain-stiffening [341], which in turn affects cell migration. So, intricate interplays between cells, fibers and matrix stiffness occur during morphogenesis. To study this, we should extend our model to include matrix fibers. More refined models of the extracellular matrix including matrix fibers are being developed. Matrix fibers can for instance be incorporated in finite element models [87, 342]. As fibers have the same spatial scale as cells, it might be more appropriate to model fibers using discrete approaches. For instance, fibers can be described by springs and the reorientation and cross-linking of fibers can be modeled [343]. Previous models including matrix fiber descriptions did not include cell shape [87, 89] or are computationally expensive for a larger number of cells [90]. By coupling matrix fiber models to our CPM framework, we can study the effect of long-range communication between cells through the matrix fibers on the tissue level. Furthermore, we could study how the interactions between cells, fibers and matrix stiffness regulate morphogenesis.

7.4.3 Chemical-mechanical interactions

Another interesting extension would be to combine models for chemical and mechanical signaling in cells. For instance, signaling of Rho-family GTPases in the cytoskeleton, which is involved in cell migration and cell polarization, regulates cell

contractility and cell-matrix forces in turn feed back on Rho-signaling. It would be interesting to implement existing models of Rho-family GTPases signaling [147] and cell-matrix interactions [344]. Coupling such models to our multiscale model including focal adhesion, could give new insights on the molecular mechanisms behind cells polarization and migration as a result of mechanical and chemical cues [345]. There also exists feedback between mechanical forces and growth factors in the extracellular matrix. For instance, the growth factor TGF-β is secreted by epithelial cells in an inactive form that subsequently can bind to the matrix [324]. Stretching of this bound molecule allows it to be released from the matrix in an active form, that can diffuse freely through the matrix [325]. On stiffer matrices, the matrix-bound TGF-β experiences more stress, which induces its release [325]. The release from TGF-β is of particular interest to fibrotic diseases [346] and branching morphogenesis. We could couple our CPM for branching morphogenesis to a FEM and include binding of TGF-β to the matrix and its release from the matrix [347] and study how matrix stresses and matrix stiffness influences branching morphogenesis. Activation of TGF-β can also occur in other ways than matrix stress [320]. The activation of TGF-β is for instance mediated by integrin binding [348]. Upon binding with integrin, the matrix stress activation of TGF-β is further promoted [349]. In turn, TGF-β feeds back on cell contractility [348]. It would be interesting to investigate such feedback dynamics with our model. Furthermore, it is possible that other growth factors can also be released from the matrix by mechanical forces [350]. So, modeling such dynamics can help explore the possible effects matrix-bound growth factors have on morphogenesis.

Another important aspect in tissue patterning is cell-cell signaling mediated by membrane bound signaling molecules. Interestingly, such signaling also depends on physical forces. For instance, internalization of the VEGF-R2 receptors and VEGF signaling is enhanced on stiffer matrices, most likely due to increased contraction [351]. Because the CPM allows to describe cell-cell membrane contact, our model may be used to study how such dynamics [351] affects the formation of vascular networks on compliant matrices. Furthermore, it has been shown that cell-cell cadherin adhesions, that mediate cell-cell signaling, can behave as catch-bonds [352]. Through cadherins, cells apply forces on each other and such forces can be transmitted through the whole tissue via actin stress fibers [26]. Actin stress fibers remodel and reorient in response to forces [176, 353]. The orientation of stress fibers regulates cell shape [354] and the direction of force application [355]. We could implement a model for stress fiber remodeling (see *e.g.* [356]) into our CPM. Due to our the multiscale nature of our model, such an approach may give insights into how feedback between forces, cell shape and stress fibers regulates cell response to matrix mechanics. On a tissue level scale, we could study how long-range intercellular cell-cell communication via forces drives morphogenesis.

7.5 Long term prospects

The type of multiscale modeling approaches as presented in this thesis may in the long run assist in developing new treatments. Here we will provide examples of some of the possibilities. For instance, our modeling approach could be used to help design tissue engineering approaches. By mechanically loading tissues, it is possible to align tissues [54]. Our model could help to investigate what experimental condition brings about the desired tissue pattern. For instance, van der Schaft *et al.* [94] showed that a tissue consisting of a mix of muscle cells and endothelial cells aligned to uniaxial stretch and that the endothelial cells started to form lumen. Models can be used to better understand the effect of a mixture of different cell types on the tissue patterning. Furthermore, we could use our modeling approach to help understand how cell alignment depends on the type of stretching. Cells typically align parallel to static uniaxial stretch but perpendicular to cyclic stretch. Interestingly, cell alignment to cyclic stretch depends on the amplitude [357] and frequency of the stretch [358] and the stiffness of the substrate [176]. Other future directions are the response of tissues to biaxial stretch [359] and the effect of tissue geometry on tissue patterning [360].

Mechanical forces also play a crucial role in cancer. Physical forces on different scales regulate cancer progression. Changes in the mechanics of the extracellular matrix are associated with cancer metastasis [53]. Cancer cells are able to excessively remodel the matrix, inducing high matrix alignment and matrix stiffening, which directs cancer cell migration. Furthermore, matrix properties, like for instance matrix stiffness, regulates the malignant phenotype of cells *in vitro* [361]. Mechanical cell-cell interactions through cadherins have also been shown to drive collective cell migration *in vitro*, suggesting an involvement in cancer invasion [362]. The modeling methods presented in this thesis may be ultimately used to give insights into how cancer growth and metastatic potential are associated with cell and tissue specific parameters derived from tissue samples. Models can also be used to help develop new targets for cancer treatment. For instance, models that relate focal adhesion dynamics to tissue level dynamics can provide clues into how focal adhesions may be targeted to inhibit cancer progression. Furthermore, models can give insights into how cancer progression could be inhibited by manipulating the extracellular matrix.

In conclusion, due to the multiscale nature of our model, it is possible to include many interesting dynamics and due to its generic set up, it is possible to study many different experimental systems. These examples range from tissue engineering, cancer migration/invasion and various morphogenetic processes like cell sorting [336, 363], angiogenesis, branching, left-right patterning [364] and somitogenesis [365].

Appendix A: deriving forces from CPM Hamiltonian

In chapter 2, 3 and 4 we presented a hybrid cellular Potts model (CPM) which we coupled to a Finite Element Model (FEM) of the substrate. Here, the forces that a cell applies on the substrate are described by a first moment of area model. Alternatively, we can derive the forces $\vec{f}$ a single cell exerts on the matrix in the FEM from the Hamiltonian in the CPM. As an example, the Hamiltonian that describes cell-matrix force H_{cm} may describe a surface tension and line tension as:

$$H_{cm} = \lambda A + \sum_{\{(\vec{x},\vec{x}\prime)|\sigma(\vec{x})\neq\sigma(\vec{x}\prime)\}} J_{01} \tag{7.1}$$

In the CPM, cell movements are simulated by making copies from lattice sites to neighboring lattice sites, which models cell membrane deformations in a discrete fashion (see figure 7.3).

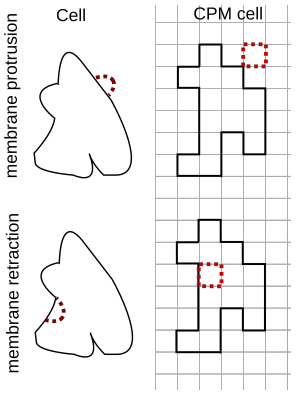

Figure 7.3: CPM discretizes cell membrane and simulates membrane protrusions and retractions

Copies only have effect on the cell membrane, as in the cell interior copies will not change the configuration and thus $\Delta H = 0$. So, forces will only be defined (non-zero) on points on the cell membrane. To couple the CPM to the FEM, the forces $\vec{f}$ need to

be approximated on the *nodes* of the grid. First, we explain how we derive forces on the cell membrane using H_{cm} in the CPM and next we explain how we approximate the forces on the nodes.

Virtual work

To derive the forces a cell exerts on the matrix $\vec{f}(\vec{x})$ from the Hamiltonian H_{cm} we need to principle of virtual work. Virtual work is defined as the work of a force acting on a body if it would move along a certain virtual displacement. For instance, if a particle is subject to a constant force $\vec{f}$, then, the virtual work W this particle experiences by virtually displacing $\vec{\delta x}$ is $W = \vec{f} \cdot \vec{\delta x}$, where $\cdot$ is the dot product. In other words, virtual work is the *scalar projection* of force in the direction of the displacement $\vec{\delta x}$, multiplied with the amount of virtual displacement $|\vec{\delta x}|$.

In the CPM, a cell experiences virtual work due to potentially extending or retracting the cell membrane in a certain direction, which are dictated by the type of lattice used. When one uses the conventional 2D square lattice, forces a defined in four directions. Now, let $\vec{f}(\vec{x})$ be the force on the cell membrane at $\vec{x}$ and let $-\Delta\hat{H}_{\vec{\delta x}}(\vec{x})$ be the virtual work of displacing the cell membrane at $\vec{x}$ in the direction of $\vec{\delta x}$. Then,

$$\vec{f}(\vec{x}) \cdot \vec{\delta x} = -\Delta\hat{H}_{\vec{\delta x}}(\vec{x}) \tag{7.2}$$

For a visual representation, see Figure 7.4. The possible directions of cell membrane deformations are determined by the lattice of the CPM (Figure 7.3 and 7.5). Because we are working on a 2D square grid, the CPM can calculate the virtual work in four directions, namely North, North-East, East and South-East (see Figure 7.5). For a given direction $\vec{\delta x}$, we can extend or retract the membrane, *i.e.* we can copy the spin of $\vec{x}$ onto $\sigma(\vec{x}+\vec{\delta x})$ or the other way around. Therefore, the virtual work $-\Delta\hat{H}_{\vec{\delta x}}$ in the direction $\vec{\delta x}$ is given by

$$\Delta\hat{H}_{\vec{\delta x}}(\vec{x}) = -\left(\frac{\Delta H_{\mathrm{cm}}(\sigma(\vec{x}) \to \sigma(\vec{x}+\vec{\delta x})) - \Delta H_{\mathrm{cm}}(\sigma(\vec{x}+\vec{\delta x}) \to \sigma(\vec{x}))}{2}\right), \tag{7.3}$$

Much in the same way as one would calculate a surface tension: (internal pressure - external pressure)/2, where the dividing by two arises from the membrane having two sides that contribute to the force.

Work on the nodes

Now note that finding $\vec{f}$ from virtual work (the *scalar projections* of $\vec{f}$) known/given in different directions, is an *inverse* problem. In the FEM, the forces $\vec{f}$ need to be defined on the *nodes* of the grid. So, given virtual work on the *cell membrane* (Figure 7.5), we want to derive the forces on the nodes. We approximate the virtual work in four directions on the *nodes* as follows. Let $f_N(\vec{n})$, $f_{NE}(\vec{n})$, $f_E(\vec{n})$ and $f_{SE}(\vec{n})$ be the *scalar*

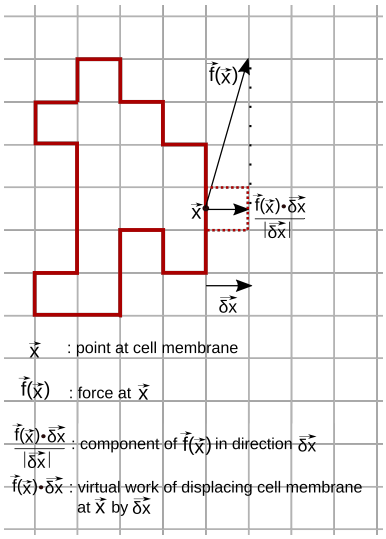

Figure 7.4: Force and virtual work in the CPM

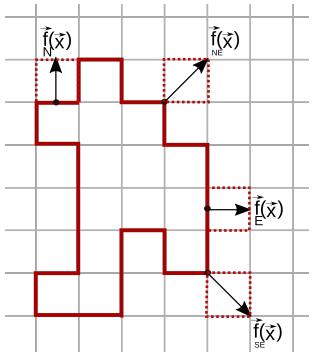

Figure 7.5: Possible direction of forces in a 2D square grid CPM

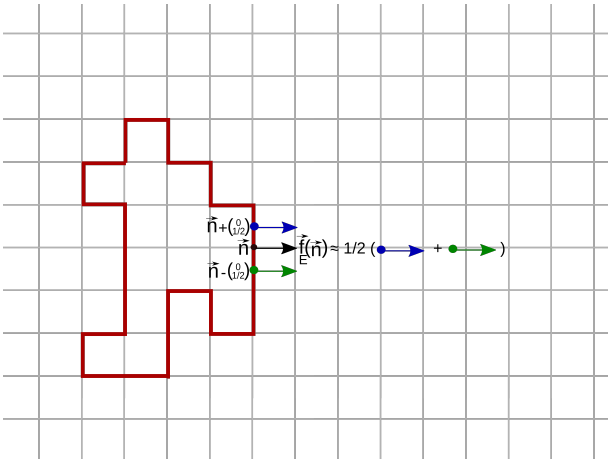

Figure 7.6: Example of approximating force component in direction East at a node

projections of the force $\vec{f}(\vec{n})$ on node $\vec{n}$ in the direction North, North, North-East, East and South-East, respectively. Then,

$$f_N(\vec{n}) \approx \frac{-\frac{1}{2}\Delta\hat{H}_{\delta\vec{x}_N}(\vec{n}-(\frac{1}{2},0)^T)-\frac{1}{2}\Delta\hat{H}_{\delta\vec{x}_N}(\vec{n}+(\frac{1}{2},0)^T)}{2} \tag{7.4}$$

$$f_{NE}(\vec{n}) = -\frac{\Delta\hat{H}_{\delta\vec{x}_{NE}}(\vec{n})}{\sqrt{2}} \tag{7.5}$$

$$f_E(\vec{n}) \approx \frac{-\frac{1}{2}\Delta\hat{H}_{\delta\vec{x}_E}(\vec{n}-(0,\frac{1}{2})^T)-\frac{1}{2}\Delta\hat{H}_{\delta\vec{x}_E}(\vec{n}+(0,\frac{1}{2})^T)}{2} \tag{7.6}$$

$$f_{SE}(\vec{n}) = -\frac{\Delta\hat{H}_{\delta\vec{x}_{SE}}(\vec{n})}{\sqrt{2}} \tag{7.7}$$

where $\delta\vec{x}_N = (0,1)^T, \delta\vec{x}_{NE} = (1,1)^T, \delta\vec{x}_E = (1,0)^T$ and $\delta\vec{x}_{SE} = (1,-1)^T$. The $\sqrt{2}$ in the terms for $f_{NE}(\vec{n})$ and $f_{SE}(\vec{n})$ arise from $|\delta x_{NE}| = |\delta x_{SE}| = \sqrt{2}$. For an example of how the force component in direction East at a node is calculated, see figure 7.6.

Deriving force from virtual work

Now, to find $\vec{f}(\vec{n})$ we can use equation 7.2 which gives us

$$\frac{\vec{f}(\vec{n}) \cdot \delta\vec{x_N}}{|\delta\vec{x_N}|} = f_N(\vec{n}) \tag{7.8}$$

$$\frac{\vec{f}(\vec{n}) \cdot \delta\vec{x_{NE}}}{|\delta\vec{x_{NE}}|} = f_{NE}(\vec{n}) \tag{7.9}$$

$$\frac{\vec{f}(\vec{n}) \cdot \delta\vec{x_E}}{|\delta\vec{x_E}|} = f_E(\vec{n}) \tag{7.10}$$

$$\frac{\vec{f}(\vec{n}) \cdot \delta\vec{x_{SE}}}{|\delta\vec{x_{SE}}|} = f_{SE}(\vec{n}) \tag{7.11}$$

This is an inverse problem. We can approximate $\vec{f}(\vec{n})$ by minimizing the sum of squares

$$\left(\frac{\vec{f}(\vec{n}) \cdot \delta\vec{x_N}}{|\delta\vec{x_N}|} - f_N(\vec{n})\right)^2 + \left(\frac{\vec{f}(\vec{n}) \cdot \delta\vec{x_{NE}}}{|\delta\vec{x_{NE}}|} - f_{NE}(\vec{n})\right)^2 + \ldots \tag{7.12}$$
$$\left(\frac{\vec{f}(\vec{n}) \cdot \delta\vec{x_E}}{|\delta\vec{x_E}|} - f_E(\vec{n})\right)^2 + \left(\frac{\vec{f}(\vec{n}) \cdot \delta\vec{x_{SE}}}{|\delta\vec{x_{SE}}|} - f_{SE}(\vec{n})\right)^2$$

We use a Levenberg-Marquardt algorithm that numerically minimizes equation 7.12 for $\vec{f}(\vec{n}) = (Vcos(\alpha), Vsin(\alpha))^T$ with $\alpha \in [0, 2\pi]$ and $V \in [0, \inf]$ with initial condition $\vec{f}(\vec{n}) = \max\{f_N(\vec{n}), f_{NE}(\vec{n}), f_E(\vec{n}), f_{SE}(\vec{n})\}$.

Bibliography

[1] Fraisl, P. et al. Regulation Of Angiogenesis By Oxygen And Metabolism. *Developmental Cell* 16(2), 2009, 167–179.

[2] Folkman, J and Kalluri, R. Chapter 11: Tumor Angiogenesis. In: *Cancer Medicine*. Ed. by Kufe, D. et al. Hamilton (ON): BC Decker, 2003.

[3] Valastyan, S. and Weinberg, R. A. Tumor Metastasis: Molecular Insights And Evolving Paradigms. *Cell* 147(2), 2011, 275–292.

[4] Doyle, A. et al. The Construction Of Transgenic And Gene Knockout/knockin Mouse Models Of Human Disease. *Transgenic Research* 21(2), 2012, 327–349.

[5] Prelich, G. Gene Overexpression: Uses, Mechanisms, And Interpretation. *Genetics* 190(3), 2012, 841–854.

[6] Hong, H. et al. Imaging Gene Expression In Live Cells And Tissues. *Cold Spring Harbor Protocols* 2011(4), 2011, pdb.top103.

[7] Harney, A. S. and Meade, T. J. Molecular Imaging Of In Vivo Gene Expression. *Future* 2(3), 2010, 503–519.

[8] Wolpert, L. Positional Information And The Spatial Pattern Of Cellular Differentiation. *Journal of Theoretical Biology* 25(1), 1969, 1–47.

[9] Turing, A. The Chemical Basis Of Morphogenesis. *Philosophical Transactions of the Royal Society B: Biological Sciences* 237(641), 1952, 37–72.

[10] Makarenkova, H. P. et al. Differential Interactions Of FGFs With Heparan Sulfate Control Gradient Formation And Branching Morphogenesis. *Science Signaling* 2(88), 2009, ra55.

[11] Artavanis-Tsakonas, S. et al. Notch Signaling: Cell Fate Control And Signal Integration In Development. *Science* 284(5415), 1999, 770–776.

[12] Collier, J. R. et al. Pattern Formation By Lateral Inhibition With Feedback: A Mathematical Model Of Delta-Notch Intercellular Signalling. *Journal of Theoretical Biology* 183(4), 1996, 429 –446.

[13] Thompson, D. *On Growth And Form*. Cambridge University Press, 1917.

[14] Savin, T. et al. On The Growth And Form Of The Gut. *Nature* 476(7358), 2011, 57–62.

[15] Goriely, A. et al. Elastic Growth Models. In: *Mathematical Modelling of Biosystems, Applied Optimization*. Ed. by Mondaini, R. and Pardalos, P. Vol. 102. Berlin, Heidelberg: Springer, 2008.

[16] Hillam, R. A. and Skerry, T. M. Inhibition Of Bone Resorption And Stimulation Of Formation By Mechanical Loading Of The Modeling Rat Ulna In Vivo. *Journal of Bone and Mineral Research* 10(5), 1995, 683–689.

[17] Huiskes, R. et al. Effects Of Mechanical Forces On Maintenance And Adaptation Of Form In Trabecular Bone. *Nature* 405(6787), 2000, 704–706.

[18] Oers, R. F. M. van et al. A Unified Theory For Osteonal And Hemi-osteonal Remodeling. *Bone* 42(2), 2008, 250–259.

[19] Harris, A. K. et al. Silicone Rubber Substrata: A New Wrinkle In The Study Of Cell Locomotion. *Science* 208(4440), 1980, 177–179.

[20] Ingber, D. E. Tensegrity I. Cell Structure And Hierarchical Systems Biology. *Journal of Cell Science* 116(7), 2003, 1157–1173.

[21] Stamenovic, D. and Ingber, D. E. Tensegrity-guided Self Assembly: From Molecules To Living Cells. *Soft Matter* 5, 6 2009, 1137–1145.

[22] Katoh, K et al. Isolation And Contraction Of The Stress Fiber. *Molecular Biology of the Cell* 9(7), 1998, 1919–1938.

[23] Balaban, N. Q. et al. Force And Focal Adhesion Assembly: A Close Relationship Studied Using Elastic Micropatterned Substrates. *Nature Cell Biology* 3(May), 2001.

[24] Nelson, W. J. et al. Interaction Of Cadherin With The Actin Cytoskeleton. *Novartis Foundation Symposium* 269, 2005, 159–177,223–230.

[25] Miller, C. J. and Davidson, L. A. The Interplay Between Cell Signalling And Mechanics In Developmental Processes. *Nature Reviews. Genetics* 14(10), 2013, 733–744.

[26] Siedlik, M. J. and Nelson, C. M. Regulation Of Tissue Morphodynamics: An Important Role For Actomyosin Contractility. *Current Opinion in Genetics and Development* 32, 2015, 80–85.

[27] Davies, J. A. Chapter 11 - Guidance By Contact. In: *Mechanisms of Morphogenesis (Second Edition)*. Ed. by Davies, J. A. Second Edition. Boston: Academic Press, 2013, 129 –145.

[28] Sapir, L. and Tzlil, S. "Talking Over The Extracellular Matrix: How Do Cells Communicate Mechanically?" In: *Seminars in Cell & Developmental Biology*. Elsevier. 2017.

[29] Smithmyer, M. E. et al. Hydrogel Scaffolds As In Vitro Models To Study Fibroblast Activation In Wound Healing And Disease. *Biomaterials Science* 2(5), 2014, 634–650.

[30] Tibbitt, M. W. and Anseth, K. S. Hydrogels As Extracellular Matrix Mimics For 3D Cell Culture. *Biotechnology and Bioengineering* 103(4), 2009, 655–663.

[31] Reinhart-King, C. A. et al. Endothelial Cell Traction Forces On RGD-derivatized Polyacrylamide Substrata. *Langmuir* 19(5), 2003, 1573–1579.

[32] Reinhart-King, C. A. et al. Cell-cell Mechanical Communication Through Compliant Substrates. *Biophysical Journal* 95(12), 2008, 6044–6051.

[33] Winer, J. P. et al. Non-linear Elasticity Of Extracellular Matrices Enables Contractile Cells To Communicate Local Position And Orientation. *PLOS ONE* 4(7), 2009, e6382.

[34] Xu, X. and Safran, S. A. Nonlinearities Of Biopolymer Gels Increase The Range Of Force Transmission. *Physical Review E* 92(3), 2015, 032728.

[35] Sieminski, A. et al. The Relative Magnitudes Of Endothelial Force Generation And Matrix Stiffness Modulate Capillary Morphogenesis In Vitro. *Experimental Cell Research* 297(2), 2004, 574–584.

[36] Califano, J. and Reinhart-King, C. A Balance Of Substrate Mechanics And Matrix Chemistry Regulates Endothelial Cell Network Assembly. *Cellular and Molecular Bioengineering* 1(2), 2008, 122–132.

[37] Helvert, S. van and Friedl, P. Strain Stiffening Of Fibrillar Collagen During Individual And Collective Cell Migration Identified By Afm Nanoindentation. *ACS Applied Materials & Interfaces* 8(34), 2016, 21946–21955.

[38] Angelini, T. E. et al. Cell Migration Driven By Cooperative Substrate Deformation Patterns. *Physical Review Letters* 104(16), 2010, 168104.

[39] Gjorevski, N. et al. Dynamic Tensile Forces Drive Collective Cell Migration Through Three-dimensional Extracellular Matrices. *Scientific Reports* 5, 2015, 11458.

[40] Balcioglu, H. E. et al. Tumor-induced Remote Ecm Network Orientation Steers Angiogenesis. *Scientific Reports* 6, 2016, 22580.

[41] De, R. et al. Do Cells Sense Stress Or Strain? Measurement Of Cellular Orientation Can Provide A Clue. *Biophysical Journal* 94(5), 2008, L29–L31.

[42] Ben-Yaakov, D. et al. Response Of Adherent Cells To Mechanical Perturbations Of The Surrounding Matrix. *Soft Matter* 11(7), 2015, 1412–1424.

[43] Brown, R. et al. Tensional Homeostasis In Dermal Fibroblasts: Mechanical Responses To Mechanical Loading In Three-dimensional Substrates. *Journal of Cellular Physiology* 175(3), 1998, 323–332.

[44] Saez, A. et al. Is The Mechanical Activity Of Epithelial Cells Controlled By Deformations Or Forces? *Biophysical Journal* 89(6), 2005, L52–L54.

[45] Bischofs, I. B. and Schwarz, U. S. Cell Organization In Soft Media Due To Active Mechanosensing. *Proceedings of the National academy of Sciences of the United States of America* 100(16), 2003, 9274–9297.

[46] Bischofs, I. B. and Schwarz, U. S. Effect Of Poisson Ratio On Cellular Structure Formation. *Physical Review Letters* 95(6), 2005, 068102.

[47] Zemel, A et al. Optimal Matrix Rigidity For Stress-fibre Polarization In Stem Cells. *Nature Physics* 6(6), 2010, 468–473.

[48] Deshpande, V. S. et al. A Bio-mechanical Model For Coupling Cell Contractility With Focal Adhesion Formation. *Journal of the Mechanics and Physics of Solids* 56(4), 2008, 1484 –1510.

[49] Besser, A. and Safran, S. A. Force-induced Adsorption And Anisotropic Growth Of Focal Adhesions. *Biophysical Journal* 90(10), 2006, 3469–3484.

[50] Ma, X. et al. Fibers In The Extracellular Matrix Enable Long-range Stress Transmission Between Cells. *Biophysical Journal* 104(7), 2013, 1410–1418.

[51] Korff, T and Augustin, H. G. Tensional Forces In Fibrillar Extracellular Matrices Control Directional Capillary Sprouting. *Journal of Cell Science* 112(19), 1999, 3249–3258.

[52] Crest, J. et al. Organ Sculpting By Patterned Extracellular Matrix Stiffness. *eLife* 27(6), 2017, e24958.

[53] Cox, T. R. and Erler, J. T. Remodeling And Homeostasis Of The Extracellular Matrix: Implications For Fibrotic Diseases And Cancer. *Disease Models & Mechanisms* 4(2), 2011, 165–178.

[54] Grenier, G et al. Tissue Reorganization In Response To Mechanical Load Increases Functionality. *Cell Motility and the Cytoskeleton* 11(1–2), 2005, 90–100.

[55] Bouten, C. et al. Substrates For Cardiovascular Tissue Engineering. *Advanced Drug Delivery Reviews* 63(4), 2011, 221 –241.

[56] Guilak, F. et al. Biomechanics And Mechanobiology In Functional Tissue Engineering. *Journal of Biomechanics* 47(9), 2014, 1933 –1940.

[57] Brodland, G. W. How Computational Models Can Help Unlock Biological Systems. *Seminars in Cell & Developmental Biology* 47-48, 2015, 62–73.

[58] Mogilner, A. et al. Quantitative Modeling In Cell Biology: What Is It Good For? *Developmental Cell* 11(3), 2006, 279–287.

[59] Baker, R. E. et al. Partial Differential Equations For Self-organization In Cellular And Developmental Biology. *Nonlinearity* 21(11), 2008, R251–R290.

[60] Merks, R. M. H. and Glazier, J. A. A Cell-centered Approach To Developmental Biology. *Physica A: Statistical Mechanics and its Applications* 352(1), 2005, 113–130.

[61] Walpole, J. et al. Multiscale Computational Models Of Complex Biological Systems. *Annual Review of Biomedical Engineering* 15, 2013, 137–154.

[62] Merks, R. "Cell-Based Modeling". In: *Encyclopedia of Applied and Computational Mathematics*. Ed. by Engquist, B. Berlin, Heidelberg: Springer Berlin Heidelberg, 2015, 195–201.

[63] Gregoire, G. et al. Moving And Staying Together Without A Leader. *Physica D: Nonlinear Phenomena* 181(3), 2003, 157 –170.

[64] Byrne, H. and Drasdo, D. Individual-based And Continuum Models Of Growing Cell Populations: A Comparison. *Journal of Mathematical Biology* 58(4-5), 2009, 657–687.

[65] Antonovici, C. et al. Multiscale Analysis Of Morphogenesis. In: *Encyclopedia of Cell Biology*. Ed. by Stahl, P. et al. Waltham: Academic Press/Elsevier, 2016, 122 –133.

[66] Szabó, A. et al. Network Formation Of Tissue Cells Via Preferential Attraction To Elongated Structures. *Physical Review Letters* 98(3), 2007, 038102.

[67] Sepúlveda, N. et al. Collective Cell Motion In An Epithelial Sheet Can Be Quantitatively Described By A Stochastic Interacting Particle Model. *PLoS Computational Biology* 9(3), 2013, e1002944.

[68] Dallon, J. C. et al. Mathematical Modelling Of Extracellular Matrix Dynamics Using Discrete Cells: Fiber Orientation And Tissue Regeneration. *Journal of Theoretical Biology* 199(4), 1999, 449–471.

[69] Dallon, J. C. Numerical Aspects Of Discrete And Continuum Hybrid Models In Cell Biology. *Applied Numerical Mathematics* 32(2), 2000, 137 –159.

[70] Newman, T. J. Modeling Multicellular Systems Using Subcellular Elements. *Mathematical Biosciences and Engineering* 2(3), 2005, 613–624.

[71] Sandersius, S. A. et al. A 'chemotactic Dipole' Mechanism For Large-scale Vortex Motion During Primitive Streak Formation In The Chick Embryo. *Physical Biology* 8(4), 2011, 45008.

[72] Graner, F. and Glazier, J. A. Simulation Of Biological Cell Sorting Using A Two-dimensional Extended Potts Model. *Physical Review Letters* 69(13), 1992, 2013–2016.

[73] Glazier, J. A. and Graner, F. Simulation Of The Differential Adhesion Driven Rearrangement Of Biological Cells. *Physical Review E* 47(3), 1993, 2128–2154.

[74] Voss-Bohme, A. Multi-scale Modeling In Morphogenesis: A Critical Analysis Of The Cellular Potts Model. *PLOS ONE* 7(9), 2012, e42852.

[75] Savill, N. J. and Hogeweg, P. Modelling Morphogenesis: From Single Cells To Crawling Slugs. *Journal of Theoretical Biology* 184(3), 1997, 229–235.

[76] Zajac, M et al. Simulating Convergent Extension By Way Of Anisotropic Differential Adhesion. *Journal of Theoretical Biology* 222(2), 2003, 247–259.

[77] Merks, R. M. H. et al. Cell Elongation Is Key To In Silico Replication Of In Vitro Vasculogenesis And Subsequent Remodeling. *Developments in Biologicals* 289(1), 2006, 44–54.

[78] Turner, S and Sherratt, J. A. Intercellular Adhesion And Cancer Invasion: A Discrete Simulation Using The Extended Potts Model. *Journal of Theoretical Biology* 216(1), 2002, 85–100.

[79] Murray, J. D. et al. A Mechanical Model For Mesenchymal Morphogenesis. *Journal of Mathematical Biology* 17(1), 1983, 125–129.

[80] Manoussaki, D et al. A Mechanical Model For The Formation Of Vascular Networks In Vitro. *Acta Biotheoretica* 44(3-4), 1996, 271–282.

[81] Manoussaki, D. A Mechanochemical Model Of Angiogenesis And Vasculogenesis. *ESAIM: Mathematical Modelling and Numerical Analysis* 37(4), 2003, 581–599.

[82] Namy, P et al. Critical Conditions For Pattern Formation And In Vitro Tubulogenesis Driven By Cellular Traction Fields. *Journal of Theoretical Biology* 227(1), 2004, 103–120.

[83] Cumming, B. D. et al. A Mathematical Model Of Wound Healing And Subsequent Scarring. *Journal of The Royal Society Interface* 7(42), 2010, 19–34.

[84] Barocas, V. H. and Tranquillo, R. T. Biphasic Theory And In Vitro Assays Of Cell-fibril Mechanical Interactions In Tissue-equivalent Gels. In: *Cell Mechanics and Cellular Engineering*. Ed. by Mow, V. et al. New York, NY: Springer, 1994, 185–209.

[85] Barocas, V. H. and Tranquillo, R. T. An Anisotropic Biphasic Theory Of Tissue-equivalent Mechanics: The Interplay Among Cell Traction, Fibrillar Network Deformation, Fibril Alignment, And Cell Contact Guidance. *Journal of Biomechanical Engineering* 119(2), 1997, 137–145.

[86] Dyson, R. J. et al. An Investigation Of The Influence Of Extracellular Matrix Anisotropy And Cell Matrix Interactions On Tissue Architecture. *Journal of Mathematical Biology* 72(7), 2016, 1775–1809.

[87] Checa, S. et al. The Emergence Of Extracellular Matrix Mechanics And Cell Traction Forces As Important Regulators Of Cellular Self-organization. *Biomech Model Mechan.* 14(1), 2014, 1–13.

[88] Yang, L. et al. A Biomechanical Model Of Wound Contraction And Scar Formation. *Journal of Theoretical Biology* 332, 2013, 228–248.

[89] Schluter, D. K. et al. Computational Modeling Of Single-cell Migration: The Leading Role Of Extracellular Matrix Fibers. *Biophysical Journal* 103(6), 2012, 1141–1151.

[90] Reinhardt, J. W. et al. Complex Matrix Remodeling And Durotaxis Can Emerge From Simple Rules For Cell-matrix Interaction In Agent-based Models. *Journal of Biomechanical Engineering* 135(7), 2013, 71003.

[91] Gardiner, B. S. et al. Discrete Element Framework For Modelling Extracellular Matrix, Deformable Cells And Subcellular Components. *PLoS Computational Biology* 11(10), 2015, e1004544.

[92] Bauer, A. L. et al. A Cell-based Model Exhibiting Branching And Anastomosis During Tumor-induced Angiogenesis. *Biophysical Journal* 92(9), 2007, 3105–3121.

[93] Bauer, A. L. et al. Topography Of Extracellular Matrix Mediates Vascular Morphogenesis And Migration Speeds In Angiogenesis. *PLoS Computational Biology* 5(7), 2009, e1000445.

[94] Schaft, D. W. J. van der et al. Mechanoregulation Of Vascularization In Aligned Tissue-engineered Muscle: A Role For Vascular Endothelial Growth Factor. *Tissue Engineering Part A* 17(21-22), 2011, 2857–2865.

[95] Eastwood, M. et al. Effect Of Precise Mechanical Loading On Fibroblast Populated Collagen Lattices: Morphological Changes. *Cell Motility and the Cytoskeleton* 40(1), 1998, 13–21.

[96] Schwarz, U. S. et al. Focal Adhesions As Mechanosensors: The Two-spring Model. *Biosystems* 83(2-3), 2006, 225–232.

[97] Tessadori, F. et al. Nodal Signaling Range Is Regulated By Proprotein Convertase-mediated Maturation. *Developmental Cell* 32(5), 2015, 631–639.

[98] Nelson, C. M. et al. Tissue Geometry Determines Sites Of Mammary Branching Morphogenesis In Organotypic Cultures. *Science* 314(5797), 2006, 298–300.

[99] Hynes, R. O. The Extracellular Matrix: Not Just Pretty Fibrils. *Science* 326(5957), 2009, 1216–1219.

[100] Mammoto, A. et al. A Mechanosensitive Transcriptional Mechanism That Controls Angiogenesis. *Nature* 457(7233), 2009, 1103–1108.

[101] Nelson, C. M. et al. Emergent Patterns Of Growth Controlled By Multicellular Form And Mechanics. *Proceedings of the National academy of Sciences of the United States of America* 102(33), 2005, 11594–11599.

[102] Folkman, J and Hauenschild, C. Angiogenesis In Vitro. *Nature* 288(5791), 1980, 551–556.

[103] Kniazeva, E and Putnam, A. J. Endothelial Cell Traction And Ecm Density Influence Both Capillary Morphogenesis And Maintenance In 3D. *American Journal of Physiology - Cell Physiology* 297(1), 2009, C179–C187.

[104] Vernon, R. B. R. and Sage, E. H. E. Between Molecules And Morphology. Extracellular Matrix And Creation Of Vascular Form. *American Journal of Pathology* 147(4), 1995, 873–883.

[105] Vernon, R. B. R. et al. Organized Type I Collagen Influences Endothelial Patterns During "spontaneous Angiogenesis In Vitro": Planar Cultures As Models Of Vascular Development. *In Vitro Cellular & Developmental Biology - Animal* 31(2), 1995, 120–131.

[106] Koolwijk, P et al. Cooperative Effect Of TNFα, BFGF, And VEGF On The Formation Of Tubular Structures Of Human Microvascular Endothelial Cells In A Fibrin Matrix. Role Of Urokinase Activity. *Journal of Cell Biology* 132(6), 1996, 1177–1188.

[107] Merks, R. M. H. and Koolwijk, P. Modeling Morphogenesis In Silico And In Vitro: Towards Quantitative, Predictive, Cell-based Modeling. *Mathematical Modelling of Natural Phenomena* 4(5), 2009, 149–171.

[108] Boas, S. E. M. et al. Computational Modeling Of Angiogenesis: Towards A Multi-scale Understanding Of Cell–Cell And Cell–Matrix Interactions. In: *Mechanical and Chemical Signaling in Angiogenesis*. Ed. by Reinhart-King, C. Berlin, Heidelberg: Springer Berlin Heidelberg, 2012, 161–183.

[109] Scianna, M et al. A Review Of Mathematical Models For The Formation Of Vascular Networks. *Journal of Theoretical Biology* 333, 2013, 174–209.

[110] Oster, G. F. et al. Mechanical Aspects Of Mesenchymal Morphogenesis. *Journal of Embryology and Experimental Morphology* 78, 1983, 83–125.

[111] Gamba, A et al. Percolation, Morphogenesis, And Burgers Dynamics In Blood Vessels Formation. *Physical Review Letters* 90(11), 2003, 118101.

[112] Serini, G. et al. Modeling The Early Stages Of Vascular Network Assembly. *EMBO Journal* 22(8), 2003, 1771–1779.

[113] Keller, E. F. and Segel, L. A. Initiation Of Slime Mold Aggregation Viewed As An Instability. *Journal of Theoretical Biology* 26(3), 1970, 399–415.

[114] Merks, R. M. H. et al. Contact-inhibited Chemotaxis In De Novo And Sprouting Blood-vessel Growth. *PLoS Computational Biology* 4(9), 2008, e1000163.

[115] Köhn-Luque, A. et al. Early Embryonic Vascular Patterning By Matrix-mediated Paracrine Signalling: A Mathematical Model Study. *PLOS ONE* 6(9), 2011, e24175.

[116] Köhn-Luque, A et al. Dynamics Of VEGF Matrix-retention In Vascular Network Patterning. *Physical Biology* 10(6), 2013, 066007.

[117] Kleinstreuer, N. et al. A Computational Model Predicting Disruption Of Blood Vessel Development. *PLoS Computational Biology* 9(4), 2013, e1002996.

[118] Singh, J. et al. Role Of Differential Adhesion In Cell Cluster Evolution: For Vasculogenesis To Cancer Metastasis. *Computer Methods in Biomechanics and Biomedical Engineering* 18(3), 2013, 282–292.

[119] Palm, M. M. and Merks, R. M. H. Vascular Networks Due To Dynamically Arrested Crystalline Ordering Of Elongated Cells. *Physical Review E* 87, 2013, 012725.

[120] Murray, J. D. et al. A Mechanical Theory Of In Vitro Vascular Network Formation. In: *Vascular Morphogenesis: In Vivo, In Vitro, In Mente*. Ed. by Mironov, V. A. et al. Boston: Birkhaüser, 1996, 173–188.

[121] Szabó, A. et al. Multicellular Sprouting In Vitro. *Biophysical Journal* 95(6), 2008, 2702–2710.

[122] Tan, J. L. et al. Cells Lying On A Bed Of Microneedles: An Approach To Isolate Mechanical Force. *Proceedings of the National academy of Sciences of the United States of America* 100(4), 2003, 1484–1489.

[123] Reinhart-King, C. A. et al. The Dynamics And Mechanics Of Endothelial Cell Spreading. *Biophysical Journal* 89(1), 2005, 676–689.

[124] Califano, J. P. and Reinhart-King, C. A. Exogenous And Endogenous Force Regulation Of Endothelial Cell Behavior. *Journal of Biomechanics* 43(1), 2010, 79–86.

[125] Winer, J. P. et al. Substrate Elasticity As A Probe To Measure Mechanosensing At Cell-cell And Cell-matrix Junctions. In: *Mechanobiology Of Cell-cell And Cell-matrix Interactions*. Ed. by Wagoner, J. A. and Harley, B. A. C. Boston, MA: Springer US, 2011, 11–22.

[126] Lo, C.-M. et al. Cell Movement Is Guided By The Rigidity Of The Substrate. *Biophysical Journal* 79(1), 2000, 144–152.

[127] Califano, J. P. and Reinhart-King, C. A. Substrate Stiffness And Cell Area Predict Cellular Traction Stresses In Single Cells And Cells In Contact. *Cellular and Molecular Bioengineering* 3(1), 2010, 68–75.

[128] Pelham, R. J. R. and Wang, Y. l. Y. Cell Locomotion And Focal Adhesions Are Regulated By Substrate Flexibility. *Proceedings of the National academy of Sciences of the United States of America* 94(25), 1997, 13661–13665.

[129] Riveline, D. D. et al. Focal Contacts As Mechanosensors: Externally Applied Local Mechanical Force Induces Growth Of Focal Contacts By An MDIA1-dependent And ROCK-independent Mechanism. *Journal of Cell Biology* 153(6), 2001, 1175–1186.

[130] Kuo, J.-C. et al. Analysis Of The Myosin-II-responsive Focal Adhesion Proteome Reveals A Role For β-pix In Negative Regulation Of Focal Adhesion Maturation. *Nature Cell Biology* 13(4), 2011, 383–393.

[131] Lemmon, C. A. and Romer, L. H. A Predictive Model Of Cell Traction Forces Based On Cell Geometry. *Biophysical Journal* 99(9), 2010, L78–L80.

[132] Stroka, K. M. and Aranda-Espinoza, H. Neutrophils Display Biphasic Relationship Between Migration And Substrate Stiffness. *Cell Motility and the Cytoskeleton* 66(6), 2009, 328–341.

[133] Peyton, S. R. and Putnam, A. J. Extracellular Matrix Rigidity Governs Smooth Muscle Cell Motility In A Biphasic Fashion. *Journal of Cellular Physiology* 204(1), 2005, 198–209.

[134] Takakuda, K. and Miyairi, H. Tensile Behaviour Of Fibroblasts Cultured In Collagen Gel. *Biomaterials* 17(14), 1996, 1393–1397.

[135] Bischofs, I. B. and Schwarz, U. S. Cell Organization In Soft Media Due To Active Mechanosensing. *Proceedings of the National academy of Sciences of the United States of America* 100(16), 2003, 9274–9279.

[136] Kubota, Y. et al. Role Of Laminin And Basement Membrane In The Morphological Differentiation Of Human Endothelial Cells Into Capillary-like Structures. *Journal of Cell Biology* 107(4), 1988, 1589–1598.

[137] Parsa, H. et al. Uncovering The Behaviors Of Individual Cells Within A Multicellular Microvascular Community. *Proceedings of the National academy of Sciences of the United States of America* 108(12), 2011, 5133–5138.

[138] Rupp, P. A. et al. $\alpha v\beta 3$ Integrin-dependent Endothelial Cell Dynamics In Vivo. *Development* 131(12), 2004, 2887–2897.

[139] Storm, C. et al. Nonlinear Elasticity In Biological Gels. *Nature* 435(7039), 2005, 191–194.

[140] Boudou, T. et al. An Extended Relationship For The Characterization Of Young's Modulus And Poisson's Ratio Of Tunable Polyacrylamide Gels. *Biorheology* 43(6), 2006, 721–728.

[141] Rudnicki, M. S. et al. Nonlinear Strain Stiffening Is Not Sufficient To Explain How Far Cells Can Feel On Fibrous Protein Gels. *Biophysical Journal* 105(1), 2013, 11–20.

[142] Boudou, T. et al. Nonlinear Elastic Properties Of Polyacrylamide Gels: Implications For Quantification Of Cellular Forces. *Biorheology* 46(3), 2008, 191–205.

[143] Balter, A et al. The Glazier–Graner–Hogeweg Model: Extensions, Future Directions, And Opportunities For Further Study. In: *Single Cell-Based Models in Biology and Medicine*. Ed. by Anderson, A. R. A. and Rejniak, K. A. Birkhaüser, Basel, 2007, 151–167.

[144] Scianna, M. et al. A Multiscale Hybrid Approach For Vasculogenesis And Related Potential Blocking Therapies. *Progress in Biophysics & Molecular Biology* 106(2), 2011, 450–462.

[145] Vroomans, R. M. A. et al. Chemotactic Migration Of T Cells Towards Dendritic Cells Promotes The Detection Of Rare Antigens. *PLoS Computational Biology* 8(11), 2012, e1002763.

[146] Marée, A. F. M. et al. How Cells Integrate Complex Stimuli: The Effect Of Feedback From Phosphoinositides And Cell Shape On Cell Polarization And Motility. *PLoS Computational Biology* 8(3), 2012, e1002402.

[147] Marée, A. F. et al. Polarization And Movement Of Keratocytes: A Multiscale Modelling Approach. *Bulletin of Mathematical Biology* 68(5), 2006, 1169–1211.

[148] Daub, J. T. and Merks, R. M. H. A Cell-based Model Of Extracellular-matrix-guided Endothelial Cell Migration During Angiogenesis. *Bulletin of Mathematical Biology* 75(8), 2013, 1377–1399.

[149] Vernon, R. B. et al. Reorganization Of Basement-membrane Matrices By Cellular Traction Promotes The Formation Of Cellular Networks In Vitro. *Laboratory Investigation* 67(6), 1992, 536–547.

[150] Rudnicki, M. S. and Billiar, K. L. "Effective Stiffness Of Thin Nonlinear Gel Substrates". In: *IEEE -2011 37th Annual Northeast Bioengineering Conference (NEBEC)*. 2011.

[151] Tranqui, L and Tracqui, P. Mechanical Signalling And Angiogenesis. The Integration Of Cell-extracellular Matrix Couplings. *Comptes Rendus de l'Académie des Sciences - Series III* 323(1), 2000, 31–47.

[152] Merks, R. M. H. et al. Cell-oriented Modeling Of In Vitro Capillary Development. *Lecture Notes in Computer Science* 3305, 2004, 425–434.

[153] Guidolin, D. et al. Mathematical Modeling Of The Capillary-like Pattern Generated By Adrenomedullin-treated Human Vascular Endothelial Cells In Vitro. *Developmental Dynamics* 238(8), 2009, 1951–1963.

[154] Scianna, M. Multiscale Extensions Of The Cellular Potts Models: Toward A Nested-hybrid Approach. *Commun Appl Indust Math* 3(1), 2012, e–411.

[155] Davies, A. J. *The Finite Element Method: An Introduction With Partial Differential Equations*. Oxford: Oxford University Press, 2011.

[156] Oers, R. F. M. van et al. Relating Osteon Diameter To Strain. *Bone* 43(3), 2008, 476–482.

[157] Szabó, A et al. Invasion From A Cell Aggregate—the Roles Of Active Cell Motion And Mechanical Equilibrium. *Physical Biology* 9(1), 2012, 016010.

[158] Ambrosi, D. Cellular Traction As An Inverse Problem. *SIAM Journal on Applied Mathematics* 66(6), 2006, 2049–2060.

[159] Soofi, S. S. et al. The Elastic Modulus Of Matrigel^{TM} As Determined By Atomic Force Microscopy. *Journal of Structural Biology* 167(3), 2009, 216–219.

[160] Aratyn-Schaus, Y et al. Dynamic And Structural Signatures Of Lamellar Actomyosin Force Generation. *Molecular Biology of the Cell* 22(8), 2011, 1330–1339.

[161] Strang, G. *Introduction to applied mathematics*. Wellesley, MA: Wellesley-cambridge Press, 1986.

[162] Stokes, C. L. et al. Migration Of Individual Microvessel Endothelial Cells: Stochastic Model And Parameter Measurement. *Journal of Cell Science* 99 (Pt 2), 1991, 419–430.

[163] Pless, D. D. et al. Specific Cell Adhesion To Immobilized Glycoproteins Demonstrated Using New Reagents For Protein And Glycoprotein Immobilization. *Journal of Biological Chemistry* 258(4), 1983, 2340–2349.

[164] Friedl, P. and Gilmour, D. Collective Cell Migration In Morphogenesis, Regeneration And Cancer. *Nature Reviews. Molecular Cell Biology* 10(7), 2009, 445–457.

[165] Reig, G. et al. Cell Migration: From Tissue Culture To Embryos. *Development* 141(10), 2014, 1999–2013.

[166] Rogers, K. and Schier, A. Morphogen Gradients: From Generation To Interpretation. *Annual Review of Cell and Developmental Biology* 27, 2011, 377–407.

[167] Shawky, J. H. and Davidson, L. A. Tissue Mechanics And Adhesion During Embryo Development. *Developments in Biologicals* 401(1), 2015, 152–164.

[168] Garita, B. et al. Blood Flow Dynamics Of One Cardiac Cycle And Relationship To Mechanotransduction And Trabeculation During Heart Looping. *American Journal of Physiology - Heart and Circulatory Physiology* 300(3), 2011, H879–91.

[169] Aigouy, B. et al. Cell Flow Reorients The Axis Of Planar Polarity In The Wing Epithelium Of Drosophila. *Cell* 142(5), 2010, 773–786.

[170] Collinsworth, A. M. et al. Orientation And Length Of Mammalian Skeletal Myocytes In Response To A Unidirectional Stretch. *Cell and Tissue Research* 302(2), 2000, 243–251.

[171] Liu, C. et al. Effect Of Static Pre-stretch Induced Surface Anisotropy On Orientation Of Mesenchymal Stem Cells. *Cellular and Molecular Bioengineering* 7(1), 2014, 106–121.

[172] Vader, D. et al. Strain-induced Alignment In Collagen Gels. *PLOS ONE* 4(6), 2009, 6e5902.

[173] Chaubaroux, C. et al. Cell Alignment Driven By Mechanically Induced Collagen Fiber Alignment In Collagen / Alginate Coatings. *Tissue Engineering Part C* 21(9), 2015, 881–888.

[174] Klebe, R. J. et al. Cells Transmit Spatial Information By Orienting Collagen Fibers. *Matrix* 9(6), 1989, 451–458.

[175] Reinhardt, J. W. and Gooch, K. J. Agent-based Modeling Traction Force Mediated Compaction Of Cell-populated Collagen Gels Using Physically Realistic Fibril Mechanics. *Journal of Biomechanical Engineering* 136(2), 2014, 021024.

[176] Tondon, A. and Kaunas, R. The Direction Of Stretch-induced Cell And Stress Fiber Orientation Depends On Collagen Matrix Stress. *PLOS ONE* 9(2), 2014, e89592.

[177] Lee, E. J. et al. Remodeling Of Engineered Tissue Anisotropy In Response To Altered Loading Conditions. *Annals of Biomedical Engineering* 36(8), 2008, 1322–1334.

[178] Pang, Y. et al. Dynamic Quantitative Visualization Of Single Cell Alignment And Migration And Matrix Remodeling In 3D Collagen Hydrogels Under Mechanical Force. *Biomaterials* 32(15), 2011, 3776–3783.

[179] Mudera, V. C. et al. Molecular Responses Of Human Dermal Fibroblasts To Dual Cues: Contact Guidance And Mechanical Load. *Cell Motility and the Cytoskeleton* 45(1), 2000, 1–9.

[180] De, R. A. Z. and Safran, S. A. Dynamics Of Cell Orientation. *Nature Physics* 3, 2007, 655–659.

[181] Bischofs, I. B. and Schwarz, U. S. Collective Effects In Cellular Structure Formation Mediated By Compliant Environments: A Monte Carlo Study. *Acta Biomaterialia* 2(3), 2006, 253–265.

[182] Oers, R. F. M. van et al. Mechanical Cell-matrix Feedback Explains Pairwise And Collective Endothelial Cell Behavior In Vitro. *PLoS Computational Biology* 10(8), 2014, e1003774.

[183] Panorchan, P. et al. Probing Intercellular Interactions Between Vascular Endothelial Cadherin Pairs At Single-molecule Resolution And In Living Cell. *Journal of Molecular Biology* 358(3), 2006, 665–674.

[184] Pelham, R. K. and Wang, Y l. Cell Locomotion And Focal Adhesions Are Regulated By The Mechanical Properties Of The Substrate. *The Biological Bulletin* 194(3), 1998, 348.

[185] Byfield, F. J. et al. OxLDL Increases Endothelial Stiffness, Force Generation, And Network Formation. *Journal of Lipid Research* 47(4), 2006, 715–723.

[186] Haston, W. S. et al. The Orientation Of Fibroblasts And Neutrophils On Elastic Substrata. *Experimental Cell Research* 146(1), 1983, 117–126.

[187] Roy, P. et al. Exertion Of Tractional Force Requires The Coordinated Up-regulation Of Cell Contractility And Adhesion. *Cell Motility and the Cytoskeleton* 43(1), 1999, 23–34.

[188] Belle, J. A. Y. et al. Stretch-induced Intussuceptive And Sprouting Angiogenesis In The Chick Chorioallantoic Membrane. *Microvascular Research* 95, 2014, 60–67.

[189] Klumpers, D. D. et al. The Effect Of Growth-mimicking Continuous Strain On The Early Stages Of Skeletal Development In Micromass Culture. *PLOS ONE* 10(4), 2015, 1–11.

[190] Aghvami, M. et al. Multiscale Mechanical Simulations Of Cell Compacted Collagen Gels. *Journal of Biomechanical Engineering* 135(7), 2013, 0710041–0710049.

[191] Albert, P. J. and Schwarz, U. S. Dynamics Of Cell Shape And Forces On Micropatterned Substrates Predicted By A Cellular Potts Model. *Biophysical Journal* 106(11), 2014, 2340–2352.

[192] Albert, P. J. and Schwarz, U. S. Dynamics Of Cell Ensembles On Adhesive Micropatterns: Bridging The Gap Between Single Cell Spreading And Collective Cell Migration. *PLoS Computational Biology* 12(4), 2016, 1–34.

[193] Kong, D. et al. Stability Of Adhesion Clusters And Cell Reorientation Under Lateral Cyclic Tension. *Biophysical Journal* 95(8), 2008, 4034–4044.

[194] Zhong, Y. et al. Frequency-dependent Focal Adhesion Instability And Cell Reorientation Under Cyclic Substrate Stretching. *Cellular and Molecular Bioengineering* 4(3), 2011, 442–456.

[195] Glazier, J. A. et al. Magnetization To Morphogenesis: A Brief History Of The Glazier-Graner-Hogeweg Model. *Single Cell-Based Models in Biology and Medicine*, 2007, 79–106.

[196] Serra, J. *Image Analysis And Mathematical Morphology*. Inc. Orlando, FL, USA: Academic Press, 1983.

[197] Bresenham, J. E. Algorithm For Computer Control Of A Digital Plotter. *IBM Systems Journal* 4(1), 1965, 25–30.

[198] Califano, J. P. and Reinhart-King, C. A. Substrate Stiffness And Cell Area Predict Cellular Traction Stresses In Single Cells And Cells In Contact. *Cellular and Molecular Bioengineering* 3(1), 2010, 68–75.

[199] Ghibaudo, M. et al. Traction Forces And Rigidity Sensing Regulate Cell Functions. *Soft Matter* 4, 9 2008, 1836–1843.

[200] Engler, A. et al. Substrate Compliance Versus Ligand Density In Cell On Gel Responses. *Biophysical Journal* 86(1), 2004, 617–628.

[201] Mullen, C. A. et al. The Effect Of Substrate Stiffness, Thickness, And Cross-linking Density On Osteogenic Cell Behavior. *Biophysical Journal* 108(7), 2015, 1604–1612.

[202] Yeung, T. et al. Effects Of Substrate Stiffness On Cell Morphology, Cytoskeletal Structure, And Adhesion. *Cell Motility and the Cytoskeleton* 60(1), 2005, 24–34.

[203] Georges, P. C. and Janmey, P. A. Cell Type-specific Response To Growth On Soft Materials. *Journal of Applied Physiology: Respiratory, Environmental and Exercise Physiology* 98(4), 2005, 1547–1553.

[204] Isenberg, B. C. et al. Vascular Smooth Muscle Cell Durotaxis Depends On Substrate Stiffness Gradient Strength. *Biophysical Journal* 97(5), 2009, 1313–1322.

[205] Vincent, L. et al. Mesenchymal Stem Cell Durotaxis Depends On Substrate Stiffness Gradient Strength. *Biotechnology Journal* 8(4), 2013, 472–484.

[206] Jansen, K. A. et al. A Guide To Mechanobiology: Where Biology And Physics Meet. *Biochimica et Biophysica Acta* 1853(11 Pt B), 2015, 3043–3052.

[207] Bershadsky, A. et al. Adhesion-dependent Cell Mechanosensitivity. *Annual Review Cell Developmental Biology* 19, 2003, 677–695.

[208] Rio, A. et al. Stretching Single Talin Rod Molecules Activates Vinculin Binding. *Science* 323(5914), 2009, 638–642.

[209] Gallant, N. D. et al. Cell Adhesion Strengthening: Contributions Of Adhesive Area, Integrin Binding, And Focal Adhesion Assembly. *Molecular Biology of the Cell* 16(9), 2005, 4329–4340.

[210] Kong, F. et al. Demonstration Of Catch Bonds Between An Integrin And Its Ligand. *The Journal of Cell Biology* 185(7), 2009, 1275–1284.

[211] Dembo, M et al. The Reaction-limited Kinetics Of Membrane-to-surface Adhesion And Detachment. *Proceedings of the Royal Society of London. Series B, Biological sciences* 234(1274), 1988, 55–83.

[212] Ezzel, R. et al. Vinculin Promotes Cell Spreading By Mechanically Coupling Integrins To The Cytoskeleton. *Experimental Cell Research* 231(1), 1997, 14–26.

[213] Broussard, J. A. et al. Asymmetric Focal Adhesion Disassembly In Motile Cells. *Current Opinion in Cell Biology* 20(1), 2008, 85–90.

[214] Prager-Khoutorsky, M. et al. Fibroblast Polarization Is A Matrix-rigidity-dependent Process Controlled By Focal Adhesion Mechanosensing. *Nature Cell Biology* 13(12), 2011, 1457–1465.

[215] Plotnikov, S. V. et al. Force Fluctuations Within Focal Adhesions Mediate Ecm-rigidity Sensing To Guide Directed Cell Migration. *Cell* 151(7), 2012, 1513–1527.

[216] Chen, Y. et al. Orientation-specific Responses To Sustained Uniaxial Stretching In Focal Adhesion Growth And Turnover. *Proceedings of the National academy of Sciences of the United States of America* 110(26), 2013, E2352–61.

[217] Kim, H. Y. et al. Apical Constriction Initiates New Bud Formation During Monopodial Branching Of The Embryonic Chicken Lung. *Development* 140(15), 2013, 3146–3155.

[218] Shenoy, V. B. et al. A Chemo-mechanical Free-energy-based Approach To Model Durotaxis And Extracellular Stiffness-dependent Contraction And Polarization Of Cells. *Interface Focus* 6(1), 2015, 20150067.

[219] Ronan, W. et al. Cellular Contractility And Substrate Elasticity: A Numerical Investigation Of The Actin Cytoskeleton And Cell Adhesion. *Biomechanics and Modeling in Mechanobiology* 13(2), 2014, 417–435.

[220] Vernerey, F. J. and Farsad, M. A Mathematical Model Of The Coupled Mechanisms Of Cell Adhesion , Contraction And Spreading. *Journal of Mathematical Biology* 68(4), 2014, 989–1022.

[221] Stolarska, M. A. and Rammohan, A. R. Center Or Periphery? Modeling The Effects Of Focal Adhesion Placement During Cell Spreading. *PLOS ONE* 12(2), 2017, 1–22.

[222] Lazopoulos KA, S. D. Durotaxis As An Elastic Stability Phenomenon. *Journal of Biomechanics* 41(6), 2008, 1289–1294.

[223] Harland, B. et al. Adhesion Dynamics And Durotaxis In Migrating Cells. *Physical Biology* 8(1), 2011, 015011.

[224] Yu, G. et al. Phenomenological Modeling Of Durotaxis. *Physical Review E* 96, 2017, 010402.

[225] Kim, M.-C. et al. Computational Modeling Of Three-dimensional Ecm-rigidity Sensing To Guide Directed Cell Migration. *Proceedings of the National academy of Sciences of the United States of America* 115(3), 2018, E390–E999.

[226] Dokukina, I. V. and Gracheva, M. E. A Model Of Fibroblast Motility On Substrates With Different Rigidities. *Biophysical Journal* 98(12), 2010, 2794–2803.

[227] Stefanoni, F. et al. A Numerical Model For Durotaxis. *Journal of Theoretical Biology* 280(1), 2011, 150–158.

[228] Aubry, D et al. Mechanical Link Between Durotaxis, Cell Polarity And Anisotropy During Cell Migration. *Physical Biology* 12(2), 2015, 026008.

[229] Allena, R et al. Mathematical Biosciences A Cellular Potts Model Of Single Cell Migration In Presence Of Durotaxis. *Mathematical Biosciences* 275, 2016, 57–70.

[230] Novikova, E. A. et al. Persistence-driven Durotaxis: Generic, Directed Motility In Rigidity Gradients. *Physical Review Letters* 118(7), 2017, 078103.

[231] Novikova, E. A. and Storm, C. Contractile Fibers And Catch-bond Clusters: A Biological Force Sensor? *Biophysical Journal* 105(6), 2013, 1336–1345.

[232] Balcioglu, H. E. et al. The Integrin Expression Profile Modulates Orientation And Dynamics Of Force Transmission At Cell–matrix Adhesions. *Journal of Cell Science* 128(7), 2015, 1316–1326.

[233] Asano, S. et al. Matrix Stiffness Regulates Migration Of Human Lung Fibroblasts. *Physiological Reports* 5(9), 2017.

[234] Paszek, M. J. et al. Tensional Homeostasis And The Malignant Phenotype. *Cancer Cell* 8(3), 2005, 241–254.

[235] Dumbauld, D. W. et al. How Vinculin Regulates Force Transmission. *Proceedings of the National academy of Sciences of the United States of America* 110(24), 2013, 9788–9793.

[236] Goffin, J. M. et al. Focal Adhesion Size Controls Tension-dependent Recruitment Of α -smooth Muscle Actin To Stress Fibers. *The Journal of Cell Biology* 172(2), 2006, 259–268.

[237] Uyeda, T. Q. P. et al. Stretching Actin Filaments Within Cells Enhances Their Affinity For The Myosin II Motor Domain. *PLOS ONE* 6(10), 2011, e26200.

[238] Ma, X. and Adelstein, R. S. In Vivo Studies On Nonmuscle Myosin II Expression And Function In Heart Development. *Frontiers in Bioscience* 17, 2012, 545–555.

[239] Sugiura, T et al. Changes In Myosin Heavy Chain Isoform Expression Of Overloaded Rat Skeletal Muscles. *The International Journal of Biochemistry* 25(11), 1993, 1609–1613.

[240] Norstrom, M. et al. Unconventional Processive Mechanics Of Non-muscle Myosin II-B. *Journal of Biological Chemistry* 285(34), 2010, 26326–26334.

[241] Kelley, C. A. et al. Xenopus Nonmuscle Myosin Heavy Chain Isoforms Have Different Subcellular Localizations And Enzymatic Activities. *Journal of Cell Biology* 134(3), 1996, 675–687.

[242] Vogel, S. K. et al. Myosin Motors Fragment And Compact Membrane-bound Actin Filaments. *eLife* 2, 2013, e00116.

[243] Wong, S. et al. Fibroblasts Probe Substrate Rigidity With Filopodia Extensions Before Occupying An Area. *Proceedings of the National academy of Sciences of the United States of America* 111(48), 2014, 1–6.

[244] Sabbir, M. G. et al. DLC1 Interaction With Non-muscle Myosin Heavy Chain II-A (MYH9) And RAC1 Activation. *Biology Open* 5(4), 2016, 452–460.

[245] Jiang, L. et al. Cells Sensing Mechanical Cues: Stiffness Influences The Lifetime Of Cell-extracellular Matrix Interactions By Affecting The Loading Rate. *ACS Nano* 10(1), 2016, 207–217.

[246] Mcbeath, R. et al. Cell Shape, Cytoskeletal Tension, And RhoA Regulate Stem Cell Lineage Commitment. *Developmental Cell* 6(4), 2004, 483–495.

[247] Roca-cusachs, P. et al. Clustering Of $\alpha 5\beta 1$ Integrins Determines Adhesion Strength Whereas $\alpha v\beta 3$ And Talin Enable Mechanotransduction. *Proceedings of the National academy of Sciences of the United States of America* 106(38), 2009, 16245–16250.

[248] Ni, Y. and Chiang, M. Y. M. Cell Morphology And Migration Linked To Substrate Rigidity. *Soft Matter* 3(10), 2007, 1285–1292.

[249] Kabaso, D. et al. Theoretical Model For Cellular Shapes Driven By Protrusive And Adhesive Forces. *PLoS Computational Biology* 7(5), 2011, e1001127.

[250] Welf, E. S. et al. A Spatial Model For Integrin Clustering As A Result Of Feedback Between Integrin Activation And Integrin Binding. *Biophysical Journal* 103(6), 2012, 1379–1389.

[251] Humphries, J. D. et al. Vinculin Controls Focal Adhesion Formation By Direct Interactions With Talin And Actin. *Journal of Cell Biology* 179(5), 2007, 1043–1057.

[252] Sawada, Y. et al. Force Sensing By Mechanical Extension Of The SRC Family Kinase Substrate P130CAS. *Cell* 127(5), 2006, 1015–1026.

[253] Bos, J. L. et al. The Role Of RAP1 In Integrin-mediated Cell Adhesion. *Biochemical Society Transactions* 31(Pt 1), 2003, 83–86.

[254] Ali, O et al. Cooperativity Between Integrin Activation And Mechanical Stress Leads To Integrin Clustering. *Biophysical Journal* 100(11), 2011, 2595–2604.

[255] Magno, R. et al. The Biophysical Nature Of Cells: Potential Cell Behaviours Revealed By Analytical And Computational Studies Of Cell Surface Mechanics. *BMC Biophysics* 8(8), 2015.

[256] Boettiger, D. Quantitative Measurements Of Integrin-mediated Adhesion To Extracellular Matrix. *Methods in Enzymology* 426, 2007, 1–25.

[257] Rens, E. G. and Merks, R. M. H. Cell Contractility Facilitates Alignment Of Cells And Tissues To Static Uniaxial Stretch. *Biophysical Journal* 112(4), 2017, 755–766.

[258] Changede, R. and Sheetz, M. Prospects & Overviews Integrin And Cadherin Clusters: A Robust Way To Organize Adhesions For Cell Mechanics. *Bioessays* 93(1), 2016, 1–12.

[259] Knorr, M. et al. Stochastic Actin Dynamics In Lamellipodia Reveal Parameter Space For Cell Type Classification. *Soft Matter* 7, 2011, 3192–3203.

[260] Nakamura, T. and Hamada, H. Left-right Patterning: Conserved And Divergent Mechanisms. *Development* 139(18), 2012, 3257–3262.

[261] Schier, A. F. Nodal Morphogens. *Cold Spring Harbor Perspectives in Biology* 1(5), 2009, a003459.

[262] Shiratori, H. and Hamada, H. The Left-right Axis In The Mouse: From Origin To Morphology. *Development* 133(11), 2006, 2095–2104.

[263] Long, S. et al. The Zebrafish Nodal-related Gene Southpaw Is Required For Visceral And Diencephalic Left-right Asymmetry. *Development* 130(11), 2003, 2303–2316.

[264] Nakayama, K. Furin: A Mammalian Subtilisin/KEX2p-like Endoprotease Involved In Processing Of A Wide Variety Of Precursor Proteins. *The Biochemical Journal* 327(3), 1997, 625–635.

[265] Thomas, G. Furin At The Cutting Edge: From Protein Traffic To Embryogenesis And Disease. *Nature Reviews. Molecular Cell Biology* 3(10), 2002, 753–766.

[266] Noel, E. S. et al. A Nodal-independent And Tissue-intrinsic Mechanism Controls Heart-looping Chirality. *Nature Communications* 4(2754), 2013.

[267] Walker, M. B. et al. Zebrafish Furin Mutants Reveal Intricacies In Regulating Endothelin1 Signaling In Craniofacial Patterning. *Developments in Biologicals* 295(1), 2006, 194–205.

[268] Nakamura, T. et al. Generation Of Robust Left-right Asymmetry In The Mouse Embryo Requires A Self-enhancement And Lateral-inhibition System. *Developmental Cell* 11(4), 2006, 495–504.

[269] Berezhkovskii, A. M. et al. How Long Does It Take To Establish A Morphogen Gradient? *Biophysical Journal* 99(8), 2010, L59–L61.

[270] Muller, P. et al. Differential Diffusivity Of Nodal And Lefty Underlies A Reaction-diffusion Patterning System. *Science* 336(6082), 2012, 721–724.

[271] Mathews, C. et al. *Biochemistry*. 3rd. Prentice Hall, 1999.

[272] Schwanhausser, B. et al. Global Quantification Of Mammalian Gene Expression Control. *Nature* 473(7347), 2011, 337–342.

[273] Zhang, Y. et al. Protein Secretion In Human Mammary Epithelial Cells Following Her1 Receptor Activation: Influence Of HER2 And HER3 Expression. *BMC Cancer* 11(69), 2011.

[274] Davies, J. *Mechanisms Of Morphogenesis: The Creation Of Biological Form*. Elsevier Academic Press, 2005. Chap. Epithelial Morphogenesis: Branching.

[275] Horowitz, A. and Simons, M. Branching Morphogenesis. *Circulation Research* 103(8), 2008, 784–795.

[276] Ochoa-Espinosa, A. and Affolter, M. Branching Morphogenesis: From Cells To Organs And Back. *Cold Spring Harbor Perspectives in Biology* 4(10), 2012, a008243.

[277] Varner, V. D. and Nelson, C. M. Cellular And Physical Mechanisms Of Branching Morphogenesis. *Development* 141(14), 2014, 2750–2759.

[278] Wang, S. et al. Patterned Cell And Matrix Dynamics In Branching Morphogenesis. *The Journal of Cell Biology* 216(3), 2017, 559–570.

[279] Davies, J. A. Do Different Branching Epithelia Use A Conserved Developmental Mechanism? *Bioessays* 24(10), 2002, 937–948.

[280] Iber, D. and Menshykau, D. The Control Of Branching Morphogenesis. *Open Biology* 3(9), 2013, 130088.

[281] Metzger, R. J. et al. The Branching Programme Of Mouse Lung Development. *Nature* 453(7196), 2008, 745–750.

[282] Watanabe, T. and Costantini, F. Real-time Analysis Of Ureteric Bud Branching Morphogenesis In Vitro. *Developments in Biologicals* 271(1), 2004, 98–108.

[283] Gjorevski, N. and Nelson, C. M. Integrated Morphodynamic Signalling Of The Mammary Gland. *Nature Reviews. Molecular Cell Biology* 12(9), 2011, 581–593.

[284] Villasenor, A. et al. Epithelial Dynamics Of Pancreatic Branching Morphogenesis. *Development* 137(24), 2010, 4295–4305.

[285] Nogawa, H. et al. Bud Formation Precedes The Appearance Of Differential Cell Proliferation During Branching Morphogenesis Of Mouse Lung Epithelium In Vitro. *Developmental Dynamics* 213(2), 1998, 228–235.

[286] Affolter, M. et al. Tissue Remodelling Through Branching Morphogenesis. *Nature Reviews. Molecular Cell Biology* 10, 2009, 831–842.

[287] Qiao, J. et al. Branching Morphogenesis Independent Of Mesenchymal–epithelial Contact In The Developing Kidney. *Proceedings of the National academy of Sciences of the United States of America* 96(13), 1999, 7330–7335.

[288] Nogawa, H. and Ito, T. Branching Morphogenesis Of Embryonic Mouse Lung Epithelium In Mesenchyme-free Culture. *Development* 121(4), 1995, 1015–1022.

[289] Greggio, C. et al. Artificial Three-dimensional Niches Deconstruct Pancreas Development In Vitro. *Development* 140(21), 2013, 4452–4462.

[290] Ben-Jacob, E. and Garik, P. The Formation Of Patterns In Non-equilibrium Growth. *Nature* 343(6258), 1990, 523–530.

[291] Måløy, K. J. et al. Viscous Fingering Fractals In Porous Media. *Physical Review Letters* 55(24), 1985, 2688.

[292] Family, F. *Growth By Gradients: Fractal Growth And Pattern Formation In A Laplacian Field*. Ed. by Landau, D. et al. Vol. 33. Springer, 1988, 65–75.

[293] Lubkin, S. R. and Murray, J. D. A Mechanism For Early Branching In Lung Morphogenesis. *Journal of Mathematical Biology* 34(1), 1995, 77–94.

[294] Halsey, T. C. Diffusion-limited Aggregation: A Model For Pattern Formation. *Physics Today* 53(11), 2000.

[295] Matsushita, M. and Fujikawa, H. Diffusion-limited Growth In Bacterial Colony Formation. *Physica A: Statistical Mechanics and its Applications* 168(1), 1990, 498–506.

[296] Gerlee, P. and Anderson, A. R. Diffusion-limited Tumour Growth: Simulations And Analysis. *Mathematical Biosciences and Engineering* 7(2), 2010, 385.

[297] Hartmann, D. and Miura, T. Modelling In Vitro Lung Branching Morphogenesis During Development. *Journal of Theoretical Biology* 242(4), 2006, 862–872.

[298] Bellusci, S et al. Fibroblast Growth Factor 10 (FGF10) And Branching Morphogenesis In The Embryonic Mouse Lung. *Development* 124(23), 1997, 4867–4878.

[299] Hirashima, T. et al. Mechanisms For Split Localization Of FGF10 Expression In Early Lung Development. *Developmental Dynamics* 238(11), 2009, 2813–2822.

[300] Menshykau, D. et al. Branch Mode Selection During Early Lung Development. *PLoS Computational Biology* 8(2), 2012, e1002377.

[301] Wittwer, L. D. et al. Simulating Organogenesis In Comsol: Phase-field Based Simulations Of Embryonic Lung Branching Morphogenesis. *Proceedings of COMSOL Conference 2016 Munich*, 2016.

[302] Menshykau, D. and Iber, D. Kidney Branching Morphogenesis Under The Control Of A Ligand–receptor-based Turing Mechanism. *Physical Biology* 10(4), 2013, 046003.

[303] Hirashima, T. et al. Dynamic Modeling Of Branching Morphogenesis Of Ureteric Bud In Early Kidney Development. *Journal of Theoretical Biology* 259(1), 2009, 58–66.

[304] Davies, J. A. et al. A Self-avoidance Mechanism In Patterning Of The Urinary Collecting Duct Tree. *BMC Developmental Biology* 14(35), 2014.

[305] Pavlovich, A. et al. Mammary Branch Initiation And Extension Are Inhibited By Separate Pathways Downstream Of TGFβ In Culture. *Experimental Cell Research* 317(13), 2011, 1872–1884.

[306] Volckaert, T. et al. Localized FGF10 Expression Is Not Required For Lung Branching Morphogenesis But Prevents Differentiation Of Epithelial Progenitors. *Development* 140(18), 2013, 3731–3742.

[307] Adivarahan, S. et al. Dynamic Image-based Modelling Of Kidney Branching Morphogenesis. *In: Gupta A., Henzinger T.a. (eds) Computational Methods In Systems Biology. Cmsb 2013. Lecture Notes In Computer Science.* 8130, 2013, 106–119.

[308] Dahl-Jensen, S. B. et al. Short-range Growth Inhibitory Signals From The Epithelium Can Drive Non-stereotypic Branching In The Pancreas. *Physical Biology* 13(1), 2016, 016007.

[309] Eden, M. A Two-dimensional Growth Process. *Dynamics of Fractal Surfaces* 4, 1961, 223–239.

[310] Graham, R. L. An Efficient Algorithm For Determining The Convex Hull Of A Finite Planar Set. *Information Processing Letters* 1(4), 1972, 132–133.

[311] Moore, K. A. et al. Control Of Embryonic Lung Branching Morphogenesis By The Rho Activator, Cytotoxic Necrotizing Factor 1. *The Journal of surgical research* 104(2), 2002, 95–100.

[312] Moore, K. A. et al. Control Of Basement Membrane Remodeling And Epithelial Branching Morphogenesis In Embryonic Lung By Rho And Cytoskeletal Tension. *Developmental Dynamics* 232(2), 2005, 268–281.

[313] Soriano, J. et al. TGF-beta1 Induces Morphogenesis Of Branching Cords By Cloned Mammary Epithelial Cells At Subpicomolar Concentrations. *Biochemical and Biophysical Research Communications* 220(3), 1996, 879–885.

[314] Montesano, R. et al. Low Concentrations Of Transforming Growth Factor-β-1 Induce Tubulogenesis In Cultured Mammary Epithelial Cells. *BMC Developmental Biology* 7(7), 2007.

[315] Joseph, H. et al. Overexpression Of A Kinase-deficient Transforming Growth Factor-β Type Li Receptor In Mouse Mammary Stroma Results In Increased Epithelial Branching. *Molecular Biology of the Cell* 10(4), 1999, 1221–1234.

[316] Piscione, T. D. et al. BMP-2 And OP-1 Exert Direct And Opposite Effects On Renal Branching Morphogenesis. *The American Journal of Physiology* 273(6 Pt 2), 1997, F961–75.

[317] Meyer, T. N. et al. Spatiotemporal Regulation Of Morphogenetic Molecules During In Vitro Branching Of The Isolated Ureteric Bud: Toward A Model Of Branching Through Budding In The Developing Kidney. *Developments in Biologicals* 275(1), 2004, 44–67.

[318] Daley, W. P. et al. BTBD7 Is Essential For Region-specific Epithelial Cell Dynamics And Branching Morphogenesis In Vivo. *Development* 144(12), 2017, 2200–2211.

[319] Martin, K. C. et al. Symmetry-breaking In Branching Epithelia: Cells On Micro-patterns Under Flow Challenge The Hypothesis Of Positive Feedback By A Secreted Autocrine Inhibitor Of Motility. *Journal of Anatomy* 230(6), 2017, 766–774.

[320] Moses, H. and Barcellos-Hoff, M. H. TGF-beta Biology In Mammary Development And Breast Cancer. *Cold Spring Harbor Perspectives in Biology* 3(1), 2011, 1–14.

[321] Daley, W. P. et al. A Focal Adhesion Protein-based Mechanochemical Checkpoint Regulates Cleft Progression During Branching Morphogenesis. *Developmental Dynamics* 240(9), 2011, 2069–2083.

[322] Brownfield, D. G. et al. Patterned Collagen Fibers Orient Branching Mammary Epithelium Through Distinct Signaling Modules. *Current Biology* 23(8), 2013, 703–709.

[323] Simian, M et al. The Interplay Of Matrix Metalloproteinases, Morphogens And Growth Factors Is Necessary For Branching Of Mammary Epithelial Cells. *Development* 128(16), 2001, 3117–3131.

[324] Lawrence, D. A. et al. Normal Embryonic Fibroblasts Release Transforming Growth Factor In A Latent Form. *Journal of Cellular Physiology* 121(1), 1984, 184–188.

[325] Hinz, B. The Extracellular Matrix And Transforming Growth Factor-β1: Tale Of A Strained Relationship. *Matrix Biology* 47, 2015, 54–65.

[326] Gjorevski, N. and Nelson, C. M. Endogenous Patterns Of Mechanical Stress Are Required For Branching Morphogenesis. *Integrative Biology* 2(9), 2010, 424–34.

[327] Galler, B. A. and Fisher, M. J. An Improved Equivalence Algorithm. *Communications of the ACM* 7(5), 1964, 301–303.

[328] Guidolin, D. et al. A New Image Analysis Method Based On Topological And Fractal Parameters To Evaluate The Angiostatic Activity Of Docetaxel By Using The Matrigel Assay In Vitro. *Microvascular Research* 67(2), 2004, 117–124.

[329] Dougherty, E. R. and Lotufo, R. A. *Hands-on Morphological Image Processing*. Vol. 59. SPIE press, 2003.

[330] Filatov, M. V. et al. A Comparison Between Coral Colonies Of The Genus Madracis And Simulated Forms. *Proceedings of the National academy of Sciences of the United States of America* 277(1700), 2010, 3555–3561.

[331] Chen, D.-Y. et al. A Cell Migration Tracking Tool Supports Coupling Of Tissue Rotation To Elongation. *Cell Reports* 21(3), 2017, 559 –569.

[332] Soiné, J. R. et al. Measuring Cellular Traction Forces On Non-planar Substrates. *Interface Focus* 6(5), 2016, 20160024.

[333] Mulligan, J. A. et al. Measurement Of Dynamic Cell-induced 3D Displacement Fields In Vitro For Traction Force Optical Coherence Microscopy. *Biomedical Optics Express* 8(2), 2017, 1152–1171.

[334] Kanchanawong, P. et al. Nanoscale Architecture Of Integrin-based Cell Adhesions. *Nature* 468(7323), 2010, 580–584.

[335] Thomas, W. E. et al. Biophysics Of Catch Bonds. *Annual Review of Biophysics* 37, 2008, 399–416.

[336] Krieg, M et al. Tensile Forces Govern Germ-layer Organization In Zebrafish. *Nature Cell Biology* 10(4), 2008, 429–436.

[337] Osborne, J. M. et al. Comparing Individual-based Approaches To Modelling The Self-organization Of Multicellular Tissues. *PLoS Computational Biology* 13(2), 2017, e1005387.

[338] Boas, S. E. et al. A Global Sensitivity Analysis Approach For Morphogenesis Models. *BMC Systems Biology* 9(85), 2015.

[339] Foteinopoulos, P. and Mulder, B. M. A Microtubule-based Minimal Model For Spontaneous And Persistent Spherical Cell Polarity. *PLOS ONE* 12(9), 2017, e0184706.

[340] Hakkinen, K. M. et al. Direct Comparisons Of The Morphology, Migration, Cell Adhesions, And Actin Cytoskeleton Of Fibroblasts In Four Different Three-dimensional Extracellular Matrices. *Tissue Engineering Part A* 17(5-6), 2010, 713–724.

[341] Stein, A. M. et al. The Micromechanics Of Three-dimensional Collagen-I Gels. *Complexity* 16(4), 2011, 22–28.

[342] Wang, H. et al. Long-range Force Transmission In Fibrous Matrices Enabled By Tension-driven Alignment Of Fibers. *Biophysical Journal* 107(11), 2014, 2592–2603.

[343] Lee, B. et al. A Three-dimensional Computational Model Of Collagen Network Mechanics. *PLOS ONE* 9(11), 2014, e111896.

[344] Holmes, W. R. and Edelstein-Keshet, L. Analysis Of A Minimal Rho-GTPase Circuit Regulating Cell Shape. *Physical Biology* 13(4), 2016, 046001.

[345] Ladoux, B. et al. Front–rear Polarization By Mechanical Cues: From Single Cells To Tissues. *Trends in Cell Biology* 26(6), 2016, 420–433.

[346] Hinz, B. Tissue Stiffness, Latent TGF-β1 Activation, And Mechanical Signal Transduction: Implications For The Pathogenesis And Treatment Of Fibrosis. *Current Rheumatology Reports* 11(2), 2009, 120–126.

[347] Cockerill, M. et al. Mechanosensitivity Of The 2nd Kind: TGF-β Mechanism Of Cell Sensing The Substrate Stiffness. *PLOS ONE* 10(10), 2015, e0139959.

[348] Pang, M. et al. Substrate Stiffness Promotes Latent TGF-β1 Activation In Hepatocellular Carcinoma. *Biochemical and Biophysical Research Communications* 483(1), 2017, 553–558.

[349] Klingberg, F. et al. Prestress In The Extracellular Matrix Sensitizes Latent TGF-β1 For Activation. *Journal of Cell Biology* 207(2), 2014, 283–297.

[350] Wells, R. G. and Discher, D. E. Matrix Elasticity, Cytoskeletal Tension, And TGF-β: The Insoluble And Soluble Meet. *Science Signaling* 1(10), 2008, pe13.

[351] LaValley, D. J. et al. Matrix Stiffness Enhances VEGFR-2 Internalization, Signaling, And Proliferation In Endothelial Cells. *Convergent Science Physical Oncology* 3(4), 2017, 044001.

[352] Manibog, K. et al. Resolving The Molecular Mechanism Of Cadherin Catch Bond Formation. *Nature Communications* 5(3941), 2014.

[353] Kaunas, R et al. Cooperative Effects Of Rho And Mechanical Stretch On Stress Fiber Organization. *Proceedings of the National academy of Sciences of the United States of America* 102(44), 2005, 15895–15900.

[354] Iba, T. and Sumpio, B. E. Morphological Response Of Human Endothelial Cells Subjected To Cyclic Strain In Vitro. *Microvascular Research* 42(3), 1991, 245–254.

[355] Ray, A. et al. Anisotropic Forces From Spatially Constrained Focal Adhesions Mediate Contact Guidance Directed Cell Migration. *Nature Communications* 8(14923), 2017.

[356] Ristori, T et al. Efficient Computational Simulation Of Actin Stress Fiber Remodeling. *Computer Methods in Biomechanics and Biomedical Engineering* 19(12), 2016, 1347–1358.

[357] Faust, U. et al. Cyclic Stress At Mhz Frequencies Aligns Fibroblasts In Direction Of Zero Strain. *PLOS ONE* 6(12), 2011, e28963.

[358] Liu, B. et al. Role Of Cyclic Strain Frequency In Regulating The Alignment Of Vascular Smooth Muscle Cells In Vitro. *Biophysical Journal* 94(4), 2008, 1497–1507.

[359] Wang, L. et al. Patterning Cellular Alignment Through Stretching Hydrogels With Programmable Strain Gradients. *ACS Applied Materials & Interfaces* 7(27), 2015, 15088–15097.

[360] Sun, J. et al. Geometric Control Of Capillary Architecture Via Cell-matrix Mechanical Interactions. *Biomaterials* 35(10), 2014, 3273–3280.

[361] Chaudhuri, O. et al. Extracellular Matrix Stiffness And Composition Jointly Regulate The Induction Of Malignant Phenotypes In Mammary Epithelium. *Nature Materials* 13(10), 2014, 970–978.

[362] Labernadie, A. et al. A Mechanically Active Heterotypic E-cadherin/N-cadherin Adhesion Enables Fibroblasts To Drive Cancer Cell Invasion. *Nature Cell Biology* 19(3), 2017, 224–237.

[363] Amack, J. D. and Manning, M. L. Knowing The Boundaries: Extending The Differential Adhesion Hypothesis In Embryonic Cell Sorting. *Science* 338(6104), 2012, 212–215.

[364] Ferreira, R. R. and Vermot, J. The Balancing Roles Of Mechanical Forces During Left-right Patterning And Asymmetric Morphogenesis. *Mechanisms of Development* 144(Pt A), 2017, 71–80.

[365] Dias, A. S. et al. Somites Without A Clock. *Science* 343(6172), 2014, 791–795.